


Fall 12-16-2016

Zirconium Diboride, Hexagonal Boron Nitride, and Amorphous Alumina Thin Films for High Temperature Applications

David Murdock Stewart
University of Maine, dmsventi@gmail.com

Follow this and additional works at: <http://digitalcommons.library.umaine.edu/etd>

 Part of the [Ceramic Materials Commons](#), [Nanoscience and Nanotechnology Commons](#), [Other Materials Science and Engineering Commons](#), and the [Physics Commons](#)

Recommended Citation

Stewart, David Murdock, "Zirconium Diboride, Hexagonal Boron Nitride, and Amorphous Alumina Thin Films for High Temperature Applications" (2016). *Electronic Theses and Dissertations*. 2534.
<http://digitalcommons.library.umaine.edu/etd/2534>

This Open-Access Dissertation is brought to you for free and open access by DigitalCommons@UMaine. It has been accepted for inclusion in Electronic Theses and Dissertations by an authorized administrator of DigitalCommons@UMaine.

**ZIRCONIUM DIBORIDE, HEXAGONAL BORON NITRIDE, AND AMORPHOUS
ALUMINA THIN FILMS FOR HIGH TEMPERATURE APPLICATIONS**

by

David M. Stewart

B.S. University of Florida, 2011

A DISSERTATION

Submitted in Partial Fulfillment of the

Requirements for the Degree of

Doctor of Philosophy

(in Physics)

The Graduate School

The University of Maine

December 2016

Advisory Committee:

Robert J. Lad, Professor of Physics and Astronomy & LASST, Advisor

Scott Collins, Professor of Chemistry & LASST

Brian Frederick, Associate Professor of Chemistry & LASST

Robert W. Meulenberg, Associate Professor of Physics and Astronomy & LASST

MacKenzie R. Stetzer, Assistant Professor of Physics and Astronomy

DISSERTATION ACCEPTANCE STATEMENT

On behalf of the Graduate Committee for David M. Stewart I affirm that this manuscript is the final and accepted dissertation. Signatures of all committee members are on file with the Graduate School at the University of Maine, 42 Stodder Hall, Orono, Maine.

Robert J. Lad, Professor of Physics and Astronomy & LASST

December 18, 2016

LIBRARY RIGHTS STATEMENT

In presenting this dissertation in partial fulfillment of the requirements for an advanced degree at the University of Maine, I agree that the Library shall make it freely available for inspection. I further agree that permission for “fair use” copying of this dissertation for scholarly purposes may be granted by the Librarian. It is understood that any copying or publication of this dissertation for financial gain shall not be allowed without my permission.

Signature: 

Date: December 18, 2016

ZIRCONIUM DIBORIDE, HEXAGONAL BORON NITRIDE, AND AMORPHOUS ALUMINA THIN FILMS FOR HIGH TEMPERATURE APPLICATIONS

By David M. Stewart

Dissertation Advisor: Dr. Robert J. Lad

An Abstract of the Dissertation Presented
in Partial Fulfillment of the Requirements for the
Degree of Doctor of Philosophy
(in Physics)
December 2016

The use of microelectronic sensors and actuators in harsh, high temperature environments, such as power plants, turbine engines, and industrial manufacturing, could greatly improve the safety, reliability, and energy efficiency of these processes. The primary challenge in implementing this technology is the breakdown and degradation of thin films used in fabricating these devices when exposed to high temperatures $>800^{\circ}\text{C}$ and oxidizing atmospheres. Zirconium diboride, hexagonal boron nitride, and amorphous alumina are candidate materials for use as thin film sensor components due to their high melting temperatures and stable phases. Zirconium diboride thin films have metallic-like electrical conductivity and remain structurally stable for prolonged periods of annealing above 800°C in vacuum, but oxidize rapidly in air. This oxidation leads to the crystallization of a zirconium oxide phase which causes the films to become electrically insulating and morphologically unstable.

In order to hinder the oxidation, protective capping layers of hexagonal boron nitride and amorphous alumina were deposited onto the zirconium diboride films, forming a compound, multilayer configuration. The oxidation resistance of hexagonal boron nitride is limited to temperatures below 700°C , above which the boron nitride oxidizes and evaporates. An amorphous alumina layer, grown by atomic layer deposition, proved to be a more robust capping layer, but was still limited to temperatures below 800°C . At higher temperatures, the slow oxidation of the zirconium diboride

and film stress from thermal expansion caused the alumina layer to crack and expose the underlying zirconium diboride to rapid oxidation.

The growth of highly crystalline hexagonal boron nitride films by reactive magnetron sputtering, as shown in this work, is of great interest not only for oxidation resistant layers, but also for novel electronic devices constructed with 2D materials such as graphene. Furthermore, this work demonstrates the remarkable high temperature stability of zirconium diboride thin films in vacuum, and their instability in air. The use of oxidation resistant capping layers to provide protection from harsh atmospheres allows zirconium diboride to operate at higher temperatures. Further refinement of these capping materials will be required, however, in order to reliably extend film operation to temperatures above 800 °C.

DEDICATION

This work is dedicated to my family, who supported me during my time in Maine, who put a roof over my head and gave me the opportunity to take the first true step in my career. And to my dear friends at UMaine, for all their friendship and support.

ACKNOWLEDGMENT

This work was carried out using facilities within the Laboratory for Surface Science and Technology (LASST) at the University of Maine. Thanks to the National Science Foundation, Division of Materials Research, for funding my Research Assistantship through the Sustainable Chemistry and Engineering Materials (SusChEM) program (grant #DMR-1309983).

I must thank my dissertation advisory committee and the other members of LASST, professors and grad students alike, who have with great patience and care helped me to achieve so much in so little time. In particular I would like to thank my advisor, Dr. Robert J. Lad, for the opportunities and guidance he has provided over the years in forming the basis of my career, not to mention the hours editing papers and this dissertation. Thanks to Dr. Robert F. Davis, John and Clare Bertucci Distinguished Professor, Member-National Academy of Engineering, Carnegie Mellon University, Materials Science & Engineering, for his insightful review and comments as the external reader for this dissertation.

I would also like to thank Drs. George Bernhardt, David Frankel, and Scott Moulzolf, all of whom got me off the ground when I first started at LASST and taught me the practical side of UHV and surface science. Also thanks to Pat Byard and Sue Ashley for all their help in the Physics Department and LASST, navigating the less scientific aspects of being a grad student. And to Dr. David Clark, for giving me the opportunities working as a teaching assistant and for being such a friendly face to a new grad student.

Thanks to Mike Call for always being available to troubleshoot equipment and for running the ALD process to produce the amorphous alumina capping layers used in my work. And to Matt Curti, a former physics undergraduate, whose senior project was setting up the vacuum and gas delivery system for *in situ* XRD. And to the Advanced Manufacturing Facility for producing the steel collar used in the sample biasing wiring for the deposition chamber.

Thanks to the Advanced Photon Source at Argonne National lab, and Drs. Josh Wright and Carlo Segre (MRCAT, Illinois Institute of Technology) for graciously hosting me for experimental time on Beamline 10-BM, and for educating me in x-ray absorption spectroscopy analysis. MRCAT operations are supported by the Department of Energy and the MRCAT member institutions. This

research used resources of the Advanced Photon Source, a U.S. Department of Energy (DOE) Office of Science User Facility operated for the DOE Office of Science by Argonne National Laboratory under Contract No. DE-AC02-06CH11357.

TABLE OF CONTENTS

DEDICATION	iii
ACKNOWLEDGMENT	iv
LIST OF TABLES	xi
LIST OF FIGURES	xii
LIST OF ABBREVIATIONS	xvii
Chapter	
1 INTRODUCTION	1
1.1 Harsh Environment Sensors	1
1.1.1 Surface Acoustic Wave Devices	2
1.1.2 Thin Film Instability	4
1.2 Zirconium Diboride	6
1.2.1 Electronic Properties	8
1.2.2 High Temperature Stability	9
1.2.3 Oxidation Resistance	10
1.3 Hexagonal Boron Nitride	12
1.3.1 Oxidation Resistance	13
1.3.2 Growth of BN	15
1.4 Summary of This Work	16

2	METHODOLOGY FOR THIN FILM GROWTH & ANALYSIS	18
2.1	Thin Film Growth	18
2.1.1	Electron Beam Evaporation of ZrB_2	19
2.1.2	Magnetron Sputtering of h-BN	21
2.1.3	Effects of Deposition Parameters on Thin Film Structure	24
2.2	X-ray Photoelectron Spectroscopy	26
2.2.1	Background in XPS Spectra	30
2.2.2	Line Shapes	34
2.2.3	Quantification	36
2.3	X-ray Diffraction Techniques	38
2.3.1	Polycrystalline Diffraction	40
2.3.2	X-ray Penetration Depth	44
2.3.3	X-ray Reflectivity	46
2.4	X-ray Absorption Spectroscopy	48
2.4.1	X-ray Absorption Near Edge	51
2.4.2	Extended Absorption Fine Structure	53
2.5	Scanning Electron Microscopy	58
2.5.1	Interpretation of SEM Images	60
2.5.2	Energy Dispersive Spectroscopy	62
2.6	Thin Film Properties at High Temperature	63
2.6.1	High Temperature Treatments	64
2.6.2	Four Point Conductivity	67

3	ZrB ₂ THIN FILM GROWTH AND THERMAL PROCESSING	69
3.1	Experimental Details	69
3.2	Composition of ZrB ₂ Thin Films	70
3.2.1	Modeling for XPS Quantification	70
3.2.2	Composition of Zr _x B _{1-x} Films	74
3.3	As-Deposited Film Structure	76
3.4	Behavior of ZrB ₂ Films with Vacuum Annealing	78
3.4.1	Annealing of Oriented Films	78
3.4.2	Long Term Vacuum Annealing	80
3.5	Electrical Conductivity of Zr _x B _{1-x} Films	82
3.6	Summary	84
4	STRUCTURAL ANALYSIS OF Zr _x B _{1-x} FILMS BY X-RAY ABSORPTION SPECTROSCOPY	86
4.1	Experimental Details	86
4.2	X-ray Absorption Near Edge Spectroscopy of Zr _x B _{1-x} Thin Films	87
4.3	X-ray Absorption Fine Structure Modeling	90
4.4	EXAFS of Near-Stoichiometric Films	92
4.5	EXAFS from Films Far from ZrB ₂ Stoichiometry	95
4.6	Summary	96

5	GROWTH AND STRUCTURE OF SPUTTER DEPOSITED H-BN FILMS	98
5.1	Experimental Details	98
5.2	Effects of substrate, temperature, and power	100
5.3	Effect of Growth Rate on Film Structure	103
5.4	Effect of Sample Biasing on h-BN Film Structure	104
5.5	Summary	107
6	PROTECTIVE CAPPING LAYERS ON ZRB ₂ FILMS	108
6.1	Experimental Details	108
6.1.1	Growth of a-Al ₂ O ₃ Capping Layers by Atomic Layer Deposition	108
6.1.2	ZrB ₂ Thin Films with Capping Layers	109
6.2	Oxidation of ZrB ₂ Films in Air	110
6.3	High Temperature Oxidation of h-BN Films	112
6.4	<i>In situ</i> XRD of ZrB ₂ Films Capped with BN or a-Al ₂ O ₃	113
6.5	Morphological Changes in Capping Layers	115
6.6	Discussion of Film Degradation Mechanisms	117
6.6.1	h-BN Evaporation	118
6.6.2	a-Al ₂ O ₃ Stress and Delamination	119
6.7	Summary	121

7	CONCLUSIONS	122
7.1	Synthesis and High Temperature Stability of ZrB ₂ Films	122
7.1.1	Nanostructure of As-Deposited Films	122
7.1.2	Stability of Atomic Structure with Annealing	122
7.1.3	Stable Electrical Conductivity with Annealing	123
7.2	Improved Oxidation Resistance of ZrB ₂ with Capping Layers	124
7.2.1	Rapid Oxidation of ZrB ₂ in Air	124
7.2.2	Sample Biasing for Growth of Homogeneous h-BN Films	124
7.2.3	Performance of ZrB ₂ Films Capped with h-BN and a-Al ₂ O ₃	125
7.3	Future Work	126
7.3.1	Fundamental Aspects of ZrB ₂ Film Growth	126
7.3.2	Improved Crystallinity of h-BN Films	126
7.3.3	Stresses in a-Al ₂ O ₃ Films	127
7.3.4	Annealing at Temperatures Above 1000 °C	128
7.3.5	Integration of ZrB ₂ Films into Sensors	128
	REFERENCES	129
A	ACCURACY OF ZR _X B _{1-X} FILM COMPOSITION MEASUREMENTS	150
B	ELECTRICAL WIRING FOR SAMPLE BIASING	156
	BIOGRAPHY OF THE AUTHOR	162

LIST OF TABLES

Table 1.1	Bulk properties of ZrB ₂ as compared to Pt.	7
Table 2.1	Parameters for ZrB ₂ depositions.	25
Table 2.2	Parameters for h-BN depositions.	26
Table 3.1	Parameters for the two synthetic peak models in Fig. 3.1.	72
Table 4.1	Preparation conditions for samples presented in Ch. 4.	86
Table 4.2	Fitting parameters derived from the EXAFS spectra in Fig. 4.3.	93
Table 4.3	Fitted values for the ZrB ₂ lattice parameters for Films 1 and 3 after annealing at 800 °C, as compared to ZrB ₂ standards.	94
Table A.1	Functional forms, fitted parameter values, and reduced χ^2 values for each fitted curve in Fig. A.1.	150
Table A.2	XPS sensitivity factors for Zr and B from three different sources.	153
Table B.1	Switch positions and the corresponding states of the A, B, and In connections in Fig. B.2.	158

LIST OF FIGURES

Figure 1.1	Trends in the total annual energy consumed in the U.S.	2
Figure 1.2	Schematic illustrations and images of SAW sensors.	3
Figure 1.3	Illustration of the agglomeration process in thin films.	5
Figure 1.4	SEM images of metallic thin films after annealing in air, showing agglomeration and recrystallization.	6
Figure 1.5	The hexagonal ZrB_2 crystal structure, as compared to pure Zr, showing the reduction in the unit cell size with the addition of B.	6
Figure 1.6	Calculated density of states for ZrB_2 from Zhang, <i>et al.</i>	8
Figure 1.7	Calculated binary phase diagram of the Zr-B system.	9
Figure 1.8	Comparisons of the high temperature oxidation of ZrB_2 with SiC and metal silicide additives.	11
Figure 1.9	Illustration of the process of growing a nano-laminate thin film electrode on a SAW device.	12
Figure 1.10	Crystal structure of h-BN, with graphitic carbon for comparison.	13
Figure 1.11	$P-T$ phase diagram of BN, and theoretical calculations of hexag- onal phase stability in some dimensionally constrained systems.	14
Figure 1.12	Images of metals coated with h-BN thin films, and theoretical calculations of the energy barriers to h-BN oxidation.	14
Figure 2.1	The layout of the multi-chambered UHV system employed in this work.	19
Figure 2.2	Schematic illustration of e-beam co-evaporation used to create ZrB_2 thin films.	20
Figure 2.3	Schematic illustration of reactive RF magnetron sputtering used to create h-BN thin films.	22
Figure 2.4	Schematic of instrumentation for a typical XPS measurement and definition of several energy levels.	27

Figure 2.5	Sample XPS spectra of ZrB_2 and ZrO_2 thin films.	28
Figure 2.6	The measured inelastic mean free path for electrons in numerous elements at different kinetic energies.	31
Figure 2.7	Plot of Si XPS spectra with multiple theoretical backgrounds.	33
Figure 2.8	Plot of the electron scattering cross section for Cu, Ag, and Au, and for four different values of energy as measured by Tougaard.	34
Figure 2.9	Plot of different theoretical line shapes used in XPS analysis.	36
Figure 2.10	Illustration of the elastic scattering of x-rays and Bragg's Law.	39
Figure 2.11	Crystal plane vectors in oriented and non-oriented thin films.	40
Figure 2.12	Schematic of the axes for a typical XRD instrument.	40
Figure 2.13	XRD scan geometry and example diffraction patterns for goniometer and grazing incidence scans.	41
Figure 2.14	XRD scan geometry and sample diffraction for pole figures.	43
Figure 2.15	Diagram of the setup for a typical x-ray reflectivity scan.	46
Figure 2.16	Calculated x-ray reflectivity from a Cu thin film on Si with varying film parameters.	47
Figure 2.17	Schematic illustration of an x-ray absorption measurement.	49
Figure 2.18	Plots of the general trend in the mass absorption coefficient for different materials in the hard x-ray regime.	51
Figure 2.19	Sample x-ray absorption spectra collected near the Zr K-edge for three different compounds.	52
Figure 2.20	EXAFS background subtraction and extraction for Zr foil.	54
Figure 2.21	Diagram of the electron scattering process after an atom absorbs a high energy x-ray.	56
Figure 2.22	Diagram of scattering shells in Zr and Fourier transform of the EXAFS from each shell.	57
Figure 2.23	Schematic of SEM and FIB columns used for imaging thin films.	59
Figure 2.24	Illustration of the interaction of electrons with the surface of a sample in SEM.	61
Figure 2.25	Illustration of temperature gradient in a tube furnace.	64

Figure 2.26	Graph of the sample temperature versus the heater set point for the deposition chamber and the XPS chamber.	65
Figure 2.27	Diagram of the hot stage and gas delivery system used for <i>in situ</i> XRD at temperatures up to 1100 °C.	66
Figure 2.28	Illustration of an electrical conductivity measurement using a co-linear 4pt-point probe.	67
Figure 3.1	Comparison of ZrB ₂ XPS peak fitting with different models.	71
Figure 3.2	Zr _x B _{1-x} film composition and density versus evaporation flux.	75
Figure 3.3	XRD gonio spectra from as-deposited Zr _x B _{1-x} films with varying deposition temperature, offset for clarity.	77
Figure 3.4	XRD and SEM of a highly crystalline ZrB ₂ thin film before and after vacuum annealing.	79
Figure 3.5	XRD and SEM of a nano-crystalline ZrB ₂ thin film before and after vacuum annealing.	80
Figure 3.6	XRD and SEM of ZrB ₂ thin films with annealing for 55 h.	81
Figure 3.7	Electrical conductivity of Zr _x B _{1-x} films as deposited.	82
Figure 3.8	Electrical conductivity of ZrB ₂ thin films versus vacuum annealing time up to 55 h.	84
Figure 4.1	XANES of films with different Zr _x B _{1-x} composition, ZrB ₂ powder, Zr foil, and ZrO ₂ thin film references.	88
Figure 4.2	Weighted EXAFS of Zr _x B _{1-x} films and standards.	90
Figure 4.3	Example plot of the magnitude of the EXAFS Fourier transform of a ZrB ₂ film.	92
Figure 4.4	Magnitude of the Fourier transform of the EXAFS for films near ZrB ₂ stoichiometry before and after annealing in UHV at 800 °C for 9 h.	94
Figure 4.5	Magnitude of the Fourier transform of the EXAFS of films with X _{Zr} = 0.60.	95

Figure 5.1	Plot of BN film composition determined by XPS versus % N ₂ in the working gas.	99
Figure 5.2	XPS spectra of Ni foil as received and after heating in vacuum to the indicated temperatures.	99
Figure 5.3	Effects of magnetron power on amorphous BN growth rate, film roughness, and morphology.	101
Figure 5.4	XPS spectra of BN films as deposited.	102
Figure 5.5	XRD and SEM of h-BN films with different magnetron powers.	104
Figure 5.6	XRD and SEM of h-BN films with different substrate biases.	105
Figure 5.7	SEM images and EDS maps of B, N, and Ni in BN films deposited on Ni foil at 850 °C.	106
Figure 6.1	SEM images from a 50 nm thick a-Al ₂ O ₃ film on a SiO ₂ /Si substrate before and after annealing.	109
Figure 6.2	SEM images from ZrB ₂ films after annealing in air.	110
Figure 6.3	XRD from ZrB ₂ films after annealing in air.	111
Figure 6.4	As-deposited XRD and SEM of BN film on Ni.	112
Figure 6.5	Effects of O ₂ exposure on BN film at high temperatures.	113
Figure 6.6	<i>In situ</i> XRD of Ni foil capped with h-BN.	114
Figure 6.7	XRD intensity maps versus time for capped ZrB ₂ thin films annealed at 700 °C and 850 °C.	115
Figure 6.8	SEM images from capped ZrB ₂ films as deposited and after annealing for 1 h at 700 °C and 850 °C in air.	116
Figure 6.9	SEM images of the large scale stress-induced delamination of the a-Al ₂ O ₃ capping layer on ZrB ₂ after annealing in air.	117
Figure A.1	Reproduction of Fig. 3.2, but with three curves fitted to the data.	151
Figure A.2	Graphs showing the effect of altering the RSF values on the measured composition.	152
Figure A.3	Trends in the uncertainty in XPS quantification dependent only on RSF.	154

Figure A.4	Global trends in XPS quantification uncertainty.	155
Figure B.1	Schematic of deposition chamber manipulator arm with original equipment and new sample biasing wiring.	157
Figure B.2	Diagram of external switch for deposition chamber biasing and grounding connections.	158
Figure B.3	Diagram of the connector pins for the new 5-pin electrical feed- through on the deposition chamber manipulator arm.	159
Figure B.4	Photographs of the sample biasing wiring for the deposition cham- ber sample manipulator arm.	161

LIST OF ABBREVIATIONS

a-Al ₂ O ₃	amorphous aluminum oxide	17
ALD	atomic layer deposition	17
at %	atomic percent	37
BE	binding energy	26
c-BN	cubic boron nitride	12
CTE	coefficient of thermal expansion	7
CVD	chemical vapor deposition	8
ΔG_f	the Gibb's free energy of formation	7
DOS	density of states	8
e-beam	electron beam	16
EDS	energy dispersive spectroscopy	62
E_f	the Fermi level	8
EXAFS	extended x-ray absorption fine structure	16
FWHM	full width at half maximum	34
h-BN	hexagonal boron nitride	12
IDT	interdigitated transducer	2
IMFP	inelastic mean free path	30
LGS	langasite	3
m-ZrO ₂	monoclinic zirconium dioxide	79
PVD	physical vapor deposition	16
QCM	quartz crystal microbalance	20
RF	radio frequency	20
RSF	reduced sensitivity factor	37
RT	room temperature	21
SAW	surface acoustic wave	2
SEM	scanning electron microscope	58
SiO ₂ /Si	Si with a native oxide	100

t-BN	turbostratic boron nitride	16
TMA	trimethylaluminum	108
t-ZrO ₂	tetragonal zirconium dioxide	78
UHTC	ultra-high temperature ceramic	6
UHV	ultra-high vacuum	16
XANES	x-ray absorption near edge spectroscopy	52
XAS	x-ray absorption spectroscopy	48
XPS	x-ray photoelectron spectroscopy	27
XRD	x-ray diffraction	17
XRR	x-ray reflectivity	46
ZrB ₂	zirconium diboride	6

CHAPTER 1

INTRODUCTION

1.1 Harsh Environment Sensors

In 2015, the U.S. industrial sector was the largest energy consumer of the end-use sectors, accounting for 32% of total energy use.¹ The transportation sector was second, consuming a further 28%. These two sectors have historically been the two largest consumers, as seen in Fig. 1.1. In these sectors a substantial portion of the energy is consumed by large scale, high temperature manufacturing and industrial processes, including gas and oil refinement, and aircraft turbine engines. On the production side, 64% of the energy supplied is from fossil fuels, with a further 22% from nuclear power.

Materials used in these industrial processes must stand up to the harsh, high temperatures, and resist degradation in corrosive, oxidizing environments. In order to maintain large scale industrial equipment in a safe and reliable condition, regular maintenance is required. The operating environment necessitates preventative maintenance, where parts are inspected and replaced based on their predicted average lifetime. The application of a sensor network to identify problematic parts without a complete inspection would be a vast improvement, since a condition-based maintenance strategy could then be used.

Detailed measurements of critical parameters such as temperature, pressure, strain, and corrosion of high temperature components during operation would allow improvements in the energy efficiency of these processes, just as such sensors in automotive engines improved vehicle efficiency over the last two decades.^{2,3} However, to do this necessitates operating electronic sensors in harsh, high temperature environments between 300 °C and 1700 °C.^{3,4} These temperatures are well above the operating temperature of conventional Si-based electronics. The confined, enclosed spaces of most high temperature equipment further requires the use of wireless, and ideally, battery-free sensor technology.^{4,5} To advance the use of sensors in both the design and operation of high temperature equipment will require both new technology and new materials capable of withstanding these conditions.

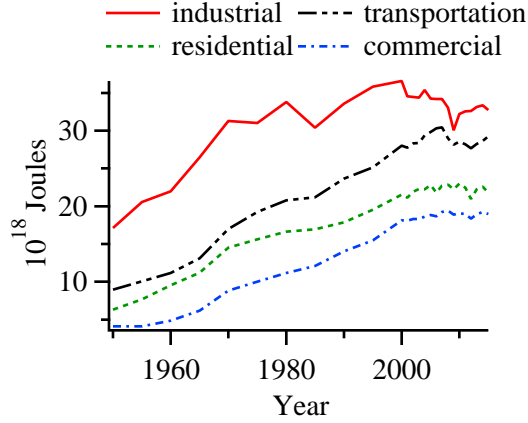


Figure 1.1: Trends in the total annual energy consumed in the U.S. Compiled by the U.S. Energy Information Administration,¹ and broken into the four primary end use sectors. This includes both on site energy production from burning of fuel or renewable sources as well as electricity purchased. In the transportation and industrial sector, energy comes mostly from burning petroleum or natural gas.

1.1.1 Surface Acoustic Wave Devices

Microwave acoustic sensor technology has already shown to be reliable at high temperatures, in particular surface acoustic wave (SAW) sensor devices.^{5,6} In a SAW device, a transverse acoustic wave is excited at the surface of a piezoelectric substrate at microwave frequencies,⁷ typically between 100 MHz to 400 MHz. The frequency and speed of the wave is dependent on surface and substrate effects such as temperature, pressure, strain, and vibration.^{8,9} The SAW also encounters interference from surface defects and adsorbed chemicals, which led to SAW devices original application in biosensing.¹⁰ Calibrating for these effects allows SAW devices to be used as highly flexible sensors for a variety of parameters.

There are two basic operating modes for a SAW sensor, schematically illustrated in Fig. 1.2. In both cases, the acoustic wave is excited by an interdigitated transducer (IDT), which consists of many pairs of thin film electrode fingers: one which receives the microwave signal, and one at ground. The oscillating electric field induces a transverse wave in the piezoelectric substrate, which propagates as a plane wave away from the IDT. In the delay line configuration (Fig. 1.2a), the surface wave travels a distance across the substrate and is received by a second IDT, which then converts the acoustic wave back into a microwave signal. Alternately, the IDT may be placed within an acoustic resonance cavity (Fig. 1.2b), trapping the SAW pulse for $\sim 4 \mu\text{s}$. In this second mode,

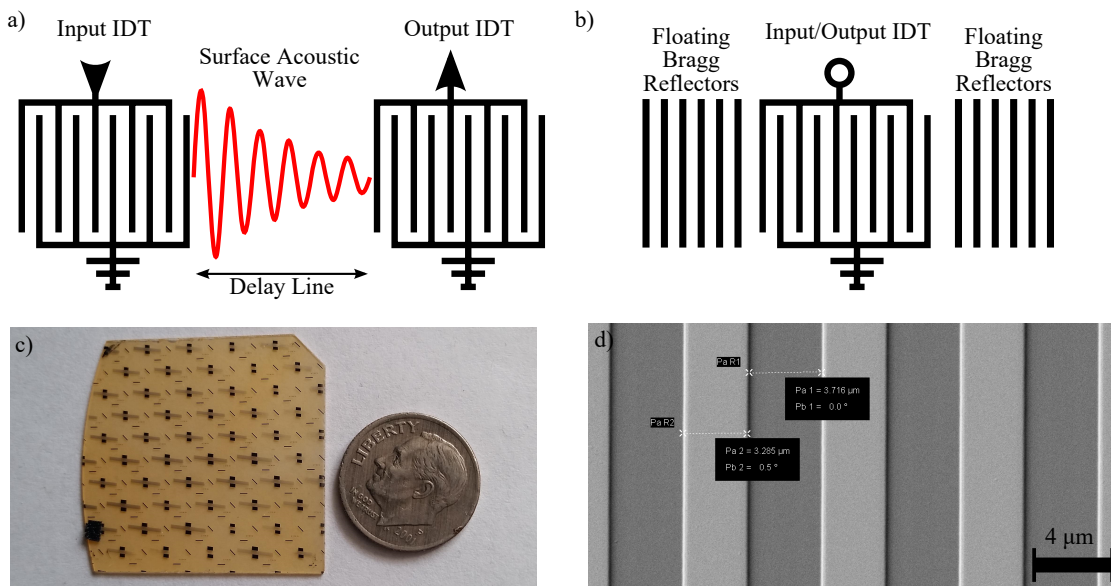


Figure 1.2: Schematic illustrations and images of SAW sensors. Two illustrations of the principle operating modes of a SAW device: (a) using a delay line provides more area for chemical and gas sensing applications, and (b) using an acoustic resonator cavity and a single IDT creates fewer losses, and a smaller device. (c) Photolithographically patterned portion of a piezoelectric LGS wafer with 49 SAW sensors made using the LASST clean room facility. (d) SEM image of bright IDT fingers on a dark LGS substrate in a working SAW device.

the wave is excited and received by the same IDT, but with a short time delay between transmission and reception, similar to a radar signal.

The main advantages of SAW sensor technology is the flexibility and simplicity. The sensors are passive sensors that require no battery, are much smaller than a dime (see Fig. 1.2c), and can be completely wireless, thus satisfying many of the requirements necessary for use inside high temperature equipment. However, only in the last two decades, with the development of stable piezoelectric langasite (LGS) crystals have the opportunities for SAW sensors at high temperatures been explored.¹¹ LGS ($\text{La}_3\text{Ga}_5\text{SiO}_{14}$) is a material which retains its piezoelectric response up to near its melting point ($\sim 1380^\circ\text{C}$),¹² unlike traditional piezoelectric substrates, such as quartz, LiTaO_3 , or LiNbO_3 , which undergo phase changes at relatively low temperatures. With a stable substrate, the stability of the other thin film components in the SAW device could be tested.

1.1.2 Thin Film Instability

The primary points of failure in thin film-based electronics at high temperature are the metallic elements, which lose electrical conductivity either through chemical reaction or morphological instability. The failure of the metallic elements becomes more probable as the scale of the IDT widths are reduced towards the sub-micron scale. Defects in the conductive pathways can arise due to thermal stresses and recrystallization. If the atomic mobility is high enough, large crystal grains may grow, which can disrupt conductivity either by grain boundary scattering of electrons, or by voids appearing between grains. Furthermore, a change in the volume of the electrode during crystallization, either by expansion or compression, can break the thin contacts between electrodes, or the interface with the substrate.

For SAW devices operating in the 100 MHz to 400 MHz range, the IDT electrodes are on the order of 1 μm to 4 μm wide and 100 nm to 200 nm thick (see Fig. 1.2d), leaving very little material for oxidation before the entire film is consumed. At high temperatures, the energetic and kinetic limitations on reaction rates can be severely reduced, and oxidation can occur in a matter of minutes. For temperatures up to 600 °C, noble metals like Pt and Au can be used because of their stability in air. Pt also has a high melting temperature of 1768 °C.¹³ However, above 600 °C thin films such as Pt suffer from agglomeration accompanied by a severe morphological rearrangement and rapid deterioration.^{14–17}

As the temperature increases, the increased atomic mobility allows for diffusion as well as recrystallization in thin films. Agglomeration, or “dewetting,” is a process in which atoms diffuse away from locations with high surface energy, such as pin hole defects or grain boundaries. A thorough review of the phenomenon was published by C. Thompson.¹⁸ As seen in Fig. 1.3, the result in extreme cases is the break up of the film into isolated islands. The extent to which a material will agglomerate is dependent on a variety of factors such as the mobility of the atoms, the amount and severity of the defects, and the interfacial energies between the substrate and the film.¹⁸

The term dewetting is sometimes used to describe agglomeration because of the similarities to the formation of water droplets on a hydrophobic surface. The higher the interface energy between the substrate and the film, the more acute the angle between the droplet and the substrate will be. In polycrystalline films, holes tend to form at grain boundaries, where the differences in surface

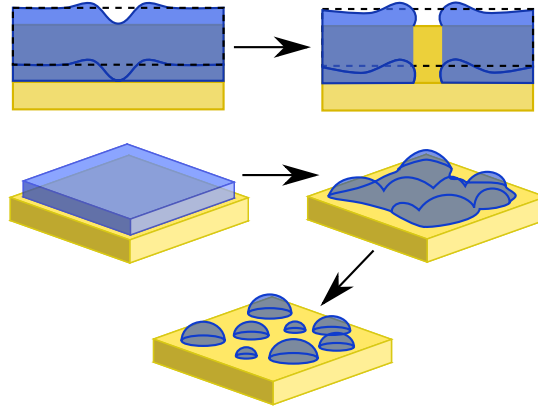


Figure 1.3: Illustration of the agglomeration process in thin films. (after C. Thompson¹⁸) Near a line defect in a thin film, the surface curvature is high, and thus so is the energy. Atoms diffuse away from the defect, reducing the surface curvature by forming a spherical interface. In a film with many defects, such as grain boundaries, dislocations, or pin holes, there are many high energy sites. If the bond between the substrate and film is weak, the film will interface with the substrate at an acute angle. The diffusion of material to form these grains leaves voids between them, breaking the continuity of the film.

energies are greatest. However, because agglomeration is driven by diffusion, rather than by grain growth, it can occur in amorphous films as well, and the rate is strongly dependent on temperature. For noble metals like Pt, agglomeration is the primary hindrance to operation at high temperatures, as seen in Fig. 1.4a.

Avoiding agglomeration is critical to maintaining a complete conducting path in thin film electrodes. Attempts to stabilize Pt thin films by making a nano-composite, two-phase structure containing Pt and an oxide phase has had some success.⁵ In the work of Moulzolf, *et al*,¹⁹ thin films of Pt-Rh/ZrO₂ were deposited as electrodes in SAW devices, which pushed the limit to 1000 °C for short periods of time (see Fig. 1.4b). More recently, in the work of Sell, *et al*,²⁰ multilayer thin films of Pt and Zr achieved stability up to 1300 °C for short periods (see Fig. 1.4c). The nano-composite thin films had good electrical conductivity and remained morphologically stable at temperatures higher than pure Pt, but above 1000 °C crystallization and agglomeration are still the dominant failure mechanisms over long time periods. To push these devices to higher temperature, new thin film materials with improved high temperature stability and resistance to chemical degradation in reactive environments need to be developed.

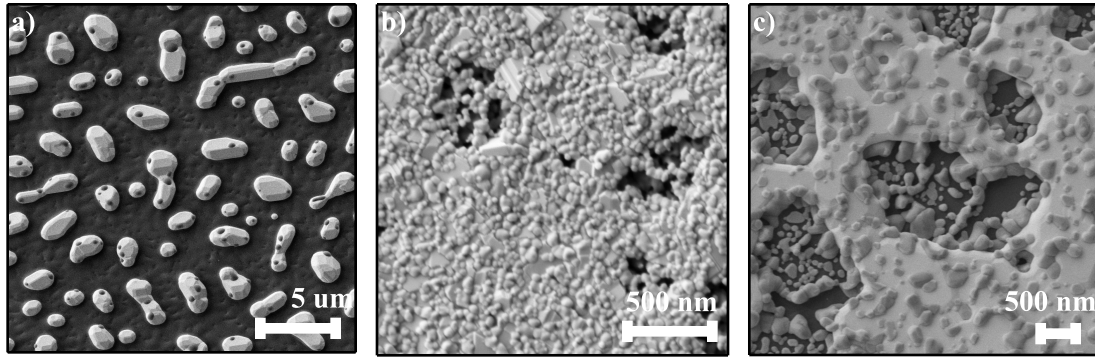


Figure 1.4: SEM images of metallic thin films after annealing in air, showing agglomeration and recrystallization. (a) Pure Pt film on langasite, annealed at 950 °C for 1 h. Initial film thickness was ~ 200 nm. (b) Pt-Rh/HfO₂ compound after annealing at 1050 °C for 16 h.¹⁹ (c) Pt/ZrO₂ multilayer thin film after annealing at 1300 °C for 1 h.²⁰

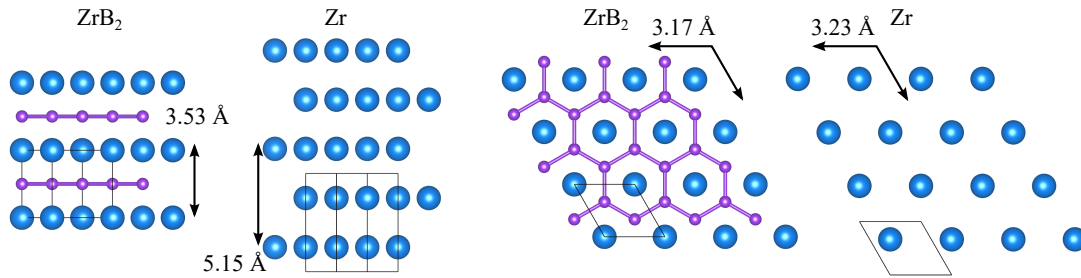


Figure 1.5: The hexagonal ZrB₂ crystal structure, as compared to pure Zr, showing the reduction in the unit cell size with the addition of B. All diboride materials share a similar lattice, with Group IV diborides, like ZrB₂, having the highest melting temperatures and the smallest unit cell due to the valency of the Group IV elements. Image produced with VESTA.²⁷

1.2 Zirconium Diboride

Zirconium diboride (ZrB₂) is one potential candidate as a high temperature electrode material.^{21,22} ZrB₂ is a metallic ceramic with a melting temperature of 3245 °C, making it a member of the ultra-high temperature ceramic (UHTC) class of materials, which includes many other borides and some carbides and nitrides.²³ The crystal structure of ZrB₂ is very similar to pure Zr, as seen in Fig. 1.5. ZrB₂ has the same hexagonal, close packed lattice as Zr, but half the Zr layers are replaced with hexagonal, graphitic rings of B. This closely packed lattice, characteristic of the Group IV diborides, gives ZrB₂ a very low diffusion coefficient for many atoms,²⁴ leading to some exploration of ZrB₂ as a diffusion barrier in electronics.^{25,26}

Table 1.1: Bulk properties of ZrB₂ as compared to Pt.

Property	ZrB ₂		Pt	
Lattice	hcp		fcc	
Primitive cell dim. (Å)				
<i>a</i>	3.17	²⁸	3.92	²⁹
<i>c</i>	3.53	²⁸		
Density (gcm ⁻³)	6.104	²⁸	21.37	²⁹
Melting Point (°C)	3245	³⁰	1768	¹³
ΔG_f (kJ mol ⁻¹)				
Zr + 2 B \rightarrow ZrB ₂ at 25 °C	-318.2	^{31,32}	0.0	
Zr + 2 B \rightarrow ZrB ₂ at 1300 °C	-293.7	³²	0.0	
Hardness (GPa)	23	²³	3.3	³³
Thermal Conductivity (W m ⁻¹ K)	60	³⁴	71.6	³⁵
CTE (ppm/K)	5.9	³⁴	9	³⁶
Heat capacity at 25 °C (J mol ⁻¹ K)	48.2	³¹	25.9	³⁶
Electrical Conductivity (S/m)	10 ⁷	³⁴	9.6 × 10 ⁶	³⁷
Coefficient of resistivity (mK ⁻¹)	4.34	³⁸	3.92	³⁹

ZrB₂ has many favorable qualities compared to Pt for applications in electronic devices, as outlined in Table 1.1. ZrB₂ is substantially lighter than Pt, which helps prevent damping of the SAW, and has almost twice the melting temperature. As a ceramic, it is substantially harder than Pt, and has a lower coefficient of thermal expansion (CTE), which minimizes stress effects during thermal cycling. Finally, ZrB₂ has similar electrical and thermal conductivity to Pt, and has no phase changes up to its melting point. The same strong bonding that gives ZrB₂ its high melting temperature, hardness, and diffusion resistance should make it resistant to agglomeration.

Since ZrB₂ has excellent mechanical properties, the bulk of the literature on ZrB₂ and other diborides is focused on studies of its application in the aerospace industry as the leading edge in future spacecraft bodies and in rocket components.^{23,40} Bulk samples are typically studied, made from sintered powder. Despite the Gibb's free energy of formation (ΔG_f) for the reaction $\text{Zr} + 2 \text{B} \rightarrow \text{ZrB}_2$ being negative, it is generally difficult to fabricate high purity, dense samples.^{41,42} Much of the work in bulk ZrB₂ is concerned with improving the density and oxidation resistance at high temperatures using mixtures of borides, carbides, and silicides.

Thin films of ZrB₂ have been typically grown by DC magnetron sputtering from a ZrB₂ target,^{26,43–46} and generally good results are achieved, although stoichiometric variations are common due to the dissimilar sputter rates of B and Zr.⁴⁷ Other means of producing ZrB₂ thin films include

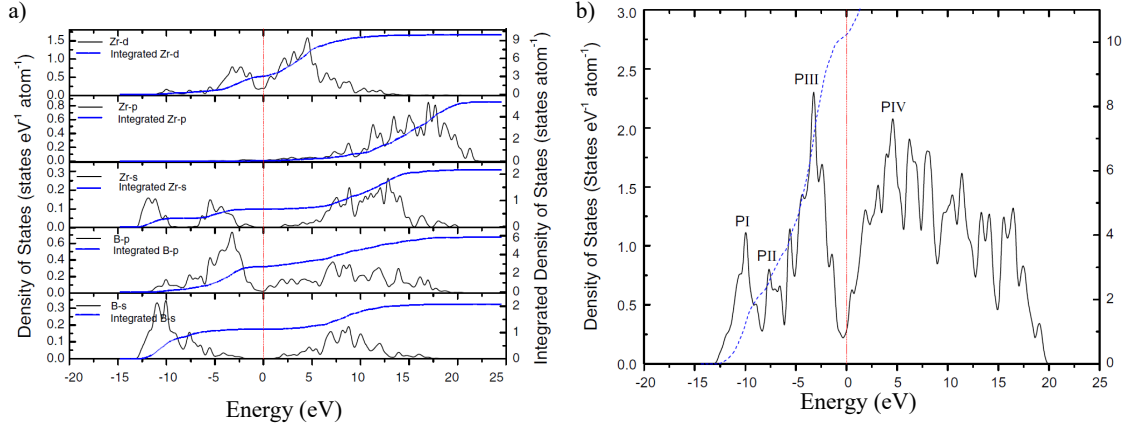


Figure 1.6: Calculated density of states for ZrB₂ from Zhang, *et al.*⁵⁰. (a) Partial DOS for the valence B ($n = 2$) and Zr ($n = 3$) orbitals and the integrated density (blue curve) near the Fermi level (red line). (b) Total occupied and unoccupied DOS and integrated density (dashed blue curve). Three primary peaks in the valence band are identified.

chemical vapor deposition (CVD),⁴⁸ pulsed laser deposition,⁴⁹ and a solid state reaction involving the rapid thermal annealing of a Zr/B multilayer thin film.⁴²

1.2.1 Electronic Properties

Although there is substantial electron transfer from Zr to B to stabilize the B layers (1.15–1.85 electrons on average⁵⁰), the bonding in ZrB₂ can be characterized as covalent. As seen in Fig. 1.6a, the valence band in ZrB₂ is constructed from overlapping Zr 5s and B 1s states near 10 eV below the Fermi level (E_f), and overlapping Zr 4d, Zr 5s, and B 2p states near 5 eV below E_f .⁵⁰ The total density of states (DOS) (Fig. 1.6b) consists of three peaks in the valence band, and a general continuum of states above E_f .^{31,50,51} The peak labeled PII is comprised of overlapping B 2s and B 2p states, making up the network of B layers.

An interesting feature of the ZrB₂ DOS is the relatively low density at E_f . This “pseudo gap”^{22,52} is a feature of many diboride compounds. The pseudo gap may provide some of the stability in the conductivity of ZrB₂. With a low DOS near E_f , there is little opportunity for phonon scattering at high temperatures. Thus, the electrical conductivity of ZrB₂ is fairly stable³⁸ compared to some metals.³⁹

Despite the unique properties of ZrB₂ and other borides, their application in electronics has been limited to diffusion barriers. The high hardness, phase stability, and close bonding in Group

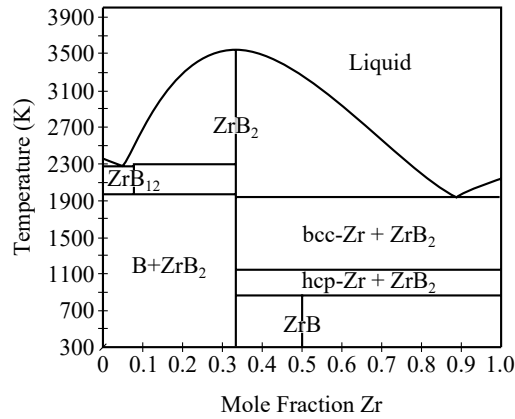


Figure 1.7: Calculated binary phase diagram of the Zr-B system.⁵⁵ Up to 1900 K, Zr-B materials are expected to decompose to pure ZrB₂ mixed with the excess pure phase, either Zr or B, at equilibrium. If atomic diffusion is slow enough, non-stoichiometric ZrB₂ thin films may be phase stable for extended durations of annealing before they decompose into two-phase mixtures.

IV diborides makes them very good diffusion barriers in GaAs technology.^{25,26} The high melting temperature and neutron capture cross section of B also lead to potential applications for diborides in nuclear reactors.²⁴ Although there has been some suggestion of applications for diborides in electronics,^{21,22,44,52} without high temperature substrates there was little demand for new electrode materials.

1.2.2 High Temperature Stability

Perhaps the most impressive quality of UHTC materials like ZrB₂ is their high melting temperature and phase stability. Unlike many nitrides, which have a wide range of compositions, bulk borides do not tolerate deviations from stoichiometry.^{21,53,54} The phase diagram for ZrB₂, shown in Fig. 1.7 shows the very stable phases in the Zr-B system. For significant deviations from ZrB₂, the equilibrium state is a two-phase mixture of ZrB₂ and Zr or B, although a ZrB phase is a well known, stable compound as well.⁵⁵ ZrB₂ is by far the most stable phase in the system, with the highest melting temperature of 3245 °C.

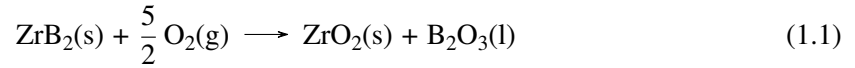
The high melting temperature, hardness, and short bond lengths in ZrB₂ imply an extremely strong network of chemical bonds within the material.²³ These strong bonds will also hinder atomic diffusion of atoms within ZrB₂, thus reducing the rate of agglomeration and crystal growth. The

bonds in Group IV borides are also the most isotropic of the diborides,²³ which leads to fairly isotropic band structure,⁵⁶ elastic moduli,^{23,50} and thermal expansion.^{57,58}

Besides being able to gauge atomic diffusion rates by the strength of the bonds, the elastic moduli and CTE are important characteristics for judging thin film stability. Thermal expansion mismatch between a thin film and the substrate can cause severe cracking and damage to the films. The CTE for ZrB₂^{57,58} is higher than sapphire^{59,60} (a common high temperature substrate and the one used exclusively in this thesis) and LGS,^{61,62} which could lead to buckling of the ZrB₂. However, the elastic moduli and Young's modulus for ZrB₂^{23,50,51,58} are quite high, and thus ZrB₂ thin films may be able to withstand stress induced by the CTE mismatch.

1.2.3 Oxidation Resistance

ZrB₂ and other Group IV borides have highly negative ΔG_f even at high temperatures, and so the rate of oxidation is reduced compared to the pure metals because the oxidation reaction must overcome the strong boride bonding. However, oxidation is still energetically favorable,⁶³ and ZrO₂ and B₂O₃ will be formed from ZrB₂. At 1000 °C the reaction is



with $\Delta G = -1506 \text{ kJ mol}^{-1}$.³² The formation of a low density, liquid B₂O₃ layer at the surface does help to hinder the diffusion of oxygen into the bulk, but the oxidation of bulk ZrB₂ still occurs rapidly, forming a 400 µm thick oxide in an hour at 1500 °C,⁶⁴ and B₂O₃ becomes volatile and evaporates between 1000 °C and 1200 °C.^{65,66} The rapid oxidation of ZrB₂ is the largest hinderance to its application in harsh environment electronics.

A substantial amount of work has been done in the literature on improving the oxidation resistance of bulk ZrB₂ for aerospace applications.^{23,40} The primary strategy has been the use of additives to form glassy silica or other oxide layers at the surface that are not volatile like B₂O₃, thus retarding the diffusion of oxygen further into the film. Silicon compounds are by far the most common additive,^{41,64,67–77} either as SiC, or a silicide, though some other materials have been attempted.^{41,66} The addition of Si compounds vastly improves the oxidation resistance of bulk ZrB₂ (see Fig. 1.8a), decreasing the rate of oxidation by two orders of magnitude over pure ZrB₂.⁶⁴

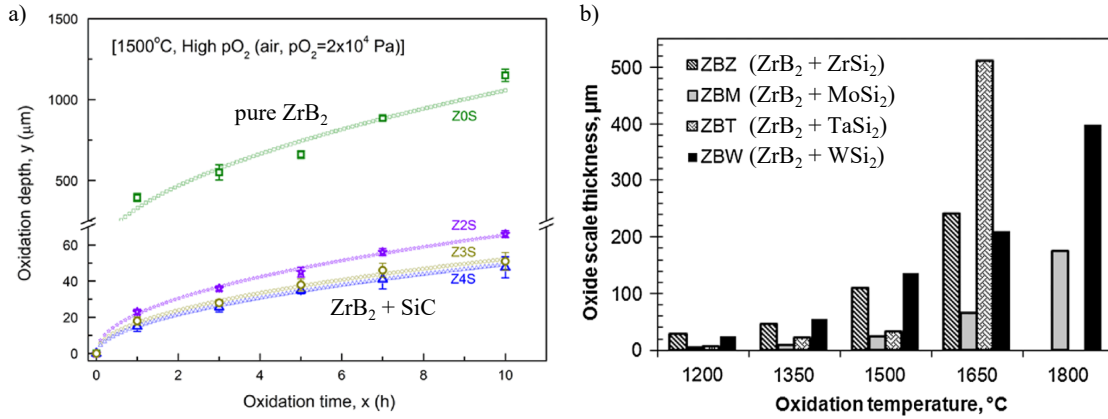


Figure 1.8: Comparisons of the high temperature oxidation of ZrB_2 with SiC and metal silicide additives. (a) Ref.⁶⁴. Comparing pure ZrB_2 to $ZrB_2 + SiC$, with three different quantities of SiC. (b) Ref.⁷⁵. Comparing oxidation of ZrB_2 with four different silicide additives at different temperatures.

Generally, the oxidation of bulk ZrB_2 results in the formation of a loose network of ZrO_2 crystals in the oxidized region, around which the liquid B_2O_3 phase forms. With the addition of Si, a borosilicate glass is formed, which coalesces at the surface and forms a thin layer. Forming this layer requires the consumption of several microns of ZrB_2 before the system approaches equilibrium. The use of different transition metals in the mixture can also affect the oxidation resistance, as seen in Fig. 1.8b. The different metals alter the density and viscosity of the silica layer, and can affect the shape of the ZrO_2 crystals.⁷⁵ Unfortunately, the resulting oxide thickness is much greater than the total electrode film thickness (~ 200 nm) required for SAW devices and other electronics.

A new strategy is needed for the protection of thin films of ZrB_2 from oxidation. One possible solution is the creation of a nano-laminate thin film, consisting of multiple layers of compatible, but specialized thin films. For SAW devices, the nano-laminate film would consist of three primary layers: an electrically conductive layer, sandwiched between a diffusion barrier (interfacial layer) underneath and an oxidation barrier (capping layer) on top. The deposition and photolithography processes used to pattern the electrodes in the SAW device are shown in Fig. 1.9. Using this approach, an oxidation resistant capping layer can be pre-built into the film, without the need to form an oxidation resistant layer during oxidation, as in the bulk ZrB_2 work discussed above.

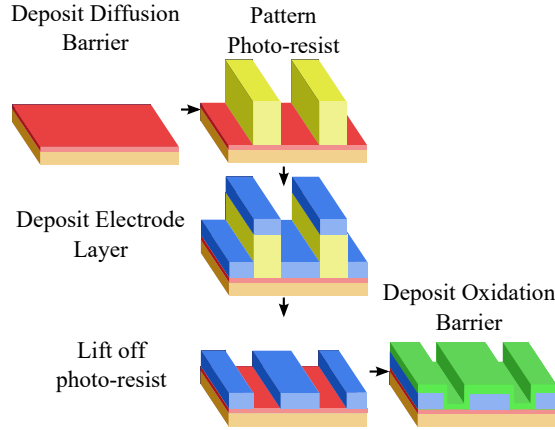


Figure 1.9: Illustration of the process of growing a nano-laminate thin film electrode on a SAW device. First a diffusion barrier is deposited, which helps prevent unfavorable interactions between the electrode and the substrate. Then photo-resist is spun and exposed, forming the pattern for the electrodes. The electrode layer is deposited over the entire device, and a lift off process removes the photo-resist and some electrode material, leaving the pattern behind. Finally, an oxidation barrier is deposited, encapsulating the entire device.

1.3 Hexagonal Boron Nitride

Boron nitride is another well known high temperature ceramic, with a melting temperature $\sim 3000^\circ\text{C}$, high hardness, and relatively good oxidation resistance. The two primary phases, cubic boron nitride (c-BN) and hexagonal boron nitride (h-BN), are both attractive for their structural similarities to the analogous diamond and graphite phases of carbon. Specifically, h-BN has gained a lot of attention as an insulating, 2D material counterpart to graphene for quantum transport and 2D devices,⁷⁸ and recent, prominent reports on the oxidation resistance of h-BN sparked interest in it as an oxidation barrier material for thin film electronics and carbon composites.^{79–82}

As a 2D material, the h-BN crystal structure consists of tightly bonded B and N in a hexagonal monolayer (see Fig. 1.10), with weak van der Waals bonding between layers. This structure is nearly identical to graphene, and shares many of the same properties, such as a low coefficient of friction⁸⁰ and the ability to chemically exfoliate single monolayers^{83,84} and create nanotubes.^{78,85} However, whereas graphene is an excellent electrical conductor, h-BN is a wide band-gap insulator.

Both c-BN and h-BN phases are high band gap insulators, with a direct band gap of $\sim 6\text{ eV}$.^{88–90} The good lattice match between h-BN and graphene makes it an ideal substrate for graphene devices, or as an insulating barrier in stacked 2D devices.^{91–93} In order for h-BN to be useful in these appli-

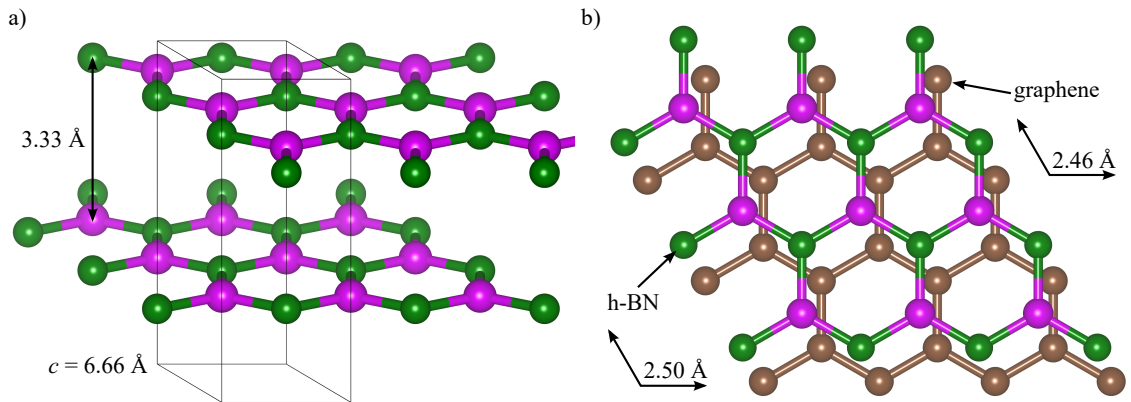


Figure 1.10: Crystal structure of h-BN, with graphitic carbon for comparison. (a) Crystal structure of h-BN, shown as a bi-layer of hexagonal meshes with A-B-A stacking between layers. (b) The h-BN lattice is isomorphous to graphene, with a +1.7% difference in the a -axis and a -0.7% difference in the c -axis.^{86,87} Image produced with VESTA.²⁷

cations, the growth of highly crystalline films with controlled thickness down to single monolayers must be achieved. This requirement is most commonly achieved by CVD deposition at temperatures above 900 °C, and subsequently transferring films to other substrates or onto devices.^{88,93–96}

Crystalline h-BN and c-BN thin films are difficult to produce at standard temperature and pressure,⁹⁷ although both phases are stable under these conditions.⁹⁷ It is generally accepted that c-BN is the more thermodynamically stable phase at standard temperature and pressure (see Fig. 1.11a) based on both experimental and theoretical evidence,^{97–100} however there is a high energy barrier between the graphitic and cubic phases, leading to their stability.^{97,100} Furthermore, there is some evidence based on theoretical calculations that h-BN is actually much more stable in extremely thin layers, such as are desired for 2D devices (see Fig. 1.11b).¹⁰¹

1.3.1 Oxidation Resistance

The use of h-BN as an oxidation resistant coating was prominently reported by Liu, *et al.*⁸¹ though the chemical stability of h-BN was well known prior to that,¹⁰² as it was used for crucibles and high temperature coatings. The surprising result of Liu, *et al.*, shown visually in Fig. 1.12a, was that a h-BN film just 5 nm thick could be effective in retarding oxidation at temperatures up to 1100 °C. This result seemed to be supported by theoretical calculations of the energy barriers for the oxidation of h-BN (see Fig. 1.12b)¹⁰³ and defect formation,^{81,98,104} and weight gain of bulk h-BN at high temperature.¹⁰⁵

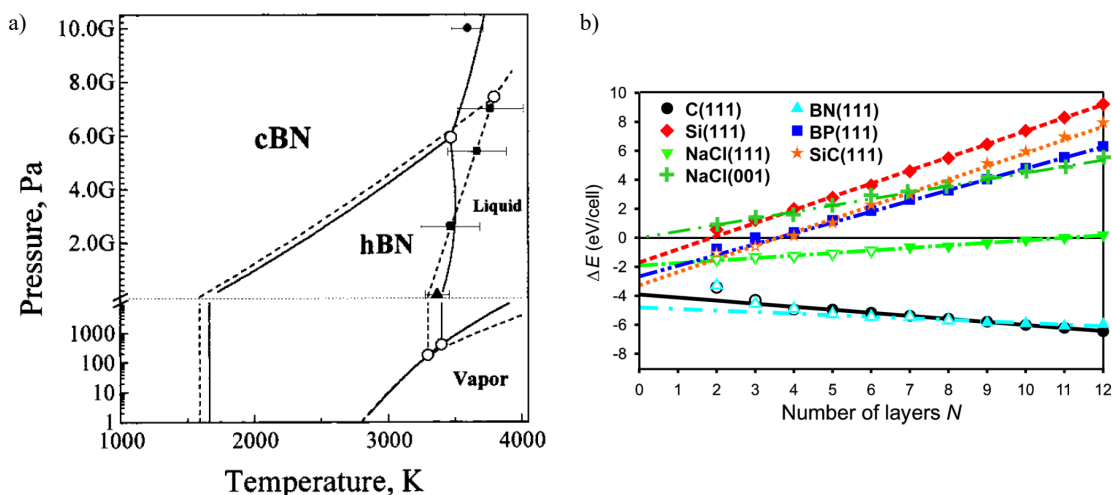


Figure 1.11: $P - T$ phase diagram of BN, and theoretical calculations of hexagonal phase stability in some dimensionally constrained systems. (a) Experimental $P - T$ phase diagram of BN from Ref.⁹⁹. The high melting temperature of BN means that temperatures above 1000 °C are required for its crystallization, however this is also the regime where h-BN is the favorable phase at low pressures. (b) Graph of the difference in cohesive energy of the cubic and graphitic phases of several materials, from Ref.¹⁰¹. For all (111) surfaces investigated, there is a critical thickness below which the hexagonal structure is favorable over the cubic phase.

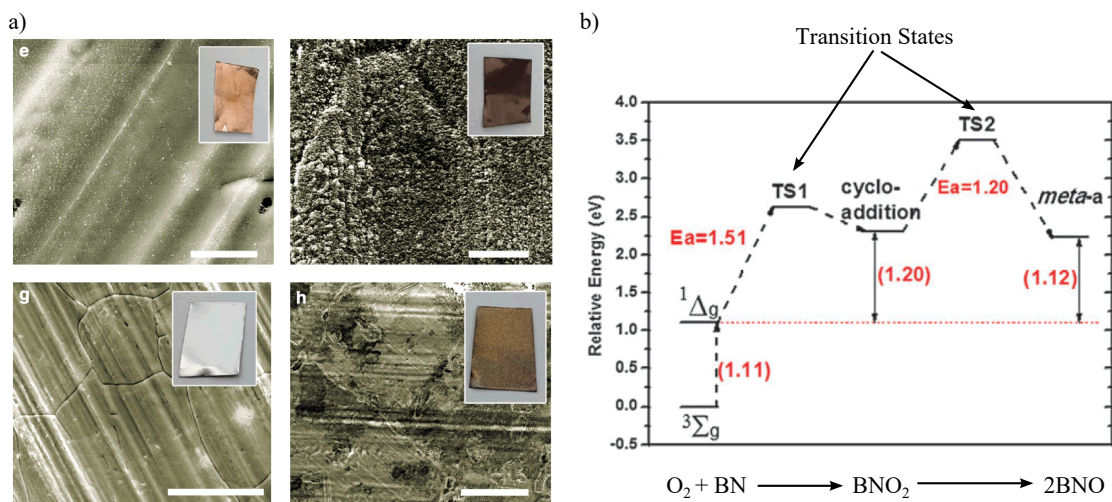
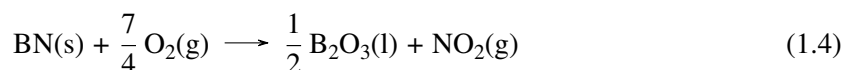
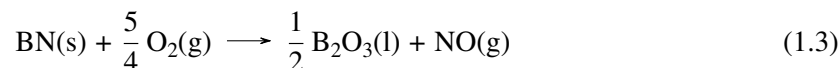
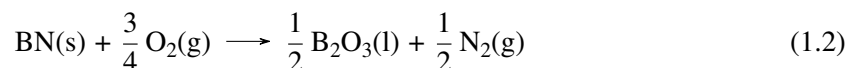


Figure 1.12: Images of metals coated with h-BN thin films, and theoretical calculations of the energy barriers to h-BN oxidation. (a) SEM images from Ref.⁸¹ of Cu (top) and stainless steel (bottom) foil coated (left) and uncoated (right) with 5 nm of h-BN after annealing in 300 mtorr O_2 for 30 min. For Cu the temperature was 500 °C and for stainless steel it was 1100 °C. (b) Calculated minimum energy path for the dissociation of O_2 on the (0002) surface of h-BN from Ref.¹⁰³, indicating several energy barriers >1 eV.

In fact, the oxidation resistance of h-BN is similar to ZrB_2 in that there is strong bonding in BN that must be broken to form the oxide. The ΔG_f for the formation reaction $\text{B} + \frac{1}{2} \text{N}_2 \rightarrow \text{BN}$ is $-225.0 \text{ kJ mol}^{-1}$ at 23°C and $-110.0 \text{ kJ mol}^{-1}$ at 1300°C .³² However, the oxidation of BN at 800°C follows the reactions:



which have $\Delta G = -350 \text{ kJ mol}^{-1}$, -275 kJ mol^{-1} and -270 kJ mol^{-1} , respectively.¹⁰⁶ Thus the oxidation of BN is very energetically favorable at high temperatures. Further reactions of B_2O_3 in the presence of water vapor lead to the formation of highly volatile boron hydroxides, as already mentioned in the oxidation of ZrB_2 , and thus a net weight loss in BN.^{79,102,106–109}

The ability of a 5 nm thin film to prevent the oxidation of the material beneath is thus highly questionable. The oxidations in Ref.⁸¹ were all performed in pure O_2 , and only for short periods of time. Nevertheless, the ΔG_f for the oxidation of h-BN is much lower than that of ZrB_2 , and there is evidence that the film crystallinity has a large impact on h-BN oxidation resistance.^{102,107} A monolithic thin film of highly crystalline h-BN, thus, should significantly improve the oxidation resistance of ZrB_2 or other electrode materials, if it can be successfully grown over large areas.

1.3.2 Growth of BN

The growth of highly crystalline and uniform films of h-BN is important for both 2D device and oxidation barrier applications. Much of the literature on the growth of h-BN uses CVD at high temperatures ($>900^\circ\text{C}$) on Cu or Ni substrates.^{81,88,94–96} This technique can produce thin films with controlled thickness down to 1 to 2 monolayers from relatively benign chemicals such as ammonia borane or trichloroborazine. The choice of substrate is extremely important, as Cu and Ni act as both a catalyst for the reaction and a lattice matched substrate. The (111) plane of Cu and Ni has a lattice mismatch of $< 0.5\%$ with the h-BN (0002) plane, which leads to the growth of highly oriented flakes.^{88,91,95}

Deposition of h-BN by physical vapor deposition (PVD) has also been demonstrated, by pulsed laser deposition^{104,110,111}, magnetron sputtering,^{89,112–119} and combined ion-beam and electron beam (e-beam) evaporation.^{120–123} By using either pure elements or compounds, and depositing in ultra-high vacuum (UHV), PVD has the capability to produce higher purity films than CVD. Magnetron sputtering is also a cheap and easily scalable process that is already compatible with modern device fabrication techniques. Although CVD is currently the more popular technique for h-BN growth, the benefits of magnetron sputter deposition of h-BN are worth continued investigation.

The growth of BN by sputtering either pure B or a BN target in Ar/N₂ mixtures has been well studied in the literature, as it pertains to synthesis of c-BN.^{97,124} However, one of the most prominent concerns in the growth of c-BN has been the formation of the undesirable h-BN and turbostratic boron nitride (t-BN) phases.^{97,119} (t-BN is a disordered form of h-BN.^{119,125}) Thus substantial information is already known about the conditions for the growth of h-BN.^{122,125–128} The deposition of highly uniform and crystalline h-BN by magnetron sputter deposition is still difficult, however, requiring high temperatures and extremely slow growth rates.^{89,112,115,118}

1.4 Summary of This Work

The main objective of this thesis work was to investigate boride-based materials as stable thin film materials for high temperature electronic applications. Thin films of ZrB₂ and h-BN were synthesized by PVD, and their properties were characterized by a variety of techniques. First, the high temperature stability of ZrB₂ electrode thin films was assessed for applications in harsh environment sensors. The growth of ZrB₂ by e-beam co-evaporation was demonstrated, and the effects of film composition and other deposition conditions on the micro- and nano-scale structure of the films was determined. The stability of the films in vacuum and air was assessed in terms of their structural and chemical stability, and their electrical conductivity. Finding only minor structural changes after annealing for more than 8 h at 800 °C in vacuum, the films were probed more deeply using extended x-ray absorption fine structure (EXAFS) analysis, which revealed the local atomic bonding environment. The suitability of ZrB₂ thin films for harsh environment sensors is found to be critically dependent on the ability to protect it from oxidation.

In the second part of this thesis, a means to protect ZrB₂ films from oxidation is explored.

Spurred by the recent results in the literature, the conditions for the growth of highly uniform, crystalline h-BN thin films by magnetron sputter deposition are assessed. Electrically biasing the sample during deposition was found to have a substantial impact on the growth, and results are reported that consistently showed improvements in the quality of the h-BN films with biasing. The oxidation resistance of BN capping layers on Ni foil and ZrB_2 thin films was explored by *in situ* x-ray diffraction (XRD) at high temperatures. The performance is compared to a well known oxidation barrier: amorphous aluminum oxide ($\text{a-Al}_2\text{O}_3$) grown by atomic layer deposition (ALD). Both capping layers improved the high temperature oxidation resistance of the ZrB_2 , but were also found to be inadequate for exposure to air above 700°C for more than 1 h.

This thesis represents a concise, clear examination of the suitability of ZrB_2 as an electrode material, and h-BN as an oxidation resistant capping layer. Based on the existing literature, both materials show great promise as components of a harsh environment sensor or other microelectronic devices. However, there are several critical flaws in their properties that restrict their use to vacuum, or to temperatures below 700°C . In the final chapter, the potential for future work with these materials is discussed.

CHAPTER 2

METHODOLOGY FOR THIN FILM GROWTH & ANALYSIS

2.1 Thin Film Growth

Thin films can be deposited by a variety of techniques, each of which has its own range of conditions, which impact both the materials that can be used and the properties of the films. Thin film deposition generally relies on the condensation of a vapor phase on a suitable substrate, and can be divided into PVD and CVD. The two categories differ only in the precursor materials used. CVD uses complex, often volatile precursors which react to form the desired pure material, while PVD uses elemental or pure compounds.

The ZrB_2 and h-BN films discussed in this thesis were grown by e-beam co-evaporation and reactive magnetron sputtering, respectively, which will be discussed in detail in §2.1.1 and §2.1.2. $\alpha\text{-Al}_2\text{O}_3$ capping layers were grown by ALD, a form of CVD, which will not be discussed in great detail here. The reader is referred to several in-depth papers from the literature on the ALD process for $\alpha\text{-Al}_2\text{O}_3$ thin films.^{129,130} PVD processes require UHV chambers to operate and produce high purity thin films. UHV is a range of vacuum with pressures between 10^{-7} torr to 10^{-12} torr (1.33×10^{-5} Pa to 1.33×10^{-8} Pa), which can be achieved using a variety of specialized pumps.¹³¹

The multi-chamber UHV system in LASST room 193 used by Dr. Lad's group is pictured schematically in Fig. 2.1.¹³² Besides PVD thin film deposition capabilities, the system also contains three surface and thin film analysis and processing chambers where experiments can be performed. The backbone of the system is a sample transportation trolley that allows many samples to be loaded and transferred through UHV between the deposition and analysis chambers. This is essential in surface science, as it allows experiments to be performed on pristine samples that have not been exposed to air. The benefits of this will be discussed further in §2.2. Specific aspects of this system used in this work are discussed below.

2.1.1 Electron Beam Evaporation of ZrB_2

To grow ZrB_2 thin films with controlled composition and crystallinity e-beam co-evaporation¹³³ from 99.5% pure pellets of Zr and B was performed in the main deposition chamber with a base

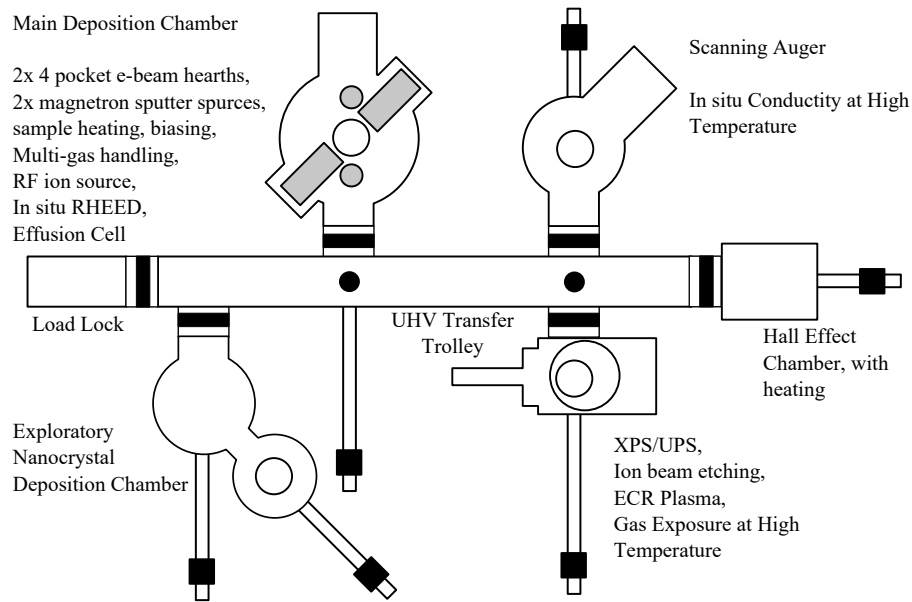


Figure 2.1: The layout of the multi-chambered UHV system employed in this work. Each chamber in the system is independently pumped and can be isolated so that maintenance or processes in other chambers do not affect the whole system. The base pressure in all the chambers is $<10^{-9}$ torr, which provides an extremely clean environment for thin film growth and surface analysis.

pressure of 10^{-9} torr. The process of e-beam evaporation is depicted schematically in Fig. 2.2. Elemental pellets were placed in separate crucibles on opposite sides of the deposition chamber. The temperature of the material in the crucible is controlled by the e-beam current, and is raised until a vapor pressure $\sim 10^{-7}$ torr is produced, corresponding to deposition rates of ~ 0.1 monolayers/sec. For most materials, including Zr, the temperature in the crucible is above the melting temperature, and so a molten pool of the material forms and evaporates. Other materials, like B, sublime at these pressures, in which case the thermal transport between pellets plays a dominant role in the evaporation, and care must be taken that the crucible is heated as evenly as possible. Accurate control of the evaporation was accomplished by rapidly sweeping the e-beam around the crucible in a pattern generated by two sine waves directing the deflection of the beam in x and y.

Because of the low pressure, the atoms in the vapor phase have extremely long mean free paths (on the order of 1 km), and so the evaporation species travel ballistically from the crucible to the sample substrate.¹³⁴ A shield placed above the crucibles is used to direct the beams of material in two directions: towards the sample substrate and to a quartz crystal microbalance (QCM). The QCM is used to monitor the rate at which each element is deposited. The quartz crystals are piezo-electrically excited at their resonance frequency by an applied radio frequency (RF) electric field.

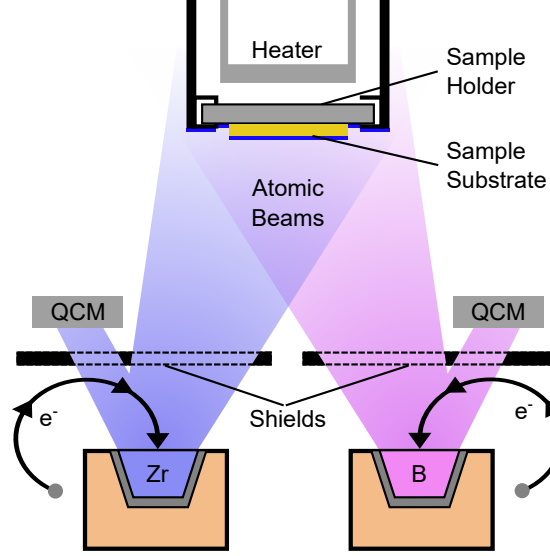


Figure 2.2: Schematic illustration of e-beam co-evaporation used to create ZrB_2 thin films. As the name implies, beams of electrons are drawn from a hot filament and directed by magnetic fields into crucibles containing the material to be evaporated.¹³⁴ The crucibles sit in a water cooled hearth, and different crucibles can be selected depending on the nature of the evaporation materials. During deposition, the growth rates from the two sources can be monitored independently by QCM. Sample rotation and heating is also used to control the uniformity and kinetics of the film growth.

As material sticks to the surface the resonant frequency shifts depending on the thickness, density, and hardness of the deposited material.¹³⁵ The deposited thickness can then be calculated from the shift by the equation:¹³⁶

$$t_f = \frac{N_{\text{at}} \rho_q}{\pi \rho_f v_c Z} \arctan \left(Z \tan \left[\frac{\pi (v_q - v_c)}{v_q} \right] \right) \quad (2.1)$$

where $N_{\text{at}} = 166.1 \text{ kHzcm}$ is the frequency constant of the AT-cut quartz, ρ_q and ρ_f are the density of quartz and the film, v_c and v_q are the resonant frequencies of the coated and bare quartz, $Z = (\rho_q u_q / \rho_f u_f)^{1/2}$ is the acoustic impedance ratio, and u_q and u_f are the shear moduli of the quartz and film, respectively.¹³⁶ Z values have been found and tabulated for a wide number of materials.

Because the sample substrate and the QCM are not the same size or distance from the source, a tooling factor is used to calibrate the flux of material received at the QCM to the flux at the sample substrate. This calibration was performed several times during the course of the project, by depositing thin films of pure Zr and B with a mask in place that created a sharp step edge on the sample. Stylus profilometry was then used to measure the height of this step, and thus determine

the ratio between the thickness measured by the QCM and the thickness of material sticking to the sample.

Because each e-beam source has its own QCM in this deposition chamber, the deposition rates of Zr and B can be tuned to provide a material flux of any desired composition. This in turn controls the composition of the resulting film. As the rate can vary slightly throughout a deposition (due to natural thermal fluctuations, or inhomogeneities in the material in the crucible), constant monitoring is required to produce uniform and reproducible thin films. For this purpose, specialized software¹³⁷ was written in Python for displaying and recording the QCM readings.

In depositing ZrB_2 films, the Zr/B ratio was varied across the entire composition range of the phase diagram. As discussed further in §3.2.1, this wide range in Zr/B flux ratio was necessary to find the correct ratio that produced measurably stoichiometric ZrB_2 thin films. Producing films off stoichiometry allowed the width of the ZrB_2 phase field to be determined and the investigation of phase segregation effects.

2.1.2 Magnetron Sputtering of h-BN

To grow h-BN films with high purity and crystallinity, RF magnetron sputtering¹³⁴ was employed in a reactive mode,¹³⁸ where an elemental B target (99.5% purity) was sputtered in an atmosphere of Ar and N_2 to produce a stoichiometric BN thin film. The process is depicted schematically in Fig. 2.3. Unlike e-beam evaporation, which is done under UHV conditions, sputtering requires pressures between 1 mtorr to 100 mtorr in order to sustain the plasma. At these pressures the mean free path is at most 10 mm, and atoms move in a random walk as they diffuse through the plasma between the target and substrate. Sputtering efficiently coats large, non-uniform areas very well,¹³⁹ but the paths of the deposition species are not directed as in e-beam evaporation.

The working gas (Ar, N_2 , and other gas species involved in the sputtering process) is generally at room temperature (RT), but the plasma species have additional energy as a consequence of being in electronically excited states. The magnetic field created in the magnetron maintains these excited states by forcing the unbound electrons to orbit several times before being collected at the grounded chamber wall, increasing the number of collisions with neutral gas species.¹³⁴ Atoms ejected from the target are generally neutral, and move into the vapor phase unimpeded by the magnetic or electric fields, where they quickly come to thermal equilibrium with the working gas through collisions. The

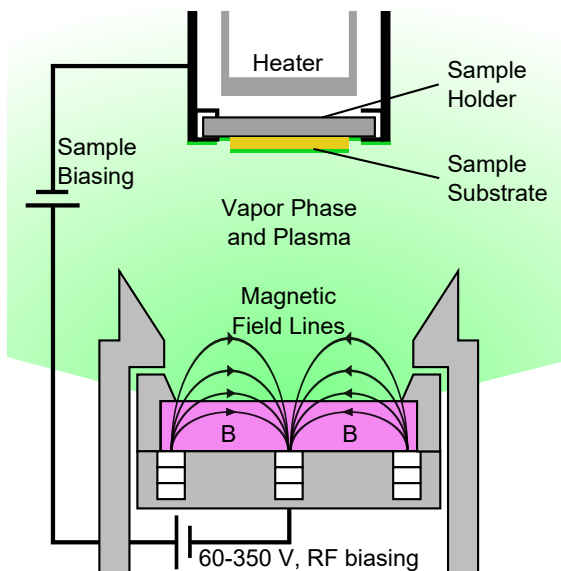


Figure 2.3: Schematic illustration of reactive RF magnetron sputtering used to create h-BN thin films. A working gas comprised of Ar and N_2 fills the chamber, and a plasma is ignited by a high voltage bias on the target below the chamber. A ring of magnets below the target sustains the plasma, which kinetically knocks atoms and molecules off the target, bringing them into the vapor phase.¹³⁴ This soup of plasma and target species eventually deposits on the sample substrate. The sample may be biased relative to the chamber which affects the energies and trajectories of electrons and ions of the plasma.

entire “soup” of plasma ions and target species impinges on the sample substrate^{117,134} and has a chance to condense. Ar is used as the primary component of the working gas due to its high mass and inertness, however small quantities of Ar are sometimes trapped in the film. In the case of reactive sputtering, N_2 or O_2 can be introduced with the Ar to form nitride and oxide films.¹³⁸

An unfortunate consequence of reactive sputtering from elemental targets is “poisoning” of the target, which is the reaction of the gas with the target surface, creating a (typically) hard nitride or oxide phase that reduces the sputter yield, thus lowering the deposition rate.^{134,138} This poisoning also changes the composition of the sputtered species, and can shift the composition of the film as it grows.¹⁴⁰ This was observed in the reactive sputtering of BN, but the reaction at the target surface was slow enough that poisoning of the target only occurred after many hours of film growth. Occasional cleaning of the B target by sputtering in pure Ar successfully reduced the buildup of the nitride phase on the surface and restored the desired sputtering behavior.

The deposition rate in magnetron sputtering is controlled by the momentum transfer from the working gas to the target surface. The mass of the working gas atoms, the target atoms, the bond

strength in the target, and the high voltage bias all play a role. Because of the disparity in the masses between B and Ar, and the high bond strength in B, the sputter yield (target atoms ejected per impacting ion) from a B target under Ar plasma is very low, and thus so is the growth rate. This proves to be a benefit in h-BN growth, however, as the low growth rate allows the accuracy to produce monolayer thin films, and gives the arriving atoms time to diffuse to equilibrium lattice sites (See further discussion in §2.1.3).

Because the sputtering process uses an energetic plasma, electric and magnetic fields can be used to further influence the deposition process. In a typical magnetron sputtering system, the magnetic field lines form a toroid above the target by passing from the outer ring to a central magnet of equal strength.¹³⁴ This toroid efficiently constrains the unbound electrons near the target, and thus increases the density of plasma and the sputter yield. In unbalanced magnetron sputtering, however, the central magnet is weaker than those in the ring, and so field lines leave the toroid and end at the sample. A further method of directing the plasma involves wrapping an inductive coil in the space between the target and the sample, driven at the same frequency as the magnetron, which contains the plasma near both the target and the sample.¹³⁴

DC biasing the sample relative to the chamber is another means of directing the plasma. If the sample is charged negatively, positive gas ions are accelerated toward it. As the sample is more negatively biased, these accelerated ions impact with greater energy, increasing momentum transfer to the growth surface. In the extreme, enough momentum is transferred that the sample is sputtered, just like the target. In the reverse scenario, where the sample is biased positively with respect to the chamber, the positive ions in the plasma are deflected and electron bombardment is increased. Positive biasing reduces the sputtering of the growth surface, and introduces local heating from the electron impact and secondary electron cascades. Biasing effects on the growth of h-BN are discussed later in §5.4.

2.1.3 Effects of Deposition Parameters on Thin Film Structure

Regardless of the technique, there are two dominant deposition parameters which affect film growth: substrate temperature and the rate at which atoms are deposited.¹⁴¹ In order for atoms to stick to the growth surface they must come into thermal equilibrium. Thus if the substrate is cool, a hot vapor phase atom must transfer energy to the substrate, and if the substrate is hot the atoms must

absorb energy. This is a complex problem involving the thermal properties of both the substrate and the vapor phase atoms, but generally has the effect of modifying the probability of an arriving atom sticking or reacting with the growth surface. However, for hard, high temperature ceramics such as ZrB_2 and h-BN, the effects of temperature on the bonding between atoms is minimal (thus their high melting temperatures) and so the temperature of the growth surface rarely impedes the sticking of deposited atoms.

Once an atom has stuck to the surface, the substrate temperature also has a substantial impact on the mobility of the atoms. At higher temperatures, the surface atoms are more mobile, and can diffuse longer distances across the surface before coming to rest. In general, this will produce a smoother, more crystalline film because the atoms will have the energy required to overcome local energy barriers and settle at energy minima such as at a lattice site. Without this mobility, the atoms are likely to freeze at non-equilibrium sites that do not match the lattice of the growing material, resulting in amorphous film growth.¹⁴² (It should be mentioned that it is not always the case that higher substrate temperature is better, as it also increases the reactivity with contaminants in the deposition chamber. Furthermore, if the atoms are extremely mobile, and the sample is cooled too rapidly, then the atoms may be frozen in non-equilibrium positions.)

While increasing the mobility of the surface atoms is beneficial to the growth of smooth, crystalline films, the atoms must have time to diffuse. If the rate at which atoms are deposited is too high, the mobile atoms become buried under subsequent layers of growth.^{143,144} The freezing in of these defects breaks the crystalline order of the growing film, and leads to nano-crystalline or amorphous films.¹⁴⁵ Thus the film growth rate must be tuned to allow adequate diffusion, while maintaining a rate that is practical. It should be pointed out that there are cases where defective, nano-crystalline, or amorphous thin films are desirable, as well.

An additional factor that can affect the crystallinity of a thin film is the nature of the substrate surface. If the substrate surface has many free bonds for arriving atoms to attach to, as with metals or a bare Si surface, then these sites become nucleation points where arriving atoms bond very strongly. If the spacing of these sites happens to closely match the spacing of a particular crystal lattice of the growing film, then these sites will act as a crystallographic pattern that directs film growth. As crystals begin to grow outward from nucleation sites, the pattern of the surface lowers

Table 2.1: Parameters for ZrB₂ depositions.

Substrate	sapphire
Temperature (°C)	RT, 600, 850
Zr rate (Å s ⁻¹)	0.1 to 1.1
B rate (Å s ⁻¹)	0.1 to 0.4
Flux composition (% Zr)	0 to 100
Thickness (nm)	100 to 300
Duration (hours)	1 to 2

Table 2.2: Parameters for h-BN depositions.

Substrate	sapphire, Ni, Zr, Si
Temperature (°C)	RT, 850
Power (W)	10 to 200
DC Bias (V)	−350 to 100
Gas Pressure (mtorr)	10
Gas Composition (% N ₂)	10 to 70
Thickness (nm)	5 to 50
Duration (hours)	2 to 10

the chance of a misalignment at crystal grain boundaries which means larger crystals can grow. (See further discussion in §5.2.)

A substrate will only affect the growth of a film if there are dangling bonds on the surface and/or if there is a good lattice match. An inert substrate, like sapphire or SiO₂, does not affect the crystallinity of a growing film as much as a metallic substrate (such as Ni or Zr), because the arriving atoms have more difficulty finding free sites to bond with. Likewise, an amorphous surface, such as the native oxide on Si, has no preferred pattern, and so no substrate induced alignment of the growing crystals occurs.

In this work, the growth rate and substrate temperature were used to modify the crystallinity of ZrB₂ and h-BN thin films. Both crystalline and amorphous thin films were examined for their high temperature properties. The effects of the substrate on the growth were only assessed for h-BN. Tables 2.1 and 2.2 contain the process parameters that were explored for these depositions. The exact set of deposition conditions depends on the experiment, and are discussed in the relevant sections later in this thesis.

2.2 X-ray Photoelectron Spectroscopy

It is well known that the energy of electrons in a hydrogen-like atom are discrete, quantized values that depend on the atomic number Z of the atom, several fundamental constants, and an integer n as¹⁴⁶

$$U_n = -\frac{c^2 \alpha^2 \mu Z^2}{2 n^2} \quad (2.2)$$

where c is the speed of light in a vacuum, α is the fine structure constant, and $\mu = m_N m_e / (m_N + m_e) \approx m_e$ is the reduced mass of the hydrogenic atom. Thus, every element has a unique pattern of electron energy levels. If a photon of sufficient energy is absorbed, an electron may be ejected from the atom, and if that atom is near the surface, the electron can escape the material and be detected by an instrument. Electrons ejected by this process are called photoelectrons. Conservation of energy dictates that the kinetic energy of the ejected photoelectron is given by

$$E_n = \hbar\omega - U_n - \phi_0 + \phi_{\text{det}} \quad (2.3)$$

where $\hbar\omega$ is the energy of the photon, U_n is the binding energy (BE) of the orbital from which the electron was ejected, and ϕ_0 and ϕ_{det} are the work functions of the sample surface and detector.

The work function of the complete spectrometer is calibrated using a standard such as atomically clean Au, Ag, or Cu,¹⁴⁷ whose electron BEs are taken to be known, and from that point the BEs of any other electron can be determined by

$$E + \phi_0 = E' + \phi_{\text{det}} \quad (2.4)$$

where E' is the kinetic energy of the electron upon arriving at the detector, and ϕ_{spectr} is the calibrated work function of the spectrometer. The use of noble metals as a standard is practical because they are generally free of contamination and the external effects discussed below.

X-ray photoelectron spectroscopy (XPS) leverages this knowledge,^{148,149} and several other effects discussed below, to enable the analysis of the surface composition,^{150–152} chemical bonding,^{153,154} and to a lesser degree, the morphology of a sample.^{155–157} XPS can be used to detect even trace amounts (~ 1 atomic percent) of elements in a sample, and with proper calibration, can identify

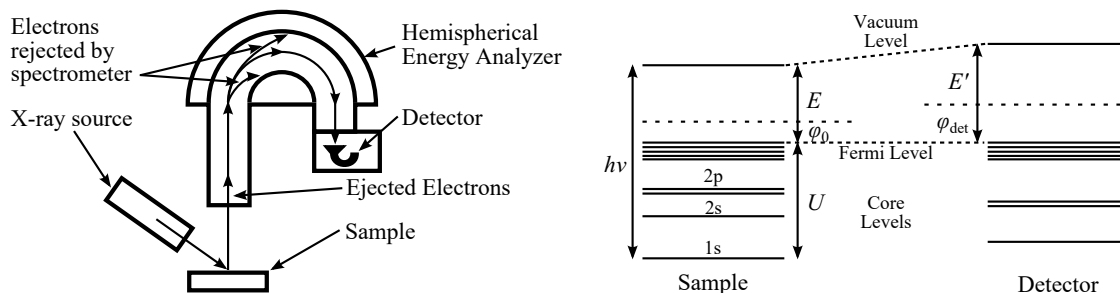


Figure 2.4: Schematic of instrumentation for a typical XPS measurement and definition of several energy levels. A sample is bombarded with x-rays, which ejects electrons upwards into a spectrometer, which measures their kinetic energy. The measured energies are used, together with the known work function of the spectrometer and the energy of the x-rays, to calculate the BE. Because the detector and sample are both grounded, it is convenient to define the BE relative to their common Fermi level.

the absolute elemental composition of a surface to within a nominal accuracy of $\sim 5\%$.^{158–161} In this thesis, XPS was used as a non-destructive means to probe the surface composition of thin films immediately after deposition, and assess chemical changes after heating and exposure to oxygen. It is highly complimentary to other techniques discussed later in this chapter.

In XPS, a spectrometer is used to count the number of electrons ejected as a function of their kinetic energy. As illustrated in Fig. 2.4, a hemispherical analyzer may be employed to distinguish the energy of the ejected electrons. The analyzer uses two concentric metal hemispheres with an adjustable voltage between them.^{162–164} This field allows only electrons with a narrow, selectable range of kinetic energies to be detected, while the rest are collected at the analyzer walls. Other types of analyzers can be used, with different properties.^{165,166} For example, a cylindrical mirror analyzer can collect photoelectrons from a much wider solid angle, and so has better intensity, but lacks the high energy resolution of the hemispherical analyzer.

A typical full spectrum XPS scan is shown in Fig. 2.5a, taken from a ZrB_2 thin film using non-monochromated $\text{Al K}\alpha$ x-rays. Peaks in the spectrum represent a high number of electrons ejected with a certain kinetic energy (converted to BE by Eq. 2.3), which for photoelectrons, corresponds to atomic energy levels. The exception are peaks with very high BE (low E), which are Auger electrons, ejected not by direct excitation from x-rays, but by the multi-step Auger process. Regardless of the excitation energy used, photoelectrons from the same orbital will have the same BE, whereas Auger electrons are always emitted with the same E , and therefore appear to have different BE depending on the excitation energy. In Fig. 2.5a, photoelectrons are labeled by their atomic orbital,

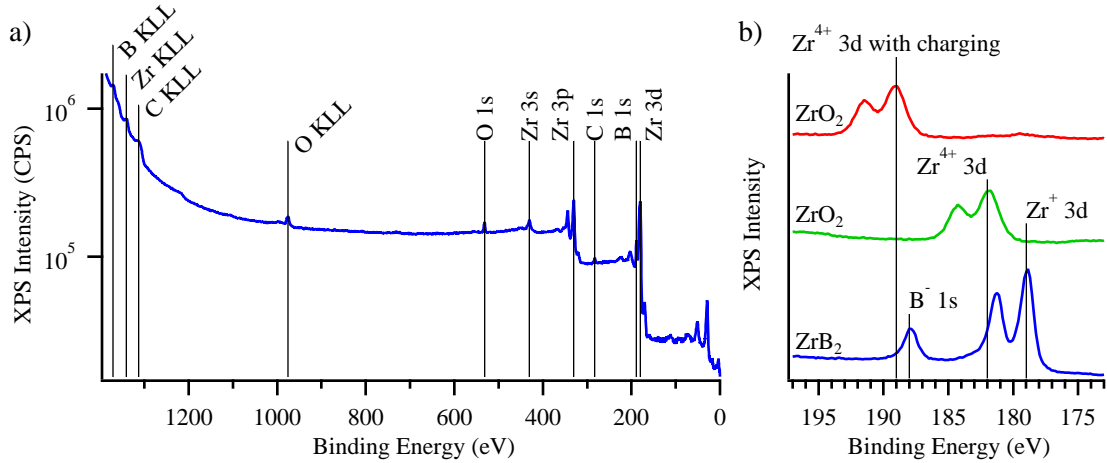


Figure 2.5: Sample XPS spectra of ZrB₂ and ZrO₂ thin films. (a) Full survey scan of a ZrB₂ thin film after deposition, showing peaks from several elements. (b) Detailed XPS spectra of the Zr 3d and B 1s region illustrating the effects of peak splitting, chemical shifting, and sample charging. In this figure, the blue curves are ZrB₂ as deposited with no charging, while the red curves correspond to ZrO₂ with ~ 7 eV of charging, and the green curves are the same ZrO₂ sample after charge correction.

whereas Auger electrons are labeled by letters corresponding to the process by which they were ejected.

This XPS spectrum is unique for every element, however, several external effects impact the exact location of the peaks, the two most common being charging and chemical shifts, which will be discussed shortly. One intrinsic effect that changes the peak position is spin-orbit splitting, which occurs for orbital states with angular momentum $l \neq 0$, as observed in the Zr 3d doublet in Fig. 2.5b. In the final state, after the electron has been ejected, the atom can be in one of two excited states, depending on the spin of the remaining electron in the orbital. Depending on whether the spin of the remaining electron and the orbital angular momentum are parallel or antiparallel, the state will have different energies, and so the ejected electron can have two different energies as well. Thus, p, d, and f orbitals are all split into two peaks (called a doublet) in XPS such as the $3p_{3/2}$ and $3p_{1/2}$ peaks, labeled with the multiplicity of the final orbital state, and separated by an energy that is characteristic of the mass of the atom.¹⁴⁸

Spin-orbit splitting is purely quantum in nature and affects all atoms the same, whereas charging and chemical shifts are electrostatic phenomena that depend on the properties of the material. XPS spectra from two different materials are shown in Fig. 2.5b: blue for a ZrB₂ sample and red and green for a ZrO₂ sample. The peaks for the same elements appear in different locations because of

charging and chemical shifts. In ZrB_2 the Zr is bonded to B atoms and the sample is electrically conductive and well grounded, whereas in the ZrO_2 the Zr is bonded to O and the sample is insulating with a low conductivity path to ground. An accurate interpretation of XPS requires understanding each of these effects and how to correct for them.

The BE for the Zr $3d_{5/2}$ peak is 178.0 eV in a pure Zr sample. In ZrB_2 , electron density is transferred from Zr to B,⁵⁰ which alters the local electric potential and energy levels, and shifts the BE of the ejected electrons.⁵⁶ This translates to a shift of ~ 1 eV for ZrB_2 , with the Zr $3d_{3/2}$ peaks moving to higher BE, and the B peaks moving to lower BE (the B 1s peak appears at 189.0 eV in pure B). The degree of electron transfer in ZrO_2 is much greater than in ZrB_2 , and hence the Zr^{4+} 3d doublet is shifted up 4 eV in the oxide, as seen in the green curve in Fig. 2.5b. Chemical shifts can affect all elements in a material differently, though as seen in ZrB_2 the effects are usually complimentary. Analysis of these shifts allows a detailed understanding of the bonding in a sample via XPS.¹⁶⁷

Charging is a common problem affecting samples with a low conductivity connection to ground, which occurs with samples that are insulating (or become insulating when oxidized, like ZrB_2) or ones which are deposited on insulating substrates like sapphire. If the sample surface is not well grounded, the ejected electrons cause the surface to charge positively to a higher potential relative to the detector, which reduces the E of the electrons as they travel to the detector. As seen in Fig. 2.5b, when comparing the red and green curves, the Zr 3d peaks have been shifted up ~ 7 eV with respect to the well grounded sample. Since charging affects all electrons the same, it is a common practice in such circumstances to use a charge reference (a XPS peak with a known BE) to correct for charging by adding a constant offset to the entire spectrum.

While conducting XPS analysis of ZrB_2 and h-BN thin films, several challenges were encountered and overcome. The proximity of the B 1s and Zr 3d peak BE meant that a refined model needed to be developed for accurate composition and chemical analyses (discussed in more detail below and in §2.2.3). Many samples were deposited on insulating substrates, such as sapphire, and so care needed to be taken to ensure a low resistance pathway to ground. When charging was encountered, a reliable charge reference needed to be used.

The choice of the charge reference was very important in the case of ZrB_2 films. High purity Au foil is often used for charge reference and energy scale calibration because the surface is

extremely clean and free of oxide or other chemical shifts. By placing the Au in good electrical contact with a sample, their E_f are in equilibrium, and so the difference between E_f and the Au 4f doublet (84.00 eV) is used for calibration. Lacking this ideal scenario, the C 1s peak is another good candidate for charge correction because there is often a small amount of graphitic C contamination on the surface under investigation, and the C 1s peak position (284.5 eV) is as well known as that of the Au 4f.

In as-deposited ZrB_2 , however, C contamination was rarely found in the graphitic phase. Rather, the C was accumulated slowly during the deposition and bonded with Zr to form a small amount of ZrC phase, which shifted the observed C 1s peak 1.5 eV to 2 eV lower in BE. The exact position of the C 1s peak in ZrC is not well known. Over time, as the XPS dataset grew, the locations of the Zr 3d, B 1s, and O 1s peaks became more well known in ZrB_2 , and so charge calibration was performed using these peaks as necessary in a self-consistent fashion. The exact locations of the XPS peaks is not important for the conclusions of this work.

2.2.1 Background in XPS Spectra

XPS is a surface sensitive technique, which is both a blessing and a curse. Since electrons arising from only the top ~ 10 nm are detected, the entire depth of most samples cannot be measured.^{168,169} However, this also means that the substrate is rarely observed and the measurement can focus on the changes to the thin film surface. This surface sensitivity is due to inelastic scattering of ejected electrons as they travel through the material, which reduces their kinetic energy, and so these scattered electrons do not contribute to the photoelectron peaks, but instead to background and spectral noise. The percentage of electrons that leave the sample without scattering, I , from a depth d is a function of the inelastic mean free path (IMFP) λ of the material (See Fig. 2.6) according to an Arrhenius-like equation

$$I(E) = e^{-d/\lambda_m(E)} \quad (2.5)$$

where λ is a function of the kinetic energy of the ejected electron and the properties of the material.¹⁷⁰ This formula predicts that 95% of the unscattered electrons come from $d = 3\lambda$, which is ~ 10 nm. This rule of thumb is the sampling depth for an XPS measurement.

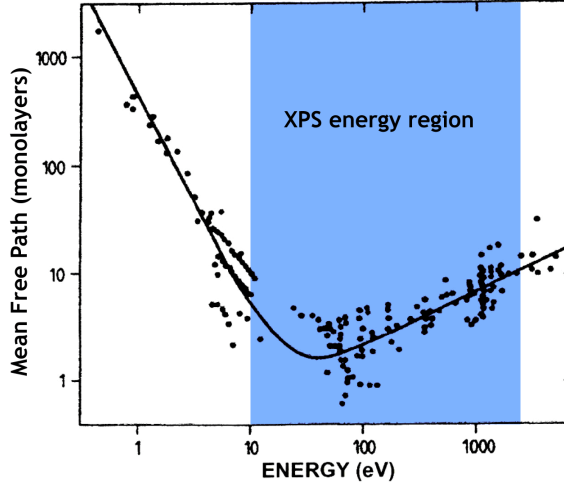


Figure 2.6: The measured inelastic mean free path for electrons in numerous elements at different kinetic energies.¹⁷¹ The vertical scale is in monolayers of material. The solid line represents a so-called “universal curve” which generally shows how the IMFP changes with energy. The marked region is the energy range for electrons ejected using Al $K\alpha$. In that region, electrons with lower BE (higher kinetic energy) can travel greater lengths, and so are detected from a greater range of depths below the sample surface.

Electrons which inelastically scatter as they leave the sample can no longer be identified with a specific atomic orbital or Auger transition (a peak), and make up the background.^{148,149} As was seen in Fig. 2.5a, the background increases with increasing BE with a very large number of electrons having very little kinetic energy.¹⁷² One can also see that the background increases suddenly following a photoelectron peak. Adjusting for this jump in the background requires modeling the probability that a photoelectron with kinetic energy E will inelastically scatter and lose energy T per unit path length. This probability is the scattering cross section, $K(E, T)$.

There are two theoretical backgrounds that are typically employed in XPS analysis^{173,174}: the first by Shirley,¹⁷⁵ was followed later by Tougaard.^{176–178} Both backgrounds begin from the same place: that the background intensity at kinetic energy E is the cumulative probability of electrons at higher kinetic energies scattering, given by

$$\text{BG}(E) = \lambda_m(E) \int_E^{\infty} K(E', T) I(E') dE' \quad (2.6)$$

where λ is the IMFP of the material and $I(E)$ is the measured XPS spectrum. In the Shirley background, $\lambda_m(E)K(E, T)$ is a constant,¹⁷⁹ whereas in Tougaard-like backgrounds the product is ap-

proximated by

$$\lambda_m(E)K(E, T) = \frac{BT}{(C - T^2)^2 + DT^2} \quad (2.7)$$

where the parameters B , C , and D are adjustable for different materials. A “universal” Tougaard background was developed¹⁷⁸ for metals and oxides where $B = 2866$, $C = 1643$, and $D = 0$. Although the values are inter-related, adjusting B most strongly affects the height of the background, while adjusting C strongly affects the slope.

Fig. 2.7 shows XPS spectra from a Si sample with several different backgrounds plotted underneath the data. Any background chosen must share some essential qualities¹⁴⁸:

1. It must generally increase with increasing BE.
2. It must never be higher than the measured intensity.
3. It changes rapidly near the photoelectron peak, and slowly far from it.
4. Its slope should approach that of the measured intensity on both sides.

Because of the assumption in the Shirley background that $\lambda(E)K(E, T)$ is a constant, the background is the integral of the measured spectrum and so has the greatest slope directly underneath the peak, with no slope on either side where the background must meet the data. This simplicity makes the Shirley background attractive in cases where little is known about the material’s properties, or where only a narrow range of data was taken.

In contrast to the Shirley background, the Tougaard background rises slowly near the peak, and rises the most ~ 15 eV above it.¹⁸⁰ The reason for this is illustrated in Fig. 2.8, which shows the rise and fall of $\lambda(E)K(E, T)$ for several different noble metals. The scattering cross section was measured using reflected electron energy loss spectroscopy,¹⁷⁷ which allows a direct measurement of the probability of losing a certain T .^{181–183} Tougaard identified a general trend in the scattering cross section that was deemed “universal,” and a function of the form in Eq. 2.7 was fitted to all 12 data sets.¹⁷⁷ Later, Tougaard would report more parameters for organic compounds and semiconductors.¹⁷⁸

The Tougaard background is substantially more robust than Shirley’s,^{173,174} with parameters that can be adjusted to better model a wide variety of samples. In practice, the choice of background

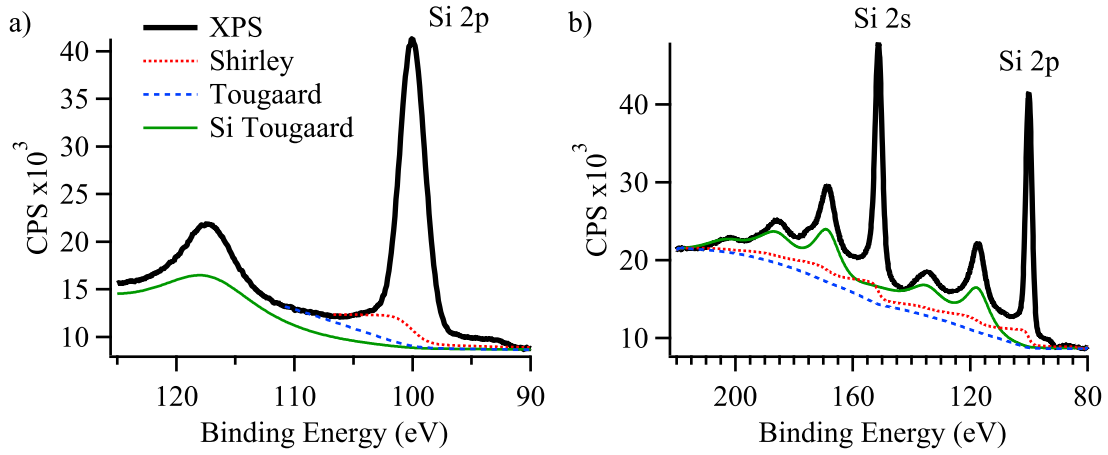


Figure 2.7: Plot of Si XPS spectra with multiple theoretical backgrounds. (a) Fitted over a small range, the Shirley and universal Tougaard backgrounds both overestimate the height of the background. (b) Over a large range of energies the Tougaard background with parameters devised specifically for Si does the best job of modeling all the background features, while the Shirley and Universal backgrounds severely underestimate the background.

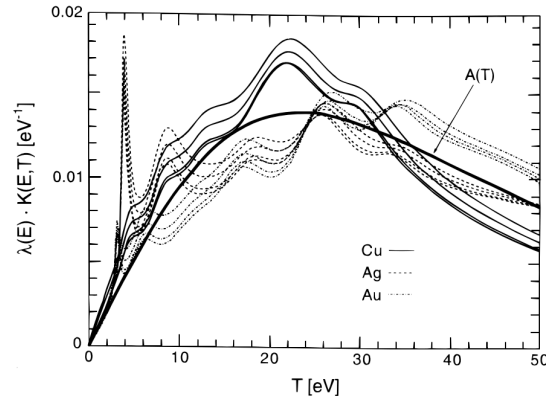


Figure 2.8: Plot of the electron scattering cross section for Cu, Ag, and Au, and for four different values of energy as measured by Tougaard.¹⁷⁷ The plasmon losses are easily seen in Ag, occurring regularly at 9 eV, 18 eV, 27 eV and 36 eV. Similar trends are seen for most transition metals.¹⁷⁸ The thick curve labeled $A(T)$ is Tougaard's universal curve for metals, discussed in the text.

is often inconsequential when peaks are either small, well separated, or doublets are not a concern. However, the choice of background is important if a large region is being considered¹⁷⁹ or if there is substantial overlap between peaks. A universal Tougaard background was thus selected for all XPS analysis in this work, as discussed in more detail in §3.2.1.

Because the universal Tougaard backgrounds average through the exact cross sections, an important nuance is lost.¹⁸⁴ The curves depicted in Fig. 2.8 have several resonance peaks, which vary from material to material. Many of these peaks correspond to plasmon excitations, which are collective oscillations of the conduction band electrons.¹⁸⁵ Ejected electrons have a high probability of exciting these plasmons, and losing $T = \hbar\omega$ energy in the process, where ω is the plasmon frequency.^{148,149} Plasmon energy losses appear at regular intervals, and can be observed in the spectrum for Si in Fig. 2.7. When the Tougaard background parameters are fitted to an electron energy loss spectrum for the material, as in¹⁷⁸ for the Si spectrum, plasmon losses can more accurately be accounted for.

2.2.2 Line Shapes

Much like the background, the shape of the peaks in XPS can be analyzed to gain insight into the material properties. The position and height of the peak obviously relates to the type and amount of an element in the sample, but the full width at half maximum (FWHM) can be a judge of the homogeneity of the sample. A broader FWHM implies that the BE of the atoms vary substantially throughout the sample, with a corresponding distribution of chemical states. Furthermore, peaks for insulating and semiconducting materials are symmetric about a center (as a Gaussian or Lorentzian function), while peaks for metals are asymmetric and have long tails on the high BE side of the peak.¹⁸⁶

The most common line shape used in XPS modeling is a Voigt-type function. A true Voigt function is the numerical convolution of a Gaussian (representing thermal broadening of the peak and the non-monochromicity of the x-ray source) and a Lorentzian (representing the intrinsic width of the atomic energy level).^{148,149} However, there is no analytical form of the Voigt function, and so to save on computation time two different approximations are commonly used:¹⁸⁷

$$GL(E; E_0, \Gamma, m) = \frac{\exp(-4\ln(2)(1-m)(E-E_0)^2/\Gamma^2)}{1 + 4m(E-E_0)^2/\Gamma^2} \quad (2.8)$$

$$\text{SGL}(E; E_0, \Gamma, m) = (1 - m) \exp\left(-4 \ln(2) \frac{(E - E_0)^2}{\Gamma^2}\right) + \frac{m}{1 + 4(E - E_0)^2/\Gamma^2} \quad (2.9)$$

where E_0 is the center of the peak, Γ is the FWHM, and m is a parameter specifying the ratio of Gaussian to Lorentzian shape in the peak. (m is typically near 0.3.)

The Voigt-type functions are widely used and describe most of the peaks observed in XPS. Beginning in the late 1960's, however, the origin of asymmetric peaks was discussed by Nozières and de Dominicis¹⁸⁸ and Doniach and Šunjić.¹⁸⁹ It was shown that in the presence of conduction band states, the ejection of an electron causes an immediate readjustment of the Fermi sea and the creation of many low energy electron-hole pairs. The result is that the photoelectron loses a very small amount of energy and appears at BEs higher than that of the atomic state. This contributes to the tail on the high BE side of the peak, which is not present in insulating and semiconducting materials due to the absence of sufficient conduction band electrons.

Doniach and Šunjić were the first to propose a theoretical line shape for metals with the form¹⁸⁹

$$\text{DS}(E; E'_0, \Gamma', \alpha) = \frac{\cos(\pi\alpha/2 + (1 - \alpha) \tan^{-1}(E - E'_0/\Gamma'))}{(\Gamma'^2 + (E - E'_0)^2)^{(1-\alpha)/2}} \quad (2.10)$$

where α is a parameter defining the degree of asymmetry, and E'_0 and Γ' are related to – but not exactly – the peak position and FWHM. Although this function is rooted in a detailed analysis of the final state effects in metals, the exact functional form is a guess.¹⁸⁹ Thus, other functions have been contrived that offer similar shapes, but with more flexibility. One such function is the “LA” lineshape in CasaXPSTM¹⁸⁷ which is a piece-wise function of two Lorentzian functions

$$\text{L}(E; E_0, \Gamma) = \left[1 + 4 \left(\frac{E - E_0}{\Gamma}\right)^2\right]^{-1} \quad (2.11)$$

$$\text{LA}(E; E_0, \Gamma, \alpha, \beta) = \begin{cases} [L(E)]^\alpha & E \leq E_0 \\ [L(E)]^\beta & E > E_0 \end{cases} \quad (2.12)$$

where α and β adjust the asymmetry on either side of the peak center. A further modification in CasaXPSTM is the LF function, which has the same form with the addition of a dampening parameter that forces the tail to zero intensity far from the peak center. An additional feature of the LA and LF lineshapes is that, unlike the DS function, they are finite integrable.

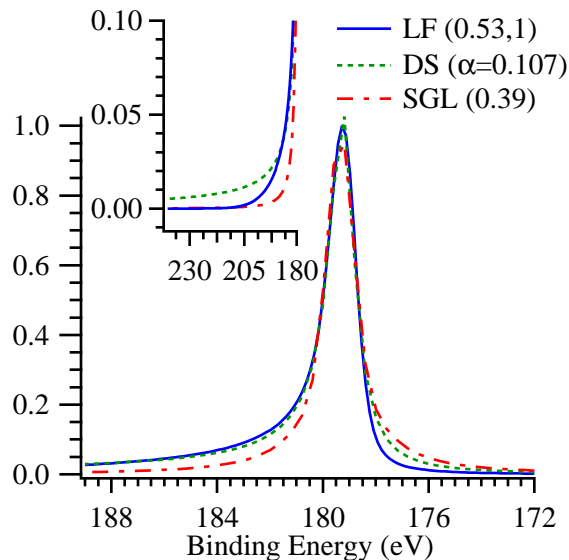


Figure 2.9: Plot of different theoretical line shapes used in XPS analysis. All three line shapes were fitted to the same dataset: a Zr 3d_{5/2} peak in a ZrB₂ sample. The inset shows the long range, high BE side of the line shapes in more detail. The primary effect of asymmetric photoelectron peak shapes is in increasing the intensity on the high BE side. Note that over long ranges the DS line shape stays above the others for much longer. This can have a substantial effect on doublets and chemical shifts, and is often incorrectly accounted for in the literature.

The SGL, DS, and LF line functions are shown in Fig. 2.9, where the three functions were all fitted to the same ZrB₂ peak. One can see that the effect of the asymmetry is a shift in intensity from the low BE side to the high. The tails on the DS and LF functions are nearly identical in the first 10 eV above the peak center, but as shown in the inset, the LF function can be made to drop off much faster over larger ranges than the DS. In either case, the effects of this asymmetry on nearby peaks is obvious. For example, in analyzing a ZrO₂ oxidation layer on Zr, the asymmetry of the Zr peak lifts the nearby Zr⁴⁺ peaks, which can affect the quantitative analysis if not accounted for.

2.2.3 Quantification

The limited sampling depth in XPS means that for 200 nm thick ZrB₂ films, only the top 5% of the film could be analyzed. However, XPS spectra reflect signal from a several mm wide lateral area. Poor consideration of the effects of inhomogeneities in XPS samples can result in inaccurate quantification.^{190,191} However, as was mentioned in §2.1, the UHV system used in this work allows the transfer of samples from the deposition chamber (or other, high temperature processing discussed later in §2.6.1) to XPS without exposure to atmosphere, resulting in a pristine surface

for analysis. Furthermore, as discussed at the end of §2.1.1, if the growth rate is monitored and controlled carefully, one can assume that the surface composition is representative of the bulk. Extensive analyses of the uncertainties in XPS analysis and quantification have been performed, based on peak modeling, background subtraction, instrumentation effects, and user error.^{158–161,192,193}

In many cases, one is interested in using XPS to analyze the composition of a surface, rather than the full sample depth.^{150,152,194} To do so, the area of the photoelectron peaks must be measured. This measured peak area is used with a calibrated sensitivity factor to determine the elemental composition in terms of atomic percent (at %). Only the area above background is valid, which is why careful background subtraction is essential (see §2.2.1).^{195–197} Whenever possible, simple integration of the area should be performed because this requires the fewest assumptions.^{192,198} However, if the area of two overlapping peaks is desired, peak modeling using the line shapes discussed in §2.2.2 is required.

The atomic sensitivity factors depend on a variety of parameters, including both quantum mechanical and instrumental effects. Generally, valid sensitivity factors are provided by instrument manufacturers, but many other tabulated values exist.^{199–201} These are often normalized such that the C 1s peak has a sensitivity factor of 1, called reduced sensitivity factors (RSFs). To calculate the concentration (in at %) of element X in a sample with N elements (including X) one uses the following formula

$$[X] = \frac{I_X/R_X}{\sum_i^N I_i/R_i} \quad (2.13)$$

where I_X is the measured peak area of *one* photoelectron peak in the spectrum, and R_X is the RSF of that element. Because most elements have multiple photoelectron peaks, the choice of which peak to use in Eq. 2.13 is often a matter of preference, but when possible, lone peaks near in BE are best because the IMFP for these electrons are similar and so they should have come from the same range of depths in the sample.

In the case of ZrB_2 , the B 1s is the only B-derived peak present in the spectrum, and it happens to be 10 eV above the Zr 3d doublet, and the Zr^{4+} oxide doublet appears in between the two, as seen in Fig. 2.5b. This high degree of overlap necessitated the model discussed in §3.2.1. In h-BN thin films there is no overlap between the B 1s and N 1s states, nor are there any other peaks, so no modeling was done for those spectra, though a universal Tougaard background was used for background

subtraction. Average matrix RSF values were used for quantification in all cases from the tables provided by the National Physics Laboratory in the UK.²⁰¹ These RSF values are theoretically calculated from atomic properties, utilizing the Scofield photoionization cross sections,²⁰² describing the quantum probability of an atom absorbing an x-ray and ejecting an electron.

When developing a model to fit real data, one should always keep Occam's razor in mind: the principle that the simplest explanation is very often the correct one. This is extremely important in fitting synthetic peak shapes to XPS data¹⁶⁰ as one can always apply additional, unconstrained variables to the model and achieve a better fit. Thus two precautions are always advised when fitting XPS data: every additional synthetic peak must have a robust justification, and whenever possible the peak parameters should be constrained.

2.3 X-ray Diffraction Techniques

Just as XPS takes advantage of the measured spacing of atomic energy levels, XRD uses x-rays to probe the inter-atomic spacing in a material. Parallel x-rays incident on a material at some angle θ are scattered by the atoms as spherical waves. At large distances from the atoms, the spherical waves again appear as parallel wave fronts. Based on the differences in their path lengths, the x-ray wave fronts can constructively or destructively interfere. For most angles at x-ray wavelengths, the x-rays will destructively interfere due to the large number of atoms in the material. The math governing this is similar to thin film interference at visible wavelengths, but the inter-atomic spacing is on the order of 1 Å, which is the wavelength of x-rays.

When the atoms are arranged in planes within a crystalline material, with a normal in the scattering plane of the x-rays as schematically shown in Fig. 2.10, the difference in the path length between the x-rays scattering from the top and bottom planes can give rise to constructive interference. The condition for constructive interference is derived from simple geometric arguments, and is known as Bragg's law³⁷:

$$\lambda = 2p = 2d_{hkl} \sin \theta \quad (2.14)$$

where λ is the wavelength of the x-rays, p is a segment of the longer scattering path, d_{hkl} is the spacing between a given Miller plane the planes, and θ is the angle between the plane and the incident x-rays. Fig. 2.10 also illustrates the x-ray propagation vector \vec{k} and the scattering vector

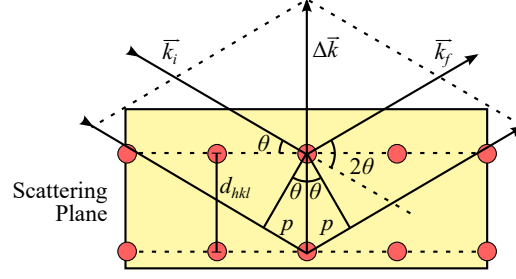


Figure 2.10: Illustration of the elastic scattering of x-rays and Bragg's Law. For x-rays at incident angle θ diffracting from atomic planes with spacing d_{hkl} , the path segments p cause a relative phase shift between the upper and lower scattering paths. The yellow rectangle is the vertical scattering plane containing the incident (\vec{k}_i) and diffracted (\vec{k}_f) x-rays and the scattering vector $\Delta\vec{k}$.

$\Delta\vec{k} = \vec{k}_f - \vec{k}_i$, which gives the direction and magnitude of the momentum transfer from the crystal to the incident x-rays.

A complete treatment of x-ray scattering from crystal lattices³⁷ is beyond the scope of this thesis, and so here we will simply state some results. The two parameters d_{hkl} and the direction $[hkl]$ can be written together in the reciprocal lattice vector $\vec{G} = h\vec{b}_1 + k\vec{b}_2 + l\vec{b}_3$, where the \vec{b}_i are reciprocal lattice unit vectors. It can be shown³⁷ that \vec{G} is parallel to the normal of the atomic plane with $d_{hkl} = 2\pi/|\vec{G}|$ and that Bragg's law is equivalent to the condition that $\Delta\vec{k} = \vec{G}$ for elastic scattering.

The diffraction measurements discussed in §2.3.1 rely on adjusting $\Delta\vec{k}$ until a peak in the intensity of diffracted x-rays is encountered, at which point the magnitude and direction of \vec{G} is known, and the atomic plane is identified. Additionally, the symmetry of the crystal forbids some diffraction due to the so-called "structure factor". In hexagonal systems, for example, l must be even, and $h + 2k$ cannot be a multiple of three. To detect diffraction from every allowed plane requires a distribution of crystal orientations, as would be found in a sample of fine powder. It is often the case in deposited thin films that the crystals (or grains) are oriented in some preferred direction, the reasons for which were discussed in §2.1.3.

It is common to discuss a film "orientation" and "texture." Texture is the degree to which the grains in a polycrystalline sample are aligned with respect to each other. Orientation is the angle at which a specified \vec{G} is aligned relative to the substrate normal \vec{n} , called the epitaxial direction. A polycrystalline sample is considered "highly epitaxially oriented" if there is a single $\vec{G} \parallel \vec{n}$, as depicted in Fig. 2.11a. If \vec{G} corresponds to the (100) plane, the film would be said to be (100)

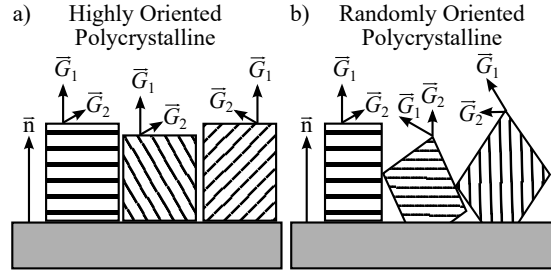


Figure 2.11: Crystal plane vectors in oriented and non-oriented thin films. Thin film texture is defined by having a predominant crystal plane orientation. Let \vec{G}_1 represent the (100) plane, and \vec{G}_2 be the (101) plane. (a) An epitaxially oriented film with (100) texture. Each crystal's \vec{G}_2 is not necessarily aligned. (b) In a randomly oriented film, there is a wide distribution of \vec{G} orientations.

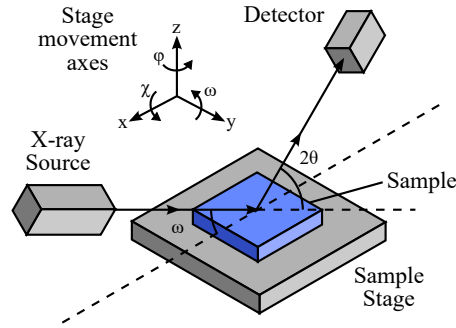


Figure 2.12: Schematic of the axes for a typical XRD instrument. The θ and 2θ arms make up the goniometer, while the sample stage handles the other six coordinates. A variety of x-rays optics and slits can be fitted to the source and detector to modify the shape, monochromicity, or divergence of the beam.

textured and epitaxial. In contrast, a randomly oriented film as depicted in Fig. 2.11b has no texture and no orientation, as there is no predominant \vec{G} .

2.3.1 Polycrystalline Diffraction

Fig. 2.12 shows a diagram of a typical x-ray diffractometer in which a sample is mounted on a stage between an x-ray source and a detector. The source is usually a Cu target excited by electrons from a hot filament, which produces non-monochromated Cu $K\alpha$ radiation with a wavelength of $1.54059290(50) \text{ \AA}$.²⁰³ The arms of the goniometer move the source and detector in a circle, adjusting θ and 2θ , while the sample stage moves and rotates the sample about three Cartesian axes. This allows the full range of motion for several different types of XRD scans.

The XRD instrument used in this work is a Panalytical X'Pert Pro MRD, which actually has a fixed source and the sample is rotated along ω to adjust the incident angle θ . To avoid confusion,

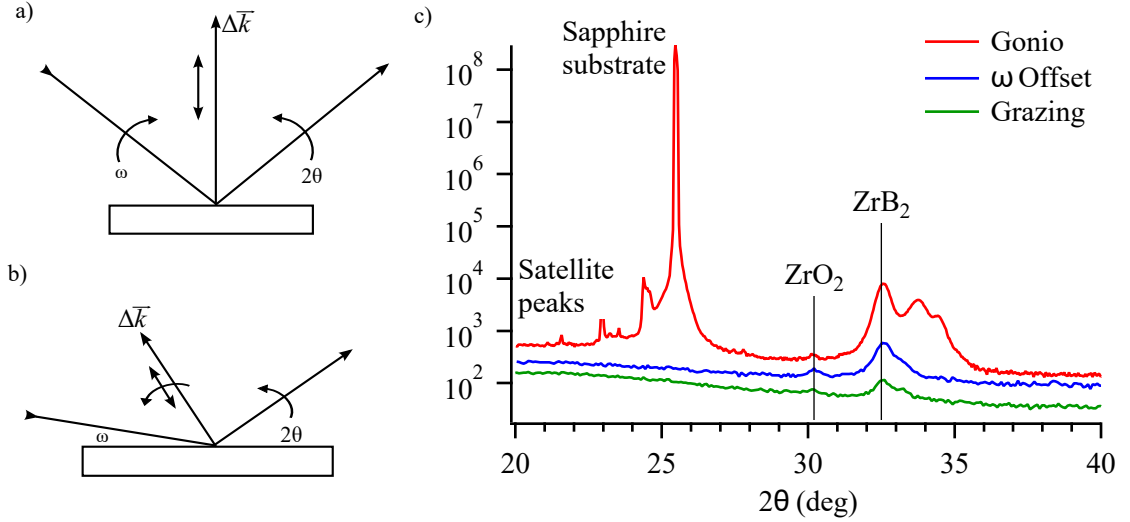


Figure 2.13: XRD scan geometry and example diffraction patterns for gonio and grazing incidence scans. (a) Gonio scan geometry in which the direction of $\Delta\vec{k}$ is not changed. (b) Grazing incidence scan in which both direction and magnitude of $\Delta\vec{k}$ changes. (c) XRD from a ZrB_2 thin film on sapphire substrate using different scan geometries. The incredibly strong diffraction from the epitaxial sapphire plane is completely removed using either an offset or grazing incidence. Also removed are the peaks just above the ZrB_2 peak.

the incident angle will be referred to as ω from this point forward. Bragg's law above holds true in all cases: $\theta = 2\theta/2$. However, ω is not necessarily equal to θ . The distinction between the angle of incidence on the crystal plane θ and the angle of incidence on the sample ω becomes important when the crystal planes are not aligned with the surface normal, or in certain measurements where the direction of a crystal is less important than the direction of the surface normal.

As the goniometer moves ω and 2θ , $\Delta\vec{k}$ is swept. The most typical scan is called a gonio scan (Fig. 2.13a) in which ω and 2θ are adjusted in a specular geometry, such that $2\theta = 2\omega$. During this scan, the magnitude of $\Delta\vec{k}$ is adjusted, but not its direction. Thus, only epitaxial crystal planes can be detected. This is the standard configuration for powder diffraction, where the crystals are randomly oriented, because the specular geometry typically yields the highest intensity.

From the position of a diffraction peak in a scan, one can use Bragg's law to determine the crystal lattice spacing. The intensity of the peak is also informative, although dependent on several factors, i.e. the intensity of the x-ray source, the density of the atomic plane, the symmetry of the crystal, and the size and number of the crystals. The width of the diffraction peak is also dependent on several factors, such as the Gaussian energy distribution of the x-ray source, stress in the film,²⁰⁴

and the crystal size.²⁰⁵ Uniaxial stress shifts the position of the diffraction peak by changing the spacing of the planes consistently throughout the crystals. Inhomogeneous stress, which is often encountered in thin films, creates a distribution of plane spacings, which effectively broadens the peak.^{206,207}

The distinction between broadening due to stress and broadening due to crystal size is not easily made. However, if one can assume that the width of a diffraction peak is predominantly due to crystal size, the Scherrer equation²⁰⁸ relates that width to the size by

$$\tau = \frac{K\lambda}{\Gamma \cos \theta} \quad (2.15)$$

where K is a constant related to the shape of the crystal, Γ is the FWHM of the diffraction peak in radians, and θ is the incident angle. K is typically 0.9, but many theoretical calculations of the constant have been made.^{208,209} Using this equation an estimate of the size of the crystal parallel to $\Delta\vec{k}$ can be estimated. However, this measure is an average of all the crystal grains in the sample.²¹⁰

There are two issues with acquiring a goniometer scan in thin film samples. The first is that there is usually crystallographic texture in thin films, and so a goniometer scan will not show all the diffraction peaks of the film, which could affect phase identification. The other is that the substrates used to grow thin films are usually single crystals cut with a certain orientation normal to the surface. Diffraction from this cut plane usually dwarfs diffraction from film crystals. However, because single crystal peaks are usually very sharp, applying an offset to ω so that $2\theta = 2\omega + \omega_0$ means that the epitaxial \vec{G} from the substrate will never be parallel to $\Delta\vec{k}$, and no diffraction from the substrate will be measured.

Another means of getting around the problems with the goniometer scan geometry is a grazing incidence scan (Fig. 2.13b), in which ω is set at a small angle (typically less than 5°) and 2θ is swept as usual.²¹¹ In this case, $\Delta\vec{k}$ is swept both in magnitude and direction, and diffraction from many crystal planes can be measured. Thus grazing incidence allows the analysis of planes other than the epitaxially oriented ones, but the diffracted intensity varies considerably at high 2θ and a highly textured film is not likely to show any diffraction. Diffraction from epitaxial planes and the substrate are also never measured in grazing incidence scans because, by Bragg's law, the plane would need

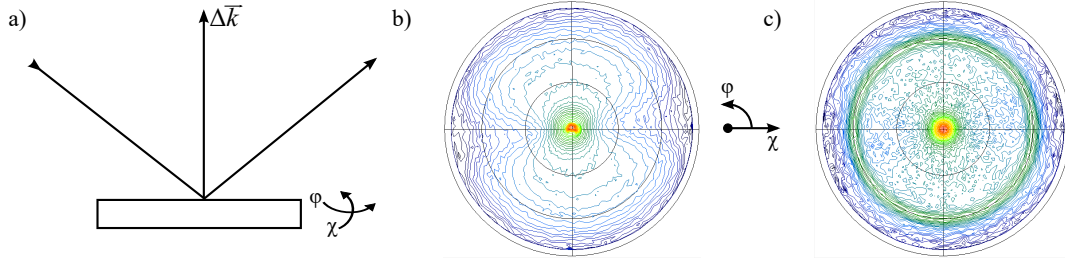


Figure 2.14: XRD scan geometry and sample diffraction for pole figures. (a) Pole figure scan geometry in which $\Delta\vec{k}$ is set and the sample is rotated through a full hemisphere in χ and ϕ . Right are pole figures from two ZrB_2 films with different epitaxial orientations. (b) (002) pole figure of Film 1, showing a single epitaxial texture. (c) (100) pole figure of Film 2, showing no in-plane texture.

to have $d_{hkl} = 8.84 \text{ \AA}$ for a 5° incident angle. Grazing incidence also allows the penetration depth of the x-rays to be adjusted, as discussed below in §2.3.2.

One may infer the texture and orientation of a film from gonio and grazing incidence scans, but in order to quantitatively measure grain orientation a pole figure is required (Fig. 2.14).^{212–215} In a pole figure, $\Delta\vec{k}$ is fixed to correspond to a desired crystal plane \vec{G} , and the sample is rotated in χ and ϕ through a large solid angle (usually a full hemisphere).^{212,216} This angular motion effectively reverses the purpose of the scan, sweeping the crystal's \vec{G} vectors and locating the crystal orientation(s) that match $\Delta\vec{k}$.

Fig. 2.14b and c show pole figure diffraction from two different ZrB_2 thin films with two different textures and orientations. The center of the pole figure is the sample normal direction. Fig. 2.14b shows a film with (002) texture, epitaxially oriented. Besides the width of the central peak, the lack of any other peaks indicates a single texture in the film. Fig. 2.14c shows a film with (100) planes epitaxially oriented. Due to the hexagonal symmetry of the crystal, these (100) planes recur 60° off normal. The ring that appears in the pole figure indicates that the planes 60° off normal are randomly oriented. Thus the film in Fig. 2.14c is textured only in one direction, the surface normal, and is random in-plane.

The same x-ray optics were used for all gonio and offset scans performed in this work. The incident beam, in line focus mode, was reduced by a 0.5° divergence slit, and conditioned into a parallel beam by a parabolic x-ray mirror. The divergence parallel to \vec{n} was nominally 0.004° , and the beam width was constrained to $\sim 24 \text{ mm}$ by a #10 mask. On the receiving side, the beam was collimated by a 0.18 rad parallel plate collimator and a 0.02 rad Soller slit before being measured by

a Xe gas proportional counter. The use of these optics minimizes the divergence of the beam while retaining high intensity, but it does not produce a monochromatic beam and so some satellite lines are observed.

For pole figures, the source was switched to point focus mode and the mirror was replaced with a 8 mm polycapillary x-ray lens. The divergence of the beam was constrained by an adjustable crossed slits mask set to 5 mm in both directions. A Ni foil filter was used prior to the x-ray lens to attenuate the Cu K β satellites. The receiving optics were the same as above. While the x-ray lens does not produce a beam with the same low divergence as the x-ray mirror, this setup provides equal divergence in all directions, which is important when the sample is rotated 180° about the axis of the beam. (The divergence of the mirror is highly asymmetric, with the divergence perpendicular to \vec{n} being $\sim 3^\circ$.)

2.3.2 X-ray Penetration Depth

As x-rays are just a short wavelength of light, it should come as no surprise that they can undergo total external reflection at grazing incidence. Unlike visible light, the refractive index for x-rays in a material for x-rays is a complex number that is always less than 1, and can be calculated by the following equations:²¹⁷

$$n = 1 - \delta - i\beta \quad (2.16)$$

$$\delta = \left(\frac{r_e \lambda^2}{2\pi} \right) N_A \rho \frac{\sum_i x_i (Z_i + f'_i)}{\sum_i x_i M_i} \quad (2.17)$$

$$\beta = \left(\frac{r_e \lambda^2}{2\pi} \right) N_A \rho \frac{\sum_i x_i (Z_i + f''_i)}{\sum_i x_i M_i} \quad (2.18)$$

where r_e is the classical radius of the electron, λ is the x-ray wavelength, N_A is Avagadro's number, ρ is the mass density (g cm^{-3}), x_i is the atomic ratio of the i-th type of atom in the material, Z_i is the atomic number, M_i is the atomic mass (g mol^{-1}), and f'_i and f''_i are the atomic scattering factors representing the dispersive and absorptive components of the atom.

With an index of refraction less than 1, Snell's law predicts that the x-ray critical angle for total external reflection in most materials is between 0.2° and 0.5° . For incident angles less than this value the x-rays are totally reflected by the surface of the material, while at angles above $\sim 5^\circ$ the

x-rays penetrate and undergo attenuation according to the Beer-Lambert law

$$I = I_0 \exp \left(-t \sum_i x_i \mu_i(\lambda) \right) \quad (2.19)$$

where I is the x-ray intensity at depth t , I_0 is the intensity at the surface, and $\mu_i(\lambda)$ is the x-ray attenuation coefficient for the atoms in the material. For an elemental material, this reduces to $I = I_0 \exp(-\mu t)$ and $\mu \approx \rho Z^4 / M(\hbar\omega)^3$.

For angles between total external reflection and penetration, an evanescent wave penetrates a small distance into the sample surface. This evanescent wave is useful because it enables surface sensitivity in XRD by using the grazing incidence scanning geometry discussed above in §2.3.1. By adjusting ω , diffraction from depths between 10 nm and 1000 nm can be set, which can be used to exclude diffraction from the substrate, or to enable qualitative depth profiling where the penetration depth is adjusted and scans repeated.

In this regime, the penetration depth of the x-rays is a sharp function of the incident angle, increasing by several orders of magnitude in a fraction of a degree. The depth is given by

$$D = \frac{\sqrt{2}\lambda}{4\pi[\sqrt{(\omega^2 - \omega_c^2)^2 + 4\beta^2} + \omega_c^2 - \omega^2]^{1/2}} \quad (2.20)$$

where ω_c is the critical angle for total external reflection discussed in the following section. As ω is increased, diffraction from a larger number of crystals in the material is observed. Thus, the appearance of new peaks at higher angles implies that they are only found deeper in the film. A further consideration not addressed so far is that the refraction of x-rays within a material will effectively shift the angle of incidence on crystals beneath the surface. The Bragg condition is thus shifted a small amount, and the peak's position in a grazing incidence scan will be affected. In many cases the effect is negligible.

2.3.3 X-ray Reflectivity

At grazing angles the partial transmission and reflection of x-rays allows for interference effects at the surface and interfaces, similar to thin film interference at visible wavelengths. Careful analysis of the fluctuations in reflected intensity at grazing angles can give insight into thin

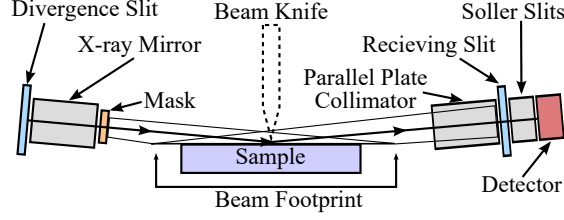


Figure 2.15: Diagram of the setup for a typical x-ray reflectivity scan. The incident optics (mirror/monochromators, divergence slits) are critical to achieve the high resolution scan.²²⁷ Collimating receiving optics are generally used to cut out diffuse reflections. A receiving slit or optional beam knife is used at these low angles to remove x-rays traveling straight from source to detector. The incident divergence slit also serves to limit the footprint of the beam.

film properties such as surface roughness,^{218,219} film thickness,^{220,221} density,^{222,223} and multilayer structures.^{224,225} X-ray reflectivity (XRR) scans correspond to a high resolution gonio scan done between 0.1° and 5° incidence in specular reflection (See Fig. 2.15). As will be seen below, the information contained in these scans requires extremely fine precision, including careful alignment of the sample to the diffractometer to ensure that the incident angle is measured accurately.²²⁶

Several examples of XRR scans are shown in Fig. 2.16, representative of the effects of various film properties on the reflectivity. Analyzing these complex, intermingled effects requires a robust model fitted by a non-linear regression algorithm.²²⁸ The equations modeling a thin film consisting of N layers on a substrate were developed more than 50 years ago,^{229,230} and are given by the following recursive relationships

$$R_{j,j+1} = \frac{R_{j+1,j+2} + F_{j,j+1}}{R_{j+1,j+2} \times F_{j,j+1} + 1} a_j^4 \quad (2.21)$$

$$F_{j,j+1} = \frac{g_j - g_{j+1}}{g_j + g_{j+1}} \exp\left(\frac{-8\pi^2}{\lambda^2} g_j g_{j+1} \sigma_{j+1}^2\right) \quad (2.22)$$

$$a_j = \exp(-i\pi g_j d_j / \lambda) \quad (2.23)$$

$$g_j = \sqrt{n_j^2 - \cos^2 \omega} \quad (2.24)$$

where σ is the roughness of the top of layer j , λ is the x-ray wavelength, d_j is the thickness, n_j is the index of refraction calculated from Eq. 2.16, and ω is the incident angle. In these equations, the layers are counted from top down, such that the vacuum or gas above the film is $j = 1$ and the substrate is $j = N + 1$. In principle, Eqs. 2.21 to 2.24 depend on the layer density, roughness,

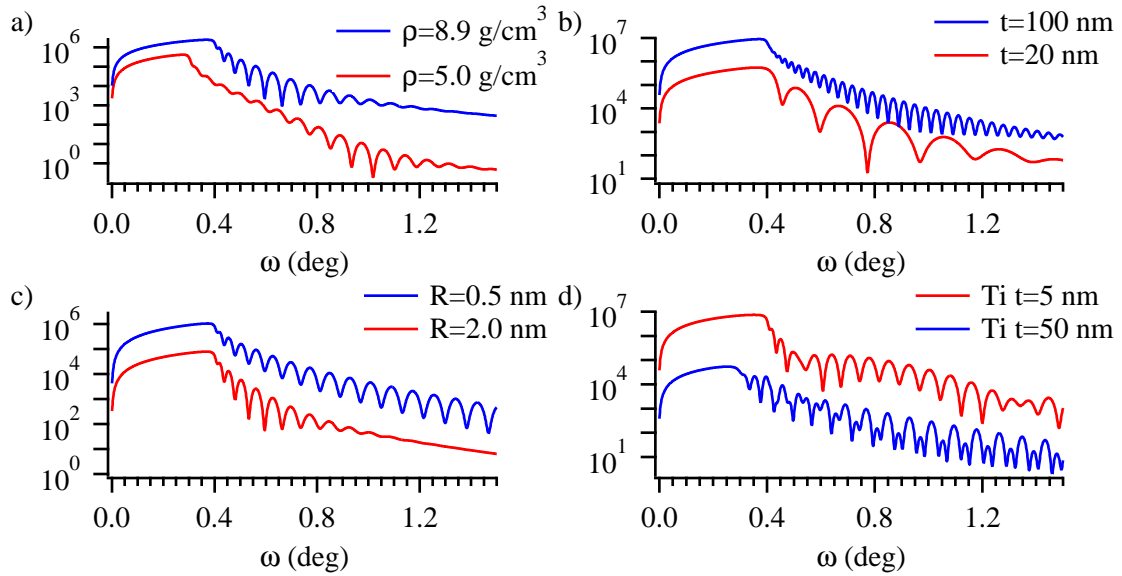


Figure 2.16: Calculated x-ray reflectivity from a Cu thin film on Si with varying film parameters. Curves are offset for clarity. (a) Varying film density affects ω_c and the resonance of the oscillations. (b) Varying film thickness affects the spacing of the oscillations. (c) Increasing the roughness damps the oscillations more quickly. (d) A Ti layer on top of the Cu modulates the oscillations by superimposing the two patterns.

thickness, and atomic composition. In practice, the density and composition are combined into an electron density function that is correlated to the crystal unit cell structure.

Although all the film parameters are intertwined within the shape of the XRR, there are some qualitative conclusions that can be drawn by an experienced analyst. The onset of the transmission of x-rays into the sample is defined by the critical angle, which is directly related to the density of the material through the real term of the x-ray index of refraction ($\omega_c = \sqrt{2\delta}$).²³¹ As ω increases the XRR oscillates, modulated by alternating constructive and destructive interference. The period of this oscillation gives the thickness of the layers, and the magnitude is related to the density contrast. The XRR is damped in two ways: (i) the background decays based on the roughness of the top layer, and (ii) the oscillations decay based on the roughness of each layer's interface.²¹⁸ Thus, a direct comparison of one XRR scan to another can immediately yield significant, qualitative results.

As mentioned above, to obtain quantitative results one must construct an adequate model of the thin film multilayer structure and then perform a non-linear regression to fit the model to the data. Substantial errors can arise when samples are non-uniform and do not conform to a slab-on-slab model, or when there is a continuous gradient of composition or density.²³² More accurate models

may be created to account for more complex nanostructured films, and the equations presented by Parratt²³⁰ are an example that accounts for non-slab geometries.

The films studied in this work by XRR were found to be well-modeled by a slab-on-slab model with sharp interfaces. All XRR scans were performed with the same mirror/collimator optics described at the end of §2.3.1, but a 0.0625° divergence slit was used to refine the beam, and a receiving slit was used after the collimator. The divergence of this set-up was such that fringes from 200 nm thick films could easily be resolved. The specific film models that were used varied considerably from system to system, including native oxide layers on Si substrates and thin oxide layers on the boride or nitride film surfaces, but in all cases Occam's razor was applied and the simplest model was chosen.

2.4 X-ray Absorption Spectroscopy

The interaction between x-rays and matter encompasses several events, some of which have already been described above. Certainly, as with any light, x-rays are either scattered (as in XRR and XRD) or absorbed (as in XPS and fluorescence). Measuring the absorption of x-rays yields complimentary structural and chemical information about materials,^{225,233} but requires x-rays of much higher energy and monochromaticity than can be achieved in a typical laboratory.^{234–236} Much of the work on x-ray absorption spectroscopy (XAS) is done at synchrotron sources at national facilities across the U.S. and abroad. Synchrotron beam time is awarded to researchers for use of a given beamline end station based on the scientific merit as judged by a peer-reviewed proposal process.

At a synchrotron source, a beam of electrons is accelerated in a circular loop at several GeV. Periodically along the loop, beam lines are positioned to direct the white x-rays produced by the acceleration of the electrons to end stations where experiments are performed. The capabilities of each beam line are unique: some do high intensity XRD or XPS studies, whereas others do XAS, and still others are customized for highly specialized work.²³⁷ The XAS measurements presented in this thesis were conducted at beam lines X1B, X18B, and X19A at the National Synchrotron Light Source, Brookhaven National Lab, and at beamline 10BM²³⁸ at the Advanced Photon Source, Argonne National Lab.

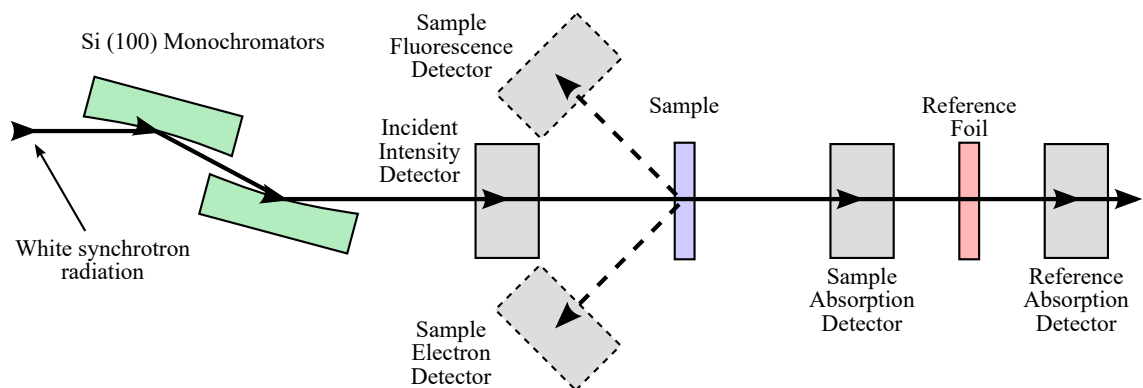


Figure 2.17: Schematic illustration of an x-ray absorption measurement. A monochromator consisting of a series of Si plates (sometimes curved to focus the beam) selects an incident x-ray energy. The beam then passes through a detector that continuously measures the intensity during the measurement. The x-ray beam hits the sample and is partially absorbed and partially transmitted, with a negligible amount that is reflected. The absorbed intensity can be measured by the transmitted intensity, by photon yield using a fluorescence detector, or by electron yield using an electron detector. When transmission is possible, a reference elemental foil is placed behind the absorption detector, and the absorption of this foil is measured as well for calibration purposes.

In an XAS measurement, a tunable monochromator is used to sweep the energy of the incident x-rays across a core energy level of an atom, and the amount of absorbed x-rays is measured (see Fig. 2.17). Monochromators are typically an array of single crystal Si plates with the Si (100) scattering vector normal to the surface.²³⁷ The crystals are rotated to adjust the incident angle ω such that the (100) plane diffracts different wavelengths at different angles, thus selecting the incident energy of the x-rays. For deep core levels, such as the Zr 1s orbital (K-edge), the energy required to excite absorption is on the order of 10^4 eV to 10^6 eV.

X-rays incident on a sample at angles near normal are either transmitted or absorbed; a negligible amount is reflected, especially at the high energy required for core level excitation. A detector with a very small absorption is placed before the sample to continuously measure the incident intensity I_0 , which varies with energy and time. After the x-rays pass through the sample, the amount transmitted I can be measured with a similar detector. In some cases little-to-no transmission occurs, either due to the thickness of the sample or the requirements of the instrument or measurement. In such cases, electron or fluorescence detectors can be used to measure the rate of relaxation processes that occur after core-level excitation, which is proportional to the absorption of the sample.

X-ray absorption is reported in terms of the absorption coefficient, mentioned previously in Eq. 2.19. From the measured quantities, the energy dependence of μ is experimentally determined

by

$$\mu(E) \propto \ln(I/I_0) \quad (2.25)$$

when transmission is measured, or by

$$\mu(E) \propto I_f/I_0 \quad (2.26)$$

when fluorescence or electron yield are used. Fortunately, the goal of most XAS experiments is not to measure the exact value of μ , but instead to derive structural information about the sample from the energy dependence of μ . The XAS measurements discussed in the following sections fall into this category, and in all cases the data have been normalized for easier comparison between sample sets.

The choice of whether to use transmission, fluorescence yield, or electron yield is often dependent on the sample and measurement conditions. High energy x-rays between 5 keV to 10 keV (called “hard x-rays”) are highly penetrating and often easily transmit through most samples and are not affected by air. Thus, hard x-ray beam lines do not typically operate under vacuum to simplify the equipment, and as such, electron yield measurements are impossible; transmission or fluorescence yield are the only possible measurements. In either case, the highly penetrating x-rays mean that signal derives from the entire depth of a thin film sample. The surface, then, has a negligible impact on the measurement.

“Soft x-rays,” with lower energy, are required when investigating light elements such as C, B, and O. These soft x-rays are more easily scattered by air, and so beam lines operating in this regime are typically under vacuum. The vacuum environment opens up the possibility of using electron yield measurements and eliminates the possibility of transmission measurements. As discussed in §2.2.1 and §2.3.2, the attenuation of electrons and x-rays is very different. This means that fluorescence and electron yield measurements sample different depths of the thin film, and can show different results. In electron yield, the surface has a significant impact on the measurements, which means that surface cleanliness and chemistry can be measured.

2.4.1 X-ray Absorption Near Edge

As the energy of x-rays increases, they are generally more easily transmitted, as seen in the general trend of Fig. 2.18. Sharp increases in $\mu(E)$ are observed periodically in the spectra, however,

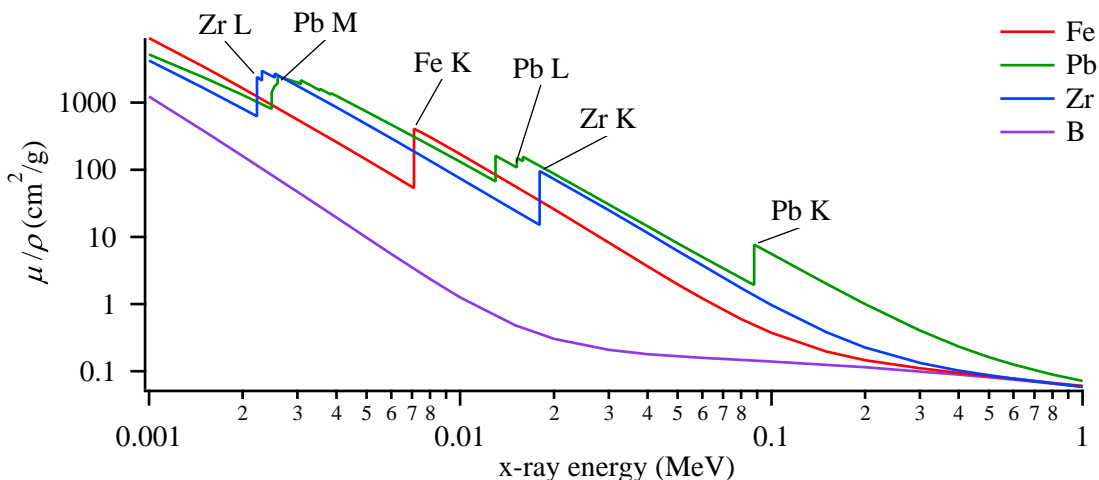


Figure 2.18: Plots of the general trend in the mass absorption coefficient for different materials in the hard x-ray regime.²³⁹ Core level transitions are labeled for each element. The B K edge is off the graph, at 189 eV, corresponding to excitation of the B 1s state.

corresponding to the BEs of electronic levels in the material.^{234–236} The onset of these absorption edges represent electrons being excited from the ground state to states near the the Fermi level (E_f), and as the energy increases photoelectrons are excited above E_f to the vacuum level and ejected from the material. (In the nomenclature of XAS, the K edge refers to the transition from $n = 1 \rightarrow E_f$; L $n = 2 \rightarrow E_f$, and so on up the alphabet.) After an edge, the absorption drops off monotonically again until the next edge. Because the L, M, and N levels of atoms are split, multiple transitions occur near these n -levels, and so multiple absorption edges occur.

Just as in XPS, the BE of the atomic states is subject to charging and chemical effects, which shift the onset of the absorption edge. This can be seen in Fig. 2.19, which shows $\mu(E)$ and it's first derivative near the Zr K edge for three different Zr compounds. The K edge shifts to higher photon energy with increasing oxidation state because the BE of the state increases,²⁴⁰ as was similarly observed in Fig. 2.5b. Fig. 2.19b shows $d\mu/dE$, which is used to locate the position of the absorption edge as the last peak before the plateau.

Charging is only a concern when electron yield measurements are used. Regardless, a good energy reference is always used to calibrate the XAS energy scale. In transmission measurements, as was mentioned in Fig. 2.17, an elemental foil can be placed behind the sample absorption detector. The beam intensity transmitted by the sample, I , acts as the new incident intensity, and the intensity

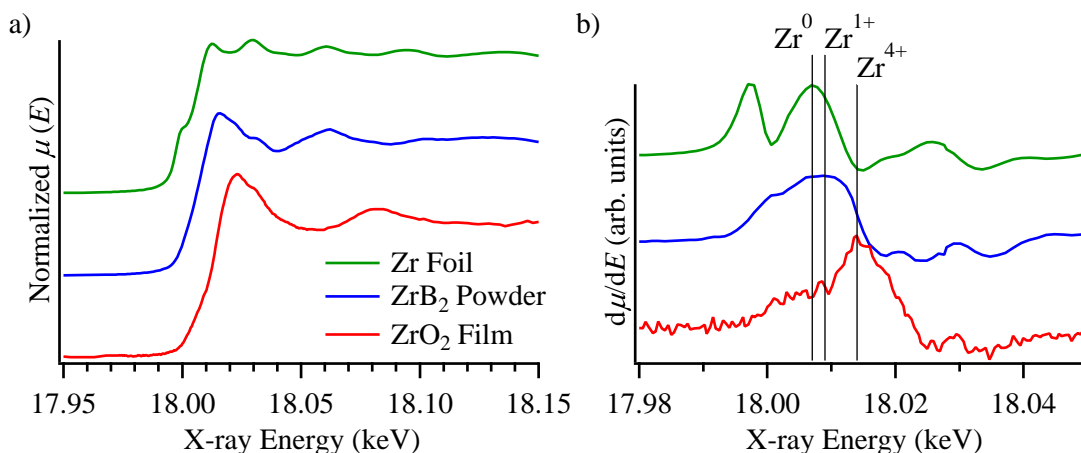


Figure 2.19: Sample x-ray absorption spectra collected near the Zr K-edge for three different compounds. (a) Normalized absorption coefficient for Zr foil, ZrB₂ powder, and a ZrO₂ thin film showing the different chemical states. (b) First derivative of the absorption coefficient used for finding the edge energy and chemical shift in the energy. A pre-edge feature is present in Zr foil and suppressed in ZrB₂ and ZrO₂, which is more apparent in the derivative spectra.

transmitted by the reference, I_{ref} , is measured. One can thus simultaneously measure $\mu(E)$ for the sample and the reference, and hence a good energy calibration is available for every scan.

As one can see in Fig. 2.19a, the absorption edge is not as sharp as was depicted in Fig. 2.18, which correspond to a broad spectrum, low resolution scan. When conducting x-ray absorption near edge spectroscopy (XANES) at high resolution, analysis of pre- and post-edge features can give insight into the electronic and local bonding in a sample.^{236,241–243} The post-edge features for the three Zr compounds in Fig. 2.19a are very different, and represent different coordination around the Zr atoms.^{234–236} XANES can be done for any atomic edge and compared to reference compounds to identify the coordination and bonding in an unknown material. Mixed coordination states can even be identified, as the post-edge features are merely superimposed on one another in the XANES.²³⁶

Identifying pre-edge features is generally less informative, but nevertheless useful. Peaks just before the absorption edge, as clearly visible in the Zr foil in Fig. 2.19, are related to excitations from the core level to valence band states below E_f . In transition metals, the intensity of pre-edge peaks have been linked to the degree of d-p hybridization in the valence band,²⁴⁴ such that a strong peak is observed for metals with tetrahedral symmetry and a low number of d electrons, such as Zr, and the intensity decreases as the valence d orbital is filled. Identification of the origin of these

inter-band transitions and the final state effects thus provides further information about the bonding in the material.

2.4.2 Extended Absorption Fine Structure

Although the post-edge features of the XANES are correlated to the local bonding and coordination of atoms, there is no exact theoretical model that describes the near-edge fine structure. The EXAFS, on the other hand, has been much more successfully analyzed. For atoms beginning with the transition metals, the core level edges are sufficiently far apart that $\mu(E)$ can be measured over a ~ 1 keV range uninterrupted by other features. In this extended range, the oscillations observed near the edge can persist and be accurately measured.

The x-ray absorption of a lone atom is approximated by^{235,236}

$$\mu(E) \approx \frac{\rho Z^4}{ME^3} \quad (2.27)$$

where ρ is the density, Z is the atomic number, and M is the atomic mass. This smooth function is modified predictably by the absorption edges. The measured $\mu(E)$ is also affected by experimental limitations such as self absorption in fluorescence yield, sample inhomogeneities, and polarization effects in the beam. However, all these influence $\mu(E)$ over a much longer energy range than the EXAFS oscillations.

In separating the EXAFS from the data, a smooth spline function $\mu_0(E)$ is fitted to the measured absorption for $E > E_0$. The spline function is tuned such that it only models long range deviations from the form in Eq. 2.27. The height of the absorption edge $\Delta\mu_0$ is found similarly, by fitting the data above and below the edge with a simple linear or quadratic function and taking the difference between the two at E_0 . These background functions are all identified in Fig. 2.20a. It perhaps goes without saying that the choices made here in processing the EXAFS can affect the results, and a careful choice of background functions and the position of E_0 is extremely important.

The EXAFS oscillations, χ are extracted using the above functions by subtracting the single atom absorption and normalizing the resulting curve by the step height

$$\chi(E) = \frac{\mu(E) - \mu_0(E)}{\Delta\mu_0} \quad (2.28)$$

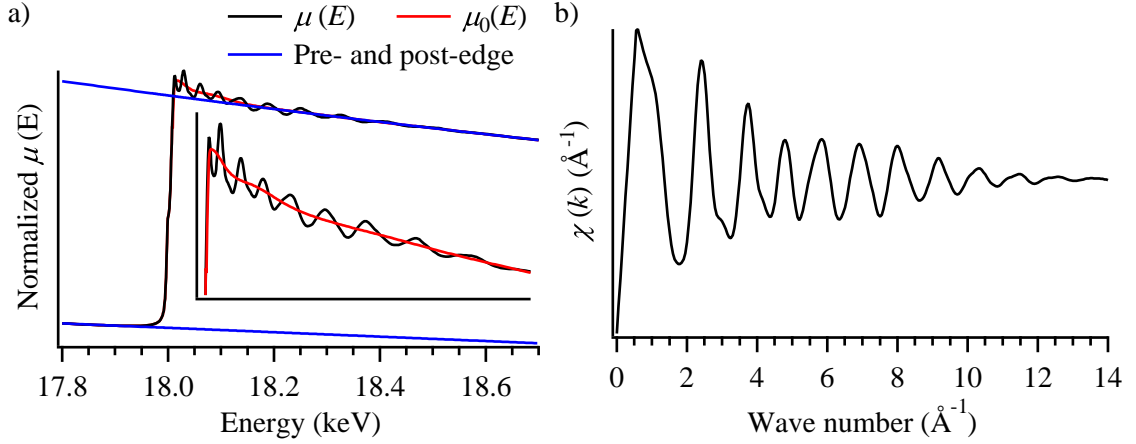


Figure 2.20: EXAFS background subtraction and extraction for Zr foil. (a) Measured $\mu(E)$ for a Zr foil, with fitted pre- and post-edge lines and smooth background $\mu_0(E)$. The pre- and post-edge lines are only fitted up to 25 eV below and after 170 eV above the edge so that they represent the long term trends in $\mu(E)$. (b) The extracted EXAFS $\chi(k)$ shows the decay in the oscillations as the energy increases above the edge.

and the energy is converted to electron wavenumbers by

$$k = \sqrt{\frac{2m(E - E_0)}{\hbar^2}} \quad (2.29)$$

where m is the mass of the electron and E_0 is the edge energy, the reference for 0 kinetic energy. The $\chi(k)$ data extracted from a Zr foil are shown in Fig. 2.20b. The oscillations damp out with increasing k , but are also damped by disorder in the sample. Often, weighting χ by powers of k is used for visualization purposes.

The origin of the EXAFS lies in the quantum event of an excited photoelectron scattering from neighboring atoms and returning to the atom from which it was.^{234–236} The probability of a lone atom absorbing a photon and creating an excited state is governed by Fermi's Golden Rule

$$\mu(E) \propto |\langle f | \mathcal{H} | i \rangle|^2 \quad (2.30)$$

where \mathcal{H} is the Hamiltonian governing the transition. When there are other atoms in the presence of the absorbing atom they modify the final state such that

$$|f\rangle = |f_0\rangle + |\delta f\rangle \quad (2.31)$$

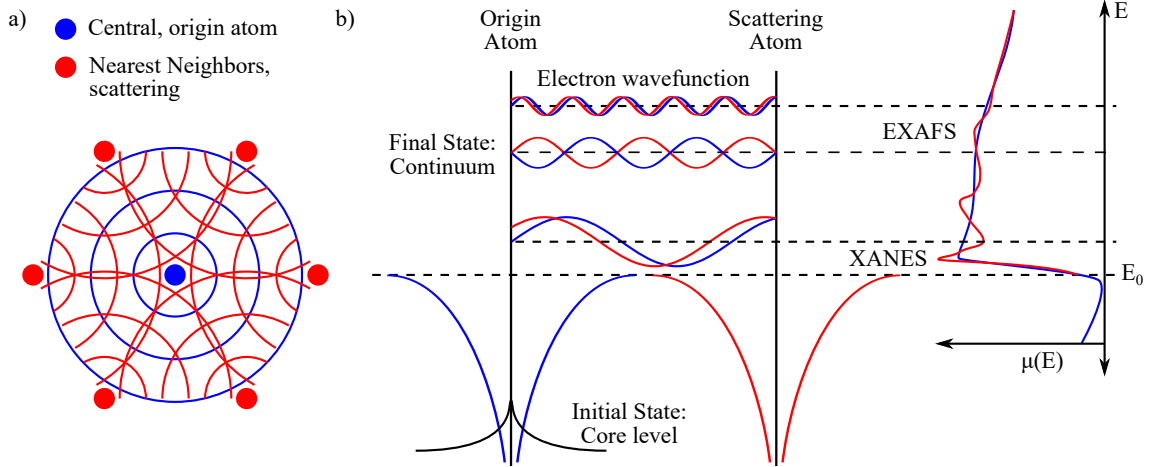


Figure 2.21: Diagram of the electron scattering process after an atom absorbs a high energy x-ray. (a) The excited electron wave function originating from the central, blue atom propagates spherically and encounters neighboring atoms, which scatter the wave and return some amplitude to the origin. (b) As the energy of the excited state increases, the wavelength shrinks, and the superposition of the outgoing and scattered wave oscillates between constructive and destructive interference, which modulates the probability of the origin atom absorbing a photon. This in turn modulates the amplitude of the absorption coefficient for the material about a smooth baseline.

where $|f_0\rangle$ is the lone atom final state and $|\delta f\rangle$ is the perturbation from the neighboring atom.²³⁶ It can be shown²³⁶ that the EXAFS amplitude is thus

$$\chi(E) \propto |\langle \delta f | \mathcal{H} | i \rangle|^2 \quad (2.32)$$

and that $\mathcal{H} \propto \exp(ikr)$. If the initial, tightly bound core electron state is approximated as a delta function then

$$\chi(E) \propto \int \delta(\vec{r}) e^{i\vec{k} \cdot \vec{r}} \psi_{\text{scatt}} d\vec{r} = |\psi_{\text{scatt}}(0)|^2 \quad (2.33)$$

where ψ_{scatt} is the wavefunction scattered from the neighboring atom. Thus the amplitude of $\chi(E)$ depends on the amplitude of the scattered wave function at the origin atom itself.

A simple physical explanation of the mechanism governing the EXAFS is presented in Fig. 2.21. The wave function of an ejected photoelectron propagates spherically from the origin.²³⁶ It is scattered by neighboring atoms and thus some amplitude returns to the origin. The outgoing and scattered wavefunctions superimpose and may constructively or destructively interfere at the origin. In a very quantum mechanical way, this interference modulates the probability of the absorption even occurring in the first place, and thus the x-ray absorption $\mu(E)$.

When the atoms are arranged randomly, as in an amorphous material, the scattering from neighbors is incoherent and does not have any compounding effect on $\mu(E)$. However, when arranged in a crystal neighboring shells of atoms coherently scatter the photoelectron, and the EXAFS is governed by a sum over these scattering shells²³⁶:

$$\chi(k) = \sum_j \frac{N_j f_j(k) \exp(-2k^2 \sigma_j^2)}{k R_j^2} \sin[2k R_j + \delta_j(k)] \quad (2.34)$$

where j is each coordination shell surrounding the central atom with N_j atoms at R_j away from the central atom. The exponential term introduces a damping effect by the Debye-Waller factor σ_j which is the mean-square displacement in R_j and a measure of the thermal vibrations in the material. The electron scattering terms $f_j(k)$ and $\delta_j(k)$ give the amplitude and phase shift of the scattering, and are dependent on the atoms in shell j . Expressed this way, $\chi(E)$ is a function of the bond length, thermal vibrations, and the type and number of atoms surrounding the central atom.

The power of EXAFS analysis lies in the ability to accurately relate the x-ray absorption to the local structure of atoms within $\sim 6 \text{ \AA}$ of a heavy core.^{245,246} The need for several hundred eV of uninterrupted $\mu(E)$ data limits the ability to measure light central atoms such as B or Na. These light atoms are still easily detected as long as they are surrounding a heavy atom. Furthermore, the environment around multiple atoms in a material can be analyzed to form a more complete picture.²⁴⁷ The local nature of the EXAFS also means that large crystals are not needed to obtain a coherent signal. The technique is thus ideal for nanocrystalline materials, such as the ZrB_2 films probed in this study.

Eq. 2.34 is written as a Fourier series in R_j , so the measured $\chi(k)$ can be easily transformed into R -space. The $\chi(R)$ are then analyzed as a sum of complex functions related to the scattering paths from the various coordination shells. (See Fig. 2.22) Each path represents scattering from neighboring shells and then back to the origin atom. Multiple-scattering paths, where the outgoing electron scatters from more than one shell before returning, are typically of low amplitude but should be included whenever possible.

The EXAFS are fitted by non-linear regression using the N , R , σ , and an arbitrary amplitude of each path as adjustable parameters. The complex, intertwining functions necessitate a healthy application of Occam's Razor: whenever possible, parameters should be constrained or fixed, and

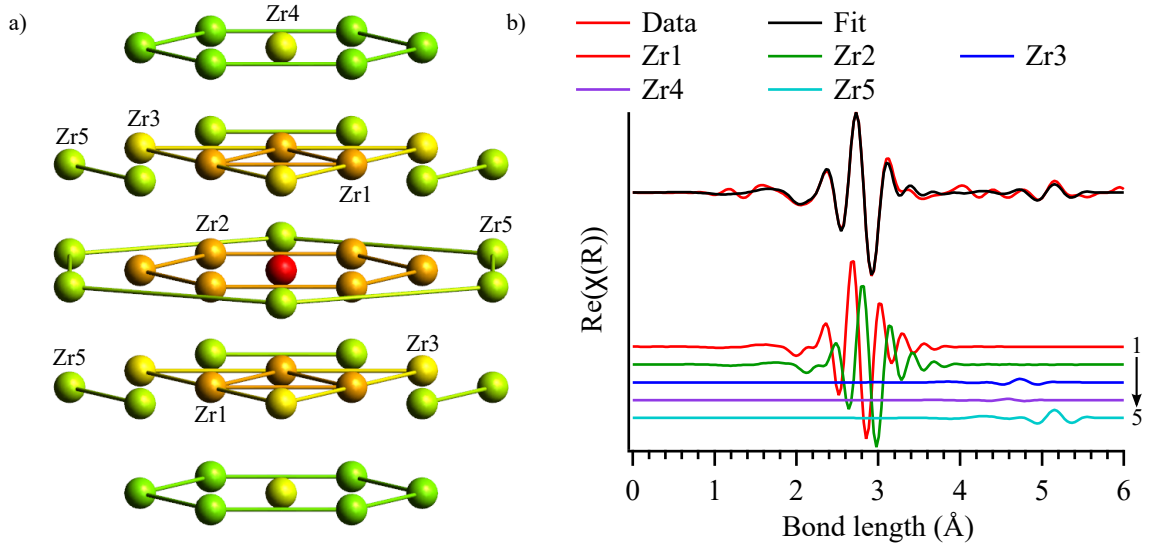


Figure 2.22: Diagram of scattering shells in Zr and Fourier transform of the EXAFS from each shell. (a) Model of the Zr cluster used in deriving the scattering paths from the central, red Zr atom to the neighboring shells in a pure Zr sample. Five shells are labeled and color coded by distance from the central atom. Zr1 and Zr2 are almost exactly the same distance from each other. Zr4 consists of only the top and bottom Zr atoms. (b) Plot of the real part of the Fourier transformed EXAFS, with theoretical fit consisting of the components of the five scattering shells in (a). Although some double scattering paths exist for the Zr structure (such as $\text{Zr0} \rightarrow \text{Zr1} \rightarrow \text{Zr2} \rightarrow \text{Zr0}$), their relative amplitudes were smaller than for Zr4, and so were neglected.

the minimum number of independent parameters should be employed. For example, in fitting the $\chi(R)$ in Fig. 2.22b, a Zr hcp crystal structure was assumed with lattice parameters a and c . All five scattering path lengths (R) were required to fit this lattice such that

$$R_1 = \sqrt{a^2/3 + c^2/4} \quad (2.35)$$

$$R_2 = a \quad (2.36)$$

$$R_3 = \sqrt{a^2 + c^2} \quad (2.37)$$

$$R_4 = c \quad (2.38)$$

$$R_5 = a\sqrt{3} \quad (2.39)$$

Further constraints such as this are discussed in §4.3 for the case of ZrB_2 thin films. Constraints

such as these are important to reinforce the conclusions derived from EXAFS analysis, where much of the data processing can be viewed as more art than science.

In Eq. 2.34, both the number and type of neighboring atoms can be defined, which allows one to fit data to model comprised of non-stoichiometric, defective, and doped compounds. The electron scattering and phase shift terms (f_j and δ_j) are terms which were originally derived from experimental data, but in the last decade theoretical calculations for all atoms have become available that are equally accurate.²⁴⁸ The EXAFS analysis in this thesis was all done using the Demeter software package²⁴⁹ for processing the data, calculating the scattering path f_j and δ_j using FEFF,²⁴⁸ and fitting the model to the data.

2.5 Scanning Electron Microscopy

The spectroscopic techniques discussed in the previous sections are stupendous for giving atomic scale information about the chemistry and structure within a thin film. However, when analyzing thin film morphology and stability, microscopy is just as essential. If one were to acquire XPS and XRD data from the Pt film shown earlier in Fig. 1.4a, the spectra would show that the Pt film had not been affected by the annealing, except that it became more crystalline. Microscopy is required to analyze the morphological changes in a thin film, and to assess failure mechanisms in devices.²⁵⁰ It often compliments spectroscopic analysis, and is required to confirm that models used in data analysis are valid.

In principle, a scanning electron microscope (SEM) operates just like a visible light microscope.²⁵⁰ As illustrated in Fig. 2.23, an electron gun column consists of a bright source of electrons, an aperture, and a condenser and objective lens to focus the beam on the sample. Electron optics use electric and magnetic fields to focus the beam to a spot <10 nm in diameter, allowing the resolution of extremely fine features well beyond the diffraction limit for visible light, owing to the high mass, and thus short wavelength of electrons. Likewise, ions such as Ga or He can be used for imaging or etching a surface by similar optics.²⁵¹ The process of etching with a focused ion beam is not discussed in this thesis, but is a common option in most SEMs.

Unlike light microscopes, a SEM does not image a large area simultaneously. 2D electron detectors are expensive and have lower signal-to-noise ratios than point detectors. To form an

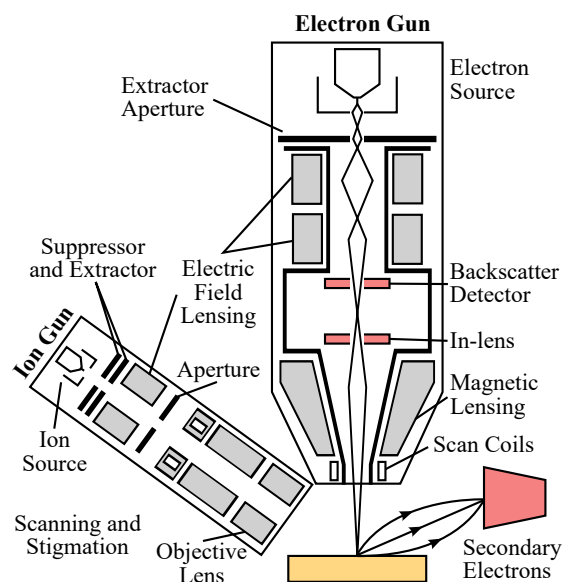


Figure 2.23: Schematic of SEM and FIB columns used for imaging thin films. In SEM a bright point source is narrowed by an aperture, focused by a condenser lens, adjusted for stigmation, and then finally focused on the sample by an objective lens. The optics use electric and magnetic fields to focus the beam down to less than 10 nm.²⁵⁰ The extractor voltage defines the energy of the incident beam. The beam is rastered across the sample and emitted electrons are detected in a variety of ways. Often, an ion gun is installed coincident with the SEM, which works under similar principles, but with a variation on the arrangement of the optics. The sample can be tilted to face the ion gun for imaging or milling of the sample surface.

image, the e-beam is scanned across the sample line-by-line, and the detectors collect all scattered electrons at a given beam position to constitute a pixel of the image. Highly accurate rastering optics and a vibrationally isolated sample stage make it possible to image objects with nm resolution.

Due to the UHV atmosphere required for normal SEM operation, and the high energy e-beam (kinetic energy between 0.5 keV to 50 keV) precautions similar to that of XPS are required. The sample must be well grounded in order to avoid charging effects, and also be thermally stable as local heating from the e-beam can cause evaporation (see §2.1.1). In many cases, a sample can be coated with a thin, electrically conducting layer (e.g. 10 nm of Au or W) via DC sputtering to give a good conductive pathway, provided that the features under investigation are significantly larger than the coating thickness. This coating technique can even be done with dessicated organic samples for imaging biological structures.

Multiple detectors are available for SEM including in-lens, “SE2,” and backscatter detectors. All are electron detectors, but as seen in Fig. 2.23 they are positioned at different locations. The SE2 and in-lens detectors are both designed to detect secondary electron emission from the sample

surface. The in-lens detector is positioned directly above the objective lens and acts as a sort of dark field image. The SE2 detector is positioned to the side of the sample and produces images with shadow and more surface sensitivity. The backscatter detector is designed to measure electrons which are scattered elastically, forming an image with high Z-contrast.

2.5.1 Interpretation of SEM Images

Although SEM is normally used to analyze surface morphology, the same physical principles apply as in §2.2. The high energy electrons will penetrate a substantial distance into the surface of the material before they are scattered. SEM imaging requires the creation of secondary electrons, which are ejected as part of the inelastic scattering of the incident beam. These secondary electrons usually have low kinetic energy (~ 100 eV) and cannot travel as far as the incident e-beam, so depth sensitivity is not much affected by the energy of the electron gun. In principle, though, the image formed is a superposition of surface and sub-surface features.

Fig. 2.24 illustrates the depths from which secondary electrons and other particles can be detected. The incident electrons scatter randomly throughout the material, but the paths are generally distributed in a tear drop shape.²⁵² During this scattering, the incident electrons lose energy by exciting electrons in the material. The probability of inelastic scattering follows the same principles that were discussed in §2.2.1 regarding the XPS background, with there being a high probability of creating many low energy electrons, which form the secondary electrons that are measured. If the incident energy is high enough, core level electrons can be excited, just as in XAS, which are then either ejected from the material, or relax by fluorescence, which is addressed in the next section.

The scattering of the incident beam creates Auger and secondary electrons near the surface, which are ejected in a cosine distribution around the surface normal.²⁵³ Most of these electrons return along the incident beam path and are collected by the in-lens detector. The SE2 detector is positioned beside the sample, and so electrons that reach it are affected by shadowing from surface features, which greatly improves their visibility compared to the in-lens detector. The intensity reaching SE2 is also much lower and hence the SE2 signal is limited by a relatively low signal-to-noise ratio.

The in-lens and backscatter detectors yield different images from a given set of surface features. As such, contrast in the in-lens detector image is primarily influenced by the secondary electron

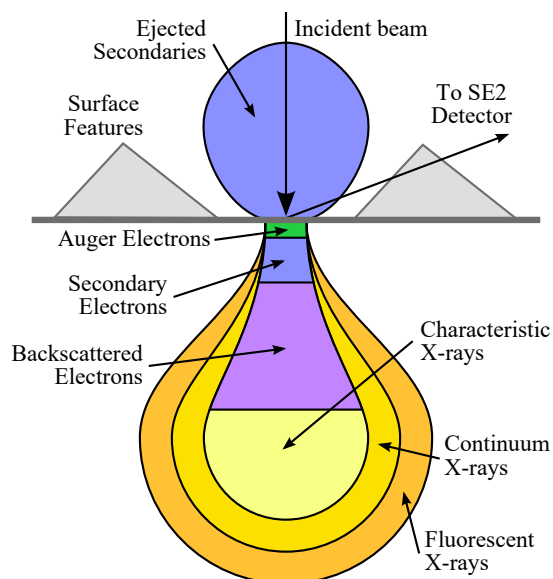


Figure 2.24: Illustration of the interaction of electrons with the surface of a sample in SEM. The incident electrons scatter at various depths producing different particles. The creation of Auger and secondary electrons occurs near the surface after inelastic scattering of the incident beam. Backscattered electrons elastically scatter from much deeper in the sample. At even greater depths excited electrons relax by fluorescence which can be detected from deep within the sample. Because the SE2 detector is positioned beside the sample, electrons that reach it are affected by shadowing of the surface features, producing the contrast in the image.

yield of the surface,²⁵⁴ which in turn is a function of the atomic, crystal, and electrical properties. The edges of surface features are generally better emitters and so are easily seen, as are heavy elements with weakly bound electrons.²⁵⁵ An image from a backscatter detector is directly related to the atomic mass, and so provides contrast that reflects the relative weight of atoms.

Charging affects SEM in unpredictable ways. Typically, charging effects are seen with insulating samples when specific, low conductivity features begin deflecting the e-beam, reducing intensity in some places and increasing it in others. In some cases, the excess charge is spontaneously discharged and the image suddenly shifts, which is detrimental when dwelling for a long time. Different averaging techniques may be used to limit charging effects, such as frame averaging, where the beam spends a short time at each pixel and does not return until a full frame is complete, giving that spot time to discharge. Under certain circumstances, when the charging is due to high resistance connections, insulating regions of the sample can be identified by the nature of how they build charge more quickly than other areas.

2.5.2 Energy Dispersive Spectroscopy

The SEM used in this work also has the capability of performing energy dispersive spectroscopy (EDS), which is similar to XPS.²⁵⁶ As was shown in Fig. 2.24, some of the incident electrons cause the generation of x-rays from deep within the sample in a two step process. First, the incident beam excites a core level electron to a state above E_f . This electron can be ejected from the sample as a secondary electron if it is close enough to the surface. If it is not, it may be conducted away to ground, but a more likely event is that it quickly thermalizes to just above E_f , and finally relaxes back to an empty core level and emits an x-ray.

This fluorescence is the reverse of the XPS process, and so the energy of the x-rays emitted can be correlated to the BE of the state and thus the mass of the atom. Unlike XPS the incident beam is rastered across the sample surface, and thus the fluorescence is spatially mapped as well. This makes EDS a powerful tool in analyzing thin film structures, because the distribution of atomic species can be monitored at reasonably high resolution.

There are two complicating factors. The emitted x-rays can travel through several μm of a sample before being absorbed, and so the range of depths from which they arise is determined by the penetration of the incident e-beam. In order to create the core holes required for fluorescence, the e-beam must be several keV in energy, and as this energy increases, so does the penetration depth, which means the signal becomes dominated by the underlying bulk. Furthermore, the teardrop shape depicted in Fig. 2.24 flares out beneath the surface, so the fluorescence measured at one pixel comes from a volume much greater than the size of the beam. The actual lateral resolution of EDS is typically about 100 nm.

The second complication is that there is no way to quantify the chemical concentrations with EDS because there are no comprehensive theoretical descriptions of the background or sensitivity factors for the process. This limits the technique to qualitative conclusions, which are none-the-less valuable.

2.6 Thin Film Properties at High Temperature

For the high temperature sensors discussed in §1.1, the primary film property of interest is high temperature stability, which is a vague, qualitative metric. All the techniques discussed in

the previous sections contribute to an understanding of the high temperature stability, which is a combination of structural, morphological, and chemical stability. The exact criteria depend on the purpose of the film.

In this work, ZrB_2 was investigated as an electrical conductor. The limits of its stability are therefore determined by the point at which it is no longer conductive, either because of chemical changes such as oxidation, or morphological changes such as agglomeration. On the other hand, h-BN and $\alpha\text{-Al}_2\text{O}_3$ were intended to be protective coatings to retard the diffusion of oxygen through themselves and serve as continuous barriers at high temperatures. These roles were selected based on the materials' excellent properties at more moderate temperatures.

The primary effect of prolonged exposure to high temperature is the increased activity of the system.²⁵⁷ For example, the diffusion of atoms in a material (the rate of a reaction) as a function of temperature follows an Arrhenius equation

$$R = A(T) \exp(-E_a/kT) \quad (2.40)$$

where R is the rate, $A(T)$ is a coefficient that typically depends on the temperature T sub-linearly, E_a is an energy barrier, and k is Boltzmann's constant. Thus, as the temperature is increased the rate increases exponentially, and the agglomeration or oxidation of a material will occur more rapidly.²⁵⁸ Due to the process specific temperature dependence in $A(T)$, experimental measures of the rate of a process at RT are only indicative of the rate at high temperatures, and so high temperature annealing remains a valuable tool for assessing the properties of materials.

The rate of oxidation (and diffusion of oxygen through a protective layer) is also dependent on the chemical potential of the gas, which corresponds to the vapor pressure above solid materials. A convenient unit of measure for comparing experiments done for different times at different pressures is the Langmuir, which is the product of the pressure and the time. It is properly defined so that $1 \text{ L} = 10^{-6} \text{ torr sec}$ ($1.333 \times 10^{-6} \text{ Pasec}$), which is roughly the amount of exposure required to saturate a surface with 1 monolayer of a vapor species. Unfortunately, there is no conventional unit that combines time, pressure, and temperature.

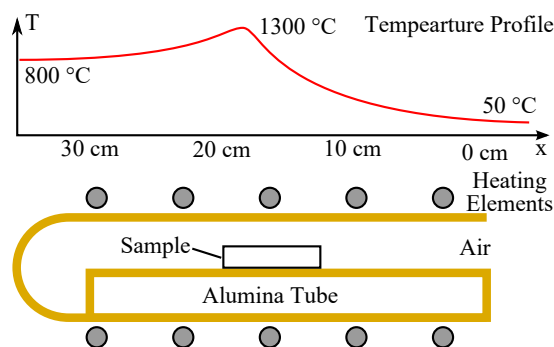


Figure 2.25: Illustration of temperature gradient in a tube furnace. An alumina tube insulates samples from direct exposure to the heaters (and vice versa). Because one end of the tube is open to the room, a temperature gradient exists. Using a thermocouple, this gradient was measured, allowing samples to be placed at different points in the tube to be annealed at different temperatures.

2.6.1 High Temperature Treatments

Air annealing of thin film samples was primarily conducted in a Blue model CC59256PCOMC tube furnace capable of reaching 1500 °C. A gradient in temperatures exists from the center of the furnace to the open side, as depicted in Fig. 2.25, which was utilized to simultaneously perform annealings at multiple temperatures. One consideration that must be made, however, is that the temperature ramp rate is not the same for these different positions in the furnace. If the furnace was set to reach 1200 °C at the center with a ramp rate of $\sim 10\text{ }^{\circ}\text{Cmin}^{-1}$, it takes 2 h to reach that temperature. Simultaneously, a sample placed closer to the open end of the tube so that it reaches 850 °C at the end of the ramp would only see a ramp rate of $\sim 7\text{ }^{\circ}\text{Cmin}^{-1}$.

Much of the annealing done in this work was performed under UHV conditions within the system in room 193 (see §2.1). The heaters in the deposition chamber and XPS chamber were used for sample heating during deposition and also for the long term annealings discussed in §3.4. A thermocouple tied to the heater was used to control the temperature via a PID circuit allowing for stable annealing for long durations. However, because there was no direct contact between the heater and the sample, heat was only transferred radiatively, and as such, the sample temperature was substantially below the heater temperature.

The sample temperature was calibrated by tying a thermocouple directly to a stainless steel sample holder and starting the heater. The calibration curves in Fig. 2.26 were generated by setting the heater temperature and measuring the sample temperature after it had come to equilibrium with

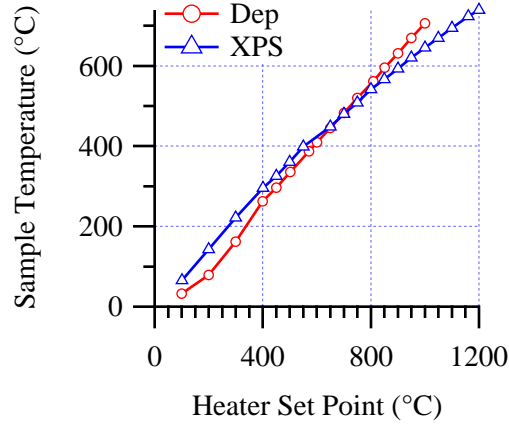


Figure 2.26: Graph of the sample temperature versus the heater set point for the deposition chamber and the XPS chamber. The thermocouples used in both measurements have an accuracy $\pm 2.5^\circ\text{C}$. Although the heaters are the same in both chambers, differences in the emissivity of the heaters, sample holder, and chamber walls contribute to the difference in equilibrium temperature.

the heater. The heaters themselves, made of a graphite serpentine pattern encased in BN, are limited to 1300°C , which places a limit of $<1000^\circ\text{C}$ on the sample temperature, or less in an oxidizing atmosphere.

When there is no direct contact between the heater and the sample, and no atmosphere for convective heat transfer, the equilibrium heat flow between two surface is given by

$$\dot{Q}_{1 \rightarrow 2} = \sigma(T_1^4 - T_2^4) \left[\frac{1 - \epsilon_1}{A_1 \epsilon_1} + \frac{1}{A_1 F_{1 \rightarrow 2}} + \frac{1 - \epsilon_2}{A_2 \epsilon_2} \right]^{-1} \quad (2.41)$$

where σ is the Stefan-Boltzmann constant, A is the area of the surface, $F_{1 \rightarrow 2}$ is the view factor from surface 1 to 2, and T is the absolute temperature. The heat flow into the sample is equated to the heat flow out of the sample by thermal radiation to the chamber walls and thermal conduction through the manipulator arm. Thus, the temperature of the sample can be increased if the emissivity of the sample were higher, and the emissivity of the chamber walls and heater were low.

Further annealing was done *in situ* in an Anton Paar DHS 1100 domed hot stage²⁵⁹ on the XRD instrument discussed previously. The hot stage (schematically illustrated in Fig. 2.27) is capable of heating samples to 1100°C under varying atmospheres while simultaneously measuring XRD. In this case, the sample is in direct contact with the heater, and so no calibration is required, even

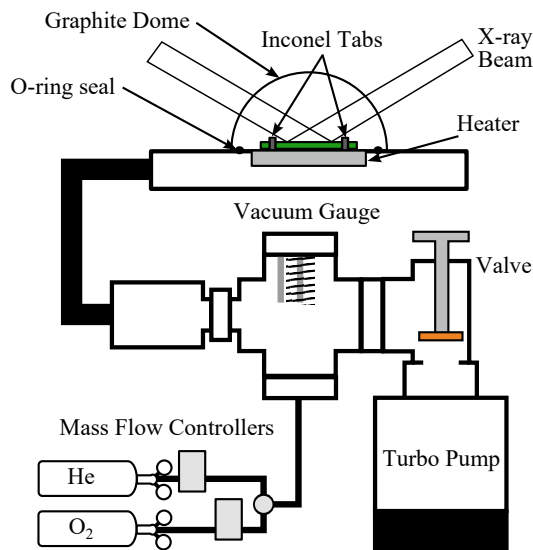


Figure 2.27: Diagram of the hot stage and gas delivery system used for *in situ* XRD at temperatures up to 1100 °C. A thin graphite dome seals the sample environment for safety and for controlled atmosphere. Inconel tabs hold the sample in contact with the heater, allowing full range of motion of the stage. A hose connects the sample environment to the gas delivery system, which consists of a turbo pump and mass flow controllers that can deliver a flowing atmosphere of O₂ and He for varying the pressure of O₂ during the heating.

for vacuum conditions. A gas delivery system, designed by undergraduate student Matt Curti, was retrofitted to the hot stage, allowing *in situ* XRD between 10^{-6} torr to 760 torr.

As mentioned above, the primary effect of high temperatures is to increase the activity in the system. Many events, such as the oxidation of a thin film, can occur in minutes, and so when performing *in situ* measurements a balance must be found between fast scans and high resolution scans.²⁶⁰ In this work, it was found that a total scan duration of no more than 5 min should be used to observe changes in the film in real time due to the high temperatures. This meant that the *in situ* XRD scans were only done over a range of 35° in 2θ , which was still large enough to detect several diffraction peaks for analysis.

XRD using the hot stage is the only example of *in situ* high temperature characterization reported in this thesis. In all other cases, samples were simply characterized before and after annealing. This means that the effects of exposure to oxygen at high temperatures, and any structural changes that occurred could not be exclusively attributed to the isothermal period, but may have occurred during temperature ramp up or cooling. Although this marginally complicates the analysis,

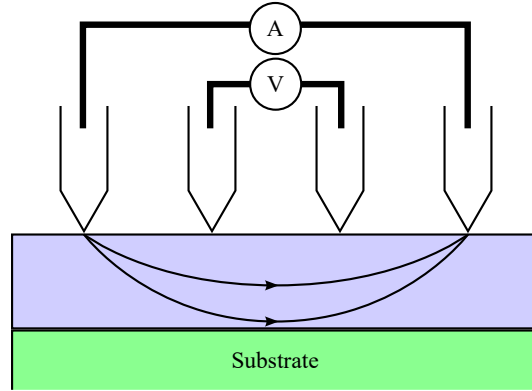


Figure 2.28: Illustration of an electrical conductivity measurement using a co-linear 4pt-point probe. A known current is passed between two of the probes and the voltage is measured between two others. In an ideal conductor, the voltage difference between any two points would be zero. Any measured voltage must be due to the resistivity of the material. By conducting current and voltage measurements on different probes, the effects of contact resistance are eliminated. An insulating substrate is ideal for these measurements, as then all the current must pass through the bulk of the film.

the effects of the temperature cycling are important to examine as well for the intended applications of these materials.

2.6.2 Four Point Conductivity

For ZrB_2 thin films, the electrical conductivity is an easy and valuable metric to determine the high temperature stability. The conductivity is affected not only by the electronic properties of the material, but also by density and crystallinity. Thin films usually have a “burn in” period whereby the conductivity improves in the initial stages of annealing as defects are annihilated. However, as a film agglomerates, the conductive pathways become constrained and the overall conductivity of the film begins to decrease. In the final stages of agglomeration, as regions become electrically isolated, the macroscopic conductivity of the film drops to zero, even when the conductivity of the individual nanoscale regions is still very high.

Fig. 2.28 shows a diagram of a typical 4-point conductivity probe measurement with a co-linear arrangement.^{261,262} Other arrangements are viable, but the co-linear probe works well when the size of the sample is small²⁶³ or varies. The resistivity of the sample is calculated from the supplied current and measured voltage by

$$\rho = F \frac{VA}{Il} \quad (2.42)$$

where V and I are the voltage and current, A is the cross sectional area of the film, and l is the length of the co-linear probe. F is a correction factor that depends on the dimensions of the probe and the ratio of the film length to its width.^{261,263} These correction factors are nearly 1 for all films measured in this work. The correction becomes important when near the edge of a sample, however, or with a semiconducting substrate.²⁶⁴

CHAPTER 3

ZrB₂ THIN FILM GROWTH AND THERMAL PROCESSING

This chapter describes the growth and thermal stability of thin films of Zr and B with varying stoichiometry. A refined model was required to be developed for analyzing the XPS of Zr_xB_{1-x} films, described in §3.2.1. The Zr_xB_{1-x} films were examined for as-deposited structure and electrical conductivity as a function of the growth temperature and composition. The high temperature stability was assessed in the absence of O₂ by annealing above 600 °C in UHV for extended periods, described in §3.4. The effects of this annealing on the film structure and conductivity was a necessary first step in assessing the applicability of ZrB₂ thin films in high temperature thin film electronics.

3.1 Experimental Details

Zr_xB_{1-x} thin films were deposited using e-beam co-evaporation from elemental sources of Zr and B in UHV, as described in §2.1.1. Films of varying composition were grown on r-cut sapphire substrates in order to assess the breadth of phases in the thin film regime. During deposition, the substrates either remained at RT (23 °C–50 °C, due to radiative heating from the e-beam sources) during which amorphous films were grown, or were heated to 600 °C or 850 °C to enhance surface diffusion and enable the growth of nanocrystalline films.

Evaporation rates from each source were independently measured by QCM rate monitors which were calibrated by stylus profilometry. For the B source, which sublimates, rates of 0.1 Å s⁻¹ to 0.4 Å s⁻¹ were obtained for e-beampowers between 245 W to 469 W. The Zr rate was between 0.2 Å s⁻¹ to 1.1 Å s⁻¹ for powers between 1400 W to 1760 W. The ratio of these rates determined the final film composition. The total growth rate at the substrate, which was limited by the maximum B evaporation rate obtainable without rate instability, was between 0.2 Å s⁻¹ to 0.9 Å s⁻¹, as determined by profilometry of the ZrB₂ film after deposition.

Following deposition, the composition of the as-deposited films and vacuum annealed films was measured by XPS without breaking vacuum. Film crystallinity and texture was determined by XRD, and density and roughness by XRR. For XRD, an offset was applied to the incident angle

to minimize diffraction from the sapphire substrates, as discussed in §2.3.1. Nanoscale surface morphology was qualitatively observed by SEM. Electrical conductivity was determined from sheet resistance as measured by a co-linear four point probe, with appropriate dimensional corrections.²⁶⁴

During the post-deposition annealing treatments, samples were briefly exposed to air at RT. In §3.4.1, the process was (i) remove samples from vacuum to be remounted on new carriers, (ii) anneal in UHV for 1 h at 800 °C, (iii) remove samples from vacuum for XRD and SEM analysis, (iv) anneal in UHV for 8 h at 800 °C, (v) remove samples for final analysis. For the samples reported in §3.4.2, a different procedure was used involving the removal of one of six samples from the carrier, and the compound annealing of the remaining samples. Each annealing step followed a parabolic trajectory (1 h, 4 h, 9 h, 16 h and 25 h) so that the cumulative annealing times were 1 h, 5 h, 14 h, 30 h and 55 h, with RT air exposure between each step.

3.2 Composition of ZrB₂ Thin Films

3.2.1 Modeling for XPS Quantification

Due to the degree of peak asymmetry and overlap between the B 1s and Zr 3d photo-peaks, synthetic line shapes were fitted to the data and used for XPS quantification. A universal Tougaard background¹⁷⁸ was fitted to the region, followed by three Gaussian peaks for the plasmon losses. For the B 1s peak and Zr 3d doublet, the LF line shape provided by CasaXPS™¹⁸⁷ was used, as described by Eqs. 2.11 and 2.12. This model was fitted to the measured spectra by a Marquardt-Levenberg²⁶⁵ non-linear regression procedure, using the reduced χ^2 as the figure of merit. The resulting curves are shown in Fig. 3.1a. This model is compared to a more naive one, consisting of three symmetric SGL functions (Eq. 2.9) and the same Gaussian plasmon peaks against a Shirley background, which is shown in Fig. 3.1b.

When fitting the data in Fig. 3.1a, the only constrained parameters were the asymmetry of the three photo-peaks, which were set to $\alpha = 0.58$ and $\beta = 1$, and the FWHM of the peaks in the Zr 3d doublet, which were set equal to each other. The resulting LF line shape is qualitatively similar to a Doniach-Sunjić line shape¹⁸⁹ with an asymmetry parameter of $\alpha_{DS} = 0.085$, which is less than the value used for fitting ZrB₂ XPS peaks elsewhere.²⁶⁶ Different thin film samples were fitted with slightly different α -values. Across the films examined in this chapter, $\bar{\alpha} = 0.55(20)$, which

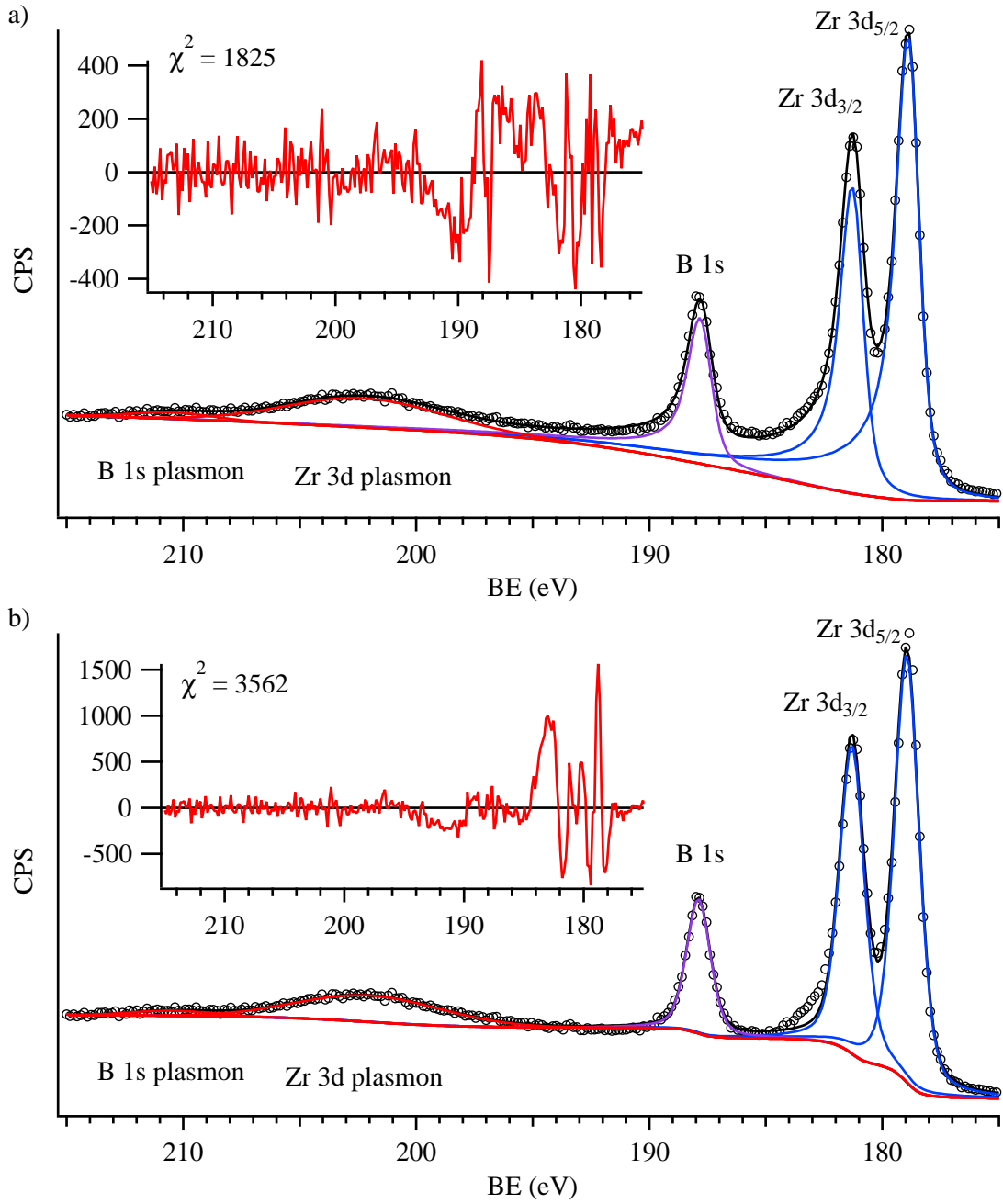


Figure 3.1: Comparison of ZrB₂ XPS peak fitting with different models. XPS spectra are from an as-deposited Zr_xB_{1-x} thin film with a measured composition of $X_{\text{Zr}} = 0.26$, showing asymmetric B 1s and Zr 3d core levels and plasmon resonance losses. (a) The data, modeled with a Tougaard background and asymmetric LF line shapes. (b) The same data, modeled with a Shirley background and symmetric SGL line shapes. See Table 3.1 for more details. Insets plot the error in the fit.

Table 3.1: Parameters for the two synthetic peak models in Fig. 3.1. The first set of peaks was fit against a Tougaard background with $B = 1208.91$ and $C = -550$ (Fig. 3.1a), while the second was fit against a Shirley background (Fig. 3.1b).

	Peak	Shape		BE (eV)	FWHM (eV)	Area (CPS eV)	at %
asymmetric	Zr 3d _{5/2}	LF	$\alpha = 0.58, \beta = 1$	178.84	1.13	45 139.0	26.51
	Zr 3d _{3/2}	LF	$\alpha = 0.58, \beta = 1$	181.23	1.13	29 879.8	
	B 1s	LF	$\alpha = 0.58, \beta = 1$	187.77	1.17	14 686.3	73.49
	1st Plasmon	GL	$m = 0$	202.26	7.90	11 559.2	
	2nd Plasmon	GL	$m = 0$	210.47	4.18	1 364.7	
symmetric	Zr 3d _{5/2}	SGL	$m = 39$	178.95	1.26	32 371.4	27.97
	Zr 3d _{3/2}	SGL	$m = 39$	181.31	1.26	23 426.2	
	B 1s	SGL	$m = 39$	187.89	1.21	9 781.4	72.03
	1st Plasmon	GL	$m = 0$	201.99	7.30	9 818.2	
	2nd Plasmon	GL	$m = 0$	210.39	4.16	1 098.2	

corresponds to α_{DS} parameters between 0.107 and 0.86. For the naive fitting in Fig. 3.1b, the mixing parameter for the SGL line shape was fixed at 0.39, which best modeled the B 1s peak. Fitted peak parameters are given in Table 3.1 for both models.

In comparing these two models of the ZrB₂ XPS spectra (hereafter referred to as the symmetric and asymmetric models, for simplicity) there are two values which are immediately relevant. The first is the measured composition, which for both films was ~ 27 at% Zr. Since the nominal accuracy of XPS quantification is at best 5%,^{155,158,267} these values are effectively identical. However, the symmetric model has a substantially worse χ^2 , by a factor of 2, and clearly misses several details of the spectra.

In the asymmetric model, the ratio of the 3d_{3/2} to the 3d_{5/2} peak is 0.661 951(3293), which is extremely close to the theoretical value of 2/3, while in the symmetric model it is 0.723 670(4856). The reason for this difference is that the asymmetric line shapes distribute intensity from the 3d_{5/2} peak to the area under the 3d_{3/2}, an effect which the Shirley background is poorly equipped to simulate. (The discrepancy would be even more severe if the symmetric peaks were used with a Tougaard background.)

The Shirley background also breaks one of the tenets presented in §2.2.1: it rises above the data by ~ 250 CPS from 195 eV to 190 eV, as shown in Fig. 3.1b. This region of the spectrum is where one would expect surface plasmon resonance losses, a feature which is lost beneath the

Shirley background. Surface plasmon losses are much weaker than their bulk counterparts, due to the small ratio of surface to volume, and their positions are highly dependent on the exact surface characteristics. For these reasons, surface plasmons were not modeled in either case. Typically, though, to analyze the spectrum with a Shirley background the left end point of the background is placed at ~ 192 eV, in order to avoid the background overshooting the data. Such a restriction is not needed for a Tougaard background analysis.

The shift in intensity by using the asymmetric peaks can also account for the region between the Zr 3d doublet and the B 1s peak, and in fact, the asymmetry shifts some intensity to the region below the B 1s peak. While the reduction in the B 1s peak intensity with the asymmetric peaks did not much affect the composition measured by the two models, the asymmetric intensity between the Zr 3d and B 1s peaks does dramatically effect analysis of ZrO_2 3d peaks, which appear at ~ 185 eV. As seen in the inset in Fig. 3.1b, a large portion of the error between the data and the symmetric model lies around the Zr 3d doublet, while for the asymmetric model this error is reduced by a factor of 3. The Zr 3d doublet, as well as the region just before the B 1s, is the main reason for the high χ^2 of the fit.

One subtle difference between the two models is the error around the B 1s peak. In the asymmetric model, the error jumps sharply around 188 eV, in a high-low-high pattern indicating a poor model of the peak shape. However, in the symmetric model, this error is dramatically reduced. There is justification for the B 1s peak exhibiting less asymmetry than the Zr 3d peaks. As discussed in §2.2.2, the asymmetry in metal samples is due to scattering of the ejected photons from conduction band states. However, the calculated partial DOS for ZrB_2 ⁵⁰ shows that the B 1s state has very little overlap with states near the conduction band, which is mostly comprised of B 2p and Zr 3d states. Thus, excited B 1s electrons have only a small chance of scattering from the conduction band, relative to the Zr 3d states.

The asymmetric model could be improved by taking the nature of the conduction band states into account, and removing a large degree of asymmetry from the B 1s state. This was not done, however, due to an adherence to Occam's razor. Although the reduced scattering of B 1s electrons is a plausible argument, there is no way of knowing (without significant theoretical calculations) how large of an effect this might be. Thus there is no justifiable way to consistently alter the asymmetry of the B 1s photo-peak, and the model presented in Fig. 3.1a should be preferred.

As stated earlier, the quantitative differences between the asymmetric and symmetric models are minor. The models agree exceptionally on the positions and FWHMs of all the peaks, as well as on the composition of the films. The intent in developing the more advanced, asymmetric model, which correctly accounts for all features of the spectra both with and without an oxide phase, was to have the smallest error for the quantification of the $\text{Zr}_x\text{B}_{1-x}$ films. In the next section, a curious result is presented: that the composition of the $\text{Zr}_x\text{B}_{1-x}$ films as measured by XPS differs substantially from what was expected based on the QCM deposition rate values.

3.2.2 Composition of $\text{Zr}_x\text{B}_{1-x}$ Films

As-deposited films with less than 45 at % Zr contained less than 10 at % O and C contamination, and no Zr oxide or B oxide peaks were observed. However, as the Zr concentration increased, so too did the O concentration in the film, and a second chemically shifted Zr 3d doublet developed 3.9 eV above the main peak, corresponding to a Zr^{4+} oxidized state. The curve fitting shown in Fig. 3.1a was applied to all films, but in cases where a Zr oxide doublet was observed in the raw spectrum, two symmetric peaks were added to account for the oxide state. The intensity from this oxide state was added to that of the main Zr doublet in determining the total Zr mole fraction

$$X_{\text{Zr}} = \frac{I_{\text{ZrB}_2} + I_{\text{ZrO}_x}}{I_{\text{ZrB}_2} + I_{\text{ZrO}_x} + I_{\text{B}}} \quad (3.1)$$

where I is the intensity corrected by tabulated RSF values²⁰¹ calculated²⁶⁷ from Scofield cross sections.

Data from 13 film depositions over a range of $\text{Zr}_x\text{B}_{1-x}$ compositions are plotted in Fig. 3.2a, showing that the Zr mole fraction in a given film is below what would be expected based on the relative deposition rates as measured by the two QCMs. The horizontal error bars represent an observed variation of approximately 10% in the measured rates during deposition, while the vertical bars represent the typical estimated ± 0.05 uncertainty in the XPS quantification due to potential errors in the synthetic peak model and RSFs. For a more complete analysis of the error in the XPS quantification, see appendix A. The data are well fit by a power function $X_{\text{Zr}} = F^p$ where $p = 2.1038(960)$, with a reduced χ^2 of 0.034. This nearly parabolic trend was used to predict the composition for subsequent depositions.

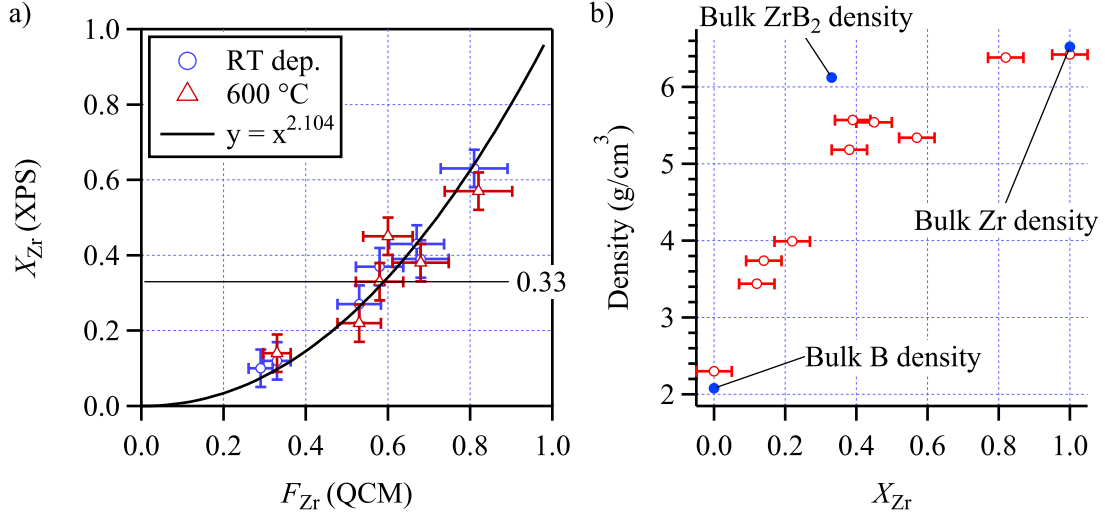


Figure 3.2: Zr_xB_{1-x} film composition and density versus evaporation flux. (a) Zr composition in as-deposited films determined from XPS versus the Zr fraction of the evaporated flux as measured by QCM. (b) Film density measured by XRR versus XPS composition.

Based on the power fit to the XPS composition, the Zr rate must be 0.5929(1070) % of the combined evaporation flux in order for the final film composition to be stoichiometric ZrB_2 ($X_{Zr} = 0.3333$). The data in Fig. 3.2a implies a low sticking coefficient for Zr relative to B in these depositions. The QCM measurements were calibrated several times during this experiment by growing pure Zr and B films grown on sapphire substrates with a mask to create a sharp step. Stylus profilometry found that these film thicknesses were within 10% of the expected values. No cross-talk was observed between sources and QCMs, either. By all accounts, the measurement of the independent evaporation rates is accurate. (Further discussion of the uncertainty in the XPS quantification can be found in Appendix A.)

At this time there is no explanation for the observed non-linearity in the XPS versus QCM data. The trend exists in films of varying thickness as well as in depositions at 50 °C, 600 °C and 850 °C, so it not likely to be caused by a gradient in the composition of the as-deposited films. The composition of the film surfaces remain unchanged after annealing in vacuum, further suggesting that the non-linearity is not a problem of atom mobility, with Zr atoms diffusing deeper into the film. Evaporation does not explain the lack of Zr in the films either, as Zr evaporates in UHV at a higher temperature than B (1600 °C, vs 1400 °C for B, to obtain a vapor pressure of 10^{-7} torr). The oxide phases of Zr are likewise more stable than those of B.

By all accounts, $\text{Zr}_x\text{B}_{1-x}$ films should be deficient in B, it being the lighter and more volatile atom. If both the XPS and QCM measurements are accurate, then the conclusion must be that the sticking coefficient of Zr on a $\text{Zr}_x\text{B}_{1-x}$ surface is less than the sticking coefficient on a pure Zr surface (or vice versa for B). The low sticking coefficient of Zr on a $\text{Zr}_x\text{B}_{1-x}$ surface is further supported by measurements of film thickness and density as measured by XRR, the latter of which is plotted in Fig. 3.2b. Based on the $\text{Zr}_x\text{B}_{1-x}$ film thickness and the density, the total film mass is less than the sum of the Zr and B masses measured by the QCMs.

The density of the $\text{Zr}_x\text{B}_{1-x}$ films showed a continuous trend in density ranging from pure B to pure Zr. For films near ZrB_2 stoichiometry, the density is consistently below the bulk density of 6.12 g cm^{-3} .²³ As seen in Fig. 3.2b, film density rises from 3.6 g cm^{-3} for $X_{\text{Zr}} < 0.2$ to 6.4 g cm^{-3} for $X_{\text{Zr}} > 0.8$, approaching the bulk density of Zr. For compositions $0.33 < X_{\text{Zr}} < 0.66$, film density averaged 5.2 g cm^{-3} . Based on SEM images shown in §3.4, this low density for ZrB_2 thin films is likely due to microscopic voids between grains in the films, and not necessarily representative of the density of the ZrB_2 grains themselves.

3.3 As-Deposited Film Structure

XRD spectra from as-deposited films with a range of $\text{Zr}_x\text{B}_{1-x}$ compositions are shown in Fig. 3.3. All depositions at RT were amorphous regardless of composition. Films with $X_{\text{Zr}} > 0.33$ deposited at elevated temperatures were typically nano-crystalline, with a single broad peak near 33° in 2θ . Films deposited with a measured composition $X_{\text{Zr}} < 0.33$ tended to form more crystalline films, with Scherrer grain sizes $\sim 20 \text{ nm}$. These results were not consistent, however, as some depositions produced a randomly oriented polycrystalline film, while others yielded highly epitaxially oriented films (c.f. the top two sets of curves in Fig. 3.3).

Unlike the polycrystalline films, which appeared morphologically as coalesced grains (see SEM images in §3.4), the amorphous films exhibited a smooth, homogeneous surface. Nano-grained films were a mix of these two states, with nano-crystallites visible on the surface, and a smooth matrix in between. Like the polycrystalline films deposited at 600°C , these nano-crystallites were highly oriented. In ZrB_2 powder diffraction,²⁸ the three most intense peaks are the $(10\bar{1}1)$, the $(10\bar{1}0)$, and the (0002) , in order of decreasing intensity. The nano-crystalline films all show diffraction from

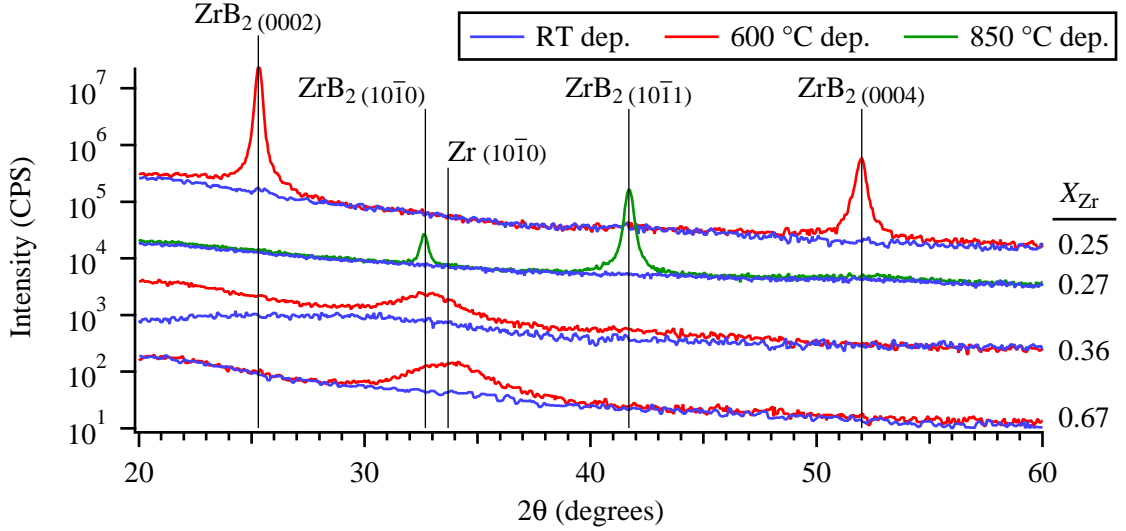


Figure 3.3: XRD gonio spectra from as-deposited $\text{Zr}_x\text{B}_{1-x}$ films with varying deposition temperature, offset for clarity. All spectra were recorded with an $\omega = 7^\circ$ incident angle offset to remove strong peaks arising from the sapphire substrate.

the $(10\bar{1}0)$ peak exclusively, a texture which persists through vacuum annealing, as discussed in the next section.

Films deposited at 850°C consistently showed multiple diffraction peaks, in an intensity ratio consistent with a random orientation. Through vacuum annealing experiments, it was observed that 600°C was an insufficient temperature to promote the growth of ZrB_2 crystals in these films, but after just 1 h at 800°C substantial grain growth was observed from a narrowing of the FWHM of the XRD peaks. The absence of any changes in the nano-grain structure during annealing at 600°C implies that the mobility of the atoms in ZrB_2 is very low below 600°C , as expected given the 3245°C melting temperature of ZrB_2 . This could also explain why films deposited at 600°C are highly oriented: certain grain orientations may require little mobility to nucleate and grow on sapphire, whereas the nucleation of other grain orientations is limited.

3.4 Behavior of ZrB_2 Films with Vacuum Annealing

This section discusses the changes in the XRD structure and SEM morphology of thin films samples near ZrB_2 stoichiometry as a function of deposition temperature and annealing time in vacuum. The first part of this section focuses on a pair of films that were deposited at 600°C near ZrB_2 stoichiometry and subsequently annealed at 800°C in 10^{-7} torr vacuum. In the second part a

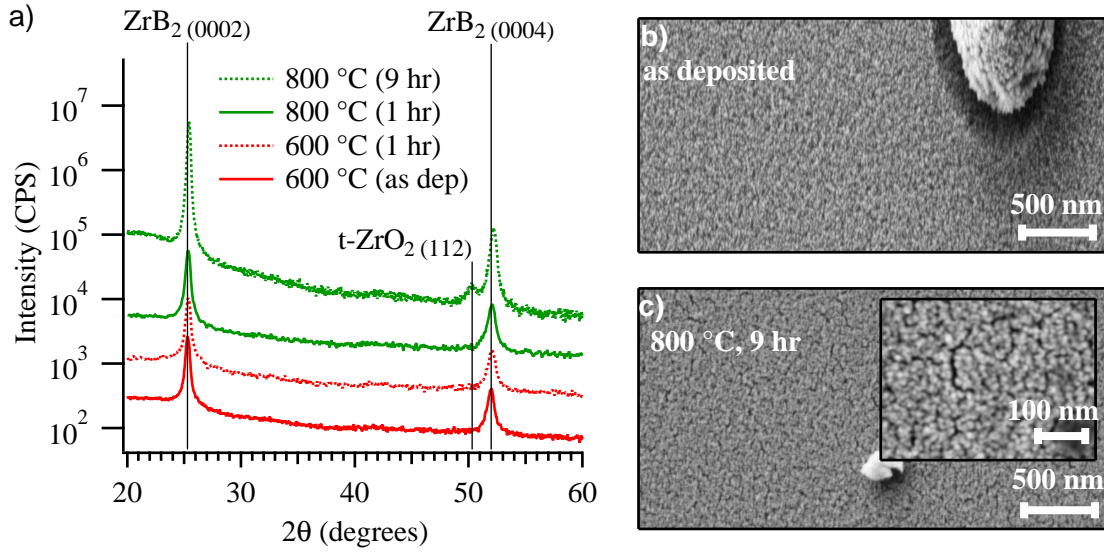


Figure 3.4: XRD and SEM of a highly crystalline ZrB₂ thin film before and after vacuum annealing. (a) XRD spectra (offset for clarity) from a thin film with $X_{\text{Zr}} = 0.25$ showing strong diffraction from $\langle 0001 \rangle$ oriented ZrB₂ crystallites after deposition at 600 °C, and after annealing at 600 °C for 1 h and 800 °C for 1 h and 9 h in UHV. (b) SEM secondary electron images from the film as deposited and (c) after the full annealing sequence shown in (a).

comparison is drawn between films grown at RT and grown at 850 °C, and their subsequent UHV annealing at 850 °C. Electrical conductivity results are presented later in §3.5. In general, vacuum annealing at 600 °C does not affect the ZrB₂ film structure, as measured by XRD. Annealing at 800 °C or higher was required to alter the film crystallinity.

3.4.1 Annealing of Oriented Films

XRD spectra and SEM images from a film deposited at 600 °C with $X_{\text{Zr}} = 0.25$ are shown in Fig. 3.4. This film exhibited strong diffraction from the (0001) ZrB₂ plane, with a Scherrer grain size of 39 nm, and a single chemical state for all peaks in XPS. This structure was not affected by annealing in UHV, as seen in both the XRD spectra and SEM images. However, a small peak can be seen in the scan after 9 h of annealing, which is identified as diffraction from the tetragonal zirconium dioxide (t-ZrO₂) (112) plane, presumably from air exposure prior to annealing or oxidation from residual H₂O vapor in the vacuum. A single oxide peak is not surprising considering the highly textured film from which it formed.

No grain growth or agglomeration was observed, owing to the high stability of the ZrB₂ crys-

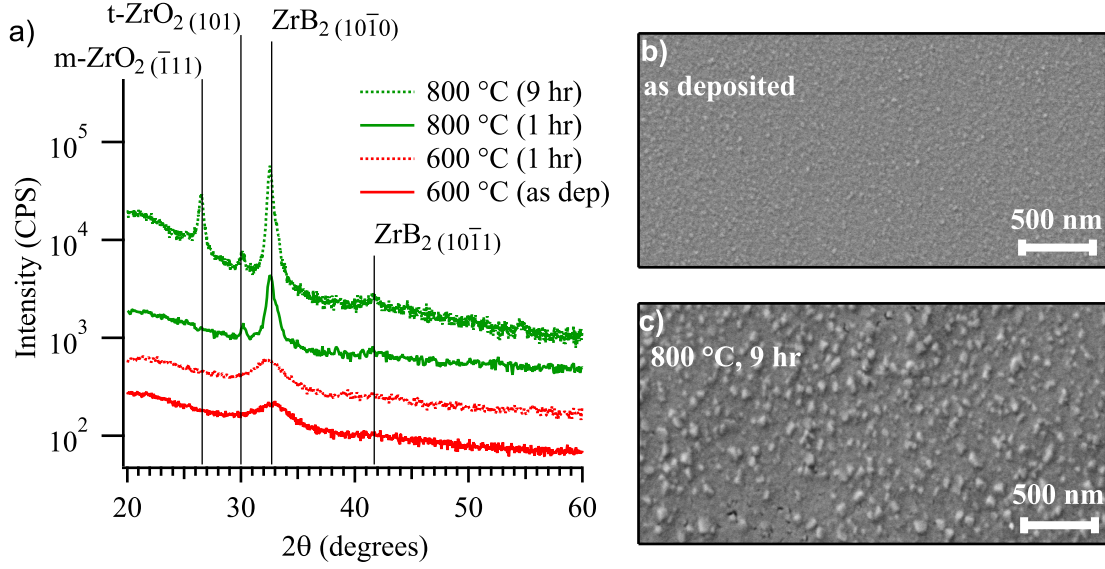


Figure 3.5: XRD and SEM of a nano-crystalline ZrB_2 thin film before and after vacuum annealing. (a) XRD spectra (offset for clarity) from a thin film with $X_{\text{Zr}} = 0.37$ showing small, $\langle 10\bar{1}0 \rangle$ oriented ZrB_2 crystallites after deposition at 600°C , and after annealing at 600°C for 1 h and 800°C for 1 h and 9 h in UHV. (b) SEM secondary electron images from the same as-deposited film and (c) after the full annealing sequence shown in (a).

talline phase. However, as seen in the inset in Fig. 3.4c, some nanometer-scale cracks have appeared in the film surface, likely due to thermal stress during annealing. Although the SEM images shown are of a small area, these surface features are representative across the entire 8 mm wide thin film sample. Large particles like the one shown in Fig. 3.4b were distributed randomly across the sample with a $\sim 50\text{ }\mu\text{m}$ spacing, and are likely from spitting during the initial stages of the deposition.

Fig. 3.5 shows XRD spectra and SEM images from another film deposited at 600°C with higher Zr content ($X_{\text{Zr}} = 0.37$). Like other Zr-rich films, the ZrB_2 crystallites are oriented in the $\langle 10\bar{1}0 \rangle$ direction and show a Scherrer grain size less than 5 nm prior to annealing. Annealing at 600°C had negligible effect on the crystalline structure of the films, which retained the same nanocrystalline peak as before the annealing. After annealing at 800°C , however, the Scherrer grain size increased to 15 nm, indicating that significant grain growth occurred. Some nanometer voids are observed in the SEM images, but they are sparse and localized to small areas which are devoid of large ZrB_2 grains, and thus may not be directly related to the grain growth.

As described above in §3.1, films were briefly exposed to atmosphere between annealing steps for XRD analysis, leading to some RT oxidation of the surface. As a result of this oxygen exposure,

the growth of a small amount of crystalline monoclinic zirconium dioxide (m-ZrO₂) and t-ZrO₂ was observed (Scherrer grain size ~37 nm) following annealing, as seen in Fig. 3.5a. Other than these randomly oriented ZrO₂ crystals, a small peak corresponding to the (10 $\bar{1}$ 1) plane of ZrB₂ can also be observed. In many samples, the high temperature t-ZrO₂ phase is formed well before the growth of a m-ZrO₂ phase, which is the equilibrium phase at RT. The formation of t-ZrO₂ is consistent with other reports of preferential growth of the tetragonal phase due to confinement during oxidation of nanolaminate films,^{20,268,269} and may be induced by compressive stresses during oxidation of ZrB₂.²⁷⁰

The SEM images in Fig. 3.5b-c show the appearance of small nano-crystalline grains on the surface of the thin film. As there is little secondary electron contrast between ZrO₂ and ZrB₂, it is difficult to tell which phase these crystallites are comprised of. An important observation, however, is that the (presumably) amorphous matrix below the nano-crystallites is still present and intact after the annealing process.

3.4.2 Long Term Vacuum Annealing

Two films were grown with measured composition $X_{Zr} = 0.26$ and thicknesses of 200 nm, one at RT and the other at 850 °C, and they subsequently underwent compound annealing up to 55 h at 850 °C in UHV, as described in §3.1. The effects of this annealing on film structure are shown in Fig. 3.6. As-deposited, the RT film was amorphous, as expected, but the 850 °C deposition produced a polycrystalline film with a random orientation, contrary to the earlier depositions at 600 °C. After vacuum annealing for 55 h, there was only a slight decrease in the XRD intensity of the two ZrB₂ peaks, but otherwise the film grown at 850 °C behaved similar to the highly crystalline film grown at 600 °C (Fig. 3.4).

For the RT deposition, the initially amorphous film began to crystallize after the first hour of annealing at 850 °C, exhibiting the (10 $\bar{1}$ 0) and (10 $\bar{1}$ 1) peaks of a ZrB₂ phase in an intensity ratio indicative of a randomly orientated film. During the subsequent 54 h of vacuum annealing, the intensity of these peaks continued to increase to the height seen in Fig. 3.6a. After the 55 h of vacuum annealing, the Scherrer grain size from the (10 $\bar{1}$ 0) peak in both films was ~25 nm, but the low intensity of the peaks in the RT deposited film indicate that it has many fewer crystallites than the film deposited at 850 °C.

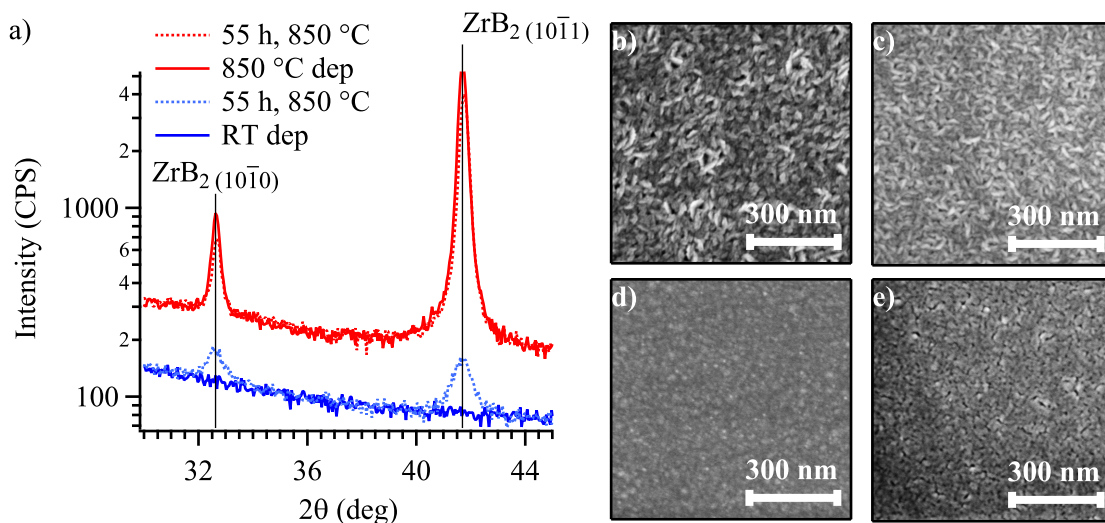


Figure 3.6: XRD and SEM of ZrB₂ thin films with annealing for 55 h. (a) XRD spectra from two films (one deposited at RT, the other at 850 °C) before and after compound annealing for 55 h in UHV. To the right are SEM images of the high temperature deposition (b) before and (c) after the full annealing treatment, as well as the RT deposition (d) before and (e) after.

SEM images of films grown at the different temperatures indicate no morphological changes in the surfaces. As discussed in §3.4, films deposited at 600 °C which were initially nano-crystalline, would grow small ZrB₂ grains on the surface during annealing. However, this is not the case for the initially amorphous ZrB₂ films. After annealing above 800 °C, the Scherrer grain size in films deposited at RT was typically <10 nm, and the grain size was not observed to increase with further annealing. Thus the surface remains smooth, although during annealing above 800 °C small nano-cracks begin to appear after 9 h, as seen in Fig. 3.6e. The increase in XRD intensity with continued annealing implies that more crystallites nucleate, but the lack of increase in the Scherrer grain size implies that grain growth is severely limited by the low diffusion in ZrB₂ thin films.

The lack of any agglomeration or grain growth after 55 h of annealing at 850 °C is good for the application of ZrB₂ as a thin film electrode. As-deposited films which are highly crystalline as deposited retain their polycrystalline structure with no further grain growth under these conditions. Likewise, initially amorphous films show no visible grain growth by SEM, and only minor changes in the XRD spectrum. In the amorphous films, grain growth is likely inhibited by the lack of nucleation sites, which also serves to inhibit any surface roughening, unlike with the nano-crystalline films grown at 600 °C which showed visible grain growth on their surfaces.

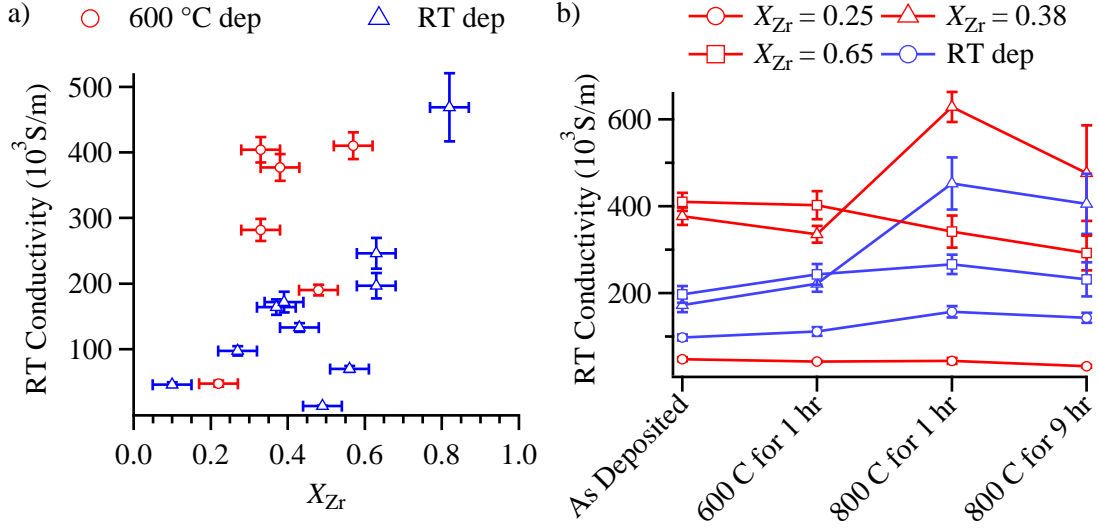


Figure 3.7: Electrical conductivity of $\text{Zr}_x\text{B}_{1-x}$ films as deposited. (a) Electrical conductivity of $\text{Zr}_x\text{B}_{1-x}$ films as a function of Zr composition measured at RT after deposition. (b) Film conductivity after annealing at the temperatures and times indicated. Red curves are for films deposited at 600 °C and blue curves are RT depositions.

3.5 Electrical Conductivity of $\text{Zr}_x\text{B}_{1-x}$ Films

Overall, film conductivities varied from $0.13 \times 10^5 \text{ S/m}$ to $6.3 \times 10^5 \text{ S/m}$ as measured by a 4-point co-linear probe. Fig. 3.7a shows the RT conductivity of all films as deposited versus the measured film composition. For depositions at RT, there is a consistent trend of increasing conductivity with increasing X_{Zr} . Depositions at 600 °C do not show the same trend, however, instead having values distributed either above those for the RT depositions, or within the same range. The conductivity of the crystalline ZrB_2 films deposited at elevated temperatures may be hindered in part by scattering from grain boundaries or voids between grains, which are not present in amorphous films.

The general trend of higher conductivity as X_{Zr} increases in the RT depositions can be rationalized by the increased Zr-Zr bonding in the film as X_{Zr} increases. The band structure of Zr is similar to many metals in that there is no gap in the DOS at E_f . However, in ZrB_2 there is a “pseudo gap” at E_f , where the the DOS is relatively low.^{21,50,51} This pseudo gap is due to the tighter binding of electrons to the B atoms that lowers the DOS below E_f . With fewer B atoms in the film, the valence band electrons are less tightly bound on average and can form more bands, and so the DOS near E_f can increase.

It was generally observed that films deposited with higher Zr flux had more O contamination and a small chemically shifted Zr 3d doublet that corresponded to the Zr^{4+} state. The appearance of this phase would imply more insulating character in the average film conductivity. The observation that this effect does not markedly influence the conductivity implies that, although some Zr atoms are bonding with O, the local bonding does not form an insulating band structure. This possibility is discussed further in §4.2.

In Fig. 3.7b the film conductivity as a function of varying composition and deposition temperature is plotted for the annealing conditions shown. In all cases, the conductivity does not vary significantly with annealing. Films with $X_{\text{Zr}} < 0.33$ showed negligible structural or morphological changes, and as expected, the conductivity was unaffected in the first 9 h of annealing treatment. Films above $X_{\text{Zr}} = 0.33$ which showed ZrB_2 grain growth (see Fig. 3.5), did show a slight increase in conductivity as the grains grew. Zr-rich films, which have greater O contamination and no ZrB_2 grain growth, decrease in conductivity as a result of the annealing treatment.

Fig. 3.8 shows the conductivity of ZrB_2 thin films with $X_{\text{Zr}} = 0.26$ as a function of annealing for longer time periods. Similar to the films in Fig. 3.7b, there is no change in the conductivity of films with high crystallinity (red curve), but for initially amorphous films the conductivity increases dramatically after the first hour of annealing, and again after 14 h. This result correlates with the growth of ZrB_2 crystallites during annealing observed by XRD. In both high temperature and RT depositions, the film density as measured by XRR increased after annealing beyond 20 h. Thus the increase in the film conductivity is due to the annihilation of voids in the film and increasing order in the atomic lattice.

3.6 Summary

Thin films of varying $\text{Zr}_x\text{B}_{1-x}$ composition have been successfully grown using e-beam co-evaporation from elemental sources. However, a non-linear trend has been observed between the composition of the evaporated fluxes and the composition of the resulting films, which is well fitted by the function

$$X_{\text{Zr}} = F_{\text{Zr}}^{2.1038} \quad (3.2)$$

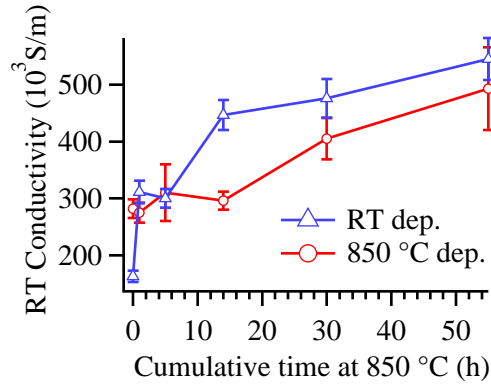


Figure 3.8: Electrical conductivity of ZrB_2 thin films versus vacuum annealing time up to 55 h. Films were 200 nm thick, deposited at RT and 850 °C, with a measured composition of $X_{\text{Zr}} = 0.26$, and the annealing was carried out at 850 °C.

where $X_{\text{Zr}} = [\text{Zr}] / ([\text{Zr}] + [\text{B}])$ is the concentration of Zr in the film ratioed against the total concentration of Zr and B, and $F_{\text{Zr}} = R_{\text{Zr}} / (R_{\text{Zr}} + R_{\text{B}})$ is the Zr percentage of the total evaporation rate. It was determined that the evaporated flux must be $\sim 60\%$ Zr to achieve films near ZrB_2 stoichiometry ($X_{\text{Zr}} = 0.33$). This unexpected result indicates that Zr has a substantially lower sticking coefficient on $\text{Zr}_x\text{B}_{1-x}$ surfaces compared to B, although no physical explanation for this effect can be made at this time.

Structurally, ZrB_2 films fall into one of three categories. When deposited at 600 °C, the films are typically nano-crystalline (Scherrer grain size < 10 nm) and the crystallites are highly oriented. When annealed in UHV above 800 °C, these films show substantial grain growth with highly textured (10 $\bar{1}$ 0) orientation accompanied by a roughening of the film surface. Films with a high degree of crystallinity, such as in Fig. 3.4 and Fig. 3.6, showed no morphological or structural changes with annealing, at 850 °C for up to 55 h in UHV. Lastly, films deposited at RT are initially amorphous, and upon annealing up to 850 °C for 55 h showed minimal grain growth and no surface roughening.

All $\text{Zr}_x\text{B}_{1-x}$ films have electrical conductivities on the order of 10^5 S/m, regardless of composition. After vacuum annealing at 850 °C there were no large changes in the conductivity of the films, though some small variations in the conductivity observed can be correlated to ZrB_2 grain growth, the annihilation of defects, and the growth of some crystalline ZrO_2 grains due to O contamination. The stability of the structure and conductivity of the films at high temperatures is desirable for applications in high temperature sensor devices. In order to investigate the deeper structural changes

in the nano-grained and amorphous $\text{Zr}_x\text{B}_{1-x}$ films, however, XAS had to be employed, as discussed in the next chapter.

CHAPTER 4

STRUCTURAL ANALYSIS OF Zr_xB_{1-x} FILMS BY X-RAY ABSORPTION SPECTROSCOPY

In the previous chapter the high temperature stability of the ZrB_2 crystal structure was observed in many thin films. However, Zr_xB_{1-x} films deposited at RT generally did not form large crystals after annealing at 800 °C. Films deposited at 600 °C similarly retained a large amount of amorphous content after annealing. To examine the bulk structure of the films, both amorphous and crystalline, XAS was performed at the Advanced Photon Source at Argonne National Lab. XANES provided insight into the trends in local bonding with varying composition, while analysis of the EXAFS was used to determine the evolution of the structure and bonding within Zr_xB_{1-x} films before and after annealing in vacuum.

4.1 Experimental Details

Thin films with different Zr_xB_{1-x} compositions were grown using e-beam co-evaporation from elemental Zr and B sources, as described previously in §2.1.1 and §3.1. As before, film composition was measured using XPS analysis of the as-grown film surfaces before exposure to air. The films discussed in this chapter were grown with stoichiometries measured to be $X_{Zr} = 0.25, 0.38$ and 0.60 , covering a range from B-rich ZrB_2 to about half way between ZrB_2 and pure Zr. Pure Zr foil, ZrB_2 powder, and a t- ZrO_2 thin film were also used as reference materials. A summary of samples and their reference labels is shown in Table 4.1.

Table 4.1: Preparation conditions for samples presented in Ch. 4. Samples will be referred to by these labels throughout this chapter.

label	X_{Zr}	Dep. Temp (°C)	label	Standard Material
1	0.25	RT	F	Zr foil reference
2	0.25	600	P	ZrB_2 powder
3	0.37	RT	O	ZrO_2 standard
4	0.37	600		
5	0.60	RT		
6	0.60	600		

Films were deposited onto polished r-cut sapphire substrates, either at RT or while the substrate was heated to 600 °C. Following deposition, films were annealed in vacuum at 800 °C (working pressure 10^{-7} torr) for a cumulative 9 h. During annealing, outgassing primarily released H₂O, CO, and CO₂ into the chamber, as determined by a residual gas analyzer. After 1 h at 800 °C, films were removed from vacuum and examined for grain growth with XRD, then reinserted for a further 8 h of annealing, after which XRD was performed again. As was seen in §3.4, very little grain growth was observed by XRD. Thus, to gain a deeper insight into the structure of the films, XAS was used.

XAS at the Zr K-edge were recorded using fluorescence measurements using the MRCAT beamline 10-BM at Argonne National Laboratory.²³⁸ Magic angle spinning at grazing incidence was employed to remove strong Bragg diffraction of the beam from the sapphire substrate and minimize the effects of crystallographic texture in the films themselves. The sample area was 8 mm square, with a film thickness of ~200 nm, and a beam spot size of 0.5 mm by 20 mm. A ZrB₂ powder standard (99.5% purity, 44 µm particle size, tape mounted) was also scanned in transmission mode. A pair of Si(111) monochromators were used, and initial energy calibration was performed with a Zr foil in the incident beam (after I₀). Thereafter, Zr reference foils were kept after the sample in the transmitted beam (after I_t) for scan-to-scan energy alignment.

4.2 X-ray Absorption Near Edge Spectroscopy of Zr_xB_{1-x} Thin Films

Fig. 4.1 shows the XANES from Zr_xB_{1-x} films with $X_{\text{Zr}} = 0.25, 0.38, \text{ and } 0.60$, as deposited and after vacuum annealing to 800 °C. XANES from a Zr foil standard and a ZrB₂ powder reference are also displayed in Fig. 4.1 for comparison. The Zr K-edge energy for ZrB₂ is found to be shifted to higher energy by 1 eV relative to the Zr foil, and the Zr foil exhibits a two step edge characteristic of elemental Zr,²⁴⁰ which is not present in the ZrB₂ powder or the t-ZrO₂ thin film. The edge energy and pre-edge feature are more easily discerned in the first derivative of the spectra, shown in Fig. 4.1c-d. The t-ZrO₂ thin film is further shifted to higher energy by 4 eV relative to the Zr foil, and the XANES shows a single broad peak just after the edge, followed by a second peak 60 eV above that.

Three trends emerge from the data in Fig. 4.1a. The first is a smooth decrease in the edge energy with increasing Zr concentration for as-deposited films. As the Zr concentration reaches 60 at %, the

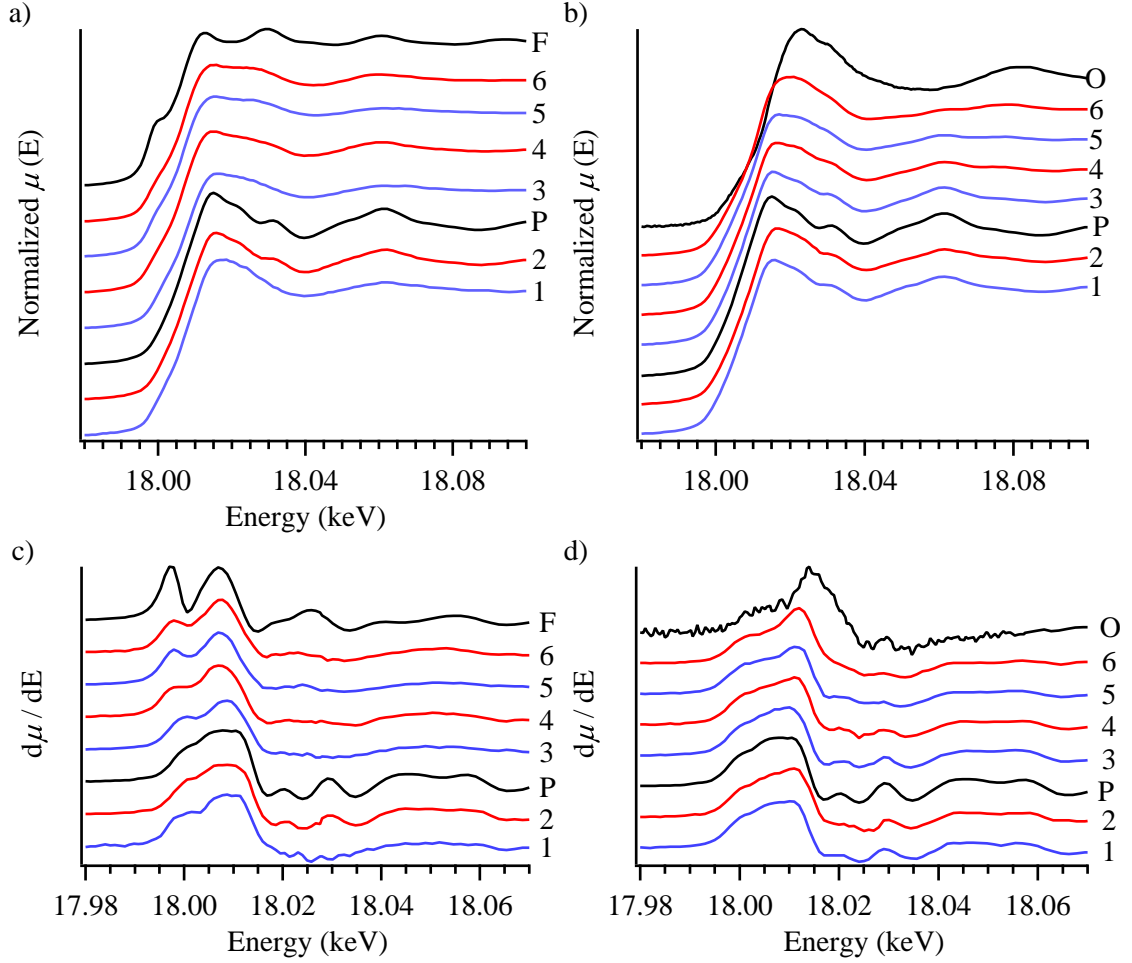


Figure 4.1: XANES of films with different Zr_xB_{1-x} composition, ZrB_2 powder, Zr foil, and ZrO_2 thin film references. Spectra are offset for clarity. (a) Normalized XAS at the Zr K-edge of films as deposited. (b) XAS of films after vacuum annealing at 800 °C for 9 h. (c) and (d) First derivative of the respective spectra in (a) and (b).

edge energy becomes aligned with that of the Zr foil. The second trend is the increased prominence of a pre-edge feature as the Zr concentration increases, beginning with Film 3. Finally, the features above the edge change from a large dip in absorption seen in the ZrB_2 standard, to a more level absorption plateau with two peaks near the edge as seen in the Zr foil.

Pre-edge features are narrow peaks in the XAS, typical in low valence transition metals where core-level electrons can be excited to unoccupied states below E_f . The feature in the Zr XANES is associated with transitions into hybridized p-d states near E_f .^{240,244} Since there is no hybridization of the valence Zr p and d states in ZrB_2 ,⁵⁰ this feature is weaker at compositions around ZrB_2

stoichiometry. The feature is also suppressed in ZrO_2 due to the tight binding of the electrons near O sites.

After vacuum annealing at 800°C (Fig. 4.1b), these trends with composition are no longer present. Prior to annealing, Films 3 and 4 show less ZrB_2 character in their XANES than Films 1 and 2, but after annealing all four films exhibit almost identical XANES features. As deposited, Film 1 ($X_{\text{Zr}} = 0.25$, deposited at 600°C) showed a highly crystalline ZrB_2 phase by XRD which was unchanged by annealing at 800°C . Likewise the XANES was also unaffected, retaining the same features indicative of the ZrB_2 phase. After vacuum annealing the edge energy of all films shifts to higher energy, indicating some degree of oxidation in all films. On average, the edge energy of Films 1–4 shifted up to 3.6 eV above that of the Zr foil standard.

Films 5 and 6 ($X_{\text{Zr}} = 0.60$, deposited with and without substrate heating, respectively), originally had similar features to the Zr foil, but after annealing lack the strong pre-edge step as well as the post-edge plateau and pair of peaks. The K-edge energy shifts upwards to 4.1 eV above the Zr foil (an energy which is consistent with a large amount of ZrO_2 phase) despite receiving the same level of exposure to atmosphere after deposition as the other films. The upward shift in edge energy and changes in the pre- and post-edge features in the XANES imply significant oxidation of Films 5 and 6, the coexistence of ZrB_2 and oxide phases, and the absence of any elemental Zr phase.

XPS analysis of the Zr 3d lineshape of Films 5 and 6 as deposited indicated the presence of a small amount (< 15 at%) of a chemically shifted ZrO_2 phase, yet this oxide phase seems to have little effect on the overall electronic structure of the films based on the XANES from as-deposited samples. The conductivity of $\text{Zr}_x\text{B}_{1-x}$ films was observed to increase with increasing X_{Zr} , as seen in Fig. 3.7a, in spite of increasing ZrO_2 contamination. It is expected that a ZrO_2 phase would decrease the film conductivity, however the XANES makes it apparent that the local bonding environment in Zr-rich films like 5 and 6 is predominantly Zr-Zr bonding, so the small amount of ZrO_2 present in the XPS analysis is not indicative of the bulk of the film. It is possible that the ZrO_2 phase identified in XPS is only in the surface region, and accumulated in UHV after deposition due to the potential for heightened oxidation of a Zr-rich surface.

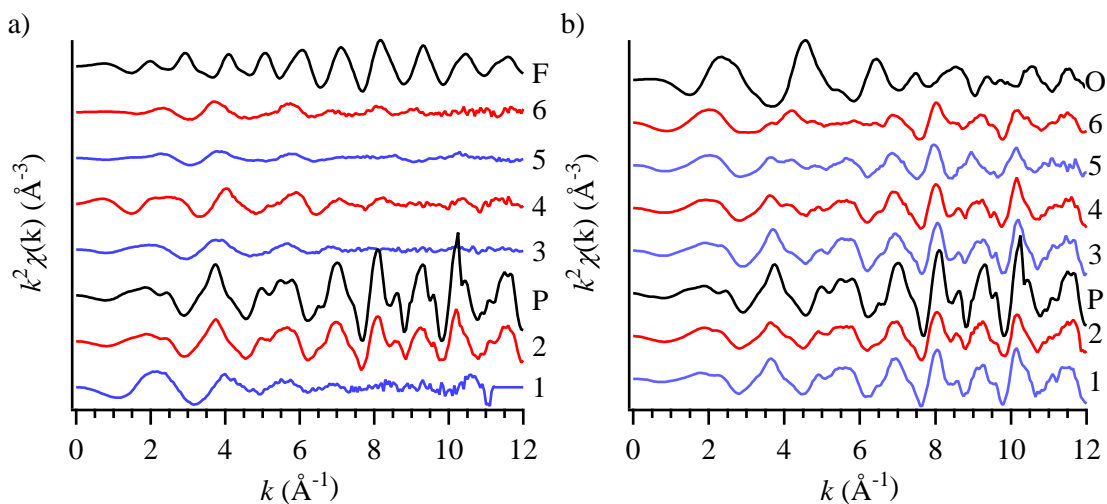


Figure 4.2: Weighted EXAFS of $\text{Zr}_x\text{B}_{1-x}$ films and standards. (a) as deposited, and (b) after vacuum annealing at 800 °C, and also for the Zr foil, ZrB_2 , and t- ZrO_2 standards. The curves are offset for clarity. The differences between crystalline and amorphous films are clear in the amplitude of the oscillations at high k .

4.3 X-ray Absorption Fine Structure Modeling

XAS data processing was performed using the Demeter software package.²⁴⁹ The XANES in Fig. 4.1 were all energy calibrated and background subtracted in ATHENA, and the EXAFS was extracted and then analyzed in ARTEMIS. The absorption edge was determined by the last, highest maximum in the first derivative, and last zero in the second derivative. As can be seen in Fig. 4.1c, two or more maxima appear in the first derivative spectra arising from pre-edge features; the true absorption edge is always the highest energy feature. Using the edge of the Zr foil as a reference, each scan was individually energy calibrated by shifting both the I and I_{ref} energy scales accordingly.

The spectra were background subtracted by fitting second-order polynomials to the pre-edge and post-edge and normalized by the difference between these polynomials at the absorption edge. The EXAFS was isolated by fitting a smooth, cubic spline polynomial above the edge and subtracting it from the data. This spline was fit up to $k = 15 \text{ \AA}^{-1}$ where possible, but in two cases aberrant oscillations prevented fitting beyond $k = 12 \text{ \AA}^{-1}$. Fig. 4.2 shows the extracted $k^2\chi(k)$ for all the samples in this chapter. These EXAFS were then Fourier transformed from 2 \AA^{-1} to 12 \AA^{-1} for consistency between spectra.

The EXAFS data were modeled using several single scattering paths (and one double scattering

path) from crystalline ZrB_2 and t- ZrO_2 structures, and fit over a range from 1.15 Å to 4.7 Å in R . As discussed in §2.4.2, the fitting parameters in Eq. 2.34 are the number and type of atoms in each coordination shell around the central atom, and the distance and thermal noise in the coordination shell. Athena uses FEF²⁴⁸ (or the newer IFEFFIT) routine to calculate all potential (non-degenerate) scattering paths for a given crystal structure. The scattering paths were calculated for ZrB_2 and t- ZrO_2 , and brought into Athena for final adjustment.

Each path can have several, independent adjustments, which should all be small deviations from the original scattering path parameters. In the model used here, many of these parameters were constrained to limit the independence of the fit. A single (arbitrary) amplitude was fitted to all ZrB_2 and t- ZrO_2 paths, along with a single offset in the edge energy (to account for any small miscalibrations due to the finite number of data points in the absorption edge). Three Debye-Waller factors (σ) were used: one for the first O and B shells, a second for the first and second Zr shells, and a third for the third Zr shell and the double scattering path. To account for multi-phase films, a parameter approximately representing the percentage composition of each phase in the film was multiplied by the amplitude, such that the sum was 1.

The ZrB_2 lattice has a very high degree of symmetry: every Zr atom in the lattice is a central atom for Zr K-edge absorption. Thus, any adjustment in the path length for scattering from the third Zr shell requires an adjustment in the path length for the second Zr shell, and so on. Thus, the half-path lengths for ZrB_2 paths were fitted with two hexagonal lattice parameters, a and c , which were used to identify the positions of all coordination shells. Meanwhile a single fitted parameter was subtracted from the two t- ZrO_2 paths, generally accounting for stress in the t- ZrO_2 phase. The number of atoms in each coordination shell is often used as an adjustable parameter in EXAFS, but here it was required to match the stoichiometry of ZrB_2 , and conclusions are drawn based on this restriction.

An example spectrum and fit of Film 1 after annealing is shown in Fig. 4.3, with corresponding fitting parameters shown in Table 4.2. The magnitude of each fitted scattering path is shown in green, and the sum is superimposed on the measured $\chi(R)$. Note that the χ_n are complex waves, and so relative phases can add or subtract intensity from the magnitude in somewhat non-obvious ways. This is easily seen in the sum of the B_1 and O_1 paths. These two paths are phase shifted such

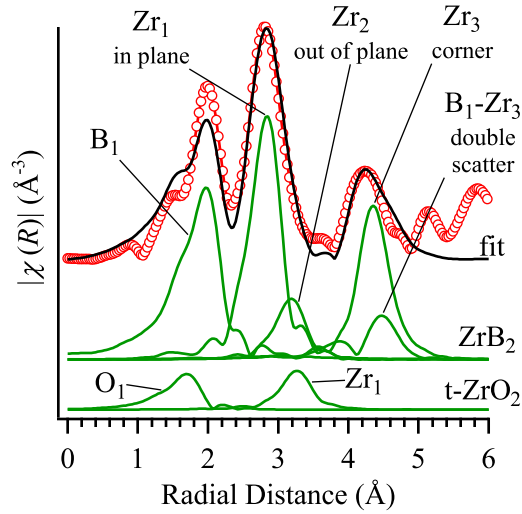


Figure 4.3: Example plot of the magnitude of the EXAFS Fourier transform of a ZrB_2 film. The film composition was $X_{\text{Zr}} = 0.25$. Table 4.2 summarizes the fitted values. Offset for clarity are the magnitudes of the component paths from the ZrB_2 and t-ZrO_2 phases.

that the O_1 path subtracts from the B_1 , and thus the low R shoulder of the sum is reduced below the B_1 intensity.

4.4 EXAFS of Near-Stoichiometric Films

The model used to fit the EXAFS data (described in §4.3) is based on the structural information deduced from the XRD data. No crystalline phases other than ZrB_2 and t-ZrO_2 were observed in these any of the $\text{Zr}_x\text{B}_{1-x}$ thin films. Therefore, the model assumes that the EXAFS is a linear combination of scattering paths from these two phases. A fitting parameter corresponding to the fraction of ZrB_2 phase, balanced by a t-ZrO_2 phase, was included as a multiplicative factor on the amplitude of the paths. Films 1–4 were all fitted in this way, and the statistical correlation between the ZrB_2 fraction and the amplitude was found to be less than 0.4 in each fit. The ZrB_2 fraction varied from 0.97 to 0.83 between films, with an average uncertainty of 0.051 in each fit. Thus, these four films contained nearly the same composition of ZrB_2 and t-ZrO_2 phases after annealing.

Fig. 4.4 shows the magnitude of the Fourier transform of the EXAFS data for Films 1–4 before and after annealing. Films deposited with substrate heating (2 and 4) show much longer range order than films deposited at RT (1 and 3), with visible peaks out to almost 4.5 \AA . Films 1 and 3 show only a small degree of nearest-neighbor order, as evidenced by the broad peak at low R . The broad

Table 4.2: Fitting parameters derived from the EXAFS spectra in Fig. 4.3. The ZrB_2 paths were constrained to the hexagonal lattice parameters a and c , while the t- ZrO_2 paths were fitted with a constant offset.

Path	Function	Half-Path Length	
		Value (Å)	$\sigma (\times 10^{-3})$
B_1	$\sqrt{\frac{a^2}{3} + \frac{c^2}{4}}$	2.546	3.99(180)
Zr_1	a	3.182(8)	3.35(100)
Zr_2	c	3.526(15)	3.35(100)
Zr_3	$\sqrt{a^2 + c^2}$	4.749	4.26(111)
$\text{B}_1\text{-Zr}_3$	$\text{B}_1 + \frac{1}{2}\text{Zr}_3$	4.921	5.84
O_1	$0.2220 - \Delta$	2.207(39)	3.99(180)
Zr_1	$0.3625 - \Delta$	3.612(39)	3.35(100)

peak around 2 Å corresponds to first shell B and O atoms, which have very similar bond lengths, as seen in Fig. 4.3. Peaks at 3 Å and 4.3 Å correspond to the first three Zr shells in the system, and the absence of these peaks in Films 1 and 3 implies very low order in the Zr–Zr bond distances at low deposition temperatures. This is not surprising for amorphous films, however, and can be explained by a lower rate of atomic diffusion during deposition.

Surprisingly, after annealing at 800 °C for 9 h, all four films have very similar EXAFS features. Figs. 4.4b and d show the magnitude of the Fourier transform of the films after annealing, as well as the best fit of the data to the two phase model. Generally, the fits are quite good, though in all four samples there is intensity in the B peak that is unaccounted for, and the shoulder produced by the O path is greater than the data. Since the path degeneracy (interpreted as the coordination number in single scattering paths) was not varied from that of pure ZrB_2 and t- ZrO_2 phases, this disagreement with the model may indicate that, on average, there are fewer than eight O nearest-neighbors at each Zr site, and that, relative to ZrB_2 , there are either more B neighbors or some Zr vacancies in the lattice.

Values for the Zr–B bond length and ZrB_2 lattice parameters derived from these fits are presented in Table 4.3 for Films 1 and 3, as well as for the ZrB_2 powder standard and results reported for bulk ZrB_2 .²⁴⁶ There is good agreement between the values in Ref. 246 and the data from the ZrB_2 powder, and the Zr–B bond lengths for all four measurements are in agreement as well. The a and

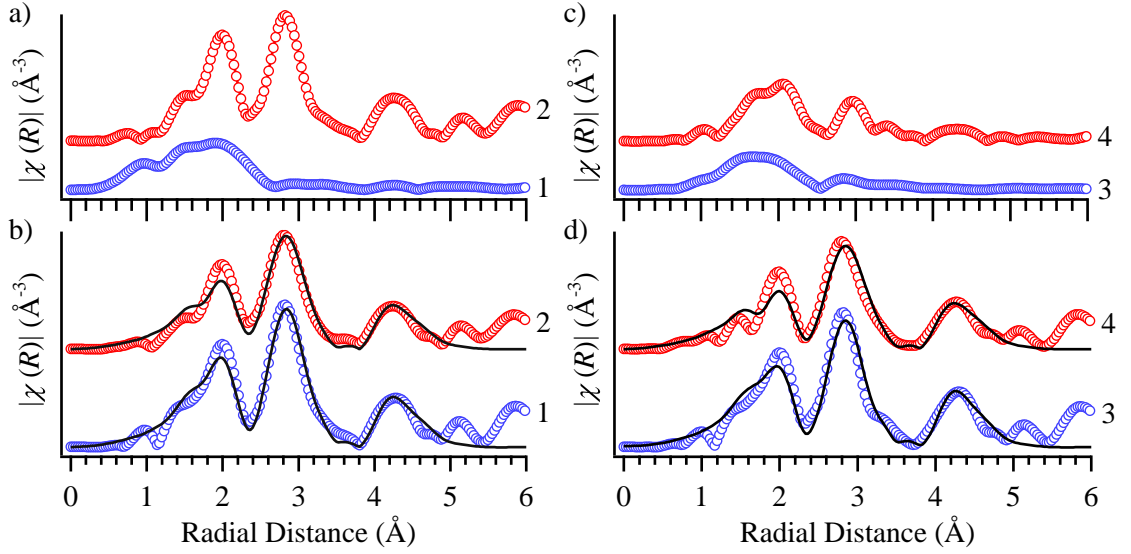


Figure 4.4: Magnitude of the Fourier transform of the EXAFS for films near ZrB_2 stoichiometry before and after annealing in UHV at 800°C for 9 h. (a) Films 1 and 2 as deposited and (b) after annealing. (c) Films 3 and 4 as deposited and (d) after annealing. Black curves are the best fit of the model discussed above.

Table 4.3: Fitted values for the ZrB_2 lattice parameters for Films 1 and 3 after annealing at 800°C , as compared to ZrB_2 standards.

Sample	Zr-B		a		c	
	Length (\AA)	$\sigma (\times 10^{-3})$	Length (\AA)	$\sigma (\times 10^{-3})$	Length (\AA)	$\sigma (\times 10^{-3})$
Ref 246	2.54(6)	4.2(6)	3.18()	2.6(5)	3.54(2)	2.9(8)
P	2.542	4.62(186)	3.175(5)	2.60(97)	3.532(20)	2.60(97)
1	2.550	4.17(156)	3.192(7)	3.73(81)	3.527(13)	3.73(81)
3	2.549	6.15(217)	3.208(8)	4.20(88)	3.504(13)	4.20(88)

c lattice parameters are somewhat different, however. The B-rich films have a longer a axis than in bulk, but the c axis is similar. For compositions just above ZrB_2 stoichiometry, the a axis is longer still, and the c axis is below the bulk values by more than twice the uncertainty in the fitted parameter. Zr-rich films were found by XRD to be preferentially oriented in the $\langle 10\bar{1}0 \rangle$ direction (see §3.3), so compression of the c axis is not unreasonable.

4.5 EXAFS from Films Far from ZrB_2 Stoichiometry

Fig. 4.5a shows EXAFS of as-deposited Zr-rich films ($X_{\text{Zr}} = 0.6$). Both films exhibit weaker EXAFS signals than Films 1–4, indicating a higher degree of disorder even in the nearest neighbor

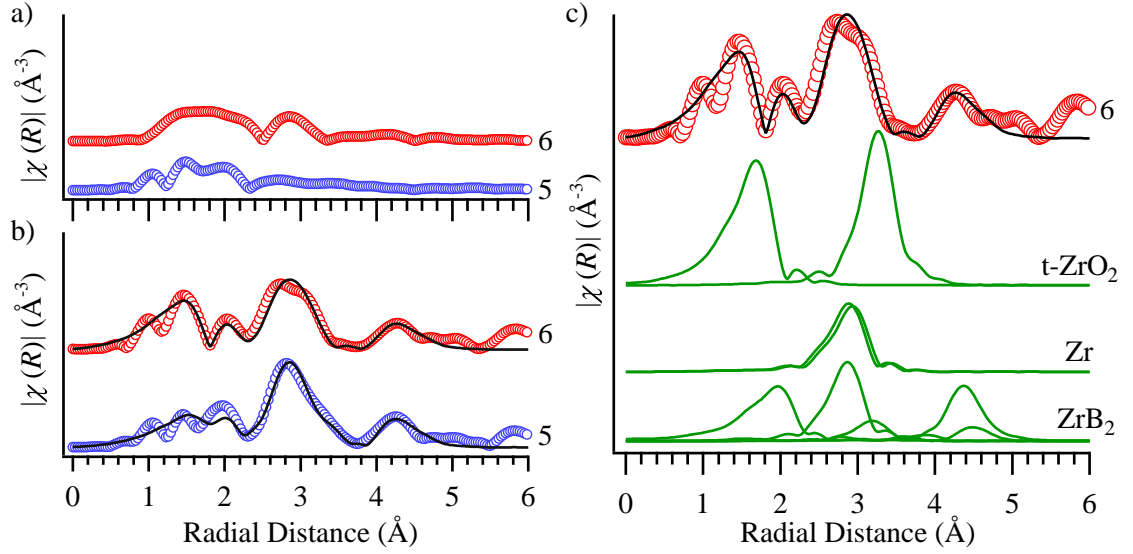


Figure 4.5: Magnitude of the Fourier transform of the EXAFS of films with $X_{\text{Zr}} = 0.60$. Films 5 and 6 (a) as deposited and (b) after UHV annealing at 800 °C for 9 h. (c) Component scattering paths and fit used for Film 5 after annealing are offset for clarity. The vertical scale in (a) and (b) is the same as in Fig. 4.4.

regions. Film 6 (deposited with substrate heating) shows a small peak just below 3 \AA , corresponding to scattering from Zr sites, which is not present in the spectra from Film 5. This peak appears at smaller lengths than in films near ZrB₂ stoichiometry, which is consistent with the shorter bond length in elemental Zr. Both Films 5 and 6 also exhibit broad peaks from 1 \AA to 2.5 \AA , similar to those seen in nearly stoichiometric films.

Fig. 4.5b shows the results of vacuum annealing Films 5 and 6 at 800 °C for 9 h. The EXAFS signal from these films did strengthen after annealing, but not as much as for the nearly stoichiometric films. It is clear from the strong peaks at 1.5 \AA , corresponding to O scattering, that the level of oxidation is much greater in Films 5 and 6 compared to nearly stoichiometric films, and that Film 5 is more oxidized than Film 6. There is also an observed splitting in the Zr scattering peak in Film 6, due to the scattering from first shell Zr in the t-ZrO₂ phase. The EXAFS of Film 5 shows a smaller shoulder on the high side of the Zr scattering peak, due to a smaller amount of t-ZrO₂ phase, which is consistent with the XANES analysis discussed in §4.2.

When attempting to apply the two phase model previously discussed to the data in Fig. 4.5, it was found that the fit considerably underestimated the intensity at the lower edge of the Zr scattering peak. The nearest neighbor Zr scattering path in elemental Zr provides strong intensity at the lower

edge of the 3 Å peak. Thus, the fitting model was modified to include contributions from elemental Zr paths, as shown in Fig. 4.5c, and used to fit the data in Fig. 4.5b. Due to the number of paths that contribute to the same region, the a and c axis lengths for the ZrB_2 paths were constrained to the average values found in fitting the near-stoichiometric films, leaving the elemental Zr and t- ZrO_2 path lengths to vary independently. An additional parameter representing the fraction of elemental Zr was used to allow the modeling of a three phase mixture, but the values for these parameters can only be discussed qualitatively due to increased correlations with other parameters in the fit.

Fitting the data from Films 5 and 6 indicates that the intensity contributions from an elemental Zr phase were less than a quarter of the contributions from ZrB_2 and t- ZrO_2 phases. In fact, overwhelmingly the strongest peaks in the Fourier transform are from the t- ZrO_2 paths. XRD spectra from these films showed only diffraction from these same two phases, with no evidence of a pure Zr crystalline phase. The lack of XRD peaks from a metallic Zr phase could be due to the fact that the majority of highly reactive Zr atoms not already in a ZrB_2 -like environment become preferentially oxidized and form the t- ZrO_2 phase seen in the EXAFS.

4.6 Summary

The XANES of as-deposited $\text{Zr}_x\text{B}_{1-x}$ films show a smooth transition in Zr K-edge energy and absorption features from B-rich ZrB_2 films towards elemental Zr. The pre-edge feature characteristic of transitions from s orbitals to p-d hybridized orbitals in Zr is reduced around ZrB_2 stoichiometry, which is expected due to the low degree of p-d hybridization in ZrB_2 . Although XPS identified an increased O contamination in films with $X_{\text{Zr}} > 0.33$, the disordered nature of the ZrO_2 nuclei do not affect the electronic structure of the films, and the scarcity of t- ZrO_2 in the film has little impact on the film conductivity.

EXAFS analysis of as-deposited films indicates a higher degree of disorder with higher Zr concentrations, which remains true after annealing in vacuum at 800 °C for 9 h. After annealing, films near ZrB_2 stoichiometry all showed a highly ordered, ZrB_2 nanostructure, with lattice parameters extracted from the EXAFS that agree well with those of bulk crystalline ZrB_2 . A small amount of t- ZrO_2 phase ($\sim 10\%$) was observed, despite deposition under UHV conditions, and the inclusion of this phase aided the EXAFS fitting. EXAFS from films with $X_{\text{Zr}} = 0.6$ indicate a much larger per-

centage of O nearest-neighbors than in films near ZrB_2 stoichiometry, and very small contributions from metallic Zr.

The high propensity for oxidation in Zr-rich films is the primary reason that the exact $\text{Zr}_x\text{B}_{1-x}$ stoichiometry is important in determining their high temperature stability. Rather than observing a two phase mixture of ZrB_2 and pure Zr at high Zr concentrations (as predicted by the bulk phase diagram), only small contributions from pure Zr were found, and instead, coexisting ZrB_2 and t-ZrO_2 phases account for the majority of the EXAFS signal. Films nearer ZrB_2 stoichiometry are much higher purity and were more well-ordered, which should provide greater phase stability at higher temperatures.

Films with compositions within ± 10 at% Zr of ZrB_2 stoichiometry are very similar in their nanostructure, and bonding parameters associated with a ZrB_2 crystalline phase are observed after annealing. Even films deposited at RT, which were initially amorphous and were seen to exhibit very little grain growth with annealing at 800°C for 9 h (see Fig. 3.6), exhibited bond lengths and coordination consistent with a highly ordered ZrB_2 crystalline phase. The fact that even amorphous films form the same ZrB_2 nanostructure after annealing with very little grain growth is particularly encouraging for high temperature thin film electronics, because highly stable electrodes may be able to be produced by e-beam evaporation without the need for any high temperature heating during film growth.

CHAPTER 5

GROWTH AND STRUCTURE OF SPUTTER DEPOSITED h-BN FILMS

As described in §1.3, h-BN is an interesting thin film material both for its applications in conjunction with graphene and other 2D materials, but also for the potential use as an ultra-thin oxidation barrier.^{80,81,103} This chapter explores the growth of highly crystalline h-BN thin films using magnetron sputtering. The growth rate and morphology of amorphous BN films produced by reactive magnetron sputtering is measured first to establish the viability of the technique. The conditions for the growth of crystalline h-BN are found and the uniformity of the films is assessed over large areas ($>100\text{ }\mu\text{m}$). Electrically biasing the substrate is then shown to be an effective means of altering the ion energy during sputter deposition and achieving better crystallinity and uniformity in the growth of h-BN thin films.

5.1 Experimental Details

BN films were grown using RF magnetron sputtering from a pure B target (Plasmaterials, 99.5% purity, 2 inch diameter) in a reactive atmosphere of Ar and N₂, as described in §2.1.2. The base pressure of the deposition chamber was 3×10^{-9} torr, and the substrate to target distance was ~ 10 cm. During sputtering the pressure in the chamber was maintained at 10 mtorr and the gas flow rates were set to 2.5 sccm and 7.5 sccm for N₂ and Ar, respectively. Fig. 5.1 shows the effects of varying the working gas composition between 10 % N₂ to 70 % N₂ on the XPS-measured composition of the films. Films deposited at different working gas compositions were found to be of the same composition, and nominally the same thickness. Film growth is thus limited by the sputter rate of the B target, and adjusting the working gas did not substantially impact the sputter rate.

Reactive sputtering allowed for complete control of the growth process, including the abundance of B and N species. However, minor poisoning of the target was observed after several depositions when low power (<100 W) was used. The growth of a second phase, presumably BN, in the surface of the B target reduced the sputter yield, but was efficiently cleaned by sputtering in pure Ar gas at 200 W. Pre-sputtering in pure Ar was thus used as a general practice before introducing N₂ and beginning a BN deposition.

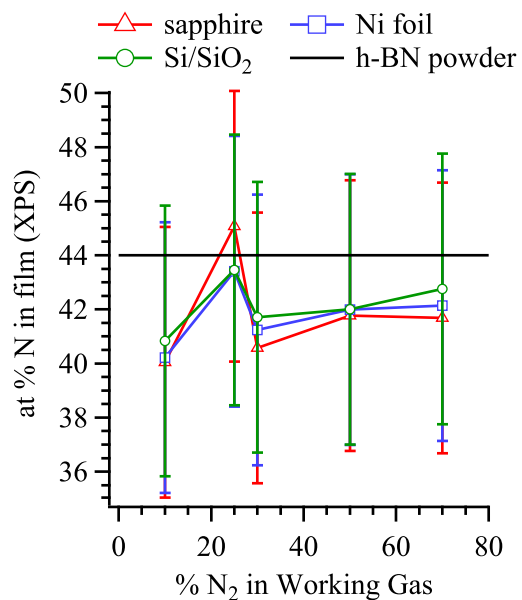


Figure 5.1: Plot of BN film composition determined by XPS versus % N₂ in the working gas. The black, dashed line is the measured composition of a h-BN powder standard.

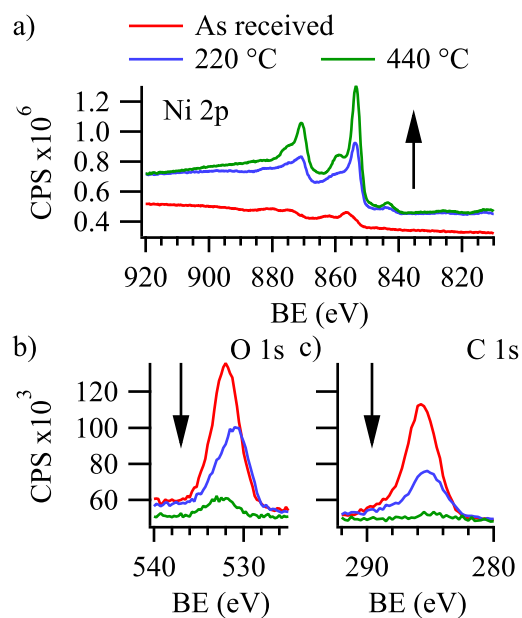


Figure 5.2: XPS spectra of Ni foil as received and after heating in vacuum to the indicated temperatures. (a) Ni 2p, (b) O 1s, and (c) C 1s spectra.

The growth of BN was examined on a variety of substrates including r-cut sapphire, Cu and Ni foils (Alfa Aesar, 99.9% purity, 0.250 mm thick), and (100) Si with a native oxide (SiO_2/Si). During deposition the substrates were either unheated or heated to 850 °C. Metal foils were highly contaminated with C and oxide phases as received (see Fig. 5.2a-c), however heating in vacuum was effective in cleaning the surfaces. Foils were annealed in UHV for 8 h at 850 °C prior to deposition to burn off carbon contamination, induce grain growth, and stabilize the surface morphology. Sapphire and Si substrates were cleaned in successive 10 min ultrasonic baths of acetone, isopropal alcohol, methanol, and deionized water.

5.2 Effects of substrate, temperature, and power

Cu and Ni foils were chosen as a substrate due to the extremely low lattice mismatch between the (111) surfaces of these metals and the (0002) surface of h-BN. However, growth on Cu foil at high temperatures was affected by substantial evaporation and sputtering of the Cu surface, resulting in a thinning of the Cu foil and little to no BN film growth. For that reason, this work focuses on Ni substrates as compared to r-cut sapphire and SiO_2/Si substrates, which have a high degree of lattice mismatch with h-BN. In general, depositions on sapphire and SiO_2/Si substrates resulted in amorphous, but highly uniform BN films, regardless of the deposition temperature or power.

The low sputter yield from B makes for slow film growth, with rates as low as $0.0025 \text{ \AA s}^{-1}$ reported in the literature.¹¹² To establish the dependence of the growth rate on the magnetron power, amorphous BN films were deposited on sapphire substrates. The composition of these films was measured by XPS to average 44.40(221), which agrees with the composition of a h-BN powder standard (Alfa Aesar, 99.5% purity, 44 μm particle size). Fig. 5.3a shows the growth rate, as determined from the resulting thickness of films deposited for the same time, as measured by XRR. Film growth rates follow an exponential trend with magnetron power.

The growth rates for depositions at 850 °C tended to be lower than those of RT depositions, though at powers <50 W the difference was negligible. A possible explanation is the evaporation of boron oxide species, which have an appreciable vapor pressure at high temperatures ($\sim 7.5 \times 10^{-7}$ torr at 800 °C).^{40,106,271,271–273} Residual oxygen and water in the chamber or in the gases used may have contributed to this evaporation during the 850 °C growth.

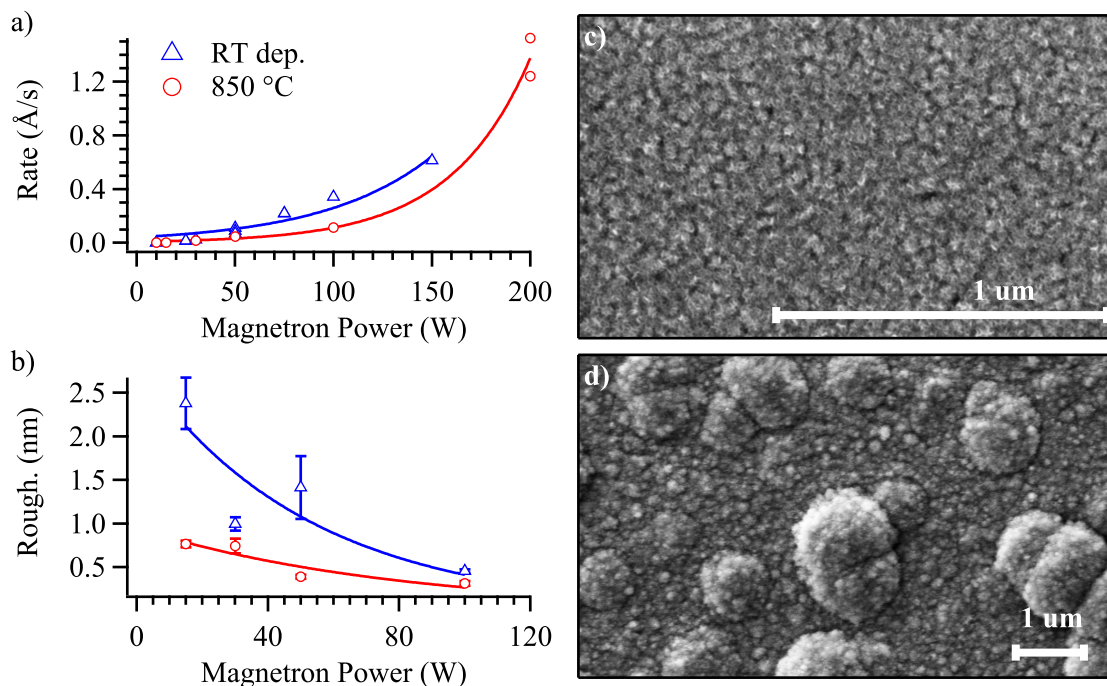


Figure 5.3: Effects of magnetron power on amorphous BN growth rate, film roughness, and morphology. (a) Growth rate of amorphous BN films deposited on sapphire versus magnetron power. Films were deposited for equal times and thickness measured by XRR to determine rate. Exponential curves are added as a guide. (b) RMS roughness of amorphous films as measured by AFM over a $25 \mu\text{m}^2$ area. All films were grown $\sim 17 \text{ nm}$ thick. SEM images of BN films (c) deposited at 15 W and 850°C , and (d) deposited at 200 W and 850°C .

The roughness of the films was measured over $5 \mu\text{m} \times 5 \mu\text{m}$ areas by contact-mode atomic force microscopy, and approaches the same value at high power for the two different temperatures, as seen in Fig. 5.3b. The decrease in roughness of the high power films might suggest more homogeneous film growth, but there was no accompanying increase in XRR-measured density, which averaged $2.07(30) \text{ g cm}^{-3}$. Rather, the roughness decreases with both substrate temperature and plasma energy, which is expected with increasing adatom mobility. Similarly, at RT adatom mobility is low, and increasing the plasma energy (power) provides enhanced diffusion. At 850°C the mobility is substantially higher, and increasing the plasma energy has only a minor effect on the film growth.

SEM imaging of amorphous BN films shows that films deposited at very low rates are extremely smooth at the nanoscale, are homogeneous, and contain a pattern of intertwined “nodules,” as seen in Fig. 5.3c. Regions of these nodules were seen to diminish as the crystallinity of the films improved, as discussed later in this chapter. When sputtering at high power, these nano-crystalline nodules are

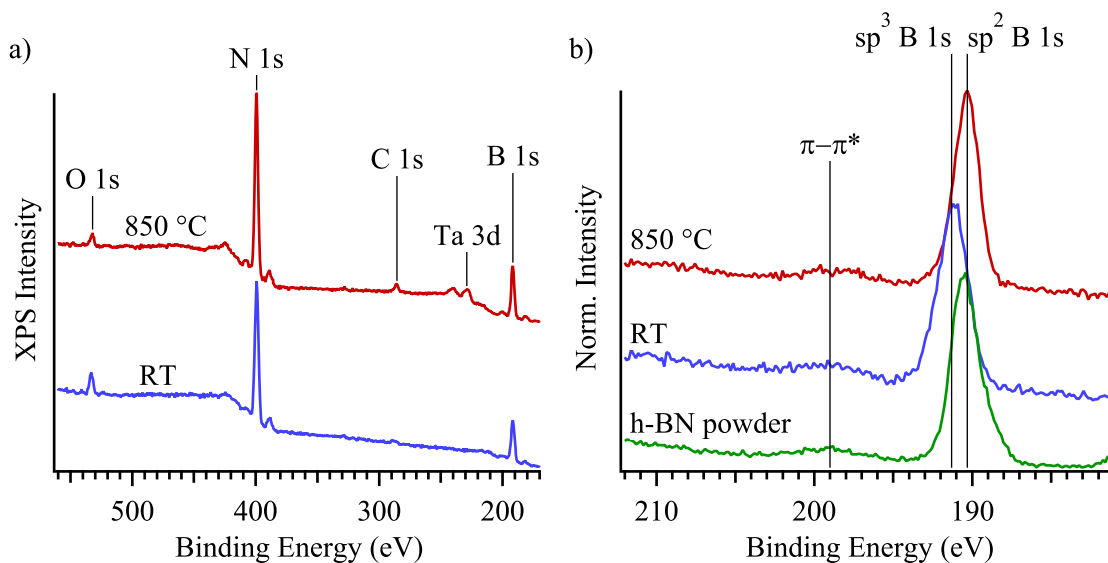


Figure 5.4: XPS spectra of BN films as deposited. (a) XPS spectrum of two h-BN films deposited at RT and 850 °C on Ni foil, using a non-monochromated source, showing minor O and C contamination. (b) High resolution B 1s spectra from the same samples and an h-BN powder standard.

not present, as seen in Fig. 5.3d. Instead, the film grows quickly, and when grown to high thickness, develops a rough texture with many hillocks present. Despite the large hillocks, the film shown in Fig. 5.3d is amorphous by XRD.

After deposition, BN films were transferred under UHV to a separate chamber for XPS analysis. Fig. 5.4a shows a broad spectrum (100 eV pass energy) scan from two BN films, one deposited at RT and the other at 850 °C, which shows residual O and C contamination. A Ta₂O₃ 3d doublet is also visible from the sample carrier, which may account for some or all of the O contamination at high temperature. The level of contamination was low at both temperatures, with an average of 3.8(23) at% O for RT depositions and an average of 1.8(12) at% O for films deposited at high temperature. The slightly lower level of O contamination in films deposited at 850 °C is consistent with the evaporation of boron oxide species, as mentioned previously.

Previous reports in the literature have identified the B 1s peak in h-BN to be between 190 eV and 191 eV,^{81,113,274,275} with peaks at higher binding energy attributed to sp³ hybridized c-BN. In this work, the B 1s and N 1s peaks were observed at 191.00(34) eV and 398.50(37) eV, respectively, averaged across all depositions. No direct evidence was seen for two chemically distinct phases in the XPS. Fig. 5.4b shows high resolution (20 eV pass energy) XPS of the B 1s peak for the two BN films and for a h-BN powder standard. The FWHM of the B 1s peak is larger in films deposited at

RT, and the median position is slightly higher (by 0.14 eV) than for films deposited at 850 °C. For depositions on sapphire, the FWHM is larger still, which implies a greater diversity in the chemical states in the amorphous films grown at RT.

As discussed in §1.3, it is generally accepted in the literature that c-BN is the equilibrium phase at STP, though there is some evidence of h-BN being dominant in thin layers. Furthermore, there exists a feature ~ 9 eV from the B 1s peak in h-BN, arising from $\pi - \pi^*$ transitions^{91,110,275} (see Fig. 5.4b), that is not present in sp^3 bonded c-BN. It is therefore likely that the high BE of the B 1s peak is the result of a mixed state of sp^2 and sp^3 bonded B. Although no peak splitting is visible in the spectra, the average FWHM of the peaks observed in the BN films was found to be 2.32(42) eV, which is large enough that two chemical phases could be present in the majority of the films.

5.3 Effect of Growth Rate on Film Structure

As stated in §5.2, BN films grown on sapphire and SiO_2/Si substrates were amorphous regardless of the growth conditions. On Ni foil, however, the crystallinity of the films varied, as measured by XRD and SEM. Fig. 5.5a shows diffraction from the (0002) plane of h-BN for three different films deposited on Ni foil. The general trend was that the growth of crystalline h-BN on Ni foil was only accomplished by heating the substrate to 850 °C and depositing at a magnetron power ≤ 30 W, corresponding to a deposition rate of 0.025 \AA s^{-1} (see Fig. 5.3a). Deposition at lower powers produced films with a higher degree of crystallinity.

Films deposited at RT exhibited a non-distinct surface morphology with low roughness, as seen in Fig. 5.5b, consistent with low diffusion rates and small density fluctuations. In contrast, films deposited on Ni foil at 850 °C, as in Fig. 5.5c-e, exhibited a polycrystalline surface of h-BN crystals, which measure ~ 200 nm across. With the lower growth rate, the frequency and size of crystals at the surface increased dramatically. However, as seen in Fig. 5.5e, the SEM image of the film is not homogeneous at larger length scales, with sporadic dark regions of high crystallinity mixed with light regions of low crystallinity. The substrate also plays a large role in the growth of h-BN crystals, as deposition onto sapphire and SiO_2/Si at the same temperature and growth rate produced an amorphous surface morphology similar to that observed for RT deposition.

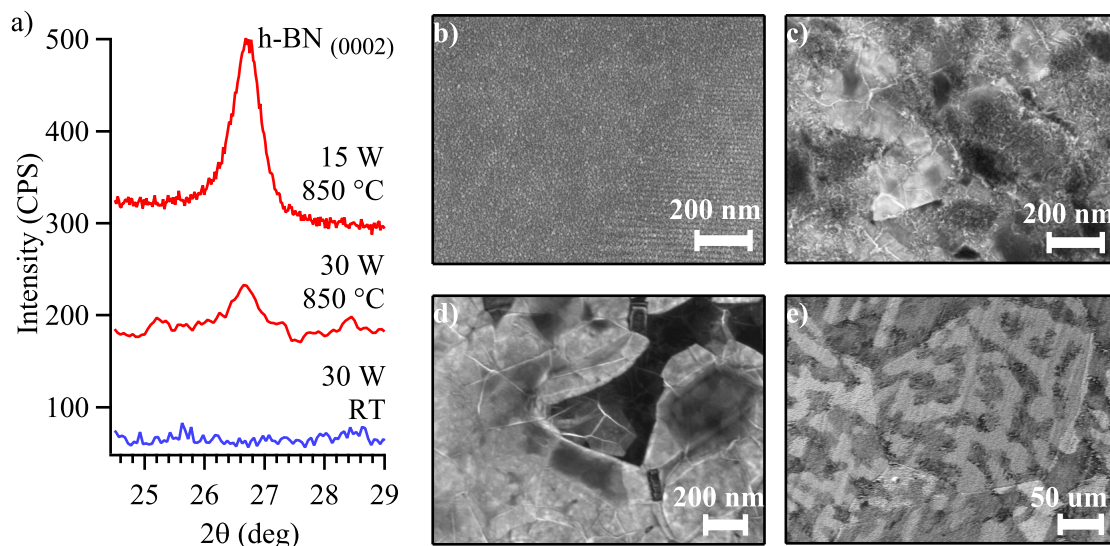


Figure 5.5: XRD and SEM of h-BN films with different magnetron powers. (a) XRD from the h-BN (0002) plane in three films grown on Ni foil with different temperature and power, offset for clarity. Right are SEM images from films deposited at (b) RT, 30 W, (c) 850 °C, 30 W, and (d, e) 850 °C, 15 W.

Under careful examination of the SEM image in Fig. 5.5c, a second phase is visible around the thin h-BN crystals, which was not observed in the XRD. These disordered regions may be t-BN,^{119,125} which is known to be a disordered form of sp^2 bonded BN. The appearance of t-BN has been reported to be a common feature in the sputter growth of c-BN, and is believed to be due to a transformation of h-BN under pressure from ion bombardment of the surface.⁹⁷ Due to the disorder and chemical similarity in t-BN and h-BN, it is difficult to positively identify the t-BN phase.

5.4 Effect of Sample Biasing on h-BN Film Structure

The bonding in t-BN is much weaker than h-BN or c-BN,⁹⁷ and so this undesired phase could be easily sputtered from the surface with sufficient ion bombardment. DC biasing was used to modify the ion bombardment on the growth surface during magnetron sputtering of the films, as described in §2.1.2 and Appendix B. It has been shown that sample biasing has a negligible effect on the total energy flux onto a sample, but the bias can substantially alter the flux of ions and electrons.¹¹⁷ Decreasing the bias below ground potential causes sputtering of the film surface during growth, which both slows the total deposition rate and dislodges weakly bonded atoms. When the

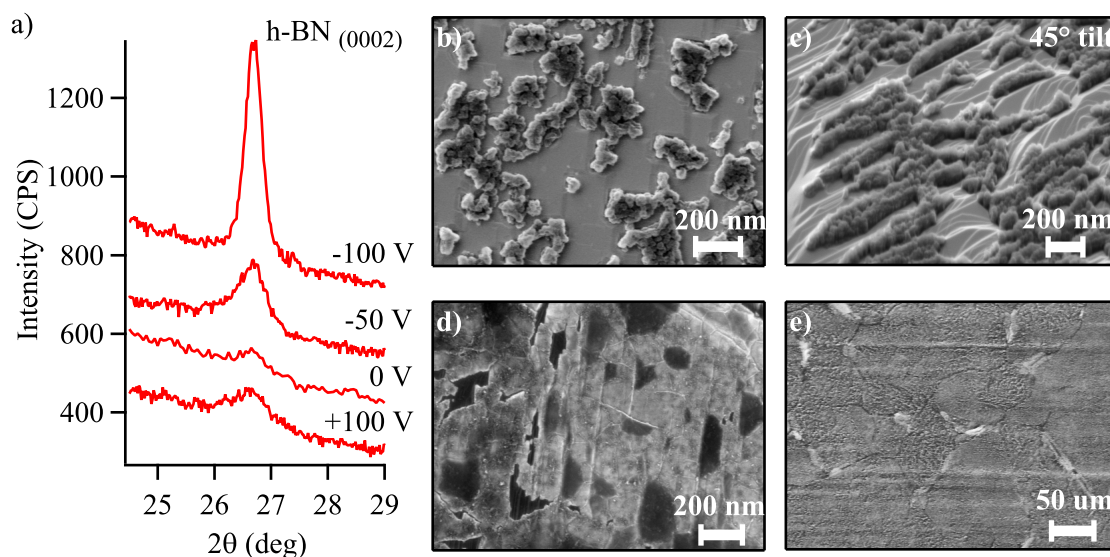


Figure 5.6: XRD and SEM of h-BN films with different substrate biases. (a) XRD from the h-BN (0002) plane in four h-BN films deposited onto Ni foil with different biasing, offset for clarity. All were deposited at 850 °C and 30 W over 5.5 h. Right are SEM images from films deposited with (b, c) –100 V in two different regions, and (d, e) –50 V.

sample was biased to –350 V relative to the chamber ground, total re-sputtering of the film from the substrate occurred, which resulted in a clean substrate surface with no BN film.

Fig. 5.6 shows the effects of sample biasing on h-BN films deposited onto Ni foil at 850 °C and 30 W. The crystallinity of negatively biased films was greater than in the unbiased depositions, such that a –50 V bias was sufficient to produce the same (0002) h-BN peak intensity as for the 15 W deposition mentioned previously, but at 10 times the growth rate. At –100 V the (0002) peak further intensified and narrowed, indicating a film with highly crystalline regions. Reducing the ion bombardment by positively biasing the substrate did not substantially affect the crystallinity of the film.

SEM imaging showed that negative sample biasing had a substantial impact on the film morphology. In Fig. 5.6b-c it can be seen that although the –100 V biasing produced the most crystallinity, the coverage on the substrate is highly non-uniform. The grains of h-BN appear to nucleate at step edges on the Ni foil, and grow ~170 nm tall, with bare Ni foil visible between these islands. The preferential h-BN grain growth at substrate step edges suggests that deposited atoms are very weakly bound on the Ni foil, and are either re-sputtered off or migrate to the h-BN grains.

EDS elemental maps are shown in Fig. 5.7 for two different BN thin films deposited at 850 °C

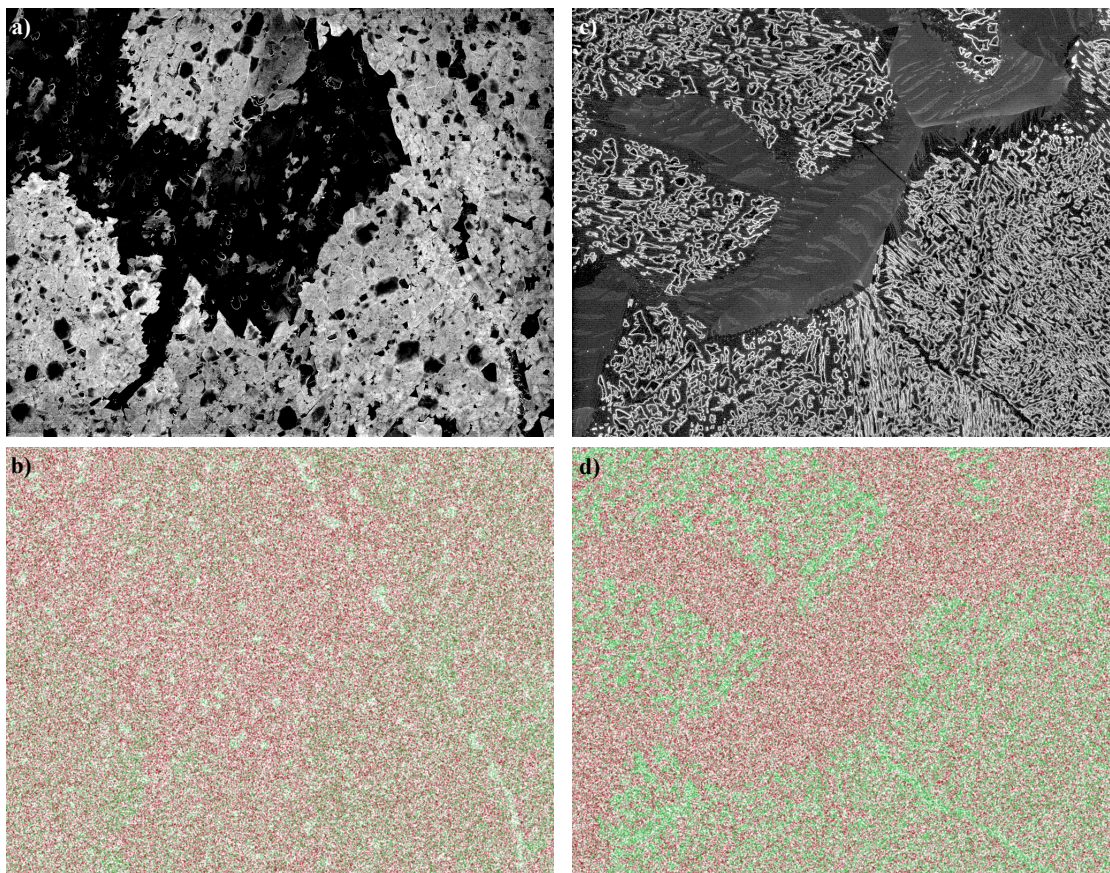


Figure 5.7: SEM images and EDS maps of B, N, and Ni in BN films deposited on Ni foil at 850 °C. (a,b) The film shown in Fig. 5.5d-e, grown at 15 W with no bias. (c,d) The film shown in Fig. 5.6b-c, grown at 30 W and -100 V bias. SEM images are shown in (a,c). EDS elemental maps (b,d) use green for BN and red for Ni.

on Ni foil, one deposited at 15 W without biasing, and the other deposited at 30 W with -100 V sample biasing. In both films, it is apparent that the dark regions of the SEM image correspond to regions of low BN concentration, with more Ni showing through. The film coverage is much more uniform in the unbiased film (Fig. 5.7a-b), however. The EDS map in Fig. 5.7c-d, confirms that the h-BN grains form tall islands as seen in Fig. 5.6b-c, and the concentration of BN is much higher in the islands than in the unbiased film, as indicated by the higher green intensity.

With a -50 V bias (Fig. 5.6d-e) the h-BN film almost completely covers the substrate as a continuous, polycrystalline film with grains approximately the same size as in unbiased depositions. The sputtering of the film surface caused by the bias reduces the presence of the presumed t-BN or disordered regions discussed previously, but the film has boundary grooves between the grains.

However, comparing the low magnification images in Fig. 5.5e and Fig. 5.6e, the complete coverage of the substrate in a uniform h-BN film has been achieved with the -50 V bias.

In the sputter growth of c-BN films it was found that ion bombardment was only necessary to nucleate the c-BN phase in the initial stages of growth, after which c-BN growth proceeded without the need for ion bombardment.^{123,142} The need for biasing only in the initial stages of film growth for c-BN may be due to the fact that it is the equilibrium phase at low pressure and temperature,⁹⁹ while h-BN is only stabilized by large energy barriers to its phase transition to cubic.¹⁰⁰ Thus, sample biasing was required throughout the duration of the h-BN film growth. BN films were grown with a -50 V sample bias for the first 30 min of growth, after which the sample was grounded for the remaining 5 h, however, the XRD and SEM images from these films were similar to films grown with no biasing.

5.5 Summary

The crystallinity of BN thin films grown by RF magnetron sputtering is affected by a large number of deposition parameters. Based on XPS results, the films generally exhibit a mixed chemical phase, with both sp^2 and sp^3 bonded B present. A low deposition rate ($<0.025 \text{ \AA s}^{-1}$) and high temperatures (850°C) are required to achieve the growth of any h-BN crystals. However, this crystalline morphology is non-uniform and appears to consist of h-BN (0002) crystals coexisting with a disordered, turbostratic phase of BN. Negatively biasing the substrate increases ion bombardment of the growth surface during deposition, which enhances the crystallinity and uniformity of the films, until the point where the sputtering of the h-BN film becomes limiting.

The substrate appears to play an important role in h-BN growth, such that crystalline h-BN was only able to be grown on Ni foil. While the lattice match between the Ni (111) and h-BN (0002) surfaces certainly plays a role, the rough surface of the foil also creates a large number of nucleation sites,^{80,95,96} not present on smooth substrates such as single crystal sapphire or SiO_2/Si . Once h-BN grains begin to nucleate, increased ion bombardment due to biasing presumably sputters the weakly bound t-BN phase, and enhances the mobility of the adsorbed atoms.

CHAPTER 6

PROTECTIVE CAPPING LAYERS ON ZrB₂ FILMS

The high temperature stability of ZrB₂ thin films in oxidizing atmospheres is extremely limited, due to the reactivity of both the Zr and B with O₂ and H₂O. First, the oxidation resistance of h-BN thin films on Ni foil is assessed at temperatures above 700 °C for initial exposures and a 1 h anneal in air. Then the capping layer strategy discussed in §1.2.3 is implemented here with h-BN and a-Al₂O₃ layers on ZrB₂ thin films. The oxidation of the multilayer films is studied by *in situ* XRD, and the relevant degradation mechanisms of the h-BN and a-Al₂O₃ capping layers are discussed.

6.1 Experimental Details

6.1.1 Growth of a-Al₂O₃ Capping Layers by Atomic Layer Deposition

The oxidation resistance of Al₂O₃ coatings and thin films is well known,^{276–281} however its stability at high temperatures is understudied. Compared to crystalline Al₂O₃, a-Al₂O₃ has enhanced resistance to O diffusion because of the lack of grains eliminates the grain boundary diffusion path through the film. A common means of depositing a-Al₂O₃ coatings uses ALD with trimethylaluminum (TMA) and H₂O as precursor gases and low substrate temperature (<300 °C), for which Puurunen has written an excellent review.¹²⁹ In ALD, a surface is saturated with one gas, i.e. H₂O, and then the chamber is purged and filled with the second gas. This second gas, i.e. TMA, reacts with the adsorbed, hydroxide-terminated surface and forms a single Al₂O₃ monolayer that saturates the surface. This process is repeated, forming one monolayer at a time until the desired film thickness is reached.

As deposited by ALD, a-Al₂O₃ films can be under either tensile or compressive stresses, depending on the substrate CTE and the growth temperature.^{59,130,282–288} Furthermore, the Young's modulus for a-Al₂O₃ is relatively low compared to other ceramics, and cracking and buckling at high temperatures can occur (see Fig. 6.1) due to a CTE mismatch.^{280,287,289} As with many other oxides, though, no agglomeration has been observed at temperatures up to 1000 °C in air, and the amorphous structure is impressively stable, ideal characteristics needed for a capping layer. Because

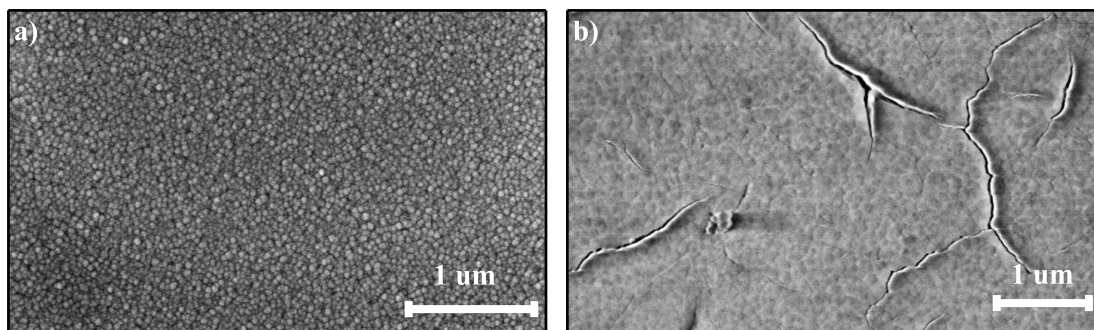


Figure 6.1: SEM images from a 50 nm thick a-Al₂O₃ film on a SiO₂/Si substrate before and after annealing. (a) As deposited, and (b) after annealing in air at 800 °C for 10 h.

of this stability and its widespread use, a-Al₂O₃ was used as a capping layer on ZrB₂ films as a point of comparison to the oxidation resistance of h-BN capping layers.

6.1.2 ZrB₂ Thin Films with Capping Layers

ZrB₂ thin films were deposited on r-cut sapphire substrates at 600 °C using electron beam co-evaporation from elemental (99.5% purity) Zr and B sources (see §3.1 and Chapter 3). This procedure resulted in the growth of nano-crystalline, stoichiometric ZrB₂ thin films 200 nm thick. The films were removed from UHV and transferred to an Oxford OPAL ALD system. Deposition of an a-Al₂O₃ capping layer was carried out at 200 °C using the TMA/H₂O process,¹²⁹ cycled 50 times to produce a 55 nm thick a-Al₂O₃ coating.

The growth of BN capping layers was carried out in the same UHV chamber as the ZrB₂ deposition, using reactive RF magnetron sputtering as described in §2.1.2 and Ch. 5. The working gas was a mix of flowing Ar (7.5 sccm) and N₂ (2.5 sccm) with the total pressure maintained at 10 mTorr, and the substrates were heated to 850 °C during deposition. The B target was sputtered in the Ar/N₂ atmosphere at 30 W for 5.5 h to produce a ~50 nm thick coating. BN films were directly grown on the ZrB₂ film surfaces without exposure to air, as well as on Ni foils (99.5% purity) for comparison.

The initial effects of O₂ exposure at high temperatures were examined by XPS (presented in §2.2). The BN film on Ni foil was annealed in a UHV chamber at 750 °C, 850 °C and 950 °C during O₂ exposures between 4.5×10^4 Langmuir to 1.275×10^6 Langmuir. Between exposures, XPS spectra were taken without breaking UHV. SEM was also used to examine morphological changes before and after all annealings used for the XPS experiments.

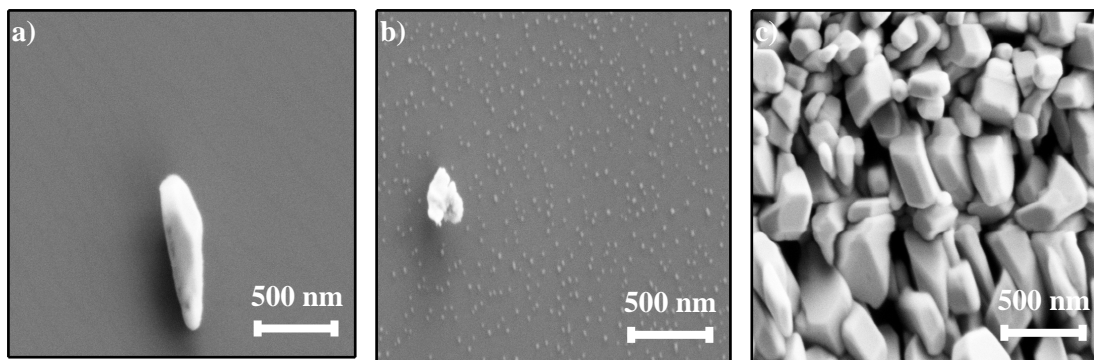


Figure 6.2: SEM images from ZrB_2 films after annealing in air. (a) 1000 °C for 15 min, (b) 800 °C for 1 h, and (c) 1000 °C for 1 h.

Some films were annealed in a tube furnace at 700 °C and 850 °C for 1 h in air. The evolution of the structure of the multilayer h-BN/ZrB_2 and $\text{a-Al}_2\text{O}_3/\text{ZrB}_2$ films was analyzed by *in situ* XRD using an Anton Paar DHS 1100 hot stage (see §2.6.1) in Bragg-Brentano geometry with a 3° offset in the incident angle to remove diffraction from the sapphire substrates. In these capped films, the rate of oxidation of the underlying ZrB_2 or Ni was observed by XRD at 700 °C and 850 °C and at pressures between 5×10^{-5} torr and 760 torr.

6.2 Oxidation of ZrB_2 Films in Air

It was shown in §3.4 that ZrB_2 thin films are morphologically stable at 850 °C for prolonged periods in UHV. In the presence of O_2 however, ZrB_2 quickly oxidizes, and at high temperatures forms m-ZrO_2 and t-ZrO_2 crystals in random orientations. Fig. 6.2 shows SEM images from ZrB_2 thin films after annealing in air for short periods of time. For a very short exposure at 1000 °C (Fig. 6.2a) the film is morphologically unchanged (i.e. remains amorphous by XRD) but XPS indicates that it is completely oxidized and electrically insulating. During annealing at 800 °C (Fig. 6.2b) nano-grains of t-ZrO_2 begin to nucleate at the surface over 1 h, and at 1000 °C (Fig. 6.2c) the grains grow very large and severely alter the morphology of the film.

These changes are also seen in the XRD, shown in Fig. 6.3a. Note that the film annealed in this case initially exhibited a $(10\bar{1}0)$ ZrB_2 nanograined structure, yet after the brief exposure at 1000 °C the film became amorphous. Although m-ZrO_2 is generally considered the equilibrium phase of ZrO_2 at RT, ZrB_2 thin films tend to form a t-ZrO_2 phase when annealed at temperatures below

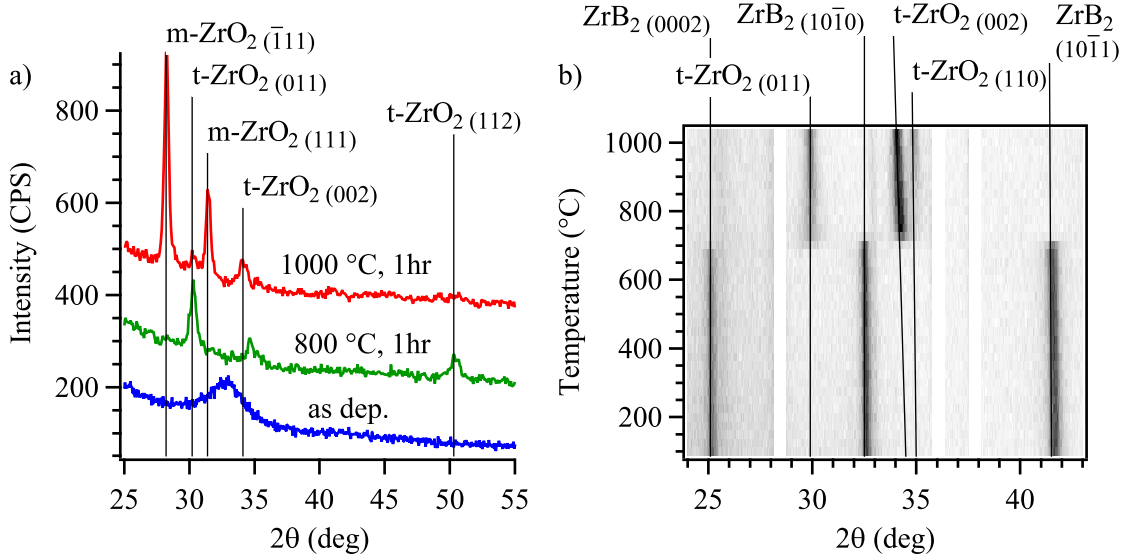


Figure 6.3: XRD from ZrB₂ films after annealing in air. (a) XRD from a ZrB₂ film, as deposited and after annealing for 1 h at 800 °C and 1000 °C. (b) *In situ* XRD intensity map from a ZrB₂ film while being heated at increasing temperature. The temperature was quickly ramped between each 50 °C step, during which the temperature was held for 6.5 min for the duration of the goniometer scan.

1000 °C. The m-ZrO₂ phase dominates when annealed above 1000 °C, however. The reason for the preferential formation of t-ZrO₂ may be due to compressive stresses on the ZrO₂ grains from the surrounding ZrB₂ matrix during oxidation at high temperatures.²⁷⁰ Stress-induced transformation of m-ZrO₂ to t-ZrO₂ has been reported in thin films where the size of the ZrO₂ is constrained.^{268,269}

Fig. 6.3b shows a 2D map of the *in situ* XRD intensity from a ZrB₂ film as a function of annealing. In this experiment, the temperature was ramped up in 50 °C increments, with a 6.5 min XRD scan after each ramp segment. The ZrB₂ phase is seen to persist to high temperatures, but upon reaching 700 °C (the equivalent of 7.98×10^{12} Langmuirs of air exposure at varying temperature) the ZrB₂ phase abruptly disappears and in the following scan a t-ZrO₂ phase begins to form. This sudden degradation of the ZrB₂ thin film is why protective capping layers are needed.

6.3 High Temperature Oxidation of h-BN Films

The BN films grown in this study were highly disordered and exhibited only sparse grains of h-BN. Sample biasing was not employed for films used in the oxidation studies to ensure a continuous coverage of the substrates at all times, without any holes of the type observed in §5.4. As seen in Fig. 6.4a, a weak XRD peak from the (0002) plane of h-BN can be observed above the noise. By

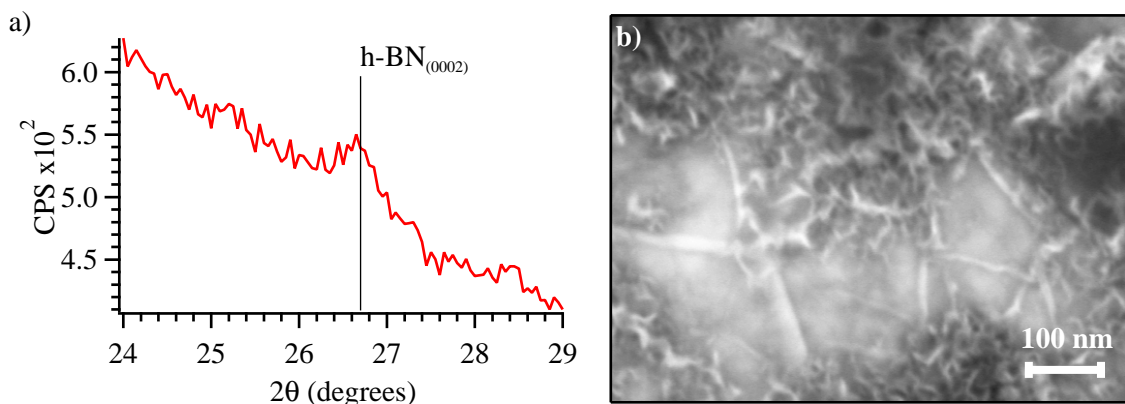


Figure 6.4: As-deposited XRD and SEM of BN film on Ni. (a) XRD pattern from BN film grown on Ni foil showing a weak peak from the (0002) plane of h-BN. (b) Secondary electron image of the same film with small h-BN grains visible.

SEM, thin crystalline grains were found scattered across the surface, preferentially collecting at Ni grain boundaries. These h-BN crystals are shown in Fig. 6.4b, with disordered regions in between.

The composition of the films was measured by XPS to be nearly identical to a h-BN standard powder (99.5% purity, Alfa Aesar), but varied by $\pm 5\%$ between depositions. Plots of the B and N 1s photoelectron peaks are shown in Fig. 6.5a-b. As-deposited peaks (solid lines) show a 1 eV shift from their standard positions (up for B and down for N), with no evidence of other chemical shifts due to a second phase. After annealing up to 950 °C for 15 min under 5×10^{-4} torr dry O₂, no changes were observed in the chemical shifts or peak shape (dashed lines). Only N, B, and a small amount of O contamination were observed in these films.

Fig. 6.5c plots the concentration of B and O in the BN films as deposited and after several brief exposures to dry O₂ at high temperature. In this process, samples were sequentially heated to and annealed for 15 min at 750 °C, 850 °C and 950 °C in 5×10^{-5} torr O₂. In the last step, the pressure was raised to 5×10^{-4} torr and the temperature was 950 °C. Initially, a small dip in the B concentration is observed, but the final concentration is within 5 at % of this dip. As stated above, this measured concentration is consistent with (< 0.5 at % above) the at % B in an h-BN powder standard measured on the same instrument. The concentration of O in the film trended upwards with increasing exposure, but only increased by 3%, resulting in a slope of $\sim 2 \times 10^{-6}$ at %/Langmuir.

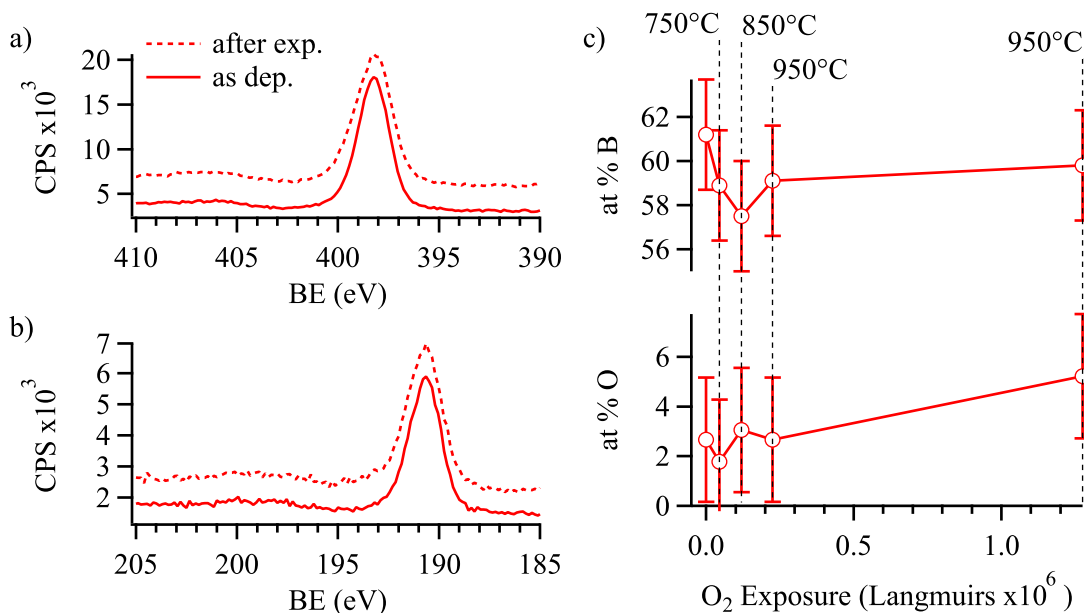


Figure 6.5: Effects of O_2 exposure on BN film at high temperatures. XPS of the (a) B 1s and (b) N 1s peaks before (solid) and after (dashed) high temperature exposure to dry O_2 . (c) at % B and at % O in the film as a function of O_2 exposure at high temperature. Error bars represent an assumed 5 at % uncertainty in the XPS quantification.

6.4 *In situ* XRD of ZrB_2 Films Capped with BN or $\alpha\text{-Al}_2\text{O}_3$

Fig. 6.6 shows the results of *in situ* XRD measurements on a Ni foil coated with 50 nm of BN heated to 850 °C in air. In Fig. 6.6a the growth of a polycrystalline NiO phase can be observed as the annealing continues. The intensity from the underlying pure Ni phase, however, does not vary during the annealing. The scan speed required for *in situ* measurements means that the small h-BN peaks were not visible above the noise. Fig. 6.6b plots the sum of the integrated XRD intensity of the NiO (100) and (111) peaks throughout the annealing.

The NiO growth rate at 850 °C was $\sim 10\times$ the rate at 700 °C. The dashed curve in Fig. 6.6b is the intensity from an uncoated Ni foil also at 850 °C. Both the uncoated and the BN coated foils approach the same amount of NiO crystallinity by the end of the annealing as measured by XRD. However, the amount of NiO crystallinity accumulated during the ramp up in temperature was substantially less for the BN coated Ni foil, and the average growth rate was also subdued.

In situ XRD was also used to measure the effectiveness of ~ 50 nm thick h-BN and $\alpha\text{-Al}_2\text{O}_3$ capping layers in protecting and stabilizing the ZrB_2 film structure. Fig. 6.7 shows the XRD intensity

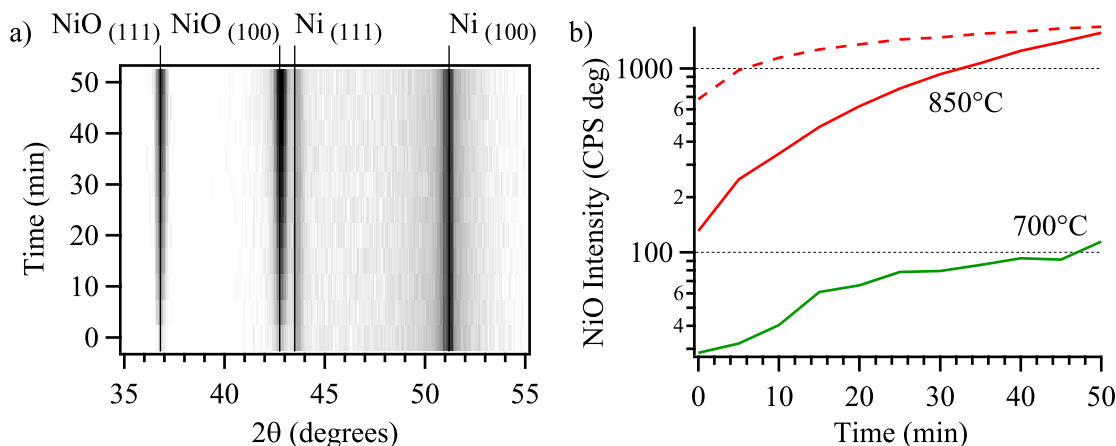


Figure 6.6: *In situ* XRD of Ni foil capped with h-BN. (a) XRD intensity map (log color scale) versus annealing time at 850 °C in air for a BN film on Ni foil. (b) Total integrated XRD NiO intensity as a function of annealing time for two different temperatures, and an uncoated Ni foil at 850 °C (dashed line).

for four samples measured during annealing. The ZrB_2 thin film is nano-crystalline as deposited, and so only weak diffraction is observed. None the less, the consumption of the ZrB_2 phase is seen in films annealed at 850 °C, accompanied by the growth of a polycrystalline t- ZrO_2 phase. A m- ZrO_2 phase is also observed in the films capped with a- Al_2O_3 , but this phase is already present following the ALD process and does not change throughout the annealing.

In Fig. 6.7a-b, the samples were annealed under 10^{-3} torr vacuum. This was necessary to slow the oxidation rate, as when annealed in air the ZrB_2 film was completely oxidized before reaching 850 °C. At 700 °C, the ZrB_2 phase persists for the entire 110 min anneal, while a small t- ZrO_2 phase slowly grows. At 850 °C the ZrB_2 phase beneath the h-BN is rapidly consumed, abruptly disappearing after 20 min. About this same time, the t- ZrO_2 phase begins to crystallize, and continues to grow steadily for the duration of the anneal.

For the ZrB_2 films capped with a- Al_2O_3 , shown in Fig. 6.7c-d, annealing was done in air. Just as with the h-BN capping layer, at 700 °C the ZrB_2 phase persisted for the entire duration of the annealing. At 850 °C the a- Al_2O_3 capping layer performed substantially better than h-BN, especially considering the much higher oxygen partial pressure. The ZrB_2 phase persists for ~90 min. The growth of t- ZrO_2 begins almost immediately, similar to the film capped with h-BN, however the growth rate was much slower than for the h-BN case.

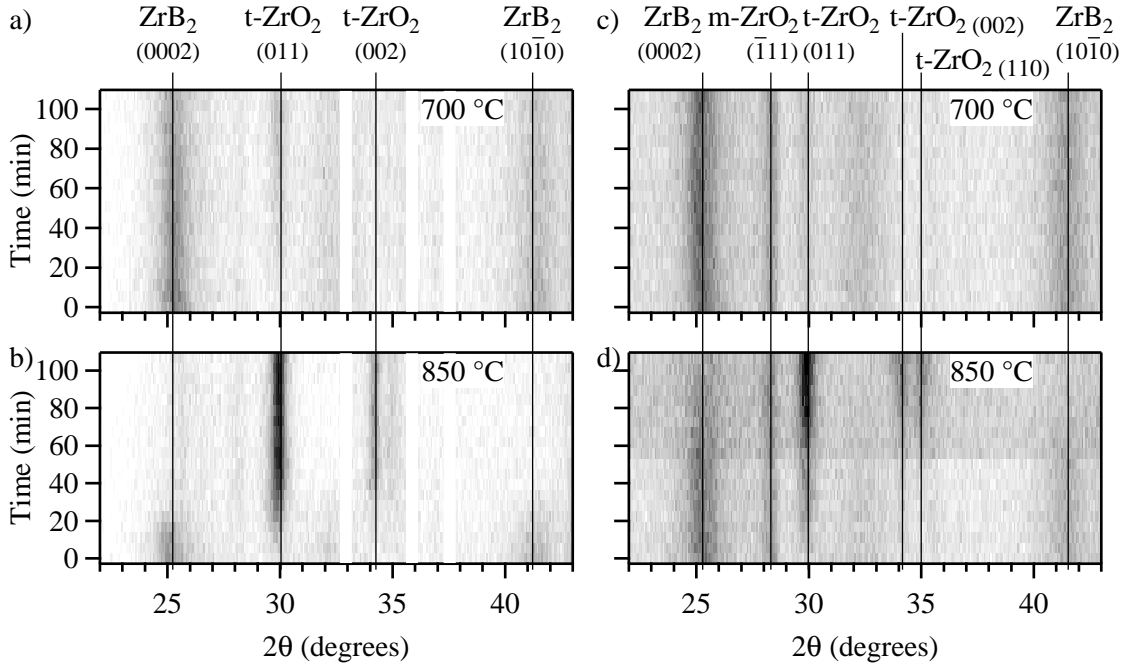


Figure 6.7: XRD intensity maps versus time for capped ZrB_2 thin films annealed at 700 °C and 850 °C. (a, b) 50 nm BN capping layer on ZrB_2 heated in 10^{-3} torr vacuum. Peaks from the AlN heater have been blocked out. (c, d) 50 nm a- Al_2O_3 capping layer on ZrB_2 in air. All images use the same color scale.

6.5 Morphological Changes in Capping Layers

Accompanying the changes in crystallinity are changes in the surface morphology of the capped ZrB_2 films. Fig. 6.8 shows SEM images of the capped ZrB_2 films before and after annealing in air for 1 h. As deposited, both the ALD a- Al_2O_3 and the sputter deposited h-BN surfaces exhibit a nano-grained morphology, yet XRD indicated an amorphous structure, which is in contrast to XRD in Fig. 6.4a, where crystalline h-BN flakes could be seen on a Ni foil substrate. Both capping layers were measured by XRR to be 55 nm thick, and are continuous and uniform across the entire ZrB_2 film.

Fig. 6.8b-c show the effects of annealing on the a- Al_2O_3 capping layer. Much like the XRD data, the film morphology is unaffected by annealing at 700 °C. The capping layer remains smooth and continuous over at least a $100\ \mu\text{m}^2$ area, and is still nano-granular. However, numerous bubbles like the one shown in Fig. 6.8b appeared, measuring $\sim 3\ \mu\text{m}$ in diameter and distributed randomly across the surface. These bubbles, which may be local regions of delamination, were also visible

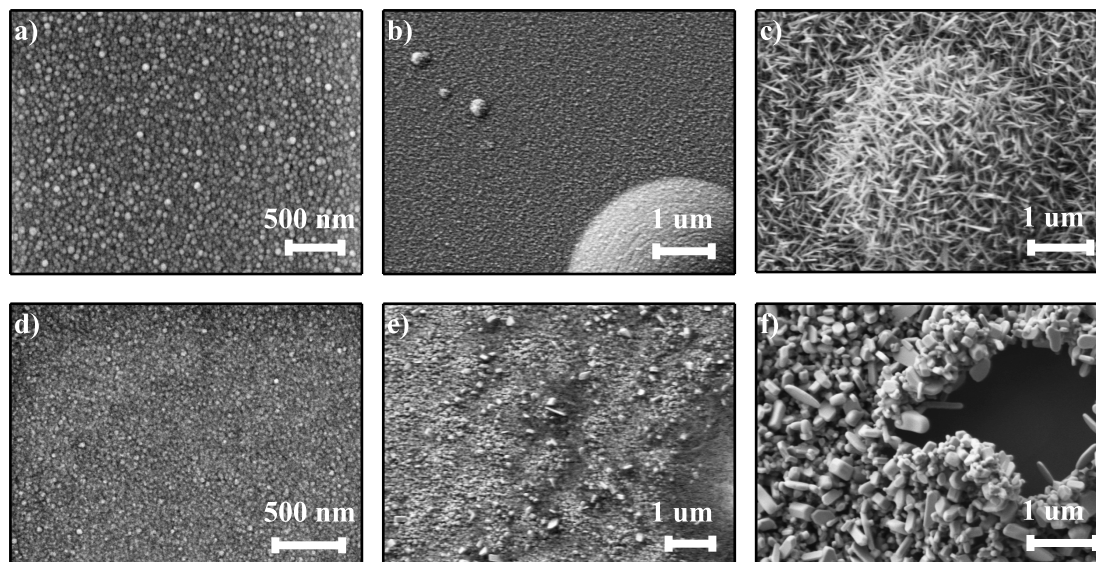


Figure 6.8: SEM images from capped ZrB_2 films as deposited and after annealing for 1 h at 700 °C and 850 °C in air. Top row: $\text{a-Al}_2\text{O}_3$ capping layer (a) as deposited, (b) after 700 °C, and (c) after 850 °C. Bottom row: h-BN capping layer (d) as deposited, (e) after 700 °C, and (f) after 850 °C.

after annealing at 850 °C, as in Fig. 6.8c. Additionally, after annealing at 850 °C in air, the $\text{a-Al}_2\text{O}_3$ has restructured into a coating of needle-like grains, although the XRD pattern shows no crystalline Al_2O_3 phase; only t-ZrO_2 was visible by XRD.

Annealing the h-BN capped films in air above 700 °C resulted in the evaporation of the BN layer, based on XPS of the films after annealing. In contrast to results of the initial oxidation experiment presented in Fig. 6.5c, at 700 °C the BN film thinned severely, based on a reduction in the $\text{B } 1\text{s}$ and a loss of the $\text{N } 1\text{s}$ in XPS. At 850 °C the evaporation of the BN was more rapid, and the oxidation of the ZrB_2 began quickly, as seen before in Fig. 6.7b. Thus large grains of t-ZrO_2 are seen in Fig. 6.8f, as well as some stress induced holes caused by the oxidation of the ZrB_2 .

The small bubbles and recrystallization of the $\text{a-Al}_2\text{O}_3$ are not the only morphological changes, however. Fig. 6.9 shows lower magnification SEM images of the same films as in Fig. 6.8b-c. Large circles are visible across the surface of the film where the $\text{a-Al}_2\text{O}_3$ capping layer has delaminated and exposed the underlying ZrB_2 to oxidation. At the center of each delamination hole is the exposed sapphire substrate, while the white regions in the SEM images appear to be ZrO_2 . The edges of each hole are curled up, which implies that the film was under a great deal of tensile stress during

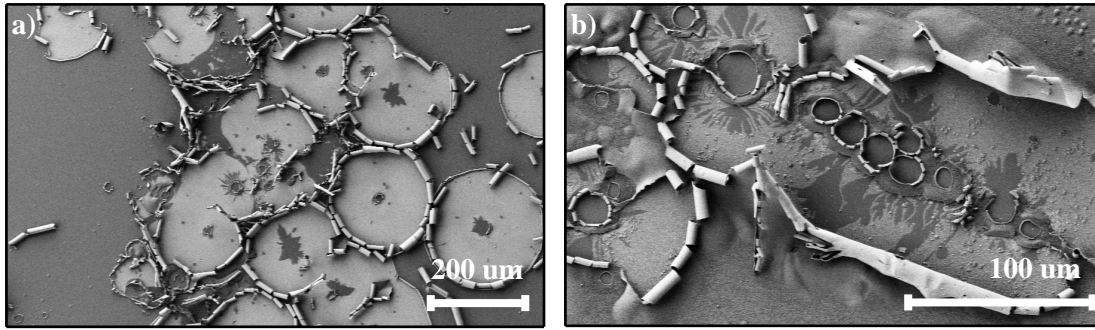


Figure 6.9: SEM images of the large scale stress-induced delamination of the α - Al_2O_3 capping layer on ZrB_2 after annealing in air. (a) 700 °C and (b) 850 °C for 1 h.

annealing. This delamination is observed in all ZrB_2 films capped with α - Al_2O_3 that were annealed above 700 °C in air, but was not seen when the same films were annealed in UHV.

6.6 Discussion of Film Degradation Mechanisms

The above results highlight several important characteristics of h-BN and α - Al_2O_3 capping layers that are relevant for improving the oxidation resistance of ZrB_2 thin films. Both types of capping layers performed equally well at 700 °C, limiting the growth of t- ZrO_2 for the entire duration of the annealing treatment. However, the processing required to produce the capping layers was substantially different. The ALD process for growing α - Al_2O_3 required moving the film to a separate deposition reactor and heating it to 200 °C under a 10^{-2} torr vacuum. This resulted in the growth of an oxide phase at the ZrB_2 surface before the capping layer could even be deposited. Because the h-BN capping layer was able to be sputter deposited onto the ZrB_2 film without removing the film from UHV, no such oxidation occurred, and the ZrB_2 surface remained pristine.

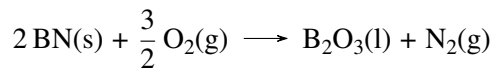
When annealed at 850 °C, however, both films failed to preserve the ZrB_2 phase, albeit for very different reasons. The h-BN capping layer was not chemically stable in low vacuum at 850 °C, and evaporated quickly at the beginning of the annealing treatment. This was also observed to a lesser degree during the *ex situ* annealing at full atmospheric pressure and 700 °C. In contrast, the α - Al_2O_3 successfully retarded the oxidation of the ZrB_2 for the entire duration of the annealing at 850 °C; the growth of the t- ZrO_2 phase begins at the same time as with h-BN, but the oxidation rate is much slower. However, the catastrophic delamination failure in certain regions of the α - Al_2O_3 capping

layer during annealing at both temperatures caused large portions of the ZrB₂ film to be suddenly exposed to oxidation.

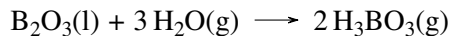
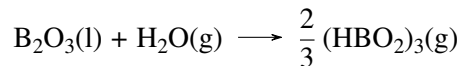
6.6.1 h-BN Evaporation

Recent reports on the oxidation resistance of CVD grown h-BN have clearly demonstrated its ability to retard the oxidation of several substrates, including Ni, Cu, and graphene.^{80,81,105} The results of initial exposure to O₂ above 700 °C, shown in Fig. 6.5, seem to corroborate these reports, as do the *in situ* oxidation measurements reported in Fig. 6.6. The primary explanation for this oxidation resistance is the large activation energy barrier for the evaporation of h-BN. Calculations of the reaction of O₂ with the (0002) surface of h-BN have shown several large (~ 1.5 eV) energy barriers,¹⁰³ and measurements of the vacancy formation energies indicate >10 eV of energy is required to break the B-N bonds in h-BN.⁸¹

While these large energy barriers explain the oxidation resistance of h-BN, the standard free energies of formation for BN and related oxides and hydroxides tell a very different story. As studied by several groups,^{102,106–109} the primary oxidation reaction at high temperature is



which has a free energy of formation of -680 kJ mol^{-1} at 1000 °C.¹⁰⁶ This reaction produces a weight gain and self limiting kinetics as the thickness of the oxide layer grows faster than B₂O₃ evaporates.^{102,105,106} However, when annealed in a low partial pressure of H₂O, such as in an open air furnace, volatile H₃BO₃ and (HBO₂)₃ are formed by the following reactions



Paralinear rate kinetics (a combination of parabolic oxidation and linear evaporation rates) are observed as the growth of the oxide layer and the evaporation of the B₂O₃ as hydroxide species compete, ultimately resulting in mass loss over time.^{102,106–109} Thus experiments on the oxidation resistance of h-BN using O₂ and ambient atmosphere are not comparable.

Film structure may play a large part in the oxidation of BN as well. Jacobson *et al.*¹⁰² compared the oxidation of high and low density CVD h-BN, where the low density film was highly disordered. Thermogravimetric analysis showed a substantial increase in the rate of oxidation of the low density phase at high temperatures. Although the BN films grown in this study showed some h-BN crystallinity when deposited on Ni, the BN capping layer on the ZrB₂ film was amorphous and nano-granular. XRR measurements indicated that the density of the films was about 2 g cm⁻³, which is below the density for bulk h-BN. This low density granular structure would enhance the diffusion of O₂ and H₂O throughout the film.

Furthermore, the film oxidation rate is dependent on its crystallographic orientation,^{102,290} with the h-BN (0002) plane being more resistant to oxidation than the (10 $\bar{1}$ 0) plane. In sputter growth of BN, it is common to observe the formation of t-BN, a disordered phase of sp² bonded BN sheets with random rotations between planes.^{119,125} This phase is likely produced by stress-induced shearing of the 2D hexagonal lattice from ion bombardment during energetic depositions. The disordered background seen in Fig. 6.4b is likely the t-BN phase. It has been known for a while that the t-BN phase formed by sputter deposition is highly $\langle 10\bar{1}0 \rangle$ oriented,^{119,125} which would allow a faster oxygen diffusion path than for a $\langle 0001 \rangle$ orientated film.

6.6.2 a-Al₂O₃ Stress and Delamination

The low temperature ALD process is ideal for creating conformal coatings of a-Al₂O₃, which has the added benefit of lacking grain boundaries, which serves to limit oxygen diffusion through the barrier. In contrast to the h-BN capping layer, the a-Al₂O₃ was chemically stable during the air annealing at 850 °C. Rather, its failure was related to stress delamination and recrystallization.

Thermal expansion mismatch between ALD a-Al₂O₃ and its substrate is a known issue when using the film as a barrier coating. The critical tensile strain for ALD a-Al₂O₃ films has been observed to scale inversely with the film thickness as $t^{-1/2}$, and ranges from 0.5 % to 2.5 % for film thicknesses less than 80 nm.²⁸⁶ This strain could correspond to stresses as low as 12 MPa.²⁸⁵ The CTE for a-Al₂O₃ films has been reported to be from 4.2 ppm/°C to 7.1 ppm/°C,^{59,291} while for ZrB₂ it is from 5.9 ppm/°C to 7.7 ppm/°C.^{23,57,58,72} Additionally, the Young's modulus for a-Al₂O₃ is ~180 GPa,²⁸⁶ which is substantially smaller than for ZrB₂ at 489 GPa.²³

As the temperature increases, the a-Al₂O₃ capping layer is placed under substantial tensile stress, which results in the catastrophic delamination observed in Fig. 6.9. However, a CTE mismatch between the a-Al₂O₃ and the ZrB₂ layers is not a sufficient explanation on its own. A Pt thin film capped with the same thickness of a-Al₂O₃ does not experience the same delamination effects, despite the fact that Pt has almost twice the CTE of ZrB₂. Furthermore, the stress delamination is not observed in multilayer a-Al₂O₃/ZrB₂ films annealed in UHV. The oxidation of the B may play a significant role as well, since delamination was not observed when an amorphous ZrO₂ film was capped with a-Al₂O₃ and annealed at 850 °C in air for 1 h. As was seen in Fig. 6.1, a-Al₂O₃ films deposited on SiO₂/Si substrates do not recrystallize even after air annealing at 800 °C for 10 h. However, based on the CTEs of SiO₂ and the cracking pattern seen in Fig. 6.1, ALD a-Al₂O₃ films on SiO₂/Si substrates are under compressive stress,^{59,286,288,289} unlike a-Al₂O₃ on ZrB₂.

Stresses in a-Al₂O₃ films depend strongly on the thickness of the films. Reports in the literature observed that for films deposited under the same conditions, the residual tensile stresses decreased with decreasing film thickness.²⁸² Films with thicknesses >25 nm also exhibited an irreversible phase change at high temperatures,²⁸² and crystallized at lower temperatures.²⁹² Given that the stresses and crystallization temperature seem to be correlated, and are in all cases much lower than the temperature required to form highly crystalline Al₂O₃ from a-Al₂O₃,²⁷⁶ it is plausible that the crystallization is stress induced.

CTE mismatch and residual stresses are certainly a concern for a-Al₂O₃ cappings layers, however these may be overcome by counteracting the stress with an interfacial layer,²⁸⁷ or by altering the deposition conditions.²⁸⁸ Reducing the stress is likely to affect the crystallization of the films as well. The catastrophic delamination might be related to defects induced by residual H in the a-Al₂O₃ layer.¹³⁰ Such defects would not only act as nucleation sites for stress relief, but would also enhance O diffusion through the film. Again, however, the delamination was only observed when a underlying ZrB₂ layer was able to be oxidized, and not when a-Al₂O₃ was deposited on Pt, amorphous ZrO₂, or SiO₂/Si substrates.

6.7 Summary

ZrB₂ thin films exhibit useful properties, such as high conductivity and high melting temperature, but are prone to failure by oxidation or agglomeration. The use of capping layers as barriers for oxidation or wear resistance in harsh, high temperature environments is necessary. However these barriers are not without their own failures, which need to be assessed in tandem with their substrates.

The success of a h-BN thin film as an oxidation barrier on ZrB₂ requires that sufficiently pristine oxide free films be prepared. The oxidation resistance of h-BN is questionable, based on the preferential free energy of formation for the reaction with O₂ and the further reactions with H₂O, which result in the evaporation of the film. Reducing this evaporation requires that crystalline films be produced, with the (0002) epitaxial orientation in order to take advantage of the reduced oxidation. Furthermore, just as with a-Al₂O₃, there are substantial problems with the CTE of h-BN, which is anisotropic, and is in fact, negative along the a-axis.^{96,293} The *in situ* XRD results do indicate that h-BN is effective at reducing the oxidation of ZrB₂ under modest conditions of 700 °C and 10⁻³ torr.

At 850 °C, a-Al₂O₃ capping layers formed by ALD outperform h-BN capping layers due to their chemical stability. Depending on the stresses induced by the substrate, however, large areas of the a-Al₂O₃ capping layer can delaminate, exposing the ZrB₂ film to the oxidizing environment. This catastrophic delamination seems to depend on the oxidation of the ZrB₂ layer, as large scale breakdown on the a-Al₂O₃ is only observed when ZrB₂ is annealed in air.

CHAPTER 7

CONCLUSIONS

7.1 Synthesis and High Temperature Stability of ZrB_2 Films

7.1.1 Nanostructure of As-Deposited Films

Synthesis of ZrB_2 films by e-beam co-evaporation of Zr and B sources is an effective means to grow homogenous films of defined composition. Depending on the growth temperature, ZrB_2 thin films are amorphous (at RT), oriented nano-crystalline (at 600 °C), or random polycrystalline (at 850 °C), with grain sizes observed to be <50 nm by SEM or XRD Scherrer analysis. For applications in high temperature sensors and other electronics, the crystallinity of the films is not of much importance, as the high temperature stability and electrical conductivity of films was similar, regardless of the deposition temperature. Deposition at RT produced amorphous films, and the low temperature is generally advantageous, as it allows the use of photo resist to pattern the electrodes and electrical contacts. The amorphous film surface was also less rough than that of films deposited at 600 °C, which could affect the interface between the top of the ZrB_2 and subsequent films.

The small crystallite size and highly textured orientation of films deposited at 600 °C suggests that 600 °C is a lower bound for the mobility of the atoms in ZrB_2 . SEM imaging of films deposited at 600 °C showed nano-crystal grains with a smooth, amorphous matrix between them. At 600 °C the mobility was high enough to allow the nucleation and growth of small crystals with preferential orientation, but the films were primarily amorphous. In contrast, ZrB_2 films deposited at 850 °C exhibited slightly larger crystal grains with a random orientation due to the enhanced mobility of the atoms.

7.1.2 Stability of Atomic Structure with Annealing

Post-deposition annealing in UHV up to 850 °C for 55 h had no substantial effect on the ZrB_2 film structure; no agglomeration was observed and crystallite growth was low (in textured nano-crystalline films) or negligible (within random polycrystalline films), while nucleation of new crystals was minimal (within amorphous films). For nano-crystalline films deposited at 600 °C and

amorphous films deposited at RT, crystalline grain growth only occurred after annealing at 800 °C for 1 h, further indicating that the atomic mobility in ZrB₂ is extremely limited at 600 °C and below.

The surface of nano-crystalline films roughened during vacuum annealing at 800 °C, which is undesirable for applications as thin film electrodes. In comparison, no roughening was seen in either the polycrystalline films or the amorphous films after annealing. For the polycrystalline films, the lack of any morphological changes can be attributed to the stability of the ZrB₂ crystal phase. For the initially amorphous films, nano-crystalline grains of ZrB₂ could be observed by XRD after annealing for 55 h in vacuum, but the low intensity of the diffracted x-rays indicates that the crystallites are not numerous. The small number of crystal grains in films deposited at RT can be attributed to a high activation barrier to nucleation in these films, and the low atomic mobility in ZrB₂.

EXAFS analysis showed that, after annealing at 800 °C for just 1 h in vacuum, films with $X_{\text{Zr}} = 0.33 \pm 0.10$ exhibited a local bonding environment with similar bond lengths and neighboring atoms as in bulk ZrB₂. Since the EXAFS measurements emphasize the short range order of the film, it is better than XRD for probing the structure of films with mixed crystalline and amorphous regions. Films deposited at RT were initially amorphous by XRD and disordered by EXAFS. After annealing, however, these films showed a small number of ZrB₂ crystallites by XRD, but a highly ordered ZrB₂ local bonding environment by EXAFS. This highly stable ZrB₂ lattice gives the films deposited at RT the same morphological and structural stability as films with higher crystallinity.

7.1.3 Stable Electrical Conductivity with Annealing

All films, regardless of deposition conditions or composition, were electrically conductive as deposited, with conductivities on the order of 10⁵ S/m. The conductivity of amorphous films was generally lower than thin films deposited at high temperature, and increased with increasing Zr content. In the first 9 h of annealing at 800 °C in vacuum, films showed slight improvements in conductivity as defects were annihilated. Films of similar composition tended to achieve similar conductivities after annealing, regardless of the initial growth temperature.

The stability of the ZrB₂ phase and highly ordered local bonding formed during the annealing produced films which were stable electrical conductors. The conductivity of films which were annealed in UHV for up to 55 h improved with time, increasing by a factor of 2 by the end. This

“bottom line” (the stable electrical conductivity after long term annealing) is encouraging for applications in high temperature electronics. After a brief burn-in period (1 h) where the conductivity improves rapidly, the films are stable for long periods of time, and also through many thermal cycles between 850 °C and RT.

7.2 Improved Oxidation Resistance of ZrB₂ with Capping Layers

7.2.1 Rapid Oxidation of ZrB₂ in Air

Despite the high temperature stability of ZrB₂ thin films in vacuum, they are extremely reactive and become heavily oxidized in air. At temperatures above 800 °C, the oxidation process completely converts a 200 nm thick ZrB₂ film to a mix of t-ZrO₂ and m-ZrO₂ in as little as 15 min. This oxidation also produces a liquid B₂O₃ phase, which is volatile in vacuum. When annealed in the presence of water vapor (ambient atmosphere), the oxidation of ZrB₂ is accompanied by a loss of boron, likely due to the formation of volatile boron hydroxides. The resulting ZrO₂ layer becomes an inhomogeneous arrangement of ZrO₂ crystals separated by large gaps and grooves presumably from the phase separation of B₂O₃ and its evaporation. These gaps allow O₂ to diffuse further into the film. In order to prevent this oxidation, capping layers must be introduced to protect the underlying ZrB₂ in oxidizing atmospheres.

7.2.2 Sample Biasing for Growth of Homogeneous h-BN Films

The oxidation resistance of h-BN films depends on the crystallinity and homogeneity of the film. Sputter growth of BN at RT produces a highly disordered, yet continuous film with a very slow growth rate ($<1 \text{ Å s}^{-1}$ at $<200 \text{ W}$ power). Deposition at 850 °C is capable of producing crystalline films, but only at growth rates $<0.01 \text{ Å s}^{-1}$. Furthermore, the crystallinity of BN films deposited at 850 °C is inhomogeneous, varying considerably over several microns, and could only be achieved on Ni substrates. This suggests that the h-BN crystallinity is limited by the atomic diffusion during growth, even more so than in ZrB₂.

The presence of an amorphous or t-BN phase was inferred from SEM imaging, XPS peak analysis, and XRR density profiles. To reduce the amount of this t-BN phase and improve the mobility of the deposited atoms, substrate biasing was implemented in the deposition chamber. Biasing the

substrate -50 V relative to the chamber ground improved film crystallinity such that the growth of a more homogeneous and crystalline film could be synthesized at a growth rate of 0.025 \AA s^{-1} . However, substrate biasing does not allow the growth of h-BN on arbitrary substrates. Deposition on SiO_2/Si substrates and amorphous ZrB_2 thin films, even with biasing, produced amorphous BN.

7.2.3 Performance of ZrB_2 Films Capped with h-BN and a- Al_2O_3

Both h-BN and a- Al_2O_3 successfully inhibited the oxidation of ZrB_2 thin films at high temperatures for limited exposures. Based on *in situ* XRD, ZrB_2 capped with 50 nm of a- Al_2O_3 did not form any oxide phases during 1 h of annealing in air at 700°C . At 850°C , a t- ZrO_2 phase formed after $\sim 15 \text{ min}$ of annealing, but the ZrB_2 phase persisted for almost 1 h . In contrast, h-BN was unsuccessful at preventing the oxidation of ZrB_2 in air at either temperature. At 1 mtorr vacuum and 700°C the h-BN cap was successful in preventing the formation of a t- ZrO_2 phase, but at 850°C in 1 mtorr vacuum the ZrB_2 phase was consumed in $\sim 20 \text{ min}$.

SEM imaging of a ZrB_2 film capped with BN after annealing at 700°C in air showed a substantial reduction in the size of ZrO_2 grains compared to uncapped films. Thus, although the ZrB_2 phase was still consumed after 1 h at 700°C in air, the h-BN did hinder the oxidation. The primary failure of the h-BN capping layers is the oxidation and subsequent evaporation of B_2O_3 . BN is not thermodynamically stable in O_2 based on the ΔG of the oxidation reaction, however a more crystalline h-BN thin film would likely survive annealing in air longer than the amorphous BN films that were tested.

Although the a- Al_2O_3 capping layer was a more robust oxidation barrier than the h-BN, thermal stresses and t- ZrO_2 grain growth caused the a- Al_2O_3 to delaminate and exposed large areas of the ZrB_2 film to air. Furthermore, although no XRD pattern was observed, the appearance of a needle-like array of Al_2O_3 crystals provides pathways for O diffusion. The low Young's modulus of a- Al_2O_3 compared to ZrB_2 means the capping layer experiences increased strain due to stresses at high temperatures. Results of annealing Pt, ZrO_2 , and SiO_2/Si capped in a- Al_2O_3 indicate that the oxidation of the ZrB_2 film is critical to the stress delamination of the a- Al_2O_3 .

7.3 Future Work

7.3.1 Fundamental Aspects of ZrB₂ Film Growth

In §3.2.2 a parabolic function was presented relating the composition of the e-beam evaporation flux to the XPS-measured composition of the thin films. This behavior has not been repeated for any other binary system, and cannot be explained. An adjustment of the RSFs used in the XPS quantification can accurately account for this trend, but the required adjustments to the RSFs are large. Improving the accuracy of the RSFs, and hence the film composition, will require a complete measurement and re-analysis of the transmission function of the XPS spectrometer and calibration of new RSFs from clean standards.

If both the XPS and QCM measurements are found to be accurate, then the mechanism for the growth of the ZrB₂ films may have unique behavior and must be investigated further. The XPS and QCM data should be accurately acquired for other thin film systems grown by e-beam evaporation, such as TiB₂, HfB₂, AlB₂, NiB, NbB₂, etc. The growth of ZrC and other covalent Zr compounds that don't contain B could be investigated as well. Potentially, trends involving the mass of the atoms, bonding, and melting points of the materials could arise, which may explain the unexpected sticking coefficients found in ZrB₂ growth.

7.3.2 Improved Crystallinity of h-BN Films

Further improvements to the crystallinity of h-BN films over large areas is desirable. A high growth temperature of 850 °C was selected in this thesis for comparison to CVD grown h-BN films. A more comprehensive study of film growth over a wide range of temperatures rather than just RT and 850 °C including the effects of biasing could provide insight into the mobility limited growth of h-BN. Higher quality h-BN films are necessary for two important technological applications:

1. For quantum (2D) device applications, a highly uniform mono- or bi-layer crystalline h-BN film is required to achieve quality devices. The low growth rate from magnetron sputtering is beneficial for nano-manufacturing; however, at present atomically smooth Ni or Cu substrates would be necessary to this exploration. Ideally, (111) oriented Ni or Cu substrates would be

used to promote the best growth possible. Improved growth on other substrates would broaden the applicability of magnetron sputtering.

2. For application as an oxidation barrier, achieving growth of crystalline h-BN on substrates other than Ni is also required. In the literature, growth of h-BN by magnetron sputtering has been shown on SiO₂/Si and sapphire substrates, but could not be reproduced here. Even a modest improvement in the quality of crystalline h-BN thin films would be of benefit to the community.

A real challenge for optimizing the growth of h-BN films with thicknesses <50 nm is that they are difficult to characterize. XPS and SEM work well in all cases, but other techniques are problematic: (i) XRR requires flat substrates (unlike foils), (ii) XRD only detects the (0002) h-BN plane due to film texture and the low scattering cross sections of B and N, and (iii) Raman spectroscopy (a mainstay of h-BN literature) requires non-metallic substrates. Future work in this area will require addressing this characterization challenge.

7.3.3 Stresses in a-Al₂O₃ Films

Delamination of a-Al₂O₃ capping layers from thermal stresses has been observed on SiO₂/Si, ZrB₂, and PtSi_x substrates. Preliminary work has shown that the delamination does not occur when films are annealed in vacuum, nor do the a-Al₂O₃ films crystallize without exposure to air. The thermal stresses in air are also greatest with ZrB₂ layers, and are substantially reduced when non-oxidizing substrates are used, such as Pt or ZrO₂. Quantitative stress measurements will be required to explore stress effects as a function of a-Al₂O₃ film thickness, substrate, and atmosphere. Unfortunately, *in situ* XRD has proven unfruitful, as the crystallization of the a-Al₂O₃ capping layer cannot be detected, possibly due to their extreme nano-crystallite size.

Since the delamination is centered at specific sites within the film, as seen by SEM, and does not occur when films are annealed in vacuum or when SiO₂/Si is the substrate, the growth of oxide crystals may be the source of localized stress. The crystallization of an initially amorphous ZrO₂ thin film capped with a-Al₂O₃ produced no stress delamination, so ZrO₂ crystallization alone is not important. Further investigation of the oxidation mechanism requires data on the nucleation and grain growth in ZrB₂ and the potential effects of the presence of the B₂O₃ phase.

7.3.4 Annealing at Temperatures Above 1000 °C

Although the limited structural changes in ZrB_2 films after annealing at 850 °C is encouraging for application as stable electrode materials, there is demand for extending sensor operating temperatures to >1000 °C. Thus, annealing ZrB_2 films at higher temperatures is an important step in this development. A newly acquired BN-graphite heater installed by undergraduate Henry Carfagno in the Auger chamber within the Thin Film Processing Facility is expected to enable vacuum annealing up to ~ 1300 °C. Long term vacuum annealing with this improved heater will certainly promote further grain growth in ZrB_2 and potentially improve high temperature stability, but with its high melting temperature (3245 °C) and excellent adhesion to sapphire substrates, no agglomeration is expected to occur.

Another area to investigate is the measurement of conductivity at these higher temperature using the *in situ* conductivity probe designed by Henry Carfagno. Bulk ZrB_2 is conductive at high temperatures, but *in situ* experiments measuring the conductivity of thin films at temperatures above 700 °C are needed. Typically, the conductivity of metals decreases with temperature due to phonon scattering of the conduction band electrons. The temperature coefficient of resistivity has been measured for bulk ZrB_2 up to 700 °C,³⁸ but it would be valuable to determine the coefficient for ZrB_2 thin films in vacuum at higher temperatures.

7.3.5 Integration of ZrB_2 Films into Sensors

One of the motivations for this thesis work has been the potential application of ZrB_2 as electrodes in wireless SAW devices operating above 1000 °C. ZrB_2 has a lower density and higher elastic modulus than Pt (a typical SAW electrode) and thus prototype SAW devices need to be designed and fabricated to test the functionality of ZrB_2 electrodes. Because of the strong tendency for ZrB_2 films to oxidize in air at high temperatures, the applications of ZrB_2 -based SAW sensors may be in reducing or vacuum environments. The knowledge gained from the investigation of ZrB_2 -based SAW sensors will also have broader impact on other types of high temperature microelectronic sensors and actuator devices.

REFERENCES

- [1] U.S. Energy Information Administration. Monthly energy review, August 2014. DOE/EIA-0035(2016/8), <http://www.eia.gov/totalenergy/data/monthly>.
- [2] PG Neudeck, RS Okojie, and LY Chen. High-temperature electronics-a role for wide bandgap semiconductors? *Proc. IEEE*, 90(6):1065–1076, 2002.
- [3] Gary W. Hunter, Philip G. Neudeck, Robert S. Okojie, et al. An Overview of High-Temperature Electronics and Sensor Development at NASA Glenn Research Center. *J. Turbomach.*, 125(4):658–664, 2003. doi: 10.1115/1.1579508.
- [4] Alex Talevski, Simon Carlsen, and Stig Petersen. Research challenges in applying intelligent wireless sensors in the oil, gas and resources industries. *2009 7th IEEE Int. Conf. Ind. Informatics*, pages 464–469, jun 2009. doi: 10.1109/INDIN.2009.5195848.
- [5] Mauricio Pereira da Cunha, R. J. Lad, T. Moonlight, et al. Recent advances in harsh environment acoustic wave sensors for contemporary applications. In *2011 IEEE SENSORS Proc.*, pages 614–617. Ieee, oct 2011. ISBN 978-1-4244-9289-3. doi: 10.1109/ICSENS.2011.6126948.
- [6] Alfred Pohl. A review of wireless SAW sensors. *IEEE Trans. Ultrason. Ferroelectr. Freq. Control*, 47(2):317–32, jan 2000. doi: 10.1109/58.827416.
- [7] R. M. White and F. W. Voltmer. Direct Piezoelectric Coupling To Surface Elastic Waves. *Appl. Phys. Lett.*, 7(12):314–316, 1965. doi: 10.1063/1.1754276.
- [8] X. Q. Bao, W. Burkhard, V. V. Varadan, and V. K. Varadan. SAW Temperature Sensor and Remote Reading System. In *IEEE 1987 Ultrason. Symp.*, pages 583–586. Ieee, 1987. doi: 10.1109/ULTSYM.1987.199024.
- [9] Fang Li, Dan Xiang, and Shan Chiang. Wireless surface acoustic wave radio frequency identification (SAW-RFID) sensor system for temperature and strain measurements. In *2011 IEEE Int. Ultrason. Symp.*, pages 822–825, 2011. ISBN 9781457712524.
- [10] Kerstin Lange, Bastian E Rapp, and Michael Rapp. Surface acoustic wave biosensors: a review. *Anal. Bioanal. Chem.*, 391(5):1509–19, jul 2008. doi: 10.1007/s00216-008-1911-5.
- [11] D. Richter, S. Sakharov, E. Forsen, et al. Thin Film Electrodes for High Temperature Surface Acoustic Wave Devices. *Procedia Eng.*, 25:168–171, jan 2011. doi: 10.1016/j.proeng.2011.12.042.
- [12] T.R. Beaucage, E.P. Beenfeldt, S.A. Speakman, et al. Comparison of High Temperature Crystal Lattice and Bulk Thermal Expansion Measurements of LGT Single Crystal. In *2006 IEEE Int. Freq. Control Symp. Expo.*, pages 658–663. IEEE, jun 2006. ISBN 1-4244-0074-0. doi: 10.1109/FREQ.2006.275465.
- [13] J. Bezemer and R.T. Jongerius. The melting temperature of platinum measured from continually melting and freezing ribbons. *Phys. B+C*, 83(3):338–346, jul 1976. doi: 10.1016/0378-4363(76)90129-7.

- [14] SK Sharma and J Spitz. Hillock formation, hole growth and agglomeration in thin silver films. *Thin Solid Films*, 65:339–350, 1980.
- [15] WC Maskell. Agglomeration of thin platinum films on a zirconia substrate. *J. Phys. D. Appl. Phys.*, 20:99–104, 1987.
- [16] S.L. Firebaugh, K.F. Jensen, and M.a. Schmidt. Investigation of high-temperature degradation of platinum thin films with an in situ resistance measurement apparatus. *J. Microelectromechanical Syst.*, 7(1):128–135, mar 1998. doi: 10.1109/84.661395.
- [17] R.M. Tiggelaar, R.G.P. Sanders, a.W. Groenland, and J.G.E. Gardeniers. Stability of thin platinum films implemented in high-temperature microdevices. *Sensors Actuators A Phys.*, 152(1):39–47, may 2009. doi: 10.1016/j.sna.2009.03.017.
- [18] Carl V. Thompson. Solid-State Dewetting of Thin Films. *Annu. Rev. Mater. Res.*, 42(1): 399–434, aug 2012. doi: 10.1146/annurev-matsci-070511-155048.
- [19] Scott C. Moulzolf, David J. Frankel, Mauricio Pereira da Cunha, and Robert J. Lad. High temperature stability of electrically conductive PtRh/ZrO₂ and PtRh/HfO₂ nanocomposite thin film electrodes. *Microsyst. Technol.*, 20(4-5):523–531, nov 2013. doi: 10.1007/s00542-013-1974-x.
- [20] Julia C. Sell, David M. Stewart, George P. Bernhardt, David J. Frankel, and Robert J. Lad. Electrically stable nanocomposite thin films formed by oxidation of Pt-ZrB₂ nanolaminate templates. *J. Vac. Sci. Technol. B, Nanotechnol. Microelectron. Mater. Process. Meas. Phenom.*, 33:021805, 2015. doi: 10.1116/1.4914313.
- [21] Wendell S Williams. Transition metal carbides, nitrides, and borides for electronic applications, 1997.
- [22] Wendell S Williams. Electrical properties of hard materials. *Int. J. Refract. Met. Hard Mater.*, 17:21–26, may 1999. doi: 10.1016/S0263-4368(99)00005-0.
- [23] William G. Fahrenholtz, Gregory E. Hilmas, Inna G. Talmy, and James a. Zaykoski. Refractory Diborides of Zirconium and Hafnium. *J. Am. Ceram. Soc.*, 90(5):1347–1364, may 2007. doi: 10.1111/j.1551-2916.2007.01583.x.
- [24] Simon C. Middleburgh, David C. Parfitt, Paul R. Blair, and Robin W. Grimes. Atomic Scale Modeling of Point Defects in Zirconium Diboride. *J. Am. Ceram. Soc.*, 94(7):2225–2229, jul 2011. doi: 10.1111/j.1551-2916.2010.04360.x.
- [25] J Shappirio, J Finnegan, R Lux, D Fox, and J Kwiatkowski. TiB₂ and ZrB₂ diffusion barriers in GaAs Ohmic contact technology. *J. Vac. Sci. Technol. A Vacuum, Surfaces, Film.*, 3(6): 2255, nov 1985. doi: 10.1116/1.572902.
- [26] M Guziewicz, A Piotrowska, E Kamińska, et al. Characteristics of sputter-deposited TiN, ZrB₂ and W₂B diffusion barriers for advanced metallizations to GaAs. *Solid. State. Electron.*, 43(6):1055–1061, jun 1999. doi: 10.1016/S0038-1101(99)00024-6.
- [27] Koichi Momma and Fujio Izumi. VESTA 3 for three-dimensional visualization of crystal, volumetric and morphology data. *J. Appl. Crystallogr.*, 44(6):1272–1276, dec 2011. doi: 10.1107/S0021889811038970.

- [28] International Centre for Diffraction Data. Card number 034-0423, Powder Diffraction File, 2013.
- [29] International Centre for Diffraction Data, 2014. Card number 04-0802, Powder Diffraction File.
- [30] A. E. McHale, editor. *Data Collected from Phase Diagrams for Ceramists*, volume X. American Ceramic Society, Westerville, OH, 1994.
- [31] P. Vajeeston, P. Ravindran, C. Ravi, and R. Asokamani. Electronic structure, bonding, and ground-state properties of AlB_2 -type transition-metal diborides. *Phys. Rev. B*, 63(4):045115, 2001. doi: 10.1103/PhysRevB.63.045115.
- [32] M. W. Chase. NIST-JANAF Thermochemical Tables, 4th Edition. *J. Phys. Chem. Ref. Data Monogr.*, 1988.
- [33] Seungmin Hyun, Oliver Kraft, and Richard P Vinci. Mechanical behavior of Pt and Pt–Ru solid solution alloy thin films. *Acta Mater.*, 52(14):4199–4211, aug 2004. doi: 10.1016/j.actamat.2004.05.034.
- [34] AL Chamberlain, WG Fahrenholtz, GE Hilmas, and DT Ellerby. High-strength zirconium diboride-based ceramics. *J. Am. Ceram. Soc.*, 87(6):1170–1172, 2004.
- [35] C. Y. Ho, R W Powell, and P E Liley. Thermal conductivity of the elements. *J. Phys. Chem. Ref. Data*, 1(2):279–421, 1972.
- [36] David R Lide, editor. *Handbook of Chemistry and Physics*. CRC Press Inc., 71st edition, 1990.
- [37] Charles Kittel. *Introduction to Solid State Physics*. John Wiley & Sons, 8th edition, 2005. ISBN 0-471-41526.
- [38] Luning Zhang, Dušan a. Pejaković, Jochen Marschall, and Matthew Gasch. Thermal and Electrical Transport Properties of Spark Plasma-Sintered HfB_2 and ZrB_2 Ceramics. *J. Am. Ceram. Soc.*, 94(8):2562–2570, aug 2011. doi: 10.1111/j.1551-2916.2011.04411.x.
- [39] Raymond A. Serway. *Principles of Physics*. Saunders College Pub., Fort Worth, TX, 2nd edition, 1988. ISBN 0-03-020457-7.
- [40] Mark M Opeka, Inna G Talmy, and James A Zaykoski. Oxidation-based materials selection for 2000C + hypersonic aerosurfaces : Theoretical considerations and historical experience. *J. Mater. Sci.*, 39:5887–5904, 2004.
- [41] Fei Peng and Robert F. Speyer. Oxidation Resistance of Fully Dense ZrB_2 with SiC, TaB_2 , and $TaSi_2$ Additives. *J. Am. Ceram. Soc.*, 91(5):1489–1494, may 2008. doi: 10.1111/j.1551-2916.2008.02368.x.
- [42] Dongwoo Lee, Gi-Dong Sim, Kechao Xiao, and Joost J. Vlassak. Low-Temperature Synthesis of Ultra-High-Temperature Coatings of ZrB_2 Using Reactive Multilayers. *J. Phys. Chem. C*, 118(36):21192–21198, sep 2014. doi: 10.1021/jp505941g.
- [43] Mattias Samuelsson, Jens Jensen, Ulf Helmersson, Lars Hultman, and Hans Höglberg. ZrB_2 thin films grown by high power impulse magnetron sputtering from a compound target. *Thin Solid Films*, 526:163–167, dec 2012. doi: 10.1016/j.tsf.2012.11.006.

- [44] J.R. Shappirio and J.J. Finnegan. Synthesis and properties of some refractory transition metal diboride thin films. *Thin Solid Films*, 107(1):81–87, sep 1983. doi: 10.1016/0040-6090(83)90010-X.
- [45] Gi-Dong Sim, Yong Seok Choi, Dongwoo Lee, Kyu Hwan Oh, and Joost J. Vlassak. High tensile strength of sputter-deposited ZrB₂ ceramic thin films measured up to 1016 K. *Acta Mater.*, 113:32–40, 2016. doi: 10.1016/j.actamat.2016.04.047.
- [46] Lina Tengdelius, Mattias Samuelsson, Jens Jensen, et al. Direct current magnetron sputtered ZrB₂ thin films on 4H-SiC(0001) and Si(100). *Thin Solid Films*, 550:285–290, jan 2014. doi: 10.1016/j.tsf.2013.11.040.
- [47] Christian Mitterer. Borides in Thin Film Technology. *J. Solid State Chem.*, 133(1):279–291, oct 1997. doi: 10.1006/jssc.1997.7456.
- [48] E. Randich and D.D. Allred. Chemically vapor-deposited ZrB₂ as a selective solar absorber. *Thin Solid Films*, 83(4):393–398, sep 1981. doi: 10.1016/0040-6090(81)90646-5.
- [49] A. De Bonis, A. Santagata, J.V. Rau, et al. Two-phase zirconium boride thin film obtained by ultra-short pulsed laser ablation of a ZrB₁₂ target. *Appl. Surf. Sci.*, 283:715–721, oct 2013. doi: 10.1016/j.apsusc.2013.06.169.
- [50] Xinghong Zhang, Xiaoguang Luo, Jiecai Han, Jinping Li, and Wenbo Han. Electronic structure, elasticity and hardness of diborides of zirconium and hafnium: First principles calculations. *Comput. Mater. Sci.*, 44(2):411–421, dec 2008. doi: 10.1016/j.commatsci.2008.04.002.
- [51] Hui Li, Litong Zhang, Qingfeng Zeng, et al. Crystal structure and elastic properties of ZrB compared with ZrB₂: A first-principles study. *Comput. Mater. Sci.*, 49(4):814–819, oct 2010. doi: 10.1016/j.commatsci.2010.06.027.
- [52] Wendell S Williams. The thermal conductivity of metallic ceramics. *JOM*, (June):62–66, 1998.
- [53] Karlheinz Schwarz. Band structure and chemical bonding in transition metal carbides and nitrides. *Crit. Rev. Solid State Mater. Sci.*, 13(March 2013):37–41, 1987.
- [54] P. I. Ignatenko and N. P. Ivanitsyn. Kinetics of the formation and growth of critical nuclei in nanostructured films of borides, nitrides, and silicides. *Phys. Solid State*, 54(12):2503–2507, dec 2012. doi: 10.1134/S1063783412120153.
- [55] H.M. Chen, F. Zheng, H.S. Liu, L.B. Liu, and Z.P. Jin. Thermodynamic assessment of B-Zr and Si-Zr binary systems. *J. Alloys Compd.*, 468(1-2):209–216, jan 2009. doi: 10.1016/j.jallcom.2008.01.061.
- [56] Hideo Ihara, Masayuki Hirabayashi, and Hiroshi Nakagawa. Band structure and x-ray photoelectron spectrum of ZrB₂. *Phys. Rev. B*, 16(2):726–730, 1977.
- [57] V Milman, B Winkler, and M I J Probert. Stiffness and thermal expansion of ZrB₂: an ab initio study. *J. Phys. Condens. Matter*, 17(13):2233–2241, 2005. doi: 10.1088/0953-8984/17/13/019.
- [58] Norihiko L. Okamoto, Misato Kusakari, Katsushi Tanaka, et al. Temperature dependence of thermal expansion and elastic constants of single crystals of ZrB₂ and the suitability of ZrB₂ as a substrate for GaN film. *J. Appl. Phys.*, 93(1):88–93, 2003. doi: 10.1063/1.1525404.

- [59] David C. Miller, Ross R. Foster, Shih-Hui Jen, et al. Thermo-mechanical properties of alumina films created using the atomic layer deposition technique. *Sensors Actuators A Phys.*, 164(1-2):58–67, 2010. doi: 10.1016/j.sna.2010.09.018.
- [60] V. Yu. Bodryakov and A. A. Bykov. Correlation Characteristics of the Volumetric Thermal Expansion Coefficient and Specific Heat of Corundum. *Glas. Ceram.*, 72(1-2):67–70, 2015. doi: 10.1007/s10717-015-9726-2.
- [61] J. Kräußlich, S. Höfer, U. Zastrau, N. Jeutter, and C. Baetz. Temperature dependence of lattice parameters of langasite single crystals. *Cryst. Res. Technol.*, 45(5):490–492, 2010. doi: 10.1002/crat.201000034.
- [62] D.C. Malocha, H. Francois-Saint-Cyr, Kathleen Richardson, and Robert Helmbold. Measurements of LGS, LGN, and LGT thermal coefficients of expansion and density. *IEEE Trans. Ultrason. Ferroelectr. Freq. Control*, 49(3):350–355, mar 2002. doi: 10.1109/58.990952.
- [63] I. B. Ban'kovskaya, I. a. Vasilyeva, and D. V. Kolovertnov. Oxidation processes in a silicon-boron-zirconium boride composite in the temperature range 1000-1300 C. *Glas. Phys. Chem.*, 38(3):327–331, may 2012. doi: 10.1134/S1087659612030030.
- [64] Young-Hoon Seong and Do Kyung Kim. Oxidation behavior of ZrB₂-xSiC composites at 1500C under different oxygen partial pressures. *Ceram. Int.*, 40(9):15303–15311, nov 2014. doi: 10.1016/j.ceramint.2014.07.036.
- [65] T.a. Parthasarathy, R.a. Rapp, M. Opeka, and R.J. Kerans. A model for the oxidation of ZrB₂, HfB₂ and TiB₂. *Acta Mater.*, 55(17):5999–6010, oct 2007. doi: 10.1016/j.actamat.2007.07.027.
- [66] Maryam Kazemzadeh Dehdashti, William G. Fahrenholtz, and Greg E. Hilmas. Oxidation of zirconium diboride with niobium additions. *J. Eur. Ceram. Soc.*, 33(10):1591–1598, sep 2013. doi: 10.1016/j.jeurceramsoc.2013.01.033.
- [67] V O Lavrenko, A D Panasyuk, O M Grigorev, O V Koroteev, and V A Kotenko. High-temperature (to 1600C) oxidation of ZrB₂-MoSi₂ ceramics in air. *Powder Metall. Met. Ceram.*, 51(1-2):102–107, may 2012. doi: 10.1007/s11106-012-9403-8.
- [68] V O Lavrenko, A D Panasyuk, O M Grigorev, O V Koroteev, and V A Kotenko. High-temperature oxidation of ZrB₂-SiC and ZrB₂-SiC-ZrSi₂ ceramics up to 1700C in air. *Powder Metall. Met. Ceram.*, 51(3-4):217–221, jul 2012. doi: 10.1007/s11106-012-9420-7.
- [69] Ju Li, Thomas J. Lenosky, Clemens J Forst, and Sidney Yip. Thermochemical and Mechanical Stabilities of the Oxide Scale of ZrB₂ + SiC and Oxygen Transport Mechanisms. *J. Am. Ceram. Soc.*, 1480(5):1475–1480, 2008. doi: 10.1111/j.1551-2916.2008.02319.x.
- [70] Alireza Rezaie, William G. Fahrenholtz, and Gregory E. Hilmas. Oxidation of Zirconium Diboride-Silicon Carbide at 1500C at a Low Partial Pressure of Oxygen. *J. Am. Ceram. Soc.*, 89(10):3240–3245, oct 2006. doi: 10.1111/j.1551-2916.2006.01229.x.
- [71] P.J. Ritt, P.A. Williams, S.C. Splinter, and J.H. Perepezko. Arc jet testing and evaluation of MoSiB coated Mo and SiCZrB₂ ceramics. *J. Eur. Ceram. Soc.*, 34(15):3521–3533, dec 2014. doi: 10.1016/j.jeurceramsoc.2014.06.011.

- [72] Andrew Rosenberger, Lia Stanciu, and Bruna Callegari. ZrB₂-SiC and ZrB₂-ZrC Ceramics with High Secondary Phase Content. *Int. J. Appl. Ceram. Technol.*, 12:E44–E52, may 2015. doi: 10.1111/ijac.12217.
- [73] Diletta Sciti, Mylène Brach, and Alida Bellosi. Long-term oxidation behavior and mechanical strength degradation of a pressurelessly sintered ZrB₂-MoSi₂ ceramic. *Scr. Mater.*, 53(11):1297–1302, dec 2005. doi: 10.1016/j.scriptamat.2005.07.026.
- [74] Diletta Sciti, Frédéric Monteverde, Stefano Guicciardi, Giuseppe Pezzotti, and Alida Bellosi. Microstructure and mechanical properties of ZrB₂-MoSi₂ ceramic composites produced by different sintering techniques. *Mater. Sci. Eng. A*, 434(1-2):303–309, oct 2006. doi: 10.1016/j.msea.2006.06.112.
- [75] Laura Silvestroni, Giacomo Meriggi, and Diletta Sciti. Oxidation behavior of ZrB₂ composites doped with various transition metal silicides. *Corros. Sci.*, 83:281–291, jun 2014. doi: 10.1016/j.corsci.2014.02.026.
- [76] Yiguang Wang, Lei Luo, Jing Sun, and Linan An. ZrB₂-SiC(Al) ceramics with high resistance to oxidation at 1500C. *Corros. Sci.*, 74:154–158, sep 2013. doi: 10.1016/j.corsci.2013.04.037.
- [77] Rubing Zhang, Xiangmeng Cheng, Daining Fang, Liaoliang Ke, and Yuesheng Wang. Ultra-high-temperature tensile properties and fracture behavior of ZrB₂-based ceramics in air above 1500C. *Mater. Des.*, 52:17–22, dec 2013. doi: 10.1016/j.matdes.2013.05.045.
- [78] Amir Pakdel, Yoshio Bando, and Dmitri Golberg. Nano boron nitride flatland. *Chem. Soc. Rev.*, 43(3):934–59, 2014. doi: 10.1039/c3cs60260e.
- [79] Nathan S. Jacobson, Gregory N. Morscher, Darren R. Bryant, and Richard E. Tressler. High-Temperature Oxidation of Boron Nitride: II, Boron Nitride Layers in Composites. *J. Am. Ceram. Soc.*, 82(6):1473–1482, dec 1999. doi: 10.1111/j.1151-2916.1999.tb01944.x.
- [80] Xuemei Li, Jun Yin, Jianxin Zhou, and Wanlin Guo. Large area hexagonal boron nitride monolayer as efficient atomically thick insulating coating against friction and oxidation. *Nanotechnology*, 25(10):105701, mar 2014. doi: 10.1088/0957-4484/25/10/105701.
- [81] Zheng Liu, Yongji Gong, Wu Zhou, et al. Ultrathin high-temperature oxidation-resistant coatings of hexagonal boron nitride. *Nat. Commun.*, 4(May):2541, jan 2013. doi: 10.1038/ncomms3541.
- [82] Min Yi, Zhigang Shen, Lei Liu, and Shuaishuai Liang. Size-selected boron nitride nanosheets as oxygen-atom corrosion resistant fillers. *RSC Adv.*, 5(4):2983–2987, dec 2014. doi: 10.1039/C4RA09156F.
- [83] J. N. Coleman, M. Lotya, A. O'Neill, et al. Two-Dimensional Nanosheets Produced by Liquid Exfoliation of Layered Materials. *Science (80-.)*, 331(6017):568–571, 2011. doi: 10.1126/science.1194975.
- [84] Mihnea Ioan Ionescu, Xueliang Sun, and Ben Luan. Multilayer graphene synthesized using magnetron sputtering for planar supercapacitor application. *Can. J. Chem.*, 93(2):160–164, feb 2015. doi: 10.1139/cjc-2014-0297.
- [85] Stephan Roche. Theoretical Spectroscopy of Boron Nitride Nanotubes and Graphene. 2009.

- [86] International Centre for Diffraction Data, 2016. Card number 04-003-6253, Powder Diffraction File.
- [87] International Centre for Diffraction Data, 2016. Card number 056-0159, Powder Diffraction File.
- [88] Yumeng Shi, Christoph Hamsen, Xiaoting Jia, et al. Synthesis of few-layer hexagonal boron nitride thin film by chemical vapor deposition. *Nano Lett.*, 10(10):4134–4139, 2010. doi: 10.1021/nl1023707.
- [89] Atsushi Anzai, Fumitaka Nishiyama, Shoji Yamanaka, and Kei Inumaru. Thin film growth of boron nitride on α -Al₂O₃ (001) substrates by reactive sputtering. *Mater. Res. Bull.*, 46(12):2230–2234, 2011. doi: 10.1016/j.materresbull.2011.09.006.
- [90] S. Reich, A. Ferrari, R. Arenal, et al. Resonant Raman scattering in cubic and hexagonal boron nitride. *Phys. Rev. B*, 71(20):1–12, 2005. doi: 10.1103/PhysRevB.71.205201.
- [91] Jun Hua Meng, Xing Wang Zhang, Hao Lin Wang, et al. Synthesis of in-plane and stacked graphene/hexagonal boron nitride heterostructures by combining with ion beam sputtering deposition and chemical vapor deposition. *Nanoscale*, 7(38):16046–16053, 2015. doi: 10.1039/C5NR04490A.
- [92] Andrei G F Garcia, Michael Neumann, François Amet, et al. Effective cleaning of hexagonal boron nitride for graphene devices. *Nano Lett.*, 12(9):4449–54, 2012. doi: 10.1021/nl3011726.
- [93] Qi Han, Baoming Yan, Teng Gao, et al. Boron nitride film as a buffer layer in deposition of dielectrics on graphene. *Small*, 10(11):2293–9, 2014. doi: 10.1002/smll.201303697.
- [94] Willi Auwärter, Hans Ulrich Suter, Hermann Sachdev, and Thomas Greber. Synthesis of One Monolayer of Hexagonal Boron Nitride on Ni(111) from B-Trichloroborazine (CIBNH)₃. *Chem. Mater.*, 16(2):343–345, 2004. doi: 10.1021/cm034805s.
- [95] Majharul Haque Khan, Zhenguo Huang, Feng Xiao, et al. Synthesis of Large and Few Atomic Layers of Hexagonal Boron Nitride on Melted Copper. *Sci. Rep.*, 5:7743, jan 2015. doi: 10.1038/srep07743.
- [96] Ki Kang Kim, Allen Hsu, Xiaoting Jia, et al. Synthesis of Monolayer Hexagonal Boron Nitride on Cu Foil Using Chemical Vapor Deposition. *Nano Lett.*, 12(1):161–166, jan 2012. doi: 10.1021/nl203249a.
- [97] P.B. Mirkarimi, K.F. McCarty, and D.L. Medlin. Review of advances in cubic boron nitride film synthesis. *Mater. Sci. Eng. R Reports*, 21(2):47–100, 1997. doi: 10.1016/S0927-796X(97)00009-0.
- [98] G. Kern, G. Kresse, and J. Hafner. Ab initio calculation of the lattice dynamics and phase diagram of boron nitride. *Phys. Rev. B*, 59(13):8551–8559, apr 1999. doi: 10.1103/PhysRevB.59.8551.
- [99] Vladimir L. Solozhenko, Vladimir Z. Turkevich, and Wilfried B. Holzapfel. Refined Phase Diagram of Boron Nitride. *J. Phys. Chem. B*, 103(15):2903–2905, 1999. doi: 10.1021/jp984682c.

- [100] W. J. Yu, W. M. Lau, S. P. Chan, Z. F. Liu, and Q. Q. Zheng. Ab initio study of phase transformations in boron nitride. *Phys. Rev. B*, 67(1):014108, jan 2003. doi: 10.1103/PhysRevB.67.014108.
- [101] Pavel B Sorokin, Alexander G Kvashnin, Zhen Zhu, and David Tománek. Spontaneous Graphitization of Ultrathin Cubic Structures: A Computational Study. *Nano Lett.*, 14(12): 7126–7130, 2014. doi: 10.1021/nl503673q.
- [102] Nathan Jacobson, Serene Farmer, Arthur Moore, and Haluk Sayir. High-Temperature Oxidation of Boron Nitride: I, Monolithic Boron Nitride. *J. Am. Ceram. Soc.*, 82(2):393–398, dec 1999. doi: 10.1111/j.1551-2916.1999.tb20075.x.
- [103] Yu Zhao, Xiaojun Wu, Jinlong Yang, and Xiao Cheng Zeng. Oxidation of a two-dimensional hexagonal boron nitride monolayer: a first-principles study. *Phys. Chem. Chem. Phys.*, 14(16):5545–50, apr 2012. doi: 10.1039/c2cp40081b.
- [104] Ignacio Caretti and Ignacio Jiménez. Point defects in hexagonal BN, BC₃ and BC_xN compounds studied by x-ray absorption near-edge structure. *J. Appl. Phys.*, 110(2), 2011. doi: 10.1063/1.3602996.
- [105] Nikolaos Kostoglou, Kyriaki Polychronopoulou, and Claus Rebholz. Thermal and chemical stability of hexagonal boron nitride (h-BN) nanoplatelets. *Vacuum*, 112:42–45, 2015. doi: 10.1016/j.vacuum.2014.11.009.
- [106] Xinmei Hou, Ziyu Yu, Zhiyuan Chen, Kuo Chih Chou, and Baojun Zhao. The reaction mechanism and kinetics of α -BN powder in wet air at 1273 K. *J. Am. Ceram. Soc.*, 96(6): 1877–1882, 2013. doi: 10.1111/jace.12276.
- [107] Wang Guangwei, Liu Yanxiang, Zhang Jianliang, Chou Kuo-chih, and Hou Xinmei. Reaction of CVD BN ceramics in water vapor at 1023 - 1173 K using different kinetic model. *J. Ceram. Soc. Japan*, 122(1430):889–894, 2014. doi: 10.2109/jcersj2.122.889.
- [108] Kohei Oda, Kaoru Aoki, Satoshi Inada, Masahiro Nagae, and Tetsuo Yoshio. Oxidation of Boron Nitride Powder in Wet Oxygen. *J. Ceram. Soc. Japan*, 1:81–82, 2003.
- [109] Hou Xinmei, Liu Yanxiang, Yu Ziyu, and Chou Kuo-Chih. Effect of temperature on reaction of hexagonal BN powder in wet air between 1073 and 1373 k. *Int. J. Appl. Ceram. Technol.*, 12(S2):E138–E145, 2015. doi: 10.1111/ijac.12259.
- [110] Nicholas R. Glavin, Michael L. Jespersen, Michael H. Check, et al. Synthesis of few-layer, large area hexagonal-boron nitride by pulsed laser deposition. *Thin Solid Films*, 572:245–250, dec 2014. doi: 10.1016/j.tsf.2014.07.059.
- [111] Muhammad Sajjad, Majid Ahmadi, Maxime J F Guinel, Yi Lin, and Peter Feng. Large scale synthesis of single-crystal and polycrystalline boron nitride nanosheets. *J. Mater. Sci.*, 48(6): 2543–2549, 2013. doi: 10.1007/s10853-012-7044-4.
- [112] P. Sutter, J. Lahiri, P. Zahl, B. Wang, and E. Sutter. Scalable synthesis of uniform few-layer hexagonal boron nitride dielectric films. *Nano Lett.*, 13(1):276–281, jan 2013. doi: 10.1021/nl304080y.

- [113] Chuanbin Wang, Xiaoshuang Luo, Song Zhang, Qiang Shen, and Lianmeng Zhang. Effects of nitrogen gas ratio on magnetron sputtering deposited boron nitride films. *Vacuum*, 103: 68–71, 2014. doi: 10.1016/j.vacuum.2013.12.009.
- [114] Xiaokang Zhang, Jinxiang Deng, Ling Wang, et al. Phase transformation in BN films by nitrogen-protected annealing at atmospheric pressure. *Appl. Surf. Sci.*, 254(21):7109–7113, 2008. doi: 10.1016/j.apsusc.2008.05.224.
- [115] D. M. Zhu, G. Jakovidis, and L. Bourgeois. Catalyst-free synthesis of carbon and boron nitride nanoflakes using RF-magnetron sputtering. *Mater. Lett.*, 64(8):918–920, 2010. doi: 10.1016/j.matlet.2010.01.058.
- [116] B BenMoussa, J D’Haen, C Borschel, et al. Hexagonal boron nitride nanowalls: physical vapour deposition, 2D/3D morphology and spectroscopic analysis. *J. Phys. D. Appl. Phys.*, 45(13):135302, 2012. doi: 10.1088/0022-3727/45/13/135302.
- [117] S. Bornholdt, J. Ye, S. Ulrich, and H. Kersten. Energy fluxes in a radio-frequency magnetron discharge for the deposition of superhard cubic boron nitride coatings. *J. Appl. Phys.*, 112(12), 2012. doi: 10.1063/1.4769800.
- [118] L Camilli, E Sutter, and P Sutter. Growth of two-dimensional materials on non-catalytic substrates: h-BN/Au(111). *2D Mater.*, 1(2):025003, 2014. doi: 10.1088/2053-1583/1/2/025003.
- [119] Olivier Cometto, Bo Sun, Siu Hon Tsang, et al. Vertically self-ordered orientation of nanocrystalline hexagonal boron nitride thin films for enhanced thermal characteristics. *Nanoscale*, 7(45):18984–18991, 2015. doi: 10.1039/C5NR05009J.
- [120] D. J. Kester, K. S. Ailey, D. J. Lichtenwalner, and R. F. Davis. Growth and characterization of cubic boron nitride thin films. *J. Vac. Sci. Technol. A Vacuum, Surfaces, Film.*, 12(6):3074, nov 1994. doi: 10.1116/1.578938.
- [121] D.J. Kester, K.S. Ailey, and R.F. Davis. Deposition and characterization of boron nitride thin films. *Diam. Relat. Mater.*, 3(4-6):332–336, apr 1994. doi: 10.1016/0925-9635(94)90181-3.
- [122] M.J. Paisley and R.F. Davis. Photo-induced phase inhibition during growth of boron nitride thin films. *Mater. Sci. Eng. B*, 18(3):275–280, apr 1993. doi: 10.1016/0921-5107(93)90143-B.
- [123] DJ Kester, KS Ailey, R.F. Davis, and K.L. More. Phase evolution in boron nitride thin films. *J. Mater. Res.*, 8(06):1213–1216, jun 1993. doi: 10.1557/JMR.1993.1213.
- [124] Ignacio Jiménez, Ricardo Torres, Ignacio Caretti, Raul Gago, and Jose María Albella. A review of monolithic and multilayer coatings within the boroncarbonnitrogen system by ion-beam-assisted deposition. *J. Mater. Res.*, 27(05):743–764, mar 2012. doi: 10.1557/jmr.2011.398.
- [125] J. Thomas, N. E. Weston, and T. E. O’Connor. Turbostratic Boron Nitride, Thermal Transformation to Ordered-layer-lattice Boron Nitride. *J. Am. Chem. Soc.*, 84(24):4619–4622, dec 1962. doi: 10.1021/ja00883a001.
- [126] A. Lipp, K.A. Schwetz, and K. Hunold. Hexagonal boron nitride: Fabrication, properties and applications. *J. Eur. Ceram. Soc.*, 5(1):3–9, jan 1989. doi: 10.1016/0955-2219(89)90003-4.

- [127] P C Yang, J T Prater, W Liu, J T Glass, and R F Davis. The formation of epitaxial hexagonal boron nitride on nickel substrates. *J. Electron. Mater.*, 34(12):1558–1564, dec 2005. doi: 10.1007/s11664-005-0165-7.
- [128] E.-S. Lee, J.-K. Park, W.-S. Lee, T.-Y. Seong, and Y.-J. Baik. Effect of deposition temperature on the alignment of hexagonal laminates in turbostratic boron nitride thin film. *Surf. Coatings Technol.*, 242:29–33, mar 2014. doi: 10.1016/j.surfcoat.2014.01.008.
- [129] Riikka L. Puurunen. Surface chemistry of atomic layer deposition: A case study for the trimethylaluminum/water process. *J. Appl. Phys.*, 97(12):1–52, 2005. doi: 10.1063/1.1940727.
- [130] M.L. Chang, L.C. Wang, H.C. Lin, M.J. Chen, and K.M. Lin. Investigation of defects in ultra-thin Al₂O₃ films deposited on pure copper by the atomic layer deposition technique. *Appl. Surf. Sci.*, 359:533–542, dec 2015. doi: 10.1016/j.apsusc.2015.10.144.
- [131] John F. O’Hanlon. *A User’s Guide to Vacuum Technology*. Wiley-Interscience, New York, 2nd edition, 1989. ISBN 0-471-81242-0.
- [132] S. C. Moulzolf, D. J. Frankel, and R. J. Lad. In situ four-point conductivity and Hall effect apparatus for vacuum and controlled atmosphere measurements of thin film materials. *Rev. Sci. Instrum.*, 73(6):2325, 2002. doi: 10.1063/1.1475349.
- [133] YK Lee. Thermal stability and interfacial reaction of TiB_x films deposited on (100) Si by dual-electron-beam evaporation. *J. Cryst. Growth*, 246:113–120, 2002.
- [134] Donald L. Smith. *Thin-Film Deposition*. McGraw-Hill, Boston, 1995. ISBN 0-07-058502-4.
- [135] J. G. Miller. Acoustic Wave Analysis of the Operation of Quartz-Crystal Film-Thickness Monitors. *J. Appl. Phys.*, 39(12):5815, 1968. doi: 10.1063/1.1656066.
- [136] Chih-Shun Lu and Owen Lewis. Investigation of film-thickness determination by oscillating quartz resonators with large mass load. *J. Appl. Phys.*, 43(11):4385, 1972. doi: 10.1063/1.1660931.
- [137] David Stewart, 2015. IC5-DRMU software, in development. <https://github.com/amstewart/IC5-DRMU>.
- [138] S. Berg and T. Nyberg. Fundamental understanding and modeling of reactive sputtering processes. *Thin Solid Films*, 476(2):215–230, apr 2005. doi: 10.1016/j.tsf.2004.10.051.
- [139] Daniel Lundin and Kostas Sarakinos. An introduction to thin film processing using high-power impulse magnetron sputtering. *J. Mater. Res.*, 27(05):780–792, feb 2012. doi: 10.1557/jmr.2012.8.
- [140] W.D. Sproul, D.J. Christie, and D.C. Carter. Control of reactive sputtering processes. *Thin Solid Films*, 491(1-2):1–17, nov 2005. doi: 10.1016/j.tsf.2005.05.022.
- [141] Rong-Fu Xiao and Nai-Ben Ming. Surface roughening and surface diffusion in kinetic thin-film deposition. *Phys. Rev. E*, 49(5):4720–4723, may 1994. doi: 10.1103/PhysRevE.49.4720.
- [142] K.F. McCarty, P.B. Mirkarimi, D.L. Medlin, T.A. Friedmann, and J.C. Barbour. On the low-temperature threshold for cubic boron nitride formation in energetic film deposition. *Diam. Relat. Mater.*, 5(12):1519–1526, 1996. doi: 10.1016/S0925-9635(96)00580-8.

- [143] Z.H. Xu, L. Yuan, D.B. Shan, and B. Guo. A molecular dynamics simulation of TiN film growth on TiN(001). *Comput. Mater. Sci.*, 50(4):1432–1436, feb 2011. doi: 10.1016/j.commatsci.2010.11.030.
- [144] Xian Chen, Yan-Wu Wang, Xin Liu, et al. Molecular dynamics study of the effect of titanium ion energy on surface structure during the amorphous TiO₂ films deposition. *Appl. Surf. Sci.*, 345:162–168, aug 2015. doi: 10.1016/j.apsusc.2015.03.183.
- [145] A. Hassani, A. Makan, K. Sbiaai, A. Tabyaoui, and A. Hasnaoui. Molecular dynamics study of growth and interface structure during aluminum deposition on Ni(100) substrate. *Appl. Surf. Sci.*, 349:785–791, sep 2015. doi: 10.1016/j.apsusc.2015.05.076.
- [146] David J. Griffiths. *Introduction to Quantum Mechanics*. Pearson Prentice Hall, Upper Saddle River, 2nd edition, 2005. ISBN 0-13-111892-7.
- [147] M. P. Seah. Summary of ISO/TC 201 standard: VII ISO 15472 : 2001 - surface chemical analysis - x-ray photoelectron spectrometers - calibration of energy scales. *Surf. Interface Anal.*, 31(8):721–723, 2001. doi: 10.1002/sia.1076.
- [148] D. Briggs and M. P. Seah, editors. *Practical Surface Analysis*. John Wiley and Sons, Chichester, 1983. ISBN 0-471-26279-X.
- [149] Gerhard Ertl and Jurgen Koppers. *Low Energy Electrons and Surface Chemistry*. VCH Verlagsgesellschaft, Weinheim, 2nd edition, 1985. ISBN 3-527-26056-0.
- [150] C. J. Powell. Growth and trends in Auger-electron spectroscopy and x-ray photoelectron spectroscopy for surface analysis. *J. Vac. Sci. Technol. A Vacuum, Surfaces, Film.*, 21(5): S42, 2003. doi: 10.1116/1.1599862.
- [151] Chun-kwei Wu, Ming Yin, Stephen O’Brien, and Jeffrey T Koberstein. Quantitative Analysis of Copper Oxide Nanoparticle Composition and Structure by X-ray Photoelectron Spectroscopy. *Chem. Mater.*, 18(25):6054–6058, 2006. doi: 10.1021/cm061596d.
- [152] C.J. Powell and A. Jablonski. Progress in quantitative surface analysis by X-ray photoelectron spectroscopy: Current status and perspectives. *J. Electron Spectros. Relat. Phenomena*, 178-179:331–346, may 2010. doi: 10.1016/j.elspec.2009.05.004.
- [153] P. D. Kirsch and J. G. Ekerdt. Chemical and thermal reduction of thin films of copper (II) oxide and copper (I) oxide. *J. Appl. Phys.*, 90(8):4256–4264, 2001. doi: 10.1063/1.1403675.
- [154] Mark C. Biesinger, Brad P. Payne, Leo W. M. Lau, Andrea Gerson, and Roger St. C. Smart. X-ray photoelectron spectroscopic chemical state quantification of mixed nickel metal, oxide and hydroxide systems. *Surf. Interface Anal.*, 41(4):324–332, apr 2009. doi: 10.1002/sia.3026.
- [155] Sven Tougaard. Surface nanostructure determination by x-ray photoemission spectroscopy peak shape analysis. *J. Vac. Sci. Technol. A Vacuum, Surfaces, Film.*, 14(3):1415, may 1996. doi: 10.1116/1.579963.
- [156] Shaaker Hajati and Sven Tougaard. XPS for non-destructive depth profiling and 3D imaging of surface nanostructures. *Anal. Bioanal. Chem.*, 396(8):2741–55, apr 2010. doi: 10.1007/s00216-009-3401-9.

- [157] Shaaker Hajati, John Walton, and Sven Tougaard. Three-dimensional X-ray photoelectron tomography on the nanoscale: limits of data processing by principal component analysis. *Microsc. Microanal.*, 19(3):751–60, jun 2013. doi: 10.1017/S1431927613000354.
- [158] C. J. Powell. Precision, accuracy, and uncertainty in quantitative surface analyses by Auger-electron spectroscopy and x-ray photoelectron spectroscopy. *J. Vac. Sci. Technol. A Vacuum, Surfaces, Film.*, 8(2):735, mar 1990. doi: 10.1116/1.576956.
- [159] K. Harrison and L. B. Hazell. The determination of uncertainties in quantitative XPS/AES and its impact on data acquisition strategy. *Surf. Interface Anal.*, 18(5):368–376, may 1992. doi: 10.1002/sia.740180510.
- [160] P. J. Cumpson and M. P. Seah. Random uncertainties in AES and XPS: I: Uncertainties in peak energies, intensities and areas derived from peak synthesis. *Surf. Interface Anal.*, 18(5): 345–360, may 1992. doi: 10.1002/sia.740180508.
- [161] C. J. Powell and J. M. Conny. Evaluation of uncertainties in X-ray photoelectron spectroscopy intensities associated with different methods and procedures for background subtraction. I. spectra for monochromatic al X-ray. *Surf. Interface Anal.*, 41(4):269–294, apr 2009. doi: 10.1002/sia.2995.
- [162] T. Sagara, L. Boesten, S. Nishida, and K. Okada. Resolution improvements for hemispherical energy analyzers. *Rev. Sci. Instrum.*, 71(11):4201, 2000. doi: 10.1063/1.1319979.
- [163] T.J.M. Zouros. Theoretical investigation of the energy resolution of an ideal hemispherical deflector analyzer and its dependence on the distance from the focal plane. *J. Electron Spectros. Relat. Phenomena*, 152(1-2):67–77, jun 2006. doi: 10.1016/j.elspec.2006.03.007.
- [164] E. P. Benis and T. J. M. Zouros. The hemispherical deflector analyser revisited. *J. Electron Spectros. Relat. Phenomena*, 163(1-3):28–39, apr 2008. doi: 10.1016/j.elspec.2008.02.001.
- [165] J. D. Lee. A Nondispersive Electron Energy Analyzer for ESCA. *Rev. Sci. Instrum.*, 44(7): 893, 1973. doi: 10.1063/1.1686272.
- [166] C. L. Allyn, T. Gustafsson, and E. W. Plummer. Analyzer system capable of determining energy and direction of charged particles in ultrahigh vacuum. *Rev. Sci. Instrum.*, 49(8): 1197, 1978. doi: 10.1063/1.1135547.
- [167] S Oswald and R Reiche. Binding state information from XPS depth profiling: capabilities and limits. *Appl. Surf. Sci.*, 179:307–315, 2001.
- [168] Peter J. Cumpson. Angle-resolved XPS and AES: Depth-resolution limits and a general comparison of properties of depth-profile reconstruction methods. *J. Electron Spectros. Relat. Phenomena*, 73(1):25–52, may 1995. doi: 10.1016/0368-2048(94)02270-4.
- [169] Peter J. Cumpson and Martin P Seah. Elastic Scattering Corrections in AES and XPS. II. Estimating Attenuation Lengths and Conditions Required for their Valid Use in Overlay/Substrate Experiments. *Surf. Interface Anal.*, 25(6):430–446, jun 1997. doi: 10.1002/(SICI)1096-9918(199706)25:6<430::AID-SIA254>3.0.CO;2-7.
- [170] S. Tanuma, C. J. Powell, and D. R. Penn. Calculation of electron inelastic mean free paths (IMFPs) VII. Reliability of the TPP-2M IMFP predictive equation. *Surf. Interface Anal.*, 35 (3):268–275, 2003. doi: 10.1002/sia.1526.

- [171] M. P. Seah and W. A. Dench. Quantitative electron spectroscopy of surfaces: A standard data base for electron inelastic mean free paths in solids. *Surf. Interface Anal.*, 1(1):2–11, feb 1979. doi: 10.1002/sia.740010103.
- [172] Heizo Tokutaka, Naganori Ishihara, Katsumi Nishimori, Satoru Kishida, and Kazuhiro Isomoto. Background removal in x-ray photoelectron spectroscopy. *Surf. Interface Anal.*, 18(10):697–704, oct 1992. doi: 10.1002/sia.740181002.
- [173] M. Repoux. Comparison of background removal methods for XPS. *Surf. Interface Anal.*, 18(7):567–570, jul 1992. doi: 10.1002/sia.740180719.
- [174] R. Hesse, M. Weiß, R. Szargan, P. Streubel, and R. Denecke. Comparative study of the modelling of the spectral background of photoelectron spectra with the Shirley and improved Tougaard methods. *J. Electron Spectros. Relat. Phenomena*, 186:44–53, feb 2013. doi: 10.1016/j.elspec.2013.01.020.
- [175] János Véghe. The analytical form of the Shirley-type background. *J. Electron Spectros. Relat. Phenomena*, 46(2):411–417, jan 1988. doi: 10.1016/0368-2048(88)85038-2.
- [176] Sven Tougaard and B. Jørgensen. Inelastic background intensities in XPS spectra. *Surf. Sci.*, 143(2-3):482–494, aug 1984. doi: 10.1016/0039-6028(84)90554-5.
- [177] Sven Tougaard. Low Energy Inelastic Electron Sattering Properties of Noble and Transition Metals. *Solid State Commun.*, 61(9):547–549, 1987.
- [178] Sven Tougaard. Universality Classes of Inelastic Electron Scattering Cross-sections. *Surf. Interface Anal.*, 25:137–154, 1997.
- [179] Arne L. Tofterup. Estimates of errors and validity of Shirley-type backgrounds. *Appl. Surf. Sci.*, 44(2):157–159, apr 1990. doi: 10.1016/0169-4332(90)90103-7.
- [180] M.P. Seah. Background subtraction: I. General behaviour of Tougaard-style backgrounds in AES and XPS. *Surf. Sci.*, 420(2):285–294, 1999. doi: 10.1016/S0039-6028(98)00852-8.
- [181] M.P. Seah, I.S. Gilmore, and S.J. Spencer. Background subtraction II: General Behaviour of REELS and the Tougaard universal cross section in the removal of backgrounds in AES and XPS. *Surf. Sci.*, 461(1-3):1–15, aug 2000. doi: 10.1016/S0039-6028(00)00373-3.
- [182] M.P. Seah. Background subtraction III: The application of REELS data to background removal in AES and XPS. *Surf. Sci.*, 471(1-3):185–202, jan 2001. doi: 10.1016/S0039-6028(00)00906-7.
- [183] P. Prieto, C. Quiros, E. Elizalde, and J. M. Sanz. Electron inelastic mean free path and dielectric properties of a-boron, a-carbon, and their nitrides as determined by quantitative analysis of reflection electron energy loss spectroscopy. *J. Vac. Sci. Technol. A Vacuum, Surfaces, Film.*, 24(3):396, 2006. doi: 10.1116/1.2183249.
- [184] Sven Tougaard. Deconvolution of loss features from electron spectra. *Surf. Sci.*, 139(1):208–218, apr 1984. doi: 10.1016/0039-6028(84)90017-7.
- [185] Abbas Alshehabi and Jun Kawai. Extrinsic and Intrinsic Contributions to Plasmon Peaks in Solids. *Zeitschrift für Naturforsch. A*, 71(1):91–93, 2016. doi: 10.1515/zna-2015-0403.

- [186] J.E Castle, H Chapman-Kpodo, A Proctor, and A.M Salvi. Curve-fitting in XPS using extrinsic and intrinsic background structure. *J. Electron Spectros. Relat. Phenomena*, 106(1): 65–80, jan 2000. doi: 10.1016/S0368-2048(99)00089-4.
- [187] Neal Fairley, 2014. CasaXPS software version 2.3.17, Casa Software Ltd, United Kingdom.
- [188] P. NOZIÈRES and C. T. DE DOMINICIS. Singularities in the X-Ray Absorption and Emission of Metals. III. One-Body Theory Exact Solution. *Phys. Rev.*, 178(3):1097–1107, feb 1969. doi: 10.1103/PhysRev.178.1097.
- [189] S. Doniach and M. Sunjic. Many-electron singularity in X-ray photoemission and X-ray line spectra from metals. *J. Phys. C Solid State Phys.*, 3:285–291, 1970.
- [190] Sven Tougaard. Inelastic background removal in x-ray excited photoelectron spectra from homogeneous and inhomogeneous solids. *J. Vac. Sci. Technol. A Vacuum, Surfaces, Film.*, 5(4):1230, jul 1987. doi: 10.1116/1.574778.
- [191] Sven Tougaard. X-ray photoelectron spectroscopy peak shape analysis for the extraction of in-depth composition information. *J. Vac. Sci. Technol. A Vacuum, Surfaces, Film.*, 5(4): 1275, jul 1987. doi: 10.1116/1.574789.
- [192] P. J. Cumpson and M. P. Seah. Random uncertainties in AES and XPS: II: Quantification using either relative or absolute measurements. *Surf. Interface Anal.*, 18(5):361–367, may 1992. doi: 10.1002/sia.740180509.
- [193] C. J. Powell and J. M. Conny. Evaluation of uncertainties in X-ray photoelectron spectroscopy intensities associated with different methods and procedures for background subtraction. II. Spectra for unmonochromated Al and Mg X-rays. *Surf. Interface Anal.*, 41(10): 804–813, oct 2009. doi: 10.1002/sia.3103.
- [194] M. P. Seah. The quantitative analysis of surfaces by XPS: A review. *Surf. Interface Anal.*, 2(6):222–239, dec 1980. doi: 10.1002/sia.740020607.
- [195] Peter M A Sherwood. Curve fitting in surface analysis and the effect of background inclusion in the fitting process. *J. Vac. Sci. Technol. A Vacuum, Surfaces Film.*, 14(3):1424–1432, 1996. doi: 10.1116/1.579964.
- [196] R. Hesse and R. Denecke. Improved Tougaard background calculation by introduction of fittable parameters for the inelastic electron scattering cross-section in the peak fit of photoelectron spectra with UNIFIT 2011. *Surf. Interface Anal.*, 43(12):1514–1526, dec 2011. doi: 10.1002/sia.3746.
- [197] A. Herrera-Gomez, M. Bravo-Sanchez, O. Ceballos-Sanchez, and M. O. Vazquez-Lepe. Practical methods for background subtraction in photoemission spectra. *Surf. Interface Anal.*, 46(10-11):897–905, 2014. doi: 10.1002/sia.5453.
- [198] Stephen Evans. Estimation of the uncertainties associated with XPS peak intensity determination. *Surf. Interface Anal.*, 18(5):323–332, may 1992. doi: 10.1002/sia.740180506.
- [199] C. D. Wagner, L. E. Davis, M. V. Zeller, et al. Empirical atomic sensitivity factors for quantitative analysis by electron spectroscopy for chemical analysis. *Surf. Interface Anal.*, 3(5):211–225, oct 1981. doi: 10.1002/sia.740030506.

- [200] C.D. Wagner. Sensitivity factors for XPS analysis of surface atoms. *J. Electron Spectros. Relat. Phenomena*, 32(2):99–102, jan 1983. doi: 10.1016/0368-2048(83)85087-7.
- [201] National Physics Laboratory. Average matrix relative sensitivity factors (AMRSFs) for x-ray photoelectron spectroscopy (XPS), 2006. The National Physics Laboratory, Teddington, Middlesex, United Kingdom.
- [202] J.H. Scofield. Hartree-Slater subshell photoionization cross-sections at 1254 and 1487 eV. *J. Electron Spectros. Relat. Phenomena*, 8(2):129–137, jan 1976. doi: 10.1016/0368-2048(76)80015-1.
- [203] G. Hölzer, M. Fritsch, M. Deutsch, J. Härtwig, and E. Förster. $K\alpha_{1,2}$ and $K\beta_{1,3}$ x-ray emission lines of the 3d transition metals. *Phys. Rev. A*, 56(6):4554–4568, dec 1997. doi: 10.1103/PhysRevA.56.4554.
- [204] Eric Chason and Pradeep R. Guduru. Tutorial: Understanding residual stress in polycrystalline thin films through real-time measurements and physical models. *J. Appl. Phys.*, 119(19):191101, 2016. doi: 10.1063/1.4949263.
- [205] Vedene H. Smith and Paul G. Simpson. Crystallite Size Distributions from X-Ray Powder Line Profiles. *J. Appl. Phys.*, 36(10):3285, 1965. doi: 10.1063/1.1702968.
- [206] J Keckes, J.W Gerlach, and B Rauschenbach. Residual stresses in cubic and hexagonal GaN grown on sapphire using ion beam-assisted deposition. *J. Cryst. Growth*, 219(1-2):1–9, oct 2000. doi: 10.1016/S0022-0248(00)00595-9.
- [207] J Keckes, S Six, W Tesch, R Resel, and B Rauschenbach. Evaluation of thermal and growth stresses in heteroepitaxial AlN thin films formed on (0001) sapphire by pulsed laser ablation. *J. Cryst. Growth*, 240(1-2):80–86, 2002. doi: 10.1016/S0022-0248(02)00877-1.
- [208] J. I. Langford and A. J. C. Wilson. Scherrer after sixty years: A survey and some new results in the determination of crystallite size. *J. Appl. Crystallogr.*, 11(2):102–113, 1978. doi: 10.1107/S0021889878012844.
- [209] Shrikant Lele and T. R. Anantharaman. Influence of crystallite shape on particle size broadening of Debye-Scherrer reflections. *Proc. Indian Acad. Sci. - Sect. A*, 64(5):261–274, 1966. doi: 10.1007/BF03047543.
- [210] Arthur Bienenstock. Calculation of Crystallite Size Distributions from X-Ray Line Broadening. *J. Appl. Phys.*, 34(5):1391, 1963. doi: 10.1063/1.1729586.
- [211] Ullrich Pietsch. Investigations of semiconductor surfaces and interfaces by X-ray grazing incidence diffraction. *Curr. Sci.*, 78(12):1484–1495, 2000.
- [212] Beulah Field Decker. The Validity of the Pole Figure. *J. Appl. Phys.*, 16(5):309, 1945. doi: 10.1063/1.1707592.
- [213] C. G. Dunn. The Analysis of Quantitative Pole-Figure Data. *J. Appl. Phys.*, 25(2):233, 1954. doi: 10.1063/1.1721610.
- [214] J. B. Newkirk and L. Bruce. Rapid X-Ray Determination of a Complete Pole Figure. *J. Appl. Phys.*, 29(2):151, 1958. doi: 10.1063/1.1723057.

- [215] M Birkholz, B Selle, F Fenske, and W Fuhs. Structure-function relationship between preferred orientation of crystallites and electrical resistivity in thin polycrystalline ZnO:Al films. *Phys. Rev. B*, 68(20):205414, nov 2003. doi: 10.1103/PhysRevB.68.205414.
- [216] J. L. Alty. Recording and Analysis of Pole Figures by Computer. *J. Appl. Phys.*, 39(9):4189, 1968. doi: 10.1063/1.1656946.
- [217] Mario Birkholz. *Thin Film Analysis by X-ray Scattering*. Wiley-VCH Verlag GmbH, Germany, 2006. ISBN 3-527-31052-5.
- [218] S. K. Sinha, E. B. Sirota, S. Garoff, and H. B. Stanley. X-ray and neutron scattering from rough surfaces. *Phys. Rev. B*, 38(4):2297–2311, 1988. doi: 10.1103/PhysRevB.38.2297.
- [219] D Lederman, Zhonghai Yu, T H Myers, and M R Richards-Babb. Surface morphology of GaN films determined from quantitative x-ray reflectivity. *Appl. Phys. Lett.*, 71(3):368, 1997. doi: 10.1063/1.119539.
- [220] R.J. Matyi, M.S. Hatzistergos, and E. Lifshin. X-ray reflectometry analyses of chromium thin films. *Thin Solid Films*, 515(4):1286–1293, dec 2006. doi: 10.1016/j.tsf.2006.03.016.
- [221] Kyung Joong (Division of Industrial Metrology Korea Research Institute of Standards Kim and Science). Uncertainty in Quantification of Binary Alloy Films and Thickness Measurement of nm Oxide Films. *J. Surf. Anal.*, 17(3):177–185, 2011.
- [222] A. C. Ferrari, A Libassi, B. K. Tanner, et al. Density, sp³ fraction, and cross-sectional structure of amorphous carbon films determined by x-ray reflectivity and electron energy-loss spectroscopy. *Phys. Rev. B - Condens. Matter Mater. Phys.*, 62(16):11089–11103, 2000. doi: 10.1103/PhysRevB.62.11089.
- [223] D Windover, E Barnat, J Y Kim, et al. Thin Film Density Determination By Multiple Radiation Energy Dispersive X-Ray Reflectivity. *Adv. X-ray Anal.*, 42(C):590–600, 2000.
- [224] E Chason and T M Mayer. Thin film and surface characterization by specular x-ray reflectivity. *Crit. Rev. Solid State Mat. Sci.*, 22(1):1, 1997.
- [225] M. Bhargava, W. Donner, a. K. Srivastava, and J. C. Wolfe. Bragg diffraction, synchrotron x-ray reflectance, and x-ray photoelectron spectroscopy studies of low temperature plasma oxidation of native SiO₂ on silicon on insulator. *J. Vac. Sci. Technol. B Microelectron. Nanom. Struct.*, 26(1):305, 2008. doi: 10.1116/1.2790927.
- [226] P. Bergese, E. Bontempi, and L.E. Depero. A simple solution to systematic errors in density determination by X-ray reflectivity: The XRR-density evaluation (XRR-DE) method. *Appl. Surf. Sci.*, 253(1):28–32, oct 2006. doi: 10.1016/j.apsusc.2006.05.067.
- [227] J D Shindler and R M Suter. Moderate resolution x-ray reflectivity. *Rev. Sci. Instrum.*, 63(11):5343, 1992. doi: 10.1063/1.1143400.
- [228] Matts Björck. Fitting with differential evolution: an introduction and evaluation. *J. Appl. Crystallogr.*, 44(6):1198–1204, 2011. doi: 10.1107/S0021889811041446.
- [229] H Kiessig. Interference of X-rays in thick layers. *Ann. Phys.*, 10(7):769–788, 1931.
- [230] L. G. Parratt. Surface Studies of Solids by Total Reflection of X-Rays. *Phys. Rev.*, 95(2):359–369, jul 1954. doi: 10.1103/PhysRev.95.359.

- [231] Sjoerd a. Veldhuis, Peter Brinks, Tomasz M. Stawski, Ole F. Göbel, and Johan E. ten Elshof. A facile method for the density determination of ceramic thin films using X-ray reflectivity. *J. Sol-Gel Sci. Technol.*, pages 118–128, apr 2014. doi: 10.1007/s10971-014-3336-2.
- [232] Mari Mizusawa, Krassimir N Stoev, and Kenji Sakurai. Density Gradient of a Mirror-Polished Rutile (110) Surface: X-ray Reflectivity Evaluation. *Jpn. J. Appl. Phys.*, 42(Part 1, No. 6A):3709–3710, jun 2003. doi: 10.1143/JJAP.42.3709.
- [233] Christopher A. Apblett, David M. Stewart, Robert T. Fryer, et al. In situ XANES and EXAFS Analysis of Redox Active Fe Center Ionic Liquids. *Electrochim. Acta*, 185:156–161, dec 2015. doi: 10.1016/j.electacta.2015.09.093.
- [234] Frank de Groot. High-resolution X-ray emission and X-ray absorption spectroscopy. *Chem. Rev.*, 101(6):1779–1808, jun 2001.
- [235] Frank de Groot. X-Ray Absorption Spectroscopy. In *Core Lev. Spectrosc. Solids*, chapter 6, pages 225–284. CRC Press, 2008.
- [236] Grant Bunker. *Introduction to XAFS*. Cambridge University Press, Cambridge, 2010. ISBN 978-0-521-76775-0.
- [237] Dennis M. Mills, editor. *Third-Generation Hard X-Ray Synchrotron Radiation Sources: Source Properties, Optics, and Experimental Techniques*. Wiley-VCH, 1st edition, 2002. ISBN 978-0471314332.
- [238] A. J. Kropf, J. Katsoudas, S. Chattopadhyay, et al. The new MRCAT (Sector 10) bending magnet beamline at the advanced photon source. In *AIP Conf. Proc.*, volume 1234, pages 299–302, 2010. ISBN 9780735407824. doi: 10.1063/1.3463194.
- [239] J. H. Hubbell and S. M. Seltzer. Tables of X-Ray Mass Attenuation Coefficients and Mass Energy-Absorption Coefficients from 1 keV to 20 MeV for Elements $Z = 1$ to 92 and 48 Additional Substances of Dosimetric Interest. In *NIST Stand. Ref. Database 126*. National Institute of Standards and Technology, Gaithersburg MD, 2004.
- [240] MK Gupta and AK Nigam. K absorption edge of zirconium in some of its compounds. *J. Phys. F Met. Phys.*, 4:947–950, 1974.
- [241] J. G. Chen. NEXAFS Investigations of Transition Metal Oxides, Nitrides, Carbides, Sulfides and Other Interstitial Compounds. *ChemInform*, 30:1–152, jun 1997. doi: 10.1002/chin.199819267.
- [242] Masahito Niibe, Kazuyoshi Miyamoto, Tohru Mitamura, and Kozo Mochiji. Identification of B-K near edge x-ray absorption fine structure peaks of boron nitride thin films prepared by sputtering deposition. *J. Vac. Sci. Technol. A Vacuum, Surfaces, Film.*, 28(5):1157, 2010. doi: 10.1116/1.3474913.
- [243] O. J. Dura, R. Boada, M. a. López de la Torre, et al. XANES and EXAFS study of the local order in nanocrystalline yttria-stabilized zirconia. *Phys. Rev. B*, 87(17):174109, 2013. doi: 10.1103/PhysRevB.87.174109.
- [244] Takashi Yamamoto. Assignment of pre-edge peaks in K-edge x-ray absorption spectra of 3d transition metal compounds: electric dipole or quadrupole? *X-Ray Spectrom.*, 37(6): 572–584, nov 2008. doi: 10.1002/xrs.1103.

- [245] H. Deng, H. Qiu, and G. Shi. EXAFS of nanophase zirconia stabilized by yttria. *Phys. B Phys. Condens. Matter*, 208-209(C):591–592, 1995. doi: 10.1016/0921-4526(94)00764-M.
- [246] Wangsheng Chu, Ziyu Wu, Wenhan Liu, et al. Lattice dynamics study of AlB₂-type 4d transition-metal diborides by extended X-ray-absorption fine structure. *Radiat. Phys. Chem.*, 75(11):2080–2084, nov 2006. doi: 10.1016/j.radphyschem.2005.07.061.
- [247] S. Calvin, E. E. Carpenter, V. G. Harris, and S. a. Morrison. Use of multiple-edge refinement of extended x-ray absorption fine structure to determine site occupancy in mixed ferrite nanoparticles. *Appl. Phys. Lett.*, 81(2002):3828–3830, 2002. doi: 10.1063/1.1520700.
- [248] Matthew Newville. EXAFS analysis using FEFF and FEFFIT. *J. Synchrotron Radiat.*, 8: 96–100, 2001. doi: 10.1107/S0909049500016290.
- [249] B Ravel and M Newville. ATHENA, ARTEMIS, HEPHAESTUS: data analysis for X-ray absorption spectroscopy using IFEFFIT. *J. Synchrotron Radiat.*, 12(Pt 4):537–41, jul 2005. doi: 10.1107/S0909049505012719.
- [250] Oliver C Wells and David C Joy. The early history and future of the SEM. *Surf. Interface Anal.*, 38:1738–1742, 2006. doi: 10.1002/sia.
- [251] Lucille A. Giannuzzi and Fred A. Stevie, editors. *Introduction to Focused Ion Beams*. Springer Science+Business Media, 2005. ISBN 0-387-23116-1.
- [252] David E. Newbury, David C. Joy, Patrick Echlin, Charles E. Fiori, and Joseph I. Goldstein. *Advanced Scanning Electron Microscopy and X-ray Microanalysis*. Plenum Press, New York, second edition, 1987. ISBN 0-306-42140-2.
- [253] J.-Ch Kuhr and H.-J Fitting. Monte Carlo simulation of electron emission from solids. *J. Electron Spectros. Relat. Phenomena*, 105(2-3):257–273, dec 1999. doi: 10.1016/S0368-2048(99)00082-1.
- [254] Tohru Ishitani and Kaoru Ohya. Comparison in spatial spreads of secondary electron information between scanning ion and scanning electron microscopy. *Scanning*, 25(4):201–209, dec 2006. doi: 10.1002/sca.4950250407.
- [255] Tohru Ishitani. Origins of material contrast in scanning ion microscope images. *J. Electron Microsc. (Tokyo)*, 51(4):207–213, jul 2002. doi: 10.1093/jmicro/51.4.207.
- [256] R. S. Frankel and D. W. Aitken. Energy-Dispersive X-Ray Emission Spectroscopy. *Appl. Spectrosc.*, 24(6):557–566, 1970.
- [257] W. W. Mullins. Theory of Thermal Grooving. *J. Appl. Phys.*, 28(3):333, 1957. doi: 10.1063/1.1722742.
- [258] Michael DiBattista and Johannes W Schwank. Determination of diffusion in polycrystalline platinum thin films. *J. Appl. Phys.*, 86(9):4902–4907, 1999.
- [259] J. Keckes, J. W. Gerlach, R. Averbek, et al. Temperature dependence of stresses in GaN thin films grown on (0001) sapphire: Modeling of thermal stresses. *Appl. Phys. Lett.*, 79(26): 4307, 2001. doi: 10.1063/1.1427424.

- [260] Solomon Agbo, Pavel Calta, Pavol Sutta, et al. Investigation of the transition phases from amorphous silicon-based multilayers to silicon nanostructures by in situ X-ray diffraction. *Phys. Status Solidi*, 211(7):1512–1518, 2014. doi: 10.1002/pssa.201330231.
- [261] F. M. Smits. Measurement of Sheet Resistivities with the Four-Point Probe. *Bell Syst. Tech. J.*, 37(3):711–718, may 1958. doi: 10.1002/j.1538-7305.1958.tb03883.x.
- [262] Nicola Bowler. Four-point potential drop measurements for materials characterization. *Meas. Sci. Technol.*, 22(1):012001, jan 2011. doi: 10.1088/0957-0233/22/1/012001.
- [263] LB Valdes. Resistivity Measurements on Germanium for Transistors. *Proc. IRE*, 42(2): 420–427, feb 1954. doi: 10.1109/JRPROC.1954.274680.
- [264] Sara Zolfaghar Tehrani, W.L. Lim, and L. Lee. Correction factors for films resistivity measurement. *Measurement*, 45(3):219–225, apr 2012. doi: 10.1016/j.measurement.2011.11.019.
- [265] Donald W. Marquardt. An Algorithm for Least-Squares Estimation of Nonlinear Parameters. *J. Soc. Ind. Appl. Math.*, 11(2):431–441, jun 1963. doi: 10.1137/0111030.
- [266] Takashi Aizawa, Shunichi Hishita, and Shigeki Otani. The 2x2 oxidized layer on ZrB₂(0001). *Appl. Surf. Sci.*, 256(4):1120–1123, nov 2009. doi: 10.1016/j.apsusc.2009.03.100.
- [267] M.P Seah, I.S Gilmore, and S.J Spencer. Quantitative XPS. *J. Electron Spectros. Relat. Phenomena*, 120(1-3):93–111, oct 2001. doi: 10.1016/S0368-2048(01)00311-5.
- [268] C.M. Scanlan, M. Gajdardziska-Josifovska, and C. Aita. Tetragonal zirconia growth by nanolaminate formation. *Appl. Phys. Lett.*, 64, 1994.
- [269] C.R. Aita, M.D. Wiggins, R. Whig, C.M. Scanlan, and M. Gajdardziska-Josifovska. Thermodynamics of tetragonal zirconia formation in a nanolaminate film. *J. Appl. Phys.*, 79, 1996.
- [270] Ziyuan Zhou, Xianghe Peng, and Zhen Wei. A Thermo-Chemo-Mechanical Model for the Oxidation of Zirconium Diboride. *J. Am. Ceram. Soc.*, 98(2):629–636, feb 2015. doi: 10.1111/jace.13333.
- [271] Wei Cho Foo, John S Ozcomert, and Michael Trenary. The oxidation of the β -rhombohedral boron (111) surface. *Surf. Sci.*, 255(3):245–258, sep 1991. doi: 10.1016/0039-6028(91)90681-H.
- [272] Yajun Wang and Michael Trenary. Surface Chemistry of Boron Oxidation. 2. The Reactions of B₂O₂ and B₂O₃ with Boron Films Grown on Ta(110). *Chem. Mater.*, 5(364):199–205, 1993. doi: 10.1021/cm00026a008.
- [273] Wei Cho Foo, John S. Ozcomert, and Michael Trenary. The reaction of B₂O₃ with the β -rhombohedral boron (111) surface. *Surf. Sci.*, 262(1-2):88–96, feb 1992. doi: 10.1016/0039-6028(92)90462-F.
- [274] Y. Panayiotatos. Homogeneous and amorphous sputtered sp³-bonded BN films at RT: a stress, spectroscopic ellipsometry and XPS study. *Diam. Relat. Mater.*, 12(3-7):1151–1156, jul 2003. doi: 10.1016/S0925-9635(02)00318-7.

- [275] K. S. Park, D. Y. Lee, K. J. Kim, and D. W. Moon. Observation of a hexagonal BN surface layer on the cubic BN film grown by dual ion beam sputter deposition. *Appl. Phys. Lett.*, 70(3):315, 1997. doi: 10.1063/1.118402.
- [276] Weion-Pil Tai, Tadahiko; Watanabe, and Nathan S Jacobson. High-Temperature Stability of Alumina in Argon and Argon/Water-Vapor Environments. *J. Am. Ceram. Soc.*, 82(1): 245–248, 1999. doi: 10.1111/j.1151-2916.1999.tb01754.x.
- [277] V.P. Deodshmukh, S.J. Matthews, and D.L. Klarstrom. High-temperature oxidation performance of a new alumina-forming NiFeCrAl alloy in flowing air. *Int. J. Hydrogen Energy*, 36(7):4580–4587, apr 2011. doi: 10.1016/j.ijhydene.2010.04.099.
- [278] Baban P. Dhonge, Tom Mathews, N. Kumar, et al. Wear and oxidation resistance of combustion CVD grown alumina films. *Surf. Coatings Technol.*, 206(22):4574–4579, jun 2012. doi: 10.1016/j.surfcoat.2012.05.011.
- [279] Friederike Kersten, Alexander Schmid, Stefan Bordihn, Jörg W. Müller, and Johannes Heitmann. Role of Annealing Conditions on Surface Passivation Properties of ALD Al₂O₃ Films. *Energy Procedia*, 38:843–848, 2013. doi: 10.1016/j.egypro.2013.07.354.
- [280] Subhasisa Nath, Indranil Manna, Samit Kumar Ray, and Jyotsna Dutta Majumdar. Studies on nanotribological and oxidation resistance properties of yttria stabilized zirconia (YSZ), alumina (Al₂O₃) based thin films developed by pulsed laser deposition. *Ceram. Int.*, 42(6): 7060–7071, may 2016. doi: 10.1016/j.ceramint.2016.01.094.
- [281] Emmanuel Scheid, Gabriel M Veith, Constantin Vahlas, and Emile Monso. Amorphous alumina thin films deposited on titanium : Interfacial chemistry and thermal oxidation barrier properties. *Phys. Status Solidi*, 480(2):470–480, 2016. doi: 10.1002/pssa.201532838.
- [282] Gunter Krautheim, Thomas Hecht, Stefan Jakschik, Uwe Schröder, and Wieland Zahn. Mechanical stress in ALD-Al₂O₃ films. In *Appl. Surf. Sci.*, volume 252, pages 200–204, 2005. ISBN 0169-4332. doi: 10.1016/j.apsusc.2005.01.118.
- [283] Ram Ekwil Sah, Rachid Driad, Frank Bernhardt, et al. Mechanical and electrical properties of plasma and thermal atomic layer deposited Al₂O₃ films on GaAs and Si. *J. Vac. Sci. Technol. A Vacuum, Surfaces, Film.*, 31(4):041502, 2013. doi: 10.1116/1.4804175.
- [284] Oili M E Ylivaara, Xuwen Liu, Lauri Kilpi, et al. Aluminum oxide from trimethylaluminum and water by atomic layer deposition: The temperature dependence of residual stress, elastic modulus, hardness and adhesion. *Thin Solid Films*, 552:124–135, 2014. doi: 10.1016/j.tsf.2013.11.112.
- [285] B.A. Latella, G. Triani, and P.J. Evans. Toughness and adhesion of atomic layer deposited alumina films on polycarbonate substrates. *Scr. Mater.*, 56(6):493–496, mar 2007. doi: 10.1016/j.scriptamat.2006.11.021.
- [286] Shih-Hui Jen, Jacob A. Bertrand, and Steven M. George. Critical tensile and compressive strains for cracking of Al₂O₃ films grown by atomic layer deposition. *J. Appl. Phys.*, 109(8): 084305, 2011. doi: 10.1063/1.3567912.
- [287] Shih Hui Jen, Steven M. George, Robert S. McLean, and Peter F. Carcia. Alucone interlayers to minimize stress caused by thermal expansion mismatch between Al₂O₃ films and Teflon substrates. *ACS Appl. Mater. Interfaces*, 5(3):1165–1173, 2013. doi: 10.1021/am303077x.

- [288] Tobias Suss, Philipp Braeuninger-Weimer, and Christofer Hierold. Stress reduction in ultra-small thin film Al₂O₃ diaphragms by atomic layer deposition. *Sensors Actuators, A Phys.*, 212:159–164, 2014. doi: 10.1016/j.sna.2014.02.021.
- [289] A. Bulusu, A. Singh, C. Y. Wang, et al. Engineering the mechanical properties of ultrabARRIER films grown by atomic layer deposition for the encapsulation of printed electronics. *J. Appl. Phys.*, 118(8):085501, aug 2015. doi: 10.1063/1.4928855.
- [290] K. Oda and T. Yoshio. Oxidation kinetics of hexagonal boron nitride powder. *J. Mater. Sci.*, 28(24):6562–6566, 1993. doi: 10.1007/BF00356394.
- [291] Vo Van Hoang. Molecular dynamics study on structure and properties of liquid and amorphous Al₂O₃. *Phys. Rev. B*, 70(13):134204, oct 2004. doi: 10.1103/PhysRevB.70.134204.
- [292] Stefan Jakschik, Uwe Schroeder, Thomas Hecht, et al. Crystallization behavior of thin ALD-Al₂O₃ films. *Thin Solid Films*, 425(1-2):216–220, 2003. doi: 10.1016/S0040-6090(02)01262-2.
- [293] B. Yates, M. J. Overy, and O. Pirgon. The anisotropic thermal expansion of boron nitride. *Philos. Mag.*, 32(4):847–857, oct 1975. doi: 10.1080/14786437508221624.
- [294] John F. Moulder, William F. Stickle, Peter E. Sobol, and Kenneth D. Bomben. Atomic Sensitivity Factors for X-ray Sources at 54.7. In Jil Chastain, editor, *Handb. X-ray Photoelectron Spectrosc.*, chapter Appendix F, page 253. Perkin-Elmer Corporation, Eden Prairie, Minnesota, 1992. ISBN 0-9627026-2-5.

APPENDIX A

ACCURACY OF Zr_xB_{1-x} FILM COMPOSITION MEASUREMENTS

As discussed in §3.2.2, the Zr_xB_{1-x} films produced by e-beam co-evaporation were measured by XPS to have a composition that deviated considerably from the QCM measured composition of the evaporation flux. It was found that all films had an XPS composition deficient in Zr from what was predicted by the evaporation flux composition. Although no satisfactory explanation for this trend has been uncovered, the result is stated with certainty. The reason for this certainty as derived from error analysis is discussed below.

Fig. A.1 shows the trend in the measured XPS film composition versus the measured QCM evaporation flux, the same data as in Fig. 3.2a, but with three different fitted functions. The linear fit is the least plausible, as it does not meet the boundary conditions of (0,0) and (1,1), and thus it has a much higher χ^2 than the other two fits. The exponential function also does not meet the lower boundary condition, while having a χ^2 closely matched by the parabolic function. Since neither the exponential nor the parabolic function have any physical justification, the parabolic one was selected to model the data due to its match of both boundary conditions.

Effects of Changing XPS Sensitivity Factors

In Fig. A.1, the atomic fraction of Zr in the film was determined by

$$X_{Zr} = \frac{I_{Zr}/R_{Zr}}{I_{Zr}/R_{Zr} + I_B/R_B} \quad (A.1)$$

where I is the measured area of the photoelectron peak after background subtraction, and R is the RSF value for the corresponding elemental transition. Eq. A.1 can be re-expressed in terms of the

Table A.1: Functional forms, fitted parameter values, and reduced χ^2 values for each fitted curve in Fig. A.1.

Function	χ^2	fitted parameters	
$a + bx$	0.1200060	$a = -0.16549(6330)$	$b = 0.93503(10400)$
x^p	0.0346773	$p = 2.1038(906)$	
$y_0 + \exp[-(x-1)/\tau]$	0.0311022	$y_0 = -0.035372(43600)$	$\tau = -0.40195(5440)$

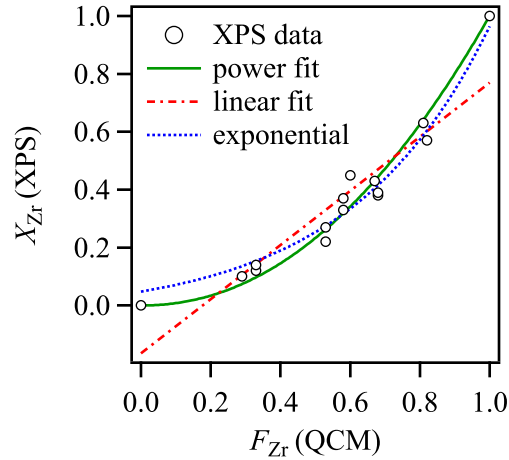


Figure A.1: Reproduction of Fig. 3.2, but with three curves fitted to the data. Plot of XPS measured film composition (X_{Zr}) versus QCM measured evaporation flux composition (F_{Zr}) fitted with linear, parabolic, and exponential curves.

ratios of the peak areas, $i = I_{Zr}/I_B$, and the ratios of the RSF values, $r = R_{Zr}/R_B$:

$$X_{Zr} = (1 + r/i)^{-1} \quad (\text{A.2})$$

A detailed discussion of the procedures followed for fitting the XPS data to measure i has already been presented in §2.2 and §3.2.1. However, by Eq. A.2 the value of r has as large an effect on the measured film composition as that of i , and so the possibility that inaccurate RSF values were used must be considered. If $r \rightarrow r'$, then Eq. A.2 becomes $X'_{Zr} = (1 + r'/i)^{-1}$. Furthermore, solving Eq. A.2 for i in terms of X and r , and substituting this into the equation for X' yields

$$X'_{Zr} = [1 + (r'/r)(X_{Zr}^{-1} - 1)]^{-1} \quad (\text{A.3})$$

Fig. A.2a shows X'_{Zr} vs. X_{Zr} for various values of r'/r . The effect of changing RSF values is to shift the composition in a non-linear fashion. For example, if the data fit a linear function with a vertical offset, as was seen in Fig. A.1, a change in the RSFs used would force the trend to become non-linear. Similarly, the other functions chosen in Fig. A.1 cannot be made linear by simply adjusting the RSFs. One may notice, however, that the curves in Fig. A.2a for $r'/r > 1$ look suspiciously close to the trend in the data from Fig. A.1.

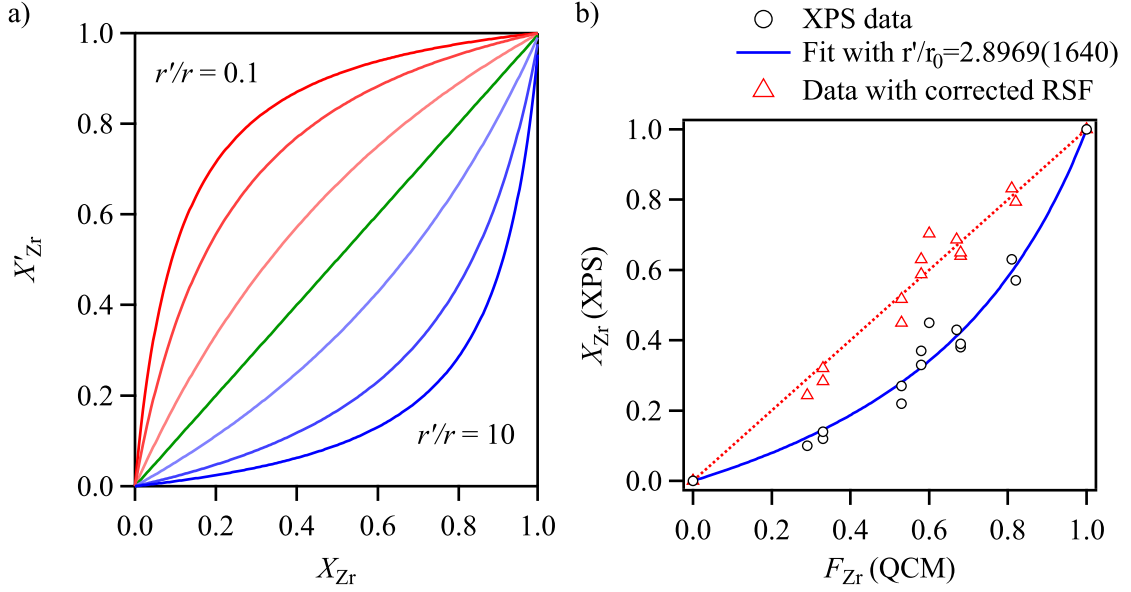


Figure A.2: Graphs showing the effect of altering the RSF values on the measured composition. (a) Graph of Eq. A.3 for seven different values of r'/r . This graph can be interpreted as the difference between the measured composition and the actual composition of the film, as a function of the RSF.¹⁴⁸ (b) Plot of measured film composition vs. evaporation flux composition, with Eq. A.3 fitted. The red crosses are the same data after being shifted by the value extracted from the fit, as discussed in the text.

Taking the QCM measurements of the evaporation flux as an accurate measurement of the true film composition, Eq. A.3 can be fitted to the film composition data, shown in Fig. A.2b. A fitted value of $r'/r = 2.8967(1640)$ gives a χ^2 of 0.0252616, which is lower than for any of the functions fit in Fig. A.1. Furthermore, the fitted r'/r value can be used to shift the measured data points by Eq. A.3 with $r'/r = 1/2.8967$, shown by the red crosses in Fig. A.2b. These shifted data points follow an almost perfectly linear trajectory. To see if this correction is justified, the uncertainty in the RSFs and data needs to be considered.

Error Propagation from RSFs and Peak Intensities

Many factors go into estimating the uncertainty of XPS composition quantification, as was discussed in §2.2.3, but for the moment we will focus on the uncertainties due to the measured intensity ratio, i , and the ratio r of the RSFs for a given transition. Using standard error propagation, the variance in Eq. A.2 is

$$\sigma_X^2 = \sigma_i^2 \left(\frac{\partial X}{\partial i} \right)^2 + \sigma_r^2 \left(\frac{\partial X}{\partial r} \right)^2 \quad (\text{A.4})$$

Table A.2: XPS sensitivity factors for Zr and B from three different sources: CasaXPS™,¹⁸⁷ the National Physics Laboratory,²⁰¹ and the Specs handbook,²⁹⁴ as well as the resulting values of r . RSFs are dependent not only on the transition and element, but on the transmission function of the spectrometer, and so RSFs from other sources are not necessarily guaranteed to be valid for the specific XPS spectrometer used in this thesis.

Transition	Sensitivity Factor Source		
	CasaXPS	NPL	Specs
Zr 3d _{5/2}	4.17	4.45	1.700
B 1s	0.486	0.516	0.159
$r = \frac{\text{RSF}_{\text{Zr}}}{\text{RSF}_{\text{B}}}$	8.58	8.62	10.7

$$\sigma_X^2 = \frac{\sigma_i^2 r^2 + \sigma_r^2 i^2}{(i+r)^4} \quad (\text{A.5})$$

The uncertainty in the measured intensity, σ_i , is dependent on several factors, including the background subtraction method and line shapes used, as well as the noise in the data. For the purposes of this analysis, we will assume that $\sigma_i = 0.1i$, owing to the choice of asymmetric line shapes. The actual uncertainty purely from data noise is $\sim 0.00321i$, so given the confidence in the asymmetric model discussed in §3.2.1, this σ_i is a dramatic overestimate.

Table A.2 shows RSFs from three different sources, including the handbook provided by Specs that accompanies the Specs HSA3000 hemispherical analyzer used in this thesis. From these three sources, r has a mean of $\bar{r} = 9.30(121)$. Using this uncertainty for σ_r , and the above estimate for σ_i , the minimum and average values of $\sigma_X(i; r)$ were calculated as a function of r , and plotted in Fig. A.3. The slope of the curves in Fig. A.3 vary considerably over the range of r , but between 8.6 and 10.7 there is only a small change, such that σ_X only varies from 0.01144 to 0.01602 for $r = 8.6$. It is not surprising that σ_X is considerably higher for $r = 2.96$, the value that linearizes the data in Fig. A.2b, considering that this r is 4.66 standard deviations away from $r = 8.6$.

More global trends in σ_X are shown in Fig. A.4. The intensity map (Fig. A.4a) shows the $\sigma_X(i, r)$ surface along with a trace of the minimum. As was seen in Fig. A.3, for large values of r the uncertainty is low and varies only slightly with i . As r decreases, the minimum in σ_X shifts to

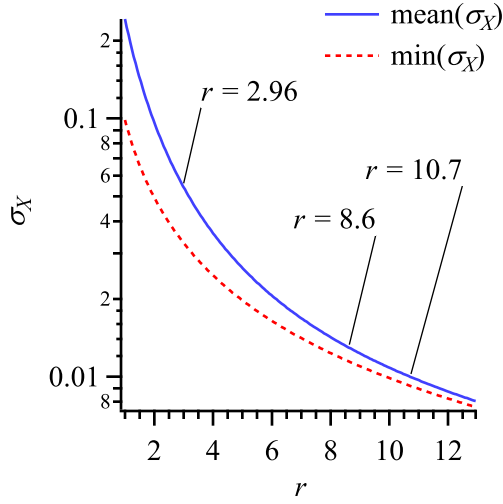


Figure A.3: Trends in the uncertainty in XPS quantification with RSF. Graph of the $\min(\sigma_X)$ and $\text{mean}(\sigma_X)$ as a function of r . Both statistics for a given r are taken from σ_X for $0 \leq i \leq 1$. See Fig. A.4 for more information.

higher values of i (lower values of X_{Zr}), and the valley narrows. The chosen range in i is equivalent to $1 \geq X_{Zr} \geq 0.1042$ for $r = 9.3$, however, a direct conversion from $i \rightarrow X_{Zr}$ is not possible, as X_{Zr} depends on r as well. One can also see that the uncertainty can vary rapidly across i , and so a single value of σ_X can be misrepresentative.

Conclusions for Zr_xB_{1-x} Film Composition

The quantitative analysis of Zr_xB_{1-x} film composition by XPS is marred by an inexplicable, non-linear trend relating the composition of the evaporation flux to the composition of the film. It has been demonstrated that the trend is best modeled by a correction to the RSFs using Eq. A.3. The fitted value of $r'/r = 2.8967(1640)$ was used to linearize the measured compositions, assuming that the QCM measurements are perfectly accurate. The value of r that linearized the data was found to be 2.96.

It was also shown that the uncertainty in the film composition varies considerably as i and r are adjusted. For the RSFs used in quantification, which give $r = 8.6$, the average uncertainty is $\bar{\sigma}_X = 0.013$, which is low enough to justify the non-linear relationship between the QCM and XPS measurements. If the RSFs are adjusted to linearize the data, then $\bar{\sigma}_X = 0.0562$, which is almost three times larger than before.

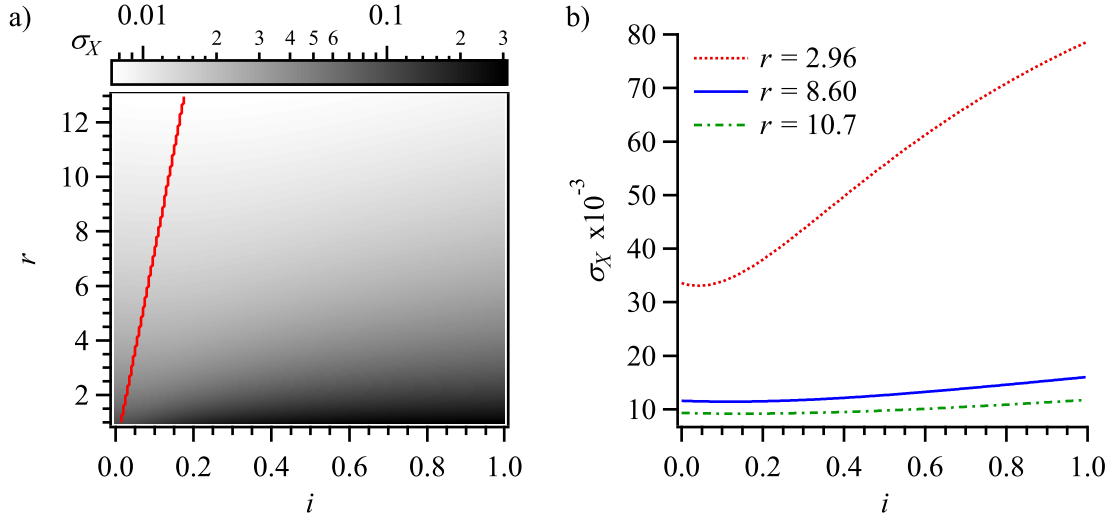


Figure A.4: Global trends in XPS quantification uncertainty. Graphs of Eq. A.5. (a) Color plot (log scale) of σ_X over a range of i and r values. The red curve traces the minimum of the contours. (b) Some cross sections from (a) at different r values, relevant to this discussion.

Although there exists an r which linearizes the XPS data, there is little justification for using it. First and foremost there is the concern that $r = 2.96$ is $4.66\sigma_r$ away from $r = 8.6$, and so is by no means a small correction. Furthermore, the fit using Eq. A.3 is not substantially better than the parabolic fit. Also, the Zr and B peaks used for quantification are ~ 10 eV from each other, and so neither a variation in the transmission function of the spectrometer or the photoelectron IMFP of the sample can justify changing the RSFs. Lastly, the results of §4.4 show that the films which were measured by XPS to be near 33 at % Zr were structurally very similar to bulk ZrB_2 , and were at worst B-rich, not Zr-rich.

Overall, even without a substantial effort to develop accurate RSFs for our specific XPS spectrometer from high purity standards, a measurement of the transmission function of the spectrometer, and a thorough investigation of films with lower at % Zr, there is very little uncertainty in the XPS quantification of the $\text{Zr}_x\text{B}_{1-x}$ films. However, given the results in Fig. A.2b, additional calibration of the XPS spectrometer may be prudent before future work requiring a range of compositions is performed.

APPENDIX B

ELECTRICAL WIRING FOR SAMPLE BIASING

Normally, the sample substrate is grounded during film deposition, but as seen in §5.4 electrically biasing the sample can provide another adjustable parameter that influences film growth. In order to provide this capability, several design features of the sample manipulator arm in the deposition chamber needed to be accounted for:

1. Although the sample carrier is in electrical contact with the Ta heater can, the can is isolated from the rest of the manipulator arm. To ground the sample, a wire normally connects the Ta can to the outer shaft of the manipulator, bypassing the isolating ceramic washers.
2. The manipulator arm consists of two sections: a static inner shaft that holds the wiring and heater, and a rotating outer shaft that connects to the heater can. Of course the chamber itself is also static.
3. The sample and Ta can are regularly heated to $>600^{\circ}\text{C}$, and are held at these temperatures for several hours at a time. The electrical connection between the Ta can and ground or the voltage source must be stable during heating at these temperatures.

Because most of the manipulator arm and chamber are stainless steel and electrically grounded, the biasing wiring and contacts must be insulated. Electrical connections inside a deposition chamber also need to be protected from the deposition flux in order to prevent shorting or the build up of insulating layers.

The electrical contact between the static part of the deposition chamber and the rotating shaft and heater can must be a slipping contact in order for the can to rotate indefinitely in either direction. Furthermore, because the manipulator shafts are not perfectly straight, the sample can precesses by as much as 1 cm as it rotates and wobbles. Thus the slipping contact must also act as a spring during the rotation.

Early versions of the biasing connection used 0.25 mm Ta foil as the slipping spring contact because Ta has high electrical and thermal conductivity, high melting temperature, and high Young's modulus. A Ni/Cr wire was run down the shaft to the can, and Ta foil was placed in contact with

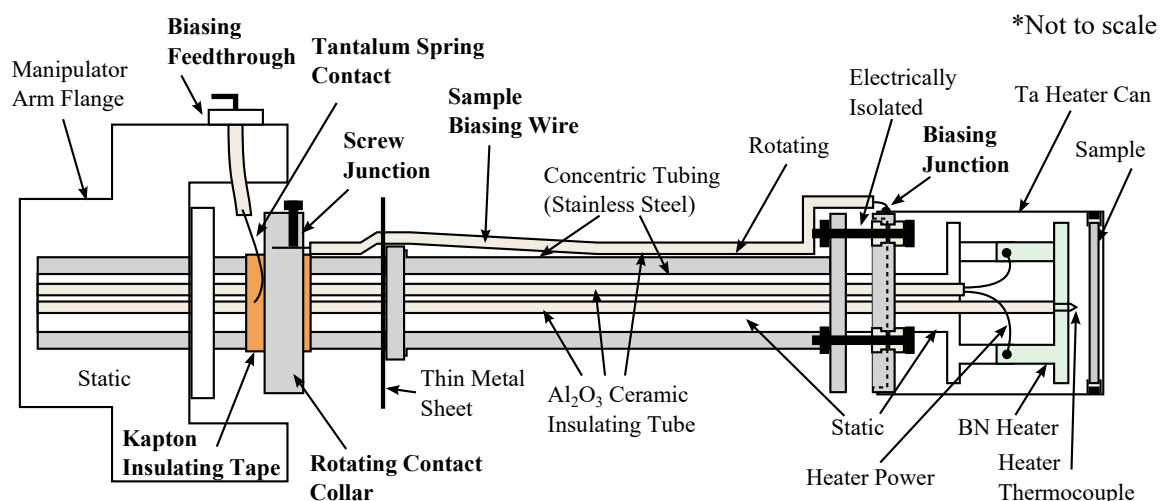


Figure B.1: Schematic of deposition chamber manipulator arm with original equipment and new sample biasing wiring. Rotating portions are colored gray and alumina ceramics are off-white. The Ta heater can at the right end is structurally connected to the outer, rotating steel shaft, while being electrically isolated by alumina washers. Two pairs of wires for the heater power and thermocouple run through double-bore alumina tubes down the center of the inner, static shaft. The biasing wire runs through single-bore alumina tubes along the outside of the rotating shaft. A steel collar is fitted to the rotating shaft, insulated from ground by DuPont™ Kapton® tape, which the biasing wire is connected to.

the inner side of the sample can. This placement provided protection from deposited material, but put the spring too close to the heater. After a brief annealing at 850 °C, the precession of the can deformed the spring such that electrical contact was only made for half a revolution. Clearly further modifications were needed.

Wiring Schematics

The final design for the sample biasing connections inside the deposition chamber is shown schematically in Fig. B.1, along with the pre-existing parts. In order to relocate the slipping, spring connection far away from the heater, a new part was fabricated by the Advanced Manufacturing Center on campus. This new collar was fitted to the rotating shaft ~60 cm above the heater, where the temperature is <100 °C when the heater is <1200 °C. A Ni/Cr wire was used to electrically connect the collar to the Ta can at the bottom of the arm. The connection to the can is made by a Ta screw at the top of the can, where the temperature is <600 °C when the heater is <1200 °C.

The electrical connections at the top of the arm are made via a high power UHV feed-through on the side of the manipulator arm flange. A thick Cu wire runs through the flange (insulated

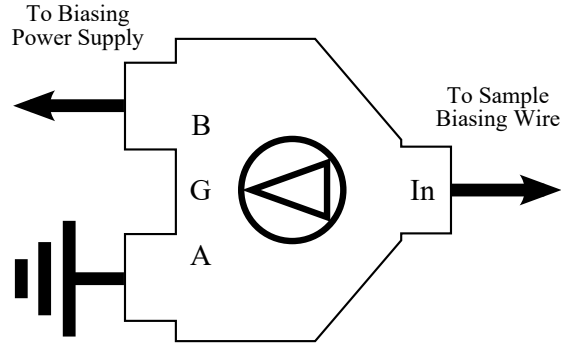


Figure B.2: Diagram of external switch for deposition chamber biasing and grounding connections. This is a high voltage, RF compatible switch that allows the heater can to be easily toggled between grounding and and a high voltage power supply.

Table B.1: Switch positions and the corresponding states of the A, B, and In connections in Fig. B.2. Because A is always grounded, A and B can be tied together by setting the switch to the “Ground” position. **This will short a connected power supply.**

State	A	B	In
A	Ground	Ground	A
Ground	Ground	Ground	Float
B	Ground	In	B

by alumina ceramic beads) and ends in a connection to a Ta foil spring (0.25 mm thick). This spring makes the slipping connection to the steel collar. A double layer of 0.003 inch Kapton® tape insulates the Ta spring and steel collar from the outer shaft of the manipulator arm, which is grounded. (Kapton® tape is a UHV compatible, adhesive polymer tape with a breakdown voltage between 2.2 kV/mil and 4.2 kV/mil and a glass transition temperature between 360 °C and 410 °C.)

When applying a DC bias to the sample relative to the deposition chamber, which is always grounded, one is effectively creating a large capacitor with a high voltage and capacitance. Thus, when the biasing is complete, the charge must be safely shunted to ground to prevent accidental discharge that could damage equipment or people. To facilitate this, as well as provide a simple means of switching between isolating, biasing, and grounding the sample, a RF switch was installed on a panel beside the deposition chamber. A diagram of this switch and the wiring to it is shown in Fig. B.2, and a brief description of the switch’s three states is given in Table B.1.

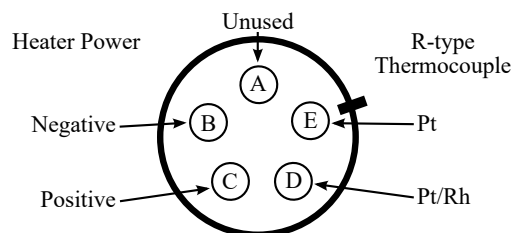


Figure B.3: Diagram of the connector pins for the new 5-pin electrical feed-through on the deposition chamber manipulator arm. The view is of the end of the cable connector. The feed-through is an ISI (MDC) model #9142006 Del Seal 2.75 inch OD conflat feed-through. Each pin is rated for up to 700 V and 10 A of power.

5-pin Electrical Feed-Through for Manipulator Arm

In initial designs for the sample biasing, the biasing wire ran down the central, static shaft of the manipulator arm, alongside the heater power and thermocouple wires. The addition of the biasing wire required purchasing a new, 5-pin feed-through for the manipulator arm, through which all electrical connections were made. The final design for sample biasing described above does not use all of this 5-pin feed through, however, but the new feed-through is sturdier and easier to use than the old electrical connections, and so was kept in place. Only four of the pins are in use, as shown in Fig. B.3.

Considerations for Stability and Longevity

To date, the sample biasing wiring has been in place for three months without losing continuity. The biasing has been tested up to ± 350 V for 5.5 h with the heater at 1200°C during magnetron sputtering. A small leakage current is observed at elevated temperatures, equating to a resistance of $\sim 500\text{ k}\Omega$ between the heater can and ground. Because this resistance varies from time to time, and because it only appears at high temperatures, it is most likely caused by a breakdown of the insulating washers that isolate the can from the outer steel shaft of the arm. These washers are coated with deposited material, and need routine cleaning and replacement.

Even with this leakage and a current carrying plasma, it is possible to maintain a 350 V bias between the sample and ground with ~ 25 mA of current with the heater at 1200°C . This represents a worst-case-scenario; lower voltages obviously require less current to sustain, and with a bias

of -350 V the current is $<15\text{ mA}$, due to the relatively low conductivity of positive ions in the sputtering plasma. With no plasma, a $\pm 400\text{ V}$ bias can be maintained with a current of $\sim 2\text{ mA}$.

Besides the high resistance short to ground at elevated temperatures, which may degrade with time as the insulating washers become more contaminated, there are several possible points of failure. The most likely problem would be the deposition of material along the biasing wire. Build up of an insulating layer either on the Ta foil spring or on the stainless steel collar would break electrical connection. However, the frequent rotation is likely to scrape deposited layers off and expose conducting metal. The Ta foil spring may also lose contact or become bent, in which case it will need to be reshaped.

The biasing wire may also become grounded if the Kapton® tape breaks or if the ceramic insulation around the Ni/Cr wire becomes contaminated by deposition flux. The buildup of deposited material on the ceramic tubing will occur, but it should not become a problem for at least several years. Similarly, the Kapton® tape should be stable unless it is exposed to high temperatures, is torn, or if the Ta foil spring wears through the tape. Should the tape become damaged, it can easily be replaced by disconnecting the stainless steel collar, removing the old tape, and replacing it with new tape in the same region.

A simple method for testing the functionality of the biasing wire without venting the chamber is to disconnect the external wire, thus isolating the heater can. A multimeter should confirm no connection between the biasing wire feed-through and ground. Following this, the trolley transfer arm can be extended until it is in contact with the sample can. A multimeter should now show a very low resistance connection to ground, which should remain stable through a full rotation of the manipulator arm. Should further testing be needed, the manipulator arm should be removed from vacuum, and visually inspected. Fig. B.4 shows a few photographs of the installed biasing wire connections.

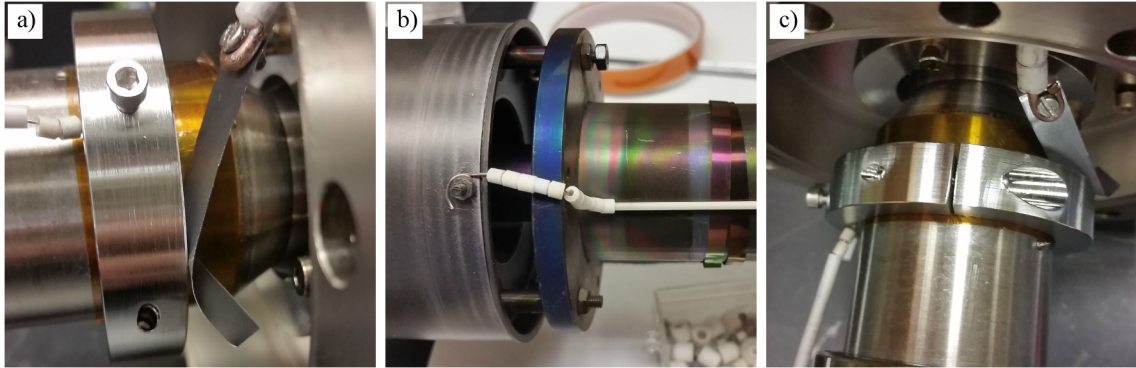


Figure B.4: Photographs of the sample biasing wiring for the deposition chamber sample manipulator arm. (a) The slipping spring connection at the top of the manipulator arm, showing the collar, Ta foil spring, Kapton insulation and ceramic insulated Ni/Cr wire. (b) Ni/Cr wire connection at the sample can. (c) Gap in the steel collar over which the spring moves.

Biography of the Author

David M. Stewart was born on July 3, 1989 in Royal Palm Beach, Florida. He graduated from Royal Palm Beach High School in May of 2007. David attended the University of Florida, Gainesville, Florida, where he worked as a research assistant to Dr. David A. Micha from Spring 2010 to Spring 2012. He received a Bachelor of Science degree in Physics from the University of Florida in 2011. He began graduate studies at the University of Maine, Orono, ME in the Fall of 2012. David worked as both a teaching assistant to Dr. David Clark in the Department of Physics & Astronomy and as a research assistant to Dr. Robert Lad in the Laboratory for Surface Science & Technology. He is a member of the $\Sigma\Pi\Sigma$ Honor Society of the Society of Physics Students, the American Physical Society, and the Materials Research Society. He is a candidate for the Doctor of Philosophy degree in Physics from the University of Maine in December, 2016.